

Thermal management of components for high energy physics experiments and space applications

Présentée le 13 septembre 2021

Centres pour l'innovation
Centre spatial suisse
Programme doctoral en microsystemes et microélectronique

pour l'obtention du grade de Docteur ès Sciences

par

Timothée Robert Sophus FREI

Acceptée sur proposition du jury

Prof. Ph. Renaud, président du jury
Prof. V. Gass, Dr A. Mapelli, directeurs de thèse
Dr B. Michel, rapporteur
Dr M. Despont, rapporteur
Prof. N. de Rooij, rapporteur

Acknowledgements

This project would have never been possible without the fantastic team of colleagues I had. Collaborating as a Ph.D. student with the European Organization for Nuclear Research (Organisation européenne pour la recherche nucléaire, CERN), the Swiss Center of Electronics and Microtechnology (Centre Suisse d'Électronique et de Microtechnique, CSEM) and Space Innovation, formerly Swiss Space Centre, at the Swiss Federal Institute of Technology of Lausanne (École polytechnique fédérale de Lausanne, EPFL) was an incredible opportunity, thanks to Prof. Volker Gass, Dr. Alessandro Mapelli, Dr. Michel Despont and Enrico Chesta.

All the enthusiastic and invaluable support I received from Dr. Diego Alvarez, Dr. Alessandro Mapelli and Dr. Elisa Laudi from CERN provided me with the opportunity to evolve as an engineer and scientist. I never felt restrained to pursue new ideas and propositions. I also would like to thank the Engineering Office team, the people orbiting around it, for the discussions, work-related or not. I am grateful to the CERN EP-DT's Thin Film Lab, Miranda van Stenis and Thomas Schneider, for the fast micromachining of glass wafers. The pieces of advice and expertise of Jerome Noel and Alexandre Gerardin were precious for the several tests. I also address special thanks to all the colleagues with whom I shared my office: Lenaïc, Michael, Michael, Jacopo, Clémentine, Ranit, Giovanna, Elise and last but not least, Riccardo.

I am furthermore very thankful to my colleagues from Neuchâtel. I am grateful to Arno, Branislav, Nemanja and Dara for the discussion and help on microfabrication. To Sarah, Gilles, Réal, Stéphanie and the rest of the bio-group, thank you for triggering my interest in bio-engineering and all the various topics we discussed more or less seriously. I also want to thank the photonic team for making me discover this part of the MEMS. Special acknowledgement to the CSEM's clean-room team for their valuable help, advice, and good company.

I am thankful to the space enthusiasts from Space Innovation. Gilles, Yannick, Julien, Grégoire and Martine for their cordiality and support. In addition to them, I would also thank Prof. Gass for his guidance, advice and trust over these four years.

I wish all my peer PhD students and colleagues from the three organisations a brilliant success in their careers, particularly to Maxime, with whom I spend countless hours of video calls during the pandemic.

Outside my everyday working environment, I have to thank the staff from the microfabrication centre from EPFL for their support. I would like to warmly thank my friends and family for their support. In particular, Martine and Constance for their unconditional support during the last stage of the thesis. Finally, I address my deepest thanks to Morgane for the unconditional support of this long period. This work would not have been possible without your encouragement, joy and love.

To the ones I did not mention here, do not worry, I will not forget you. I am grateful full to have met all of you.

Abstract

High-energy physics (HEP) experiments and space missions share a common challenge: thermal management in harsh environments. The severe constraints in both fields make cooling of electronic components a major design concern. This thesis aims to develop high thermal conductivity, radiation hard devices for thermal management in HEP and space application with the help of micro-technologies.

Continuous advances in micro-engineering have opened the door to the development of smaller and more efficient cooling devices capable of handling increasing power densities with minimum mass and volume penalties. In this respect, previous works have focused on the use of micro-channels etched in single crystal silicon (ScSi) wafers to circulate a cooling fluid. However, whilst this technique represents the state-of-the-art for thermal management of silicon detectors, it poses several challenges, particularly those associated with the fluidic interconnections, compatibility with high operating pressures and coverage of large areas. A cooling scheme relying on two independent fluidic loops is proposed to overcome these limitations. The two cooling loops, referred to as the primary and the secondary cooling loops (i.e. PCL and SCL respectively), are connected through thermal and mechanical interfaces but do not share any fluidic interface. Both circuits work together to remove heat and control the temperature of multiple electronic components. The SCL transfers the heat generated at the source to the PCL, which transports it further away and dissipates it to the environment.

The present thesis investigates the use of micro-oscillating heat pipes (μ OHPs) to implement the secondary cooling loops. These devices offer great potential, particularly if embedded in silicon substrates. However, a better understanding of the mechanisms responsible for their self-actuated, two phase flow is essential to produce high performance devices which meet the stringent requirements of particle detectors and spacecraft.

Two types of dual-diameter μ OHPs were microfabricated: the first version used a glass wafer to close trenches etched in a silicon substrate, while an all-silicon construction was adopted in the second type. The thermo-compressed interface used to bond the two silicon wafers yielded excellent pressure resistance. The thermal performance of the μ OHPs was studied for different working fluids, charging ratios, orientations, and heat inputs, taking advantage of the transparent cover in the glass devices to monitor the two-phase flow for the different conditions. The results revealed that the performance of the proposed μ OHPs was orientation-independent. Furthermore, under certain conditions the equivalent thermal conductivity of acetone-charged devices exceeded that of an equivalent copper strip.

Finally, an innovative technique for charging and sealing the micro-cooling heat pipes was developed. It offers a low-volume, small-footprint solution to enclose working fluids in the devices.

The proposed technique, which relies on a compressed Indium preform to seal the inlet charging port, yield very good leak-tightness results.

Keywords: thermal management; micro oscillating heat pipe; microfabrication; hermetic sealing; on-detector cooling

Résumé

Les environnements complexes des expériences de physique à haute énergie et des missions spatiales partagent un défi majeur commun : la gestion thermique. Les contraintes sévères propres à ces deux domaines induisent un degré de complexité élevé pour le refroidissement de des composants électronique. Cette thèse vise à développer - à l'aide de la micro-fabrication - des dispositifs microfluidiques de gestion thermique résistant aux radiations et possédant une haute conductivité thermique, adaptés aux expériences HEP et aux missions spatiales.

Les progrès de la micro-ingénierie des dernières décennies ont ouvert la voie au développement de dispositifs de refroidissement toujours plus petits et efficaces, capables de gérer des densités de puissance croissantes des dimensions réduite. En effet, depuis 2013 des réseaux microfluidiques gravés dans des plaques de silicium monocristallin (ScSi) sont utilisés au CERN pour le refroidissement de détecteurs pixel. Bien que cette technique présente un avantage certain pour la gestion thermique des détecteurs en silicium, elle comporte cependant plusieurs faiblesses liées notamment celles associées l'interconnexion fluidiques et à l'intégration, le conditionnement et la qualification des dispositifs adaptés aux hautes pressions ou aux grandes surfaces. Un schéma de refroidissement fondé sur deux boucles fluidiques de refroidissement indépendantes est proposé pour surpasser ces limitations. Ces deux boucles de refroidissement, nommées les boucles de refroidissement primaires et secondaires - abrégées respectivement par PCL et SCL de par leurs dénominations anglaises -, sont thermo-mécaniquement interfacées, mais aucun échange fluidique n'a lieu. Les deux circuits travaillent de concert à enlever la chaleur et contrôler la température des multiples composants électroniques présent. La SCL transfère la chaleur générée par la source vers la PCL. Cette dernière transporte à son tour la chaleur plus loin et la dissipe dans l'environnement.

La présente thèse explore l'utilisation de micro caloducs oscillants (μ OHPs) implémentés en tant que boucles de refroidissement secondaires. Ces dispositifs possèdent un grand potentiel, particulièrement s'ils se trouve intégrées dans des substrats en silicium. Toutefois, une meilleure compréhension de leur fonctionnement, en particulier de leur mécanisme de démarrage bi-phasique, est essentielle pour obtenir des dispositifs à haute performance thermique compatible avec les exigences strictes des détecteurs de particules et vaisseaux spatiaux.

Deux types de μ OHPs à deux diamètres hydrauliques ont été réalisés. Le premier type consiste en microcanaux gravés dans du silicium et scellés par du verre, alors que le second type adoptait une construction entièrement en silicium. Les microcanaux de ce dernier type ont été scellés par thermocompression et démontrer une excelle résistance aux pressions statiques internes. Les performances thermiques des dispositifs ont été étudiées avec différent fluides et quantités de fluide, pour diverse orientations et puissances. Les différents types de circulation des fluides bi-phasiques ont été suivis grâce à l'accès visuel laissé par les couvercles en verre des dispositifs.

Les résultats ont révélé que les performances atteintes par les μ OHPs ne dépendaient pas de l'orientation de ces derniers. De plus, sous certaines conditions, la conductivité thermique apparente des dispositifs remplis d'acétone dépassa celle d'une bande de cuivre.

Finalement, une nouvelle méthode de remplissage et fermeture pour les micro-caloducs a été développée. Elle offre une fermeture étanche pour les fluides calo-transporteurs dans ces dispositifs avec un faible volume et une faible empreinte surfacique. La technique proposée pour fermer définitivement les ports de chargement a démontré une très bonne étanchéité.

Mots-clés : gestion thermique, micro caloducs oscillant, micro-fabrication, fermeture étanche, refroidissement intégré

Table of Contents

Acknowledgements.....	iii
Abstract	v
Résumé	vii
List of Figures	xiii
List of Tables	xx
List of Symbols	xxii
Chapter 1 Introduction.....	27
1.1 Structure of the thesis	29
Chapter 2 Literature review	31
2.1 Silicon-based semiconductors sensors.....	31
2.1.1 Micro-strip sensors	31
2.1.2 Pixel Sensors	32
2.1.3 Use of Silicon Sensors	33
2.2 Radiations	36
2.2.1 Radiation Damages.....	36
2.2.2 Radiation Levels.....	37
2.2.3 Material Budget.....	37
2.3 Need for Cooling	38
2.3.1 Forced Gas Convection	40
2.3.2 Minichannels MPFL.....	40
2.3.3 Microchannels MPFL.....	43
2.3.4 Micro Heat Pipes (μ HPs)	49
2.3.5 Thermal Straps	64
Chapter 3 A Two-circuit Cooling Approach Based on Micro Oscillating Heat Pipes.....	67
3.1 Beyond the Used Single-loop Scheme	67
3.2 μ OHP Design for the SCL.....	69
3.3 Test Device Overview	72
3.3.1 Device Microfabrication.....	72
3.3.2 Device Sealing	72
3.3.3 Tested Parameters.....	72
3.4 Summary.....	73
Chapter 4 Methods & Experimental Apparatus	75
4.1 Thermal Performance Test Setup	75
4.1.1 μ OHP Test-Section.....	76
4.1.2 Working Fluid	77
4.1.3 TEC Module.....	78

4.1.4	Heating	79
4.1.5	Instruments & Data Acquisition	80
4.1.6	Experiment Validation and Protocol.....	81
4.1.7	Data Reduction	82
4.2	Evaluation of the Wafer Bond Quality.....	84
4.2.1	Standardized Test Structures	85
4.3	Summary	86
Chapter 5	μOHPs Microfabrication	87
5.1	Wafer Bonding Techniques Review.....	87
5.2	Microfabrication of the Prototypes.....	89
5.2.1	Layout	89
5.2.2	Fabrication Process Flow	90
5.2.3	Results.....	93
5.3	Microfabrication of the Proof-Of-Concept Demonstrator	95
5.3.1	Layout	96
5.3.2	Fabrication Process Flow	96
5.3.3	Results.....	97
5.3.4	Pressure Resistance.....	98
5.3.5	Discussion.....	110
5.4	Conclusions	111
Chapter 6	Flow Patterns & Thermal Performance.....	113
6.1	Flow Patterns.....	113
6.1.1	Acetone	115
6.1.2	Isopropyl Alcohol	116
6.1.3	C ₆ F ₁₄	117
6.2	Thermal Performance	119
6.2.1	Acetone	121
6.2.2	Isopropyl Alcohol	123
6.2.3	C ₆ F ₁₄	124
6.3	Discussion.....	126
6.4	Conclusion	132
Chapter 7	Lightweight Sealing Solution for Leak-tight Charging Port.....	133
7.1	Working Principle of the Proposed Sealing Method.....	133
7.2	Sealing Setup	134
7.2.1	Indium Pre-shaping	137
7.2.2	Flat Gasket.....	139
7.2.3	Alignment of the Charing Port	140

7.2.4	Vertical Displacement Control.....	140
7.2.5	Adhesive Reinforcement of the Indium	141
7.3	Results and Discussion.....	142
7.4	Conclusion	144
Chapter 8	Conclusions.....	145
8.1	Summary.....	145
8.2	Future Work.....	146
References	149
Appendix A.	Uncertainty analysis	173
Appendix B.	Applications-based Trade-off	175
B.1	Criteria.....	175
B.2	Scenarios	176
B.3	Evaluation	178
Appendix C.	LabVIEW software documentation.....	181
Appendix D.	Microfabrication Process Flows.....	189
D.1	Silicon and Glass Prototypes	189
D.2	Silicon Proof-of-Concept Demonstrators	192
Appendix E.	Charging methods.....	199
E.1	Back-filing	199
E.2	Micro-syringe	199
E.3	Thermodynamic Equilibrium Method.....	199
E.4	Capillary Tubing Methods	200
E.5	Vapour Flushing and Condensation	200
E.6	Liquid Pumping.....	200
E.7	Integration during the Fabrication.....	201
E.8	Discussion and Trade-off.....	201
Appendix F.	Complementary Review for the Design of μOHPs.....	203
F.1	Geometry and Hydraulic Diameter.....	203
F.1.1	Criterion for Horizontal Operation.....	204
F.1.2	Dual-diameter for Horizontal Operations.....	205
F.1.3	Microgravity and Hydraulic Diameter	206
F.1.4	Number of Turns	207
F.2	Heat Fluxes	208
F.3	Working Fluids	210
F.4	New Lower Hydraulic Diameter Limit	211
F.5	Figure of Merit of the Working Fluid	212
F.6	Latent and Sensible Heat	213

Appendix G. High-speed Times Strips	215
Appendix H. Existing Packaging and Sealing Solutions	219
I.1 Valve Sealing.....	219
I.2 Tube Crimping	219
H.3 Induction Hole Sealing	219
H.4 Low Melting Point Alloy Pumping	220
H.5 Solutions Comparison	221
Appendix I. Finite Elements Methods simulation	223
I.1 Volume-of-Fluid method	223
I.2 Physical model and method	223
I.2.1 Physical model	223
I.2.2 Method.....	224
I.2.3 Mesh	225
I.2.4 Conditions	225
I.3 Results.....	225
I.3.1 CASE I: Imposed temperature gradient	225
I.3.2 CASE II: Imposed heat flux.....	228
I.4 Conclusion	230
Copyright Licenses	231
Curriculum Vitae.....	233

List of Figures

Figure 2.1. (a) Representation of an n-type silicon strip detector. (b) Representation of real and ghost hits with a strip sensor with orthogonal arrangement when two particles traversing the detector. (c) Unambiguous hits when two particles traverse a pixel sensor	32
Figure 2.2. Schematic cross-section of (a) a planar sensors design and (b) a 3D sensor design.....	32
Figure 2.3. (a) Cross-section of a hybrid pixel sensor with the read-out electronic (ASIC) bump-bonded to the sensor. (b) Cross-section of a monolithic silicon sensor in which the ASIC and the sensors are integrated on the same substrate.	33
Figure 2.4. Cooling scheme of a hybrid silicon sensor. (a) Mini-channel cooling. The mini-channel is fixed to the support of the substrate at a distance from the sensor. The cooling performance is limited by this distance and the conductivity of the substrate. (b) The mini-channel is embedded in the supporting elements (carbon foam with carbon fleece), with a closer location to the sensor and an intermediate substrate. (c) Cold plate with microchannels. The plate supports the sensor while providing efficient cooling closer to the sensor. (d) Embedded microchannels in the ASIC reduce the thermal path.	39
Figure 2.5. (a) ALICE SPD stave: the thermal connection between the squeezed cooling tubes, the sensors and the carbon support is done by thermal grease [86]. (b) ATLAS IBL stave cross-section [83].....	41
Figure 2.6. (a) ALICE ITS IB stave fully assembled [87] (b) Schematic layout of a stave of ALICE ITS OB (mechanical and cooling structure) [54].....	41
Figure 2.7. Design propositions for ATLAS ITK OB staves: schematic of the module connecting the pixel sensor to the evaporative CO ₂ cooling line (adapted from [90], [91]).	42
Figure 2.8. Picture of the (a) a NA62 GTK station [135] and (b) cooling plate alone, assembled with capillaries [142]. (c) Partial cross-section scheme of the cooling plate assembled to the silicon sensor.....	44
Figure 2.9. (a) Cross-section of the proposed VeLo module with front end hybrid circuit construction [147]. (b) Picture of three constructed VeLo module with the four sensors and the front end electronics assembled on each silicon plate [135]; here in the SPS test-beam.	45
Figure 2.10. (a) AlN cooling plate with brazed capillaries and carbon supporting structures [146]. (b) Titanium 3D printed cooling plate with dummy heaters place on it, mimicking the heat load from the electronics and the sensors [147]. (c) Schematic of the layout of the silicon cold plate with the dimension of the restrictions and microchannels (adapted from [148])......	45
Figure 2.11. Polyimide micro-cooling system for silicon sensors [136]. (a) Sketch of in-going and out-going flows. (b) Cross-section of the microchannels.	46
Figure 2.12. Concept of integration of silicon frames with microchannels into the staves for the Inner Layers of ALICE ITS [54].....	46
Figure 2.13. DEFPFET monolithic sensor of the BELLE II Vertex detector and the integrated ladder [138], [150], [151]. (a-d) Process flow of the production of the silicon ladder and embedded microchannels. (e) Illustration of one DEFPFET ladder with the inlet, outlet and main heat input locations. (f-g) Layout and SEM image of the pillars located at the inlet manifold. (d) Cross-section of the inlet and outlet microchannels. (h) 3D-printed connector glued to the silicon ladder and connected the fluidic lines.	47
Figure 2.14. Buried microchannels [135]. (a) Schematic of the process flow. (b) SEM image of the cross section of buried micro channels in silicon.....	48
Figure 2.15. Schematic of an μ GHP with a channel which serves as common cold pool or just as charging channel.	50

Figure 2.16. Cross-sections of complex channel geometries of μ GHPs. The substrate is in grey, the liquid phase in blue and the vapour in white. (a) Stacked triangular groove with triangular artery constituted of three layers. (b) Star groove constituted of three layers. (c) Rhombus groove layer. (d) Triangular groove with small return arteries in the same plane.	50
Figure 2.17. Schematics of (a) a μ LHP and (b) a μ CPL.....	53
Figure 2.18. Schematic representation of a closed-loop μ OHP. The heat supplied vaporizes the liquid entering the area, while the vapour entering the condenser condenses and cools down.	55
Figure 2.19. Schematic of a μ VC. The heat is spread by evaporation of the fluid on one side and condensation on the opposite side. The wicking structures along the edges of the chamber help to liquid to return to the evaporator and for structural resistance, support pillars might be integrated with, or without, capillary role.....	60
Figure 2.20. (a) Schematic of encapsulated graphite, which adapts several heat source with different heights and locations. (b) Schematic of supported graphite	64
Figure 2.21. Model of the thermal straps used to control the temperature of the SXS on board JAXA's ASTRO-H [270].	65
Figure 3.1. Cooling schemes for (a) a single heat source from which the SCL removes the heat and transfers it to the PCL. (b) Several heat sources connected to independent SCLs while the PCL remove the heat from the cold side of the SCLs.....	68
Figure 3.2. Schematic representation of a μ OHP with eleven turns, with the evaporative and condensing area represented in in red and blue respectively. The values of the different parameters used in this thesis are summarised in Table 3-1.	70
Figure 3.3. Schematic representation of (a) a U-turn with two different diameters with a facettet perimeter, (b) the cross-section for a dual-diameter pair of microchannels.....	70
Figure 3.4. 3D Representation of the μ OHP with the connector.....	73
Figure 4.1. Schematic representation of the experimental setup with the connected instruments.	75
Figure 4.2. CAD view of the μ OHP test section with cold air intake and hot air exhaust.	76
Figure 4.3. Illustration of the orientation angle α	77
Figure 4.4. μ OHP mounted on the heat sink and TEC module.	77
Figure 4.5. Picture a μ OHP charged with acetone ($\phi = 50\%$). Acetone is distinguishable inside the microchannels.	78
Figure 4.6. TEC module. (a) Picture of the Adaptive™ ET-071-10-13, here with a PT100 temperature sensor mounted on the cold side. (b) Geometrical tolerances of the TEC module from the datasheet of the manufacturer.	79
Figure 4.7. (a) Picture of the polyimide thin-film heaters produced at CERN. (b) Scheme with dimensions of the heaters.	80
Figure 4.8. Schematic of the position of the temperature sensors used.	80
Figure 4.9. Schematics of a frame sequence capture and transformed in a time strip. (a) Slug-plug flow in the evaporator, (b) straightened microchannel on the central axis and (c) corresponding time strip.	83
Figure 4.10. Illustration of the extraction of the position of the liquid-gas interfaces.	84
Figure 4.11. CERN EP-DT standard pressure test setup for silicon device Manual pressure pump (right) and safety chamber (left) with the dedicated clamping inside.	85
Figure 4.12. Drawing of the standardized design for pressure tests of microchannels (Design by CERN)	86

Figure 4.13. Drawing of a pressure test sample with circular cavity.	86
Figure 5.1. Layout for 6in wafers for the test vehicles. The etched microchannels are in blue. The green areas are covered by titanium and gold.	89
Figure 5.2. Images of two bonded pairs of wafers with etched μ OHPs. Defects are visible on the image (a) on the periphery of the wafers and several locations over the etched microchannels, whereas (b) only show defects on the periphery.	91
Figure 5.3. Laser-cut stainless steel stencil used to pattern the metal layers on 6in wafers.	91
Figure 5.4. Schematic process of the preparation of the connector.	92
Figure 5.5. Schematic of the thermocompression of the connector by the mean of a dedicated tool with heated chuck.	93
Figure 5.6. Temperature profile for the thermocompression of the connector.	93
Figure 5.7. μ OHP with a connector. The device presented here measures 60mm by 20mm.	94
Figure 5.8. SEM cross-section of the microfabricated μ OHPs in silicon capped by a glass (top of the SEM image).	94
Figure 5.9. Burst pressure of the pressure test samples from four pairs of wafers.	95
Figure 5.10. Burst pressure of the pressure test samples from four pairs of wafers.	95
Figure 5.11. Layout on 6in wafers for the end-product devices. Blue and green areas represent the etching area for the microchannels. The magenta areas delimit the deposition of the titanium and gold layers deposited after the bonding. The red identifiers of the samples and μ OHPs are present only for reference.	96
Figure 5.12. Illustration of the safety margin kept to avoid exposition of gold during the silicon and silicon oxide etching steps. The etching layout for gold is in purple and the one of Si and SiO_2 in teal.	97
Figure 5.13. μ OHPs after dicing remaining on the dicing frame and tape. Fractures are visible on the μ OHPs no.1 and no.6.	98
Figure 5.14. Close view of the fracture on μ OHP no.6. Fracture are visible on the top surface and tends to favour a path parallel to the microchannels.	98
Figure 5.15. Burst pressure of rectangular microchannels microfabricated by gold thermocompression with different membrane thickness t_2 . Direct bonding values for comparison[292].	99
Figure 5.16. Sample Btl – Fracture of the membrane. The microchannel is visible. A part of the membrane remained attached despite the fracture, while two distinct parts detached entirely from the sample.	100
Figure 5.17. Sample B3 – Partial fracture of the membrane above a 1.5mm-wide channel. The fracture is visible on the left, top and bottom sides of the sample. It did not propagate to the right side.	100
Figure 5.18. Sample C1 – A deformation of the membrane above the microchannel is visible, but leaks appeared at the edges of the sample.	100
Figure 5.19. Dicing scheme for samples for SEM.	101
Figure 5.20. Sample A2 - Dicing and cross sections. The green area represent the part of the membrane t_2 that disappeared during the dicing.	101
Figure 5.21. Sample A2 (B-B) – SEM image of the fractured membrane and microchannel.	102
Figure 5.22. Sample A2 (B-B) – EDS image of the fractured membrane and microchannel.	102

Figure 5.23. Sample A2 (B-B) – Zoomed SEM image on the ledge of channels. The gap between the etched microchannel and gold is visible. Roughness on the gold covered area is visible.	103
Figure 5.24. Sample A2 (B-B) – EDS image of the fractured membrane and microchannel. Partial delamination of the titanium and gold layers from the Si-SiO ₂ substrate is visible on several location at the ledge of the microchannel.....	103
Figure 5.25. Sample A2 (B-B) – SEM image of the silicon tip. Roughness in visible on the gold layer. A gap between the tip and the substrate is noticeable.....	104
Figure 5.26. Sample A2 (B-B) – EDS image of the silicon tip. Gold and titanium remains on visible on the lower edge of the tip.	104
Figure 5.27. Sample A2 (A-A). SEM image of a fracture of the interface that changed path through the <i>t</i> ₂ membrane.	105
Figure 5.28. Sample A2 (A-A) – SEM image of a cohesive failure 130μm from the wall of the microchannels.	105
Figure 5.29. Samples B4 - Dicing and cross section. The green area represent the part of the membrane <i>t</i> ₂ that disappeared during the dicing.	106
Figure 5.30. Samples B4 (A-A) – SEM image of the 300μm-wide microchannel. Gold and titanium adhesive failure is visible on both sides of the microchannel.	106
Figure 5.31. Samples B4 (A-A) – SEM image of the top of the wall of the microchannel. Ti-Au layers are seen to roll on them-self.....	107
Figure 5.32. Samples B4 (A-A) – EDS image of the top of the wall of the microchannel. Titanium or gold are absent from the ledge of the channel. They are seen further away on the right (clear areas).	107
Figure 5.33. Samples C1 - Dicing and cross section. The green area represent the part of the membrane <i>t</i> ₂ that disappeared during the dicing.	108
Figure 5.34. Sample C1 (A-A) – SEM image of the fractured membrane and microchannel. The right side of the membrane is missing and a default in the <i>t</i> ₁ membrane at the bottom left is revealed by the SEM picture.....	108
Figure 5.35. Samples C1 (A-A) – EDS image of the releveled gold. Adhesive failure is deductible as the Ti-Au layers are missing locally.	109
Figure 5.36. Sample C1 (A-A). Detailed SEM image of the default in the membrane <i>t</i> ₁	109
Figure 5.37. Sample C1 (B-B) – SEM image of the microchannel wall and the capping membrane <i>t</i> ₂ . The deformation of <i>t</i> ₂ remains invisible when observed with an SEM. Cohesive failure is distinguishable.....	110
Figure 6.1. Illustration of the different flow patterns occurring in a μOHP and OHP.	114
Figure 6.2. Flow pattern map of the μOHP charged with Acetone and operating at (a) α = 0°, (b) α = -90°, (c) α = 45° and (d) α = 90°.	116
Figure 6.3. Flow pattern map of the μOHP charged with IPA and operating at (a) α = 0°, (b) α = -90°, (c) α = 45° and (d) α = 90°.	117
Figure 6.4. Flow pattern map of the μOHP charged with C ₆ F ₁₄ and operating at (a) α = 0°, (b) α = -90°, (c) α = 45° and (d) α = 90°.	118
Figure 6.5. Time-strip obtained at 11W in horizontal position for (a) C ₆ F ₁₄ (φ = 75%, 10 th U-turn) and (b) Acetone (φ = 50%, 3 rd U-turn).....	119
Figure 6.6. Schematic of the position of the temperature sensors used.	120

Figure 6.7. Evaporator's temperature T_e for acetone, an empty μ OHP and a copper thermal strap. The empty device and the copper display quasi-linear rising temperatures, while an inflection is visible for acetone.....	120
Figure 6.8. Apparent thermal conductivity as a function of the heat input of μ OHP charged with acetone for different orientations and charging ratios. Values for an empty μ OHP and a copper thermal strap with the same length and cross section are given for comparison.	122
Figure 6.9. Apparent thermal conductivity as a function of the heat input of IPA-charged μ OHP for different orientations and charging ratios. Values for an empty μ OHP and a copper thermal strap with the same length and cross section are given for comparison.	124
Figure 6.10. Apparent thermal conductivity as a function of the heat input of μ OHP charged with C_6F_{14} for different orientations and charging ratios. Values for an empty μ OHP and a copper thermal strap with the same length and cross section are given for comparison.	126
Figure 6.11. Effects of the charging ratio on the figure of merit M_{PHP} for several working fluids with the following parameters for the microchannel: $w_1 = 400\mu m$, $w_2 = 255\mu m$ and $h = 400\mu m$; with a total of eleven dual-diameter pairs and no symmetric microchannel pairs ($Nt = N = 11$).	128
Figure 6.12. Operational map for Acetone in all tested conditions.	129
Figure 6.13. Operational map for IPA in all tested conditions.	130
Figure 6.14. Operational map for C_6F_{14} in all tested conditions.....	130
Figure 7.1. Schematic view of the procedure used for the initial Indium cold welding. (a) Tube's tip inserted through the flat gasket. (b) Fluid injection. (c) Indium deformation.	134
Figure 7.2. Charging and sealing system with the shims placed between the different blocks. Here without silicon micro heat pipe.....	135
Figure 7.3. Exploded CAD view of the charging and sealing apparatus used to seal inlets by Indium cold welding. (A) Support back plate. (B) Gas chromatography syringe. (C) Manual shut-off valve. (D) High pressure low dead volume T connector and supports. (E) Stainless steel tube 1/32"OD – 100 μm ID. (F) Syringe alignment support. (G) M3 screws (ISO4762). (H) Spacer – Tip travel. (I) Gasket clamp with syringe pass-through. (J) Spacer – Gasket clamp. (K) Base plate. (L) Flat gasket. (M) Syringe supports. (N) Syringe-to-valve adapter. (O) Stainless steel tube 1/16inOD – 500 μm ID. (P) 3mm pins. (Q) Silicon device.	136
Figure 7.4. Schematics (Not to scale) of the two inlets for (a) the prototypes, glass on top and silicon on the bottom)and (b) the proof of concept demonstrators (silicon for both top and bottom).	138
Figure 7.5. Inlet filled with Indium. (a) Result of the reflow process. Surface tension moved the wire from the centre of the inlet. (b) Correctly formed Indium preform, wire removed.	139
Figure 7.6. μ OHP after Indium reflow. Protruding wire is visible on the right side of the device. The inlet at the top is sealed, while the bottom one will remains unobstructed once the wire removed.	139
Figure 7.7. (a) Flat gasket positioned on the tip of tube E that pass-through the block I. (b) Setup of the setup used to align a μ OHP with the gasket and the clamping Al block though using a microscope	140
Figure 7.8. Schematic cross section of the setup for charging and sealing with labels and corresponding thicknesses.....	141
Figure 7.9. (a) View from above of a sealed charging port with Indium. The diameter of the inlet is 800 μm . (b) Detailed view of the inlet at 45°. The microchannel is hidden by the visible Indium (grey).	142

Figure 7.10. Glue deposited on a freshly sealed μ OHP. The central deformation of Indium, with deformation on the wall is visible through the glue.....	142
Figure 7.11. Scheme of a clamped seal sample used for leak-tightness test and pressure resistance.....	143
Figure 7.12. μ OHP after sealing. The two charging ports blocked by Indium and glue are visible on the left side.....	143
Figure B.1. Scheme of the possible integration with bump-bonded or wire-bonded components.	176
Figure B.2. Schematic of the silicon heating elements distributed on a stave with different orientations. (a) Isolated stave with elements' description. (b) Illustration of integration of staves in a cylindrical way.	177
Figure B.3. (a) Schematic view of the apparatus considered for the third scenario. (b) Cross-section of the apparatus.	177
Figure C.1. Data acquisition loop.	181
Figure C.2. Loop queuing current and voltage measurements.	182
Figure C.3. Loop writing queued elements to file and displaying the elements on a wave chart.	182
Figure C.4. Loop controlling the cooling fan of the heatsink.....	183
Figure C.5. Loop control of the heating element.	184
Figure C.6. PID loop controlling the TEC module.....	185
Figure C.7. Overview of the user interface.	186
Figure C.8. Details of the configuration panel.....	186
Figure C.9. Details of the Acquisition panel.	187
Figure C.10. Details of the control panel.	187
Figure E.1. A schematic of charging a micro heat pipe by vapour flushing and condensation (adapted from [320]). (a) Vapour fills the μ HP. (b) Vapour condensates when the μ HP is cooled and the outlet valve is closed. (c) Inlet valve is closed once the target quantity is reached.	200
Figure F.1. Parameters affecting the flow pattern and thermal performance of the OHP and μ OHPs.	203
Figure F.2. Influence of the number of turn on the maximal heat flux in horizontal position accordingly to (F.20).	208
Figure F.3. Heat flu for PHP start-up as a function of bulk fluid temperature ($\epsilon = 2.5\mu\text{m}$, $r_{in} = 1\text{mm}$, $\delta l = 10\mu\text{m}$) [326].....	210
Figure F.4. Schematic representation of the values L_w and L_t used for the determination of the lower limit for hydraulic diameter of the microchannels.	212
Figure G.1. Identification of the different U-turn in the evaporator for time-strips.....	215
Figure H.1. Induction hole sealing [193]. (a) Schematic of the magnetic sealing system. Example of successful sealing of a sample immersed in water (0.17g, 8.4s, 400W): (b) initial pad, (c) front view after melting, (d) View from the back after melting.....	220
Figure H.2. Magnetic sealing technique. (a) Picture of the charging channel with the LMPA in place before sealing. (b) Picture of the charging channel after charging. The LMPA reached the charging hole and continued in the channel, sealing it. (c) Schematic of the LMPA charging method. [312].....	220
Figure I.1. Scheme of phase affectation in Cartesian grid using piecewise linear interface calculation. (Ikosaeder – 11 march 2014 – CC By-SA 3.0).....	223

Figure I.2. Model representation (left) and the two different volumes patched (right).....	224
Figure I.3. Detail of the mesh at the U-turn.	225
Figure I.4. Temperature and volume fraction of water at different time steps.	226
Figure I.5. Temperature and liquid water volume fraction at the last step with details of the evaporator. Small bubbles rises from the heated wall.	227
Figure I.6. Temperature and liquid water volume fraction side-by-side at different time steps of the second case.....	228
Figure I.7. Temperature and liquid water volume fraction side-by-side at different time steps of the second case.....	229

List of Tables

Table 2-1. Non-exhaustive list of sensor types, experiments and space missions in which they are in use and their respective advantages and disadvantages. Adapted from Allport [22].	35
Table 2-2. Summary table of radiation levels (TID and NIEL) for several orbits and experiments.	37
Table 2-3. Material budget for various materials and refrigerants.	38
Table 2-4. Non-exhaustive summary of studies on μ GHPs	51
Table 2-5. Non-exhaustive summary of μ CPL and μ LHP researches.	54
Table 2-6. Non-exhaustive summary of studies on μ OHPs and mini-OHPs.	57
Table 2-7. Non-exhaustive summary of investigations on μ VCs.	61
Table 2-8. Summary table of recently conducted studies on mini and micro heat pipe for microgravity.	63
Table 3-1. Selected design parameters of the tested geometry.	71
Table 3-2. Critical diameters, static and dynamic, for different fluids on ground and in microgravity conditions. The critical bond number in microgravity is not included as the values are unrealistic.	72
Table 4-1. Main properties of working fluids.	78
Table 4-2. Properties of the TEC module.	79
Table 5-1. Summary table of wafer bonding techniques	88
Table 5-2. Bonding parameters used for the anodic bonding on the <i>Süss Microtec SB6L</i> .	90
Table 5-3. Layer deposition thicknesses and tools.	92
Table 5-4. Summary of pressure samples with thinned thickness t_2 , burst pressure and the corresponding fracture mode observed (illustrated in Figure 5.16 to Figure 5.18).	99
Table 6-1. Apparent thermal conductivity for different heat loads and condenser's temperatures for acetone and C_6F_{14} . ^(a) Linear interpolation of nearest neighbouring values.	127
Table 6-2. Calculated value for the heat flux for start-up and dry-out for the selected working fluids.	131
Table A-1. Error uncertainties of the instruments.	173
Table A-2. Propagation of the uncertainties.	174
Table B-1. Selection criteria definitions and weights for each scenarios.	175
Table B-2. Evaluation results of the passive heat transport devices according to the scenario 1.	178
Table B-3. Evaluation results of the passive heat transport devices according to the scenario 2.	179
Table B-4. Evaluation results of the passive heat transport devices according to the scenario 3.	180
Table D-1. Masks and substrates for anodic bonding.	189
Table D-2. Anodic bonding - Processing wafers A	189
Table D-3. Anodic bonding - Processing wafers B.	190
Table D-4. Anodic bonding – Wafers A to wafers B.	191
Table D-5. Anodic bonding – Thin-films deposition at the inlets.	191
Table D-6. Masks and substrates for thermocompression	192

Table D-7. Gold thin-films wafer thermocompression - Processing wafers A.....	192
Table D-8. Gold thin-films wafer thermocompression - Processing wafers B.....	195
Table D-9. Gold thin-films wafer thermocompression - Wafer Bonding (wafer A to wafer B).....	197

List of Symbols

Roman symbols

A	Area	$[m^2]$
Au	gold	
Bo	Bond number	$[-]$
Ca	Capillary number	$[-]$
C_f	Friction coefficient	$[-]$
c_p	Specific heat capacity	$[J/(kg \cdot K)]$
D	diameter	$[m]$
E	Energy	$[J]$
Ec	Eckert number	$[-]$
G	Gravitational acceleration	$[m^2/s]$
H	Channel height	$[m]$
h_{fg}, h_{lv}	Latent heat of vaporisation	$[J/kg]$
I	Electrical current	$[A]$
Ja	Jackob number	$[-]$
K	Thermal conductivity	$[W/m \cdot K]$
k	Correction factor	$[-]$
L	Length	$[m]$
M, m	Mass	$[kg]$
N	Number of asymmetric microchannel pairs	$[-]$
N_t	Total number of microchannel pairs	$[-]$
P	pressure	$[Mpa]$
Q	Supplied power input	$[W]$
q	heat flux	$[W/cm^2]$
R	radius	$[m]$
Re	Reynolds	$[-]$
R_{th}	Thermal resistance	$[K/W]$
Si	Silicon	
SiO_2	Silicon dioxide	
t	Thickness	$[m]$
T	Temperature	$[^{\circ}C]$
Ti	Titanium	
TiW	Tungsten-titanium	
U	Electrical voltage, speed	$[V], [m/s]$
w	Width	$[m]$
We	Weber number	$[-]$

Greek symbols

α	Orientation angle	$[^{\circ}]$
β	Fraction of channel occupied by liquid slugs	$[-]$
Δ	Difference, gradient	$[-]$
δ	Liquid film thickness	$[m]$
θ	Contact angle	$[^{\circ}]$

κ	Specific heat ratio	[-]
μ	Viscosity , micro	[Pa · s]
ρ	Density	[kg/m ³]
σ	Surface tension	[N/m]
ϕ	Charging ratio [-]	[-]
χ	Vapour quality	[-]

Subs- and superscripts

*	Modified standard relation
μg	Microgravity
avg	Average
c	Condenser
e	Evaporator
fall	Falling
form	Formation
Ga	Garimella
in	Inner
k	Kinetic
max	Maximum
min	Minimum
n	Nucleation cavity
s	Surface
tp	Two-phase
wf	Working fluid

Acronyms

AIC	Aluminium Carbide
ALD	Atomic Layer Deposition
ALICE	A Large Ion Collider Experiment
APG	Annealed Pyrolytic Graphite
ASIC	Application-Specific Integrated Circuit
ATLAS	A Large Toroidal Appartus
CCD	Charge-Coupled Device
CERN	European Centre Of Nuclear Research
CFRP	Carbon Fibre Reinforced Polymer
CMi	Centre De Microtechnique
CMOS	Complementarity Metal Oxide Sensor
CPL	Capillary Pumped Loop
CSEM	Centre Suisse d'Electronique Et Microtechnique
CTE	Coefficient of Thermal Expansion
DISR	Descent Imager / Spectral Radiometer
DRIE	Deep Reactive Ion Etching
EPFL	Ecole Polytechnique Fédérale De Lausanne
FCC	Future Circular Collider
GAIA	

<i>GHP</i>	<i>Grooved Heat Pipe</i>
<i>GTK</i>	<i>GigaTraKer</i>
<i>HEO</i>	<i>High Earth Orbit</i>
<i>HEP</i>	<i>High Energy Experiment</i>
<i>HP</i>	<i>Heat Pipe</i>
<i>IB</i>	<i>Inner Barrel</i>
<i>IPA</i>	<i>Isopropyl Alcohol</i>
<i>IR</i>	<i>Infrared</i>
<i>ISRO</i>	<i>Indian Space Research Organisation</i>
<i>ISS</i>	<i>International Space Station</i>
<i>Itk</i>	<i>Inner Tracker</i>
<i>ITS</i>	<i>Inner Tracking System</i>
<i>JAXA</i>	<i>Japan Aerospace Exploration Agency</i>
<i>JWST</i>	<i>James Webb Space Telescope</i>
<i>LEO</i>	<i>Low Earth Orbit</i>
<i>LHC</i>	<i>Large Hadron Collider</i>
<i>LHCb</i>	<i>Large Hadron Collider Beauty</i>
<i>LHP</i>	<i>Loop Heat Pipe</i>
<i>LMPA</i>	<i>Low Melting Point Alloy</i>
<i>MALTA</i>	
<i>MEMS</i>	<i>Micro-Electro-Mechanical Systems</i>
<i>MEO</i>	<i>Medium Earth Orbit</i>
<i>MER</i>	<i>Mars Exploration Rover</i>
<i>MPFL</i>	<i>Mechanical Pumped Fluid Loop</i>
<i>MVD</i>	<i>Molecular Vapour Deposition</i>
<i>NA62</i>	<i>North Area 62</i>
<i>NASA</i>	<i>National Aeronautics And Space Administration</i>
<i>NCG</i>	<i>Non-Condensable Gas</i>
<i>NIEL</i>	<i>Non-Ionising Energy Loss</i>
<i>NIR</i>	<i>Near Infrared</i>
<i>OB</i>	<i>Outer Barrel</i>
<i>OHP</i>	<i>Oscillating Heat Pipe</i>
<i>PCL</i>	<i>Primary Cooling Loop</i>
<i>PE-CVD</i>	<i>Plasma Enhanced Chemical Vapour Deposition</i>
<i>PEEK</i>	<i>Polyetheretherketone</i>
<i>PHP</i>	<i>Pulsating Heat Pipe</i>
<i>PI</i>	<i>Polyimide</i>
<i>RTG</i>	<i>Radioisotope Thermoelectric Generator</i>
<i>SCL</i>	<i>Secondary Cooling Loop</i>
<i>ScSi</i>	<i>Single crystal Silicon</i>
<i>SLAC</i>	<i>Stanford Linear Accelerator Centre</i>
<i>SLD</i>	<i>SLAC Large Detector</i>
<i>SWIR</i>	<i>Short-Wavelength Infrared</i>
<i>TEC</i>	<i>Thermo-Electric Cooler</i>
<i>TID</i>	<i>Total Ionizing Dose</i>
<i>TIM</i>	<i>Thermal Interface Material</i>
<i>TPFLEX</i>	<i>Two-Phase Fluid Loop Experiment</i>
<i>TRL</i>	<i>Technology Readiness Level</i>

<i>TTCS</i>	<i>Tracker Thermal Control System</i>
<i>UV</i>	<i>Ultraviolet</i>
<i>VC</i>	<i>Vapour Chamber</i>
<i>VeLo</i>	<i>Vertex Locator</i>
<i>VIS</i>	<i>Visible</i>
<i>VoF</i>	<i>Volume of Fluid</i>
<i>ZARM</i>	<i>Center of Applied Space Technology and Microgravity</i>

Chapter 1 Introduction

This thesis aims to develop a highly thermally conductive micro oscillating heat pipe (μ OHP) compatible with HEP experiments and space applications' requirements for sensor and electronic cooling.

To fully understand the matters of this work, it is necessary to map the framework of the silicon sensors and their thermal management. Silicon-based semiconductor sensors are used in high-energy physics (HEP) experiments and space applications, but are also extensively present in consumer electronics and as imagers in other fields. Nowadays, silicon detector systems of HEP experiments are the core components of every particle detector in HEP experiments. Their tasks are precise tracking of charged incident particles to measure their momentums in a magnetic field and locating the decaying vertices. The former task implies increasing the silicon detectors' outer dimensions, while the second leads to placing the innermost sensing elements close to the collision regions. In space, sensors are widely adopted for navigation with star trackers and observations in different light spectrums. In HEP experiments, both types of measurements (tracking particles and locating decaying vertices) are negatively affected by the scattering in the materials used. Therefore, minimizing the material in the system with lightweight structures is a major design goal, to achieve low mass and to reduce scattering of the particles. Except for the AMS-02 experiment [1], [2], scattering is not an issue for space-born silicon sensors since they either monitor radiations or capture images. The demand for low mass creates two challenges: (i) the demand for a stable and stiff structure to obtain precise position measures, and (ii) the low thermal capacity associated with low mass structures. Low mass is also a dominant driving factor in space applications as the mass guides the launch costs.

Modern materials and fabrication methods facilitated to find solutions to these challenges. While aluminium alloys remain predominant in space applications, carbon fibre-reinforced plastics (CFRP) give the possibility to achieve high stiffness for a very low mass and efficient heat transfer properties. However, the mechanical loads imposed by the nature of both applications lead to different implementations of the low mass designs.

Nevertheless, all these electronic components produce varying levels of heat when operating. The inherent inefficiency of electronic devices and sensitivity to heat makes thermal management a critical point to address. Sensors evolve in confined environments where maintenance is not always possible or expensive. Thus, reliable sensors functioning over their planned life-time is mandatory. Furthermore, NASA estimated that thermal-related interconnects failures are responsible for 90% of all mission failures [3]. Moreover, many semiconductor device failure mechanisms are related to thermally induced processes, like diffusion or thermal expansion [4], [5]. Consequently, whenever levels of heat generated cannot be managed solely by the environment,

it preterits service-life. Thus, adequate cooling solutions have to be implemented to prevent premature and permanent failures due to radiations or over-heating.

Thermal management systems typically have two defined tasks: heat removal and temperature maintenance at a fixed point. The heat comes from the front-end electronics and the currents in the sensors, ranging from the mW/cm^2 to several W/cm^2 . Controlling the temperature is motivated by the control of leakage current and depletion voltage.

The operations in harsh environments, such as HEP experiments and space, often exclude natural convection for heat transfer. Heat removal capacity of this this technique is limited and hard to predict. Furthermore, natural convection is inapplicable in space and some HEP experiments. HEP experiments rarely rely on radiation to transfer heat out, unlike space-born applications where it is the only way to reject unwanted heat.

Structural elements often have a secondary role in conducting heat, affecting the material choice and the geometries adopted. Increasing the cross-section of the structures improves heat transport, implying a trade-off between heat transfer and the detector material for mass and particle scattering concerns.

When maintaining the sensors' thermal stability around a fixed point over the full life-time is required, especially in large-scale silicon systems, simple heat conduction is not always sufficient, and forced convection is used. It provides a well-controlled temperature to the heat-critical components over large distances using cooling pipes circulating under the heat spots or along the chips' edges for a reduced thermal path. The solution's bottleneck lie in the fact that heat is conducted through the sensors' substrate to the refrigerant circulating in the tubes. Substrate's thermal conductivity has to be high to minimize the thermal gradient along its length.

Microfabricated planar arrays of microchannels, covering the whole area of the heating elements, exceed this limitation. The micro-engineered microchannel devices, by circulating a cooling fluid, efficiently handle the detector modules' power density and provide a uniform temperature over large surfaces at all times. Etching such micro-cooling devices in single crystal silicon (ScSi) results in sub-millimetre thickness, minimizing the scattering of the particles. Additionally, using the same material for both the cooling substrate and the sensors reduces thermally induced stresses due to the expansion and contraction of materials. However, while this technology represents an appealing solution for thermal management in detector modules, it poses several challenges, particularly for high fluid pressures and long staves. Among these, the brittle nature of ScSi, the lack of suitable interconnections and the difficulties for the integration, packaging and qualification of such devices delay their application in areas where reliability is paramount.

The envisioned solution to address these challenges is developing a highly conductive, rad-hard device as an independent cooling loop. One cooling loop placed directly behind the critical elements extracts the heat from the sensitive area, which is referred to as the secondary cooling loop (SCL); and the other one, the primary cooling loop (PCL) transfers the heat from the SCL to the exterior. Two independent loops without fluidic exchange alleviate the issue caused by interconnection, as both contribute to the heat transfer and mechanical support. Additionally, one PCL can accommodate several SCLs, which extends the possibility. Therefore, independent cooling loops would benefit inner trackers and vertex locators within the frame of HEP experiments,

in addition to silicon sensors and electronics for space applications. Thus, the innovation proposal is articulated around three axes: (i) the design of μ OHPs aimed for HEP experiments and space applications, (ii) the realisation of these μ OHPs using gold thin films for wafer bonding and (iii) the permanent sealing of the device using Indium.

To these ends, the work was based on the large available literature on micro heat pipes (μ HPs) and microelectromechanical system (MEMS) microfabrication, in addition to the scarce literature dealing with the heat pipes' sealing solutions. Beside the literature study, dedicated experiments were conducted at CERN, EPFL-CMi and CSEM. Two sets of μ OHPs were microfabricated, one in silicon and one in silicon and glass. The second set served to observe the behaviour of the flow inside the devices. A new method solution was developed as the existing solutions, containing large quantities of metallic material or magnetic heating elements, did not correspond to the requirements. It resulted in gas-tight and pressure resistant seal with low mass in low volume.

1.1 Structure of the thesis

The work can be separated into two major parts: (i) the development, fabrication and testing of the micro-device (chapters 2 to 6); and (ii) the development of a new sealing solution for the developed μ OHP, which can be extended to other applications (chapter 7).

Chapter 2 reviews the use of silicon semiconductors sensors in HEP experiments and in space, in addition to the thermal management solutions developed or under-development in both domains, including pumped fluid loops, self-actuated and passive solutions. Summarizing tables were necessary to map the existing literature for base comparison studies.

Chapter 3 introduces the challenges of silicon-based cold plates and presents the two-cooling loop scheme to alleviate them. This chapter includes the design of the μ OHP for the secondary cooling loop.

Chapter 4 presents the methods and apparatus used to evaluate the thermal performance and the resistance of the bonded microchannels to pressure.

Chapter 5 details the microfabrication of the two sets of the μ OHP, and the resistance of the interface of both sets. Scanning electron microscopy (SEM) images complements the test. Interfacial failure modes are observed and used as basis for potential microfabrication enhancement.

Chapter 6 describes the observed flow patterns and thermal characterisation. The link between the visual observations and thermal performance is analysed. This performance is further discussed while a comparison is done with recent researches. Improvements for the developed device are also suggested.

Chapter 7 treats the development of a sealing solution. The innovative solution allows to obtain a low-volume seal compatible with low temperature by compressing Indium to obstruct the device inlet. To this end, a dedicated apparatus to charge and seal μ OHPs was developed.

Chapter 2 Literature review

This chapter is divided in two parts. The first sections introduce silicon semiconductors based sensors, with a focus on those used for particle detection and tracking, followed by an overview of radiations resulting from the interactions of the particles and the materials on their paths. The third section of the chapter reviews the different cooling solutions developed for silicon-based devices in high energy physics (HEP) experiments and in space applications.

2.1 Silicon-based semiconductors sensors

Technological progress and growth of the market for silicon devices have driven the costs of equipment and material down, making silicon sensors more affordable and widely used. Silicon detectors are reversely biased semiconductor diode used in particle detection. They can measure ionisation charges left by charged particles passing through silicon in the depletion region. The essential structure is the p-n junction obtained after highly doping a delimited strip or pad on low-doped substrate with the opposite doping type [6]. Doping is done using ion implantation and heat treatment, or by thermal diffusion. Applying an external potential to the p-n junction will drift electron-hole pairs. Thus, generating a current whose is detectable by the read-out electronics.

Semiconductor-based silicon sensors can be separated into two main categories: micro-strip sensors and pixel sensors. Each one possessing their own advantages and limitations. A non-exhaustive summary of the advantages and limitations of each categories and associated sub-categories is done in Table 2-1 , with examples of their use in HEP experiments.

2.1.1 Micro-strip sensors

Early generation of solid-state semiconductor-based detectors used a large number of identical strips laid on one face of a silicon chip along one axis and distributed over different layers or sides as illustrated in Figure 2.1(a). Double-sided layouts offer an improved design with higher resolution. Most of the last generation micro-strip detectors are based on polysilicon resistors implanted at the end of the strip so that the aluminium strip located on the opposite side is coupled to it.

One disadvantage linked to micro-strip sensors is the existence of a non-negligible probability that two particles travel through the same sensing micro-strip. Even with double-sided micro-strip sensors, this probability exists, which would generate ghost hits if a high number of particles tracks are present simultaneously, as illustrated by Figure 2.1(b-c). Ghosts hits make impossible to distinguish the two tracks [7]. On the other hand, micro-strips sensors offer simple fabrication processes for large surface sensors.

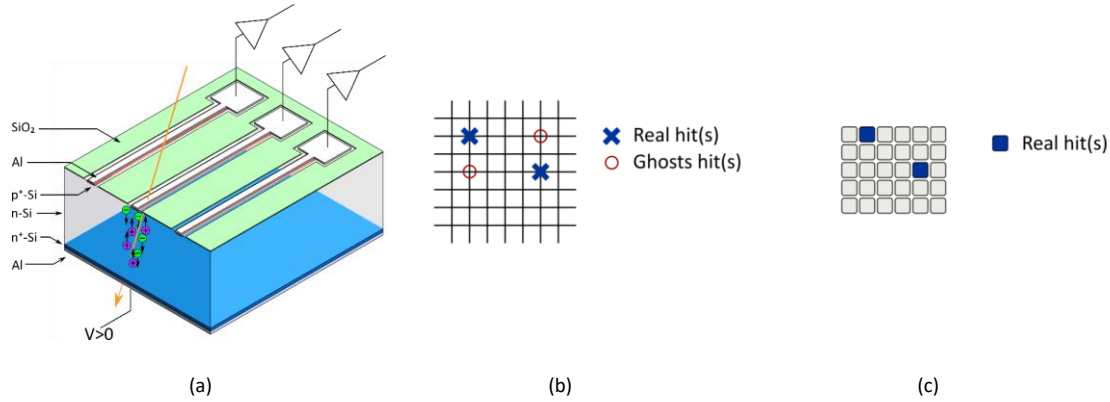


Figure 2.1. (a) Representation of an n-type silicon strip detector. (b) Representation of real and ghost hits with a strip sensor with orthogonal arrangement when two particles traversing the detector. (c) Unambiguous hits when two particles traverse a pixel sensor

2.1.2 Pixel Sensors

Pixel detectors offer the advantages of the most recent microfabrication techniques and the large expertise from commercial application manufacturers. The sensing elements are arranged in two-dimensional, densely packed arrays, hence the denomination pixel. The structure of the pixel sensors, unlike the micro-strip sensors, places its pre-amplifier chips directly under their sensing elements.

Pixel sensors are preferred for the innermost layers of the tracking system because of their fine spatial resolution, which outcompetes that of micro-strip sensors [8]. Furthermore, signal-to-noise ratio of the pixel sensors is higher than for micro-strip sensors due to the small surface of the pixel channel area and its low capacitance. The operating temperature influences the sensitivity of pixel sensors: it increases at low temperature, and vice versa at high temperature, due to the conductivity of the substrate. The number of electron-hole pairs rises with temperature, in addition to the dependence of the leakage current on the temperature. But it does not increase from the particles' crossings. The layout of pixel sensors comes with the disadvantage of requiring a special attention for the design and during the processing due to the very fine structures.

Usually, pixel detectors are found in planar layouts. However, three-dimensional layouts exist [9], [10]: electrodes columns pass through the substrate's thickness, perpendicularly to its surface. Planar and vertical layouts are shown in Figure 2.2. This last geometry reduces the drift distance between electrodes resulting in faster signals in planar cases as the signal charge is decoupled from the charge collection process. Furthermore, it increases the radiation hardness compared to the two dimensional counterparts [11].

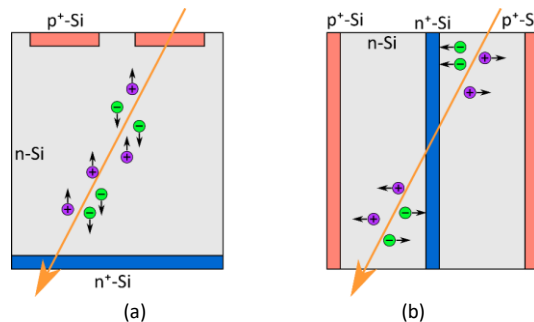


Figure 2.2. Schematic cross-section of (a) a planar sensors design and (b) a 3D sensor design.

2.1.2.1 Hybrid

Hybrid pixel sensors production divides the processing of the sensing elements matrix and the readout electronics on two differed substrates, as illustrated in Figure 2.3(a), that are then connected, typically via bump bonding. Processing the sensors this way allows the materials and the processes to be individually optimized.

However, densely packed pixel sensors carry some disadvantages. The high number of bump-bond connections of hybrids makes rework of the failed bump-bond connection challenging, if it is ever attempted. Bumps carry additional concerns on their reliability and long-time service life for the same reason. Furthermore, chip bonding technology and the creation of the required bumps increase significantly the cost of the hybrid pixel sensors. Also, the hybrid geometry introduces supplementary material in the detection volume, reducing the resolution of the position. One other challenge for the hybrid pixel detectors is that electronics have to be compacted under the area of each pixel.

2.1.2.2 Monolithic

Monolithic pixel detectors comprise the same elements as the hybrids: a matrix of sensing elements and the associated readout electronics. Unlike hybrid pixel detectors, monolithic sensors integrate these elements on a single substrate as illustrated in Figure 2.3(b). This avoids inter-connection, which reduces the cost, and lowers the noise, which produces a more robust sensor. The processing of the ASIC and sensor parts on the same substrate leads to an increased complexity of the design as both have been guided by one or the other.

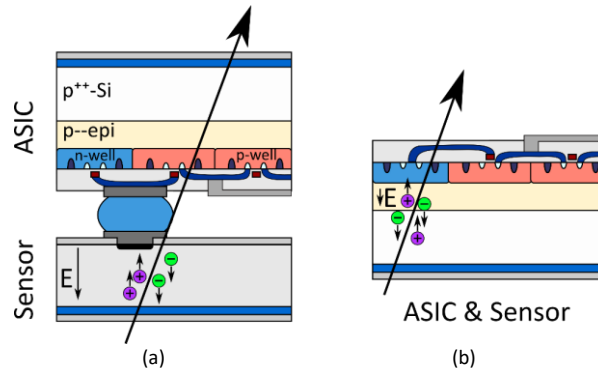


Figure 2.3. (a) Cross-section of a hybrid pixel sensor with the read-out electronic (ASIC) bump-bonded to the sensor. (b) Cross-section of a monolithic silicon sensor in which the ASIC and the sensors are integrated on the same substrate.

2.1.3 Use of Silicon Sensors

Silicon detectors constitute a key detection technology for HEP experiments thanks to their spatial resolution, semiconductor structure, insensitivity to magnetic fields, compact design, mechanical strength and ability to work at low temperature [12], [13]. Their relevance is also ubiquitously validated in the imaging industry [14], where charge-couple device (CCD) and complementary metal–oxide–semiconductor (CMOS) sensors prevails, as well as for the medical field [15]. The imaging industry largely dominates the market in terms of quantity and market share, due to the uses of sensors in portable devices.

2.1.3.1 *HEP experiments*

The study of silicon detectors for HEP experiments started in the early 1960s with the possibility of using them for HEP experiments, demonstrated in 1961 [16], [17], [18], led to an increase of interest for them in this field. As the fabrication processes and electronic designs matured, the possibility to integrate them in position sensitive detectors materialised. Nowadays, thousands of silicon detectors are arranged around the primary collision point, or as vertex locator, in particle detectors. Thus, an accurate picture of the particles' tracks can be painted with higher resolution than older technologies as wire or cloud chambers.

The use of micro-strip detectors started in 1980 with the NA11 fix target experiment, and continued with the current activities in HEP projects [10] : the ATLAS experiment also plans to use the micro-strip detectors with shortened lengths and higher densities for high luminosity runs of the LHC. The first pixel sensor developed for use in HEP experiments was the CCD-based SLD vertex detector located at the SLAC [19] and in the fixed target experiment NA32 [20]. The requirements of the LHC, in terms of spatial and temporal resolution, pushed further the development of pixel detectors. CMOS-based sensors have taken advantage of mass production technologies and intrinsic properties to replace CCDs. Allport [21], [22] and Hartmann [10] detailed the history of silicon sensor in HEP.

2.1.3.2 *Space applications*

Silicon sensors are widely used in space, either on commercial or scientific satellites. Common star tracker consists in an optical device that measures the position of the stars using silicon pixel sensors. From these observations, the attitude of the spacecraft is determined relatively to the stars by comparing their positions in the apparent frames to their known absolute positions from a star catalogue [23]. Space-borne silicon pixel sensors are also used to conduct Earth observations in UV, VIS, NIR and SWIR bands [24], [25]. Astronomical observations from space also relied on pixel sensors, as it is the case with Hubble and Kepler, GAIA and JWST. Pixel sensors also play an essential role in planetary exploration. Cameras on board of the rovers on the surface of Mars use silicon pixel sensors to navigate and perform visual analyses. For this purpose, Perseverance rover embarks a total of twenty-three cameras [26]. In 2005, the atmospheric entry probe Huygens successfully reached Titan, one of the many moons of Saturn. Huygens' Descent Imager/Spectral Radiometer (DISR) consisted in three imagers sharing the same CCD sensor. The DISR was specially designed to study the radiation balance in the atmosphere of Titan in the IR, UV and VIS bands. Silicon pixel sensors also serve as radiation monitoring devices in space. The Timepix detector, an hybrid pixel produced by the Medipix2 collaboration from CERN, is deployed in several space missions to characterize the mixed radiations encountered [27]–[32]. The most noticeable example of this is the radiation monitoring system located in the cupola of the ISS that use Timepix detector. AMS-02 on the ISS studies the flux of charged particles in space [1]. An array of 2264 silicon double-sided micro-strip sensors composes the tracking system, while additional instruments determine the type of particles encountered by analysing the incoming energy spectra and fluxes. Silicon micro-strip sensors were also employed to observe the x-ray spectrum in space. The *Hitomi* x-ray observatory, a satellite mission led by JAXA, uses double-sided silicon micro-strip sensors coupled with a low-noise ASIC [33]. The first observation was conducted on the pulsar wind nebula G21.5-0.9 shortly followed the calibration of the x-ray instrument by observing the isolated neutron star RX J1856-3754. *Hitomi* then observed the *Crab* nebula over an accumulated period of six hours, which corresponds to four orbits.

Table 2-1. Non-exhaustive list of sensor types, experiments and space missions in which they are in use and their respective advantages and disadvantages. Adapted from Allport [22].

Sensor type	HEP Experiments	Space applications/mis- sions	Advantages	Disadvantages
Micro-strip	Na32, STAR, DEL- PHI, Belle, ATLAS, LHCb, CMS, ALICE, ILC ^a , FCC ^a	AMS-02	<ul style="list-style-type: none"> • Simple fabrication for large area • Can be thinned at the cost of signal • Connection at the edges 	<ul style="list-style-type: none"> • Read-out on one or two sides • High read-out capacitance • Doping varies with radiation over lifetime
Pixel			<ul style="list-style-type: none"> • Accurate space-point information • Low noise (low capacitance) 	<ul style="list-style-type: none"> • Radiation influence the charge trapping and depleted volume
• Hybrid	NA62, ALICE, AT- LAS, CMS		<ul style="list-style-type: none"> • Separate processing of sensor and electronics with indi- vidual optimisation 	<ul style="list-style-type: none"> • Expensive flip-chip technology • Bump-bonds reliability and service-life
○ CMOS hy- brid	FCC ^a	TimePix	<ul style="list-style-type: none"> • CMOS technology with fine feature size • Multiplexing pixels' outputs in one connected pad 	<ul style="list-style-type: none"> • Bump-bonds can be avoided at the cost of expensive flip-chip alternatives
• Monolithic			<ul style="list-style-type: none"> • No flip-chip step 	<ul style="list-style-type: none"> • Simultaneous processing of sensor and electronics
○ DEPFET	Belle II		<ul style="list-style-type: none"> • Data storage in-sensor possible 	<ul style="list-style-type: none"> • Poor radiation tolerance • Low read-out speed
○ CCDs	NA32, SLD, ILC ^a , CLIC ^a	PLEIADES-HR	<ul style="list-style-type: none"> • CCD technology heritage • Small pixel size • Gain uniformity • Signal region can be thinned 	<ul style="list-style-type: none"> • Slow readout speed • Low tolerances to radiation damages
○ SOI	ILC ^a	Kyoto FORCE mission	<ul style="list-style-type: none"> • Established technology • Electronics and sensor on separate substrates, but still monolithic sensor • TSV technology for flexible design 	<ul style="list-style-type: none"> • Long processing time with lower yield • Presence of high number of oxide interfaces that can trap charges
○ MAPS	STAR, ALICE, AT- LAS, LHCb, Mu3e, ILC ^a , CLIC ^a , FCC ^a	2 nd gen, MetOp EU- METSAT, JUICE mission, TAOS II	<ul style="list-style-type: none"> • CMOS technology heritage • Fast charge collection 	<ul style="list-style-type: none"> • Electronics position impacts charge collection • Doping and depletion depth influenced by radiation

CMOS, Complementary Metal-Oxide-semiconductor. CCD, Charge-Coupled Device. DEPFET, Depleted P-channel Field Effect Transistor. SOI, Silicon-on-Insulator. MAPS, Monolithic Active Pixel Sensor.

^a proposed future collider(s)

2.2 Radiations

Radiations are inseparable from the environments encountered in space and or during HEP experiments. Silicon sensors are sensitive to radiation as any other electronic devices. Their degradation affects the applications in which they are used.

Particles travelling through material lose energy along their paths due to the interaction with atoms of the material. This actually is the underlying principle of all the sensors, but the transfer of energy caused by the passage of the particles also creates damages.

The energy losses depend on the type of the particles:

- **Heavy particles:** Heavy particles interact mostly with electrons surrounding the nucleus. The electrons gain enough energy to escape their orbits, causing energy loss from the particle traveling through the material. After losing the majority of their energy by ionisation, the travelling particles elastically collide with the nuclei of the material [34].
- **Fast electrons:** Fast electrons also lose energy through electromagnetic radiation (bremsstrahlung)[16].
- **Neutrons:** Neutrons interact only with the atomic nuclei of the material, and not the orbital electrons. Two types of scattering are observed with neutrons: elastic and inelastic scattering. The first case designs a case where the neutron is scattered by a nucleus without modifying its structure, nor its state of excitation, leading to release of gamma radiation. The second case indicates the capture of the neutron by the nucleus, generating radiation or fission.
- **Electromagnetic rays:** Electromagnetic rays are completely absorbed by the material, leading to an increase of excitation of the electrons.

Electron hole pairs are generated by the electron excitation. With an electric field in vicinity of these pairs, they drift, generating a current that can be detected [16].

2.2.1 Radiation Damages

The incident particles also damage the material as they pass through it. Damages are not caused only to the detector, but also to all the parts involved in its construction and servicing, as the mechanical structures and cooling system. The material's physical properties may be affected by the radiation doses encountered as they often induce accelerated ageing, as seen in the case of carbon fibre-reinforced plastic resins [35]. On the other hand, some physical properties might increase, as exemplified by the improved thermal conductivity of different polymers exposed to radiations [36]. The modification of the material morphology has also an effect: surface and crystallinity are altered, resulting in a diminished yield and tensile strength, hardness and porosity [37]. The dissociation of molecules by action of nuclear radiation, also known as radiolysis, can produce dangerous and very reactive compounds for the detectors and surrounding infrastructures. Additionally, refrigerants often have a high hydrogen content with weak hydrogen chemical bonds and upon exposition to radiations, atoms could group forming a highly explosive gas. CERN gathered extensively data on damage testing for most engineering material and fluids [37]–[42].

Total Ionizing Dose (TID) and Non-Ionising Energy Loss (NIEL) count the quantity of defects due to incident particles. The ionisation results in a generation of electron hole pairs, which accumulates as electrically active defects. NIEL refers to all energy losses by an incident particle through material absorption and interaction with the nuclei of the lattice atoms. When the travelling particle delivers only a small energy, the recoil of the atom remains an isolated displacement. If the travelling particle has sufficient energy, the recoiling atom gains sufficient energy through this collision to cause additional cascading defects [43], [44]. Such interactions are generally not reversible, unlike the ionisation interactions [45].

2.2.2 Radiation Levels

Radiations are present in both space and HEP experiments. However, the resulting TID and NIEL depends on their location. In HEP experiments, the detectors closest to the interaction point will be subject to higher radiation levels than outer layers. In space, it is the selected orbits and flight paths that determine radiation environments. The radiation exposition for the HEP experiments is simulated in advance to fix the requirements of the sensors for a well controlled environment, whereas the radiation environment in space is not controlled and emanates from galactic cosmic rays, solar events and trapped particles. However, several static average models exist to establish the requirements for the equipment planned to be used during space missions (to name a few: AE8, AP8, AE9, AP9, IGE2006, MEOv2, SPENVIS). Thus, depending on the selected model for the specific orbit, a variability of radiation levels is possible and must be considered in space missions [46]. The use of NIEL proved to be a relevant tool to extrapolate the radiation tests conducted under limited particles and energies to the expected degradation within the actual environment [47], [48].

Table 2-2. Summary table of radiation levels (TID and NIEL) for several orbits and experiments.

	Ionisation dose	Non ionizing energy loss	Ref.
Low Earth Orbit (LEO)	1-100 krad/year	1.27×10^4 10MeV n_{eq}/cm^2s	[49]–[52]
Medium Earth Orbit (MEO)	3-10 krad/year	4.6×10^4 10MeV n_{eq}/cm^2s	[49]–[51]
Geostationary orbit (GEO)	10 -10000 krad/year	8.46×10^4 10MeV n_{eq}/cm^2s	[49]–[52]
ALICE ITS upgrade	270 krad	1.7×10^{12} 1MeV n_{eq}/cm^2	[53], [54]
ATLAS ITk (HL-LHC)	10 MGy	1.4×10^{16} 1MeV n_{eq}/cm^2	[55], [56]
FCC	10-5000 MGy	$1-100$ 10^{16} 1MeV n_{eq}/cm^2	[57]

Despite involving both harsh environments in terms of radiations, the space applications and the HEP experiments do not affect the material and components at the same rate: the radiations are several orders of magnitude higher in the future HEP experiments than in space.

2.2.3 Material Budget

One strict and unique requirement for HEP experiments almost driving entirely the concept and design of the detectors, is the material budget (MB). Since any material introduced in the sensitive are of the detector interacts with the particles, multiple particle scatterings occur, which negatively impact the resolution of the detector. Multi-layered arrangements of sensors increase this negative effect on the detector resolution.

The material budget is defined as:

$$MB = \frac{x}{X_0} \cdot 100 [\%] \quad (2.1)$$

With x the material thickness particles traverse and X_0 the radiation length of the material, which is defined as follows:

$$X_0 = \frac{716.4 A_N}{Z(Z+1) \ln\left(\frac{287}{\sqrt{Z}}\right) \rho} \quad (2.2)$$

Where X_0 depends on the atomic and mass number A_N and Z , as well as on the material density ρ .

Materials possessing high X_0 values are therefore preferable for detectors. Conventional solutions based on metallic materials used for structures or for cooling, as aluminium, stainless steel or copper, cannot be employed in HEP detectors. Minimizing the material budget, while providing efficient cooling systems and mechanical structures, has become one of the main goals for the conception of HEP silicon detectors.

Refrigerants used for thermal management within the detectors are also considered during the estimation of the material budget and reducing the size of the cooling channel is critical to decrease the average material budget. Note that for the same channel's size, two-phase flows systems possess a lower MB due to the presence of low density of vapour.

Table 2-3. Material budget for various materials and refrigerants.

Material	ρ [g/cm^3]	X_0 [cm]
Copper (pure)	8.90	1.4
Aluminium (pure)	2.699	8.897
CFRP (K13D2U2K)	1.80	23.7
Silicon	2.329	9.37
Water (vapour)	$7.562 \cdot 10^{-4}$	47720
Water (liquid)	1	36.08
R245fa (liquid)	1.4	26
Polyimide (film)	1.420	28.57

2.3 Need for Cooling

The unavoidable consequence of the exposition to radiations for silicon sensors, resulting in radiation damage, is the increase of current leakage, which starts even at low radiation levels [58]. Consequently, the signal-to-noise ratio (SNR) decreases, leading to an increased noise at the output and a hindered sensing resolution. An issue arises in parallel, the depletion voltage required to pass the charge out of the detector increases, which could eventually reach the break-through threshold. Silicon sensors will ultimately experience thermal runaway, resulting in unstable and unreliable outputs, and in the worst case, the destruction of the sensitive parts of the sensors [59].

Reparation or replacement of damaged silicon detectors in space applications is uncommon since maintenance is limited by the accessibility to the sensor. In HEP physics, silicon sensors are replaced on occasion during the shutdown of the accelerators. However, reparation during the op-

erations remains impossible. The radiation dose they will be subject to has to be taken into account during design stages. Hereby, adapted cooling strategies help to reduce the leakage current, delaying the detector's end-of-life. The leakage current produced in a detector subject to radiation damage can be lowered by decreasing the operating temperature [60].

An additional justification for cooling is that every subsystem, or component having integrated circuits, produces heat. Advances in micro-and nano-technologies greatly help in reducing power consumption and in the densification of transistors [61]. Nevertheless, they also drive to faster computing associated with the implementation of more functionalities, which are calculated faster, in the chips, therefore increasing the power to dissipate. The thermomechanical effects linked to the generated heat lead to the failure of the chips. Connection failure is a type of failure frequently observed. The power is delivered to the silicon chips through a power bus. It also retrieve the generated signals. These connections usually rely on metals from the chip to the cabling. A broken connection would lead to an increased current in the others, inducing an early failure of the silicon detector. This could be mitigated by reducing the thermal gradient across the chip.

Therefore, a well-suited thermal management system is mandatory for silicon sensors, and more generally for any electronics, to extend their life, keeping their efficiency and improve their reliability, as in both our applications maintenance is very costly (HEP experiments) or impossible (space) [62]–[64].

The generated heat has to be evacuated from its origin, whether onboard a spacecraft or in a HEP experiment. Several solutions exist to do so and can be categorized as forced gas convection, mini-channel (pipe flow) cooling and microchannel cooling for the active strategies; while thermal straps and heat pipe are in a second category: passive cooling systems. The mini- and micro-channel offer a wide variety of implementation possibilities as illustrated in Figure 2.4.

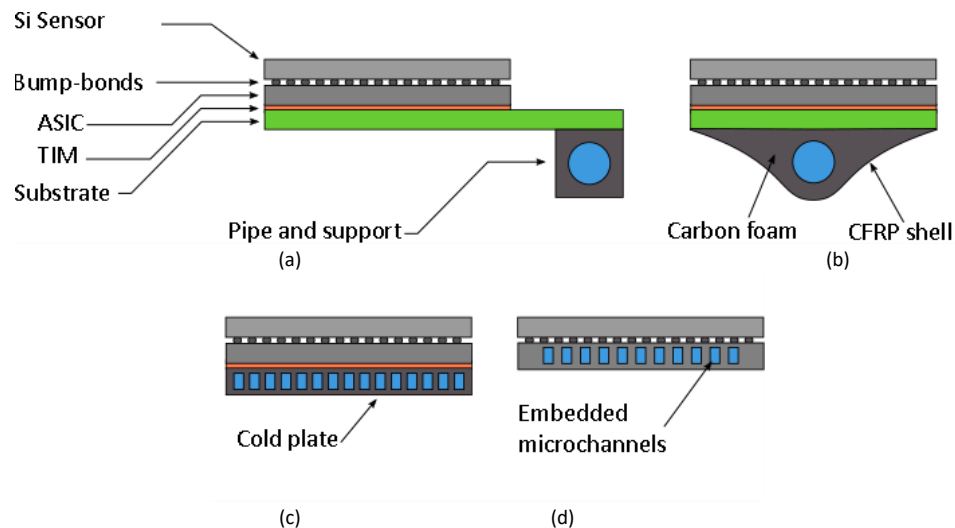


Figure 2.4. Cooling scheme of a hybrid silicon sensor. (a) Mini-channel cooling. The mini-channel is fixed to the support of the substrate at a distance from the sensor. The cooling performance is limited by this distance and the conductivity of the substrate. (b) The mini-channel is embedded in the supporting elements (carbon foam with carbon fleece), with a closer location to the sensor and an intermediate substrate. (c) Cold plate with microchannels. The plate supports the sensor while providing efficient cooling closer to the sensor. (d) Embedded microchannels in the ASIC reduce the thermal path.

2.3.1 Forced Gas Convection

Forced gas convection cooling is a widely used solution to dissipate heat to the ambient for consumer electronics, but not in HEP experiments. The PiXeL sub-detector of the STAR HFT is the first silicon detector operated with air-cooling operating at 23°C [65], [66]. The vertex detector of the Belle 2 experiment also proved that this solution could be implemented [67], [68]. Furthermore, the Mu3e design is based on the forced convection of gas [69], and the recent thermal management concepts project for the linear colliders ILC [70] and CLIC [71], [72] rely on air-flow combined with intelligent pulse powering of the detectors [72]–[75]. However, the operating conditions are very specific for this cooling system in HEP experiments and are not suited for all experiments. Additional concerns emerge from the stability of the flow due to the length of the flow path and the supply systems.

2.3.2 Minichannels MPFL

Many common cooling systems use pumped liquid flow through mini-channels, being single- or two-phase [76]–[78], also known as pipe flow. This flow is supplied by a pumping system or a compressor and goes through a tube to evacuate the heat either by convection in the case of single-phase or by evaporation in the case of a two-phase flow. The single-phase option has several advantages over the two-phase one. Even if the design and modelling of single-phase systems are simpler, they show lower heat transfer, less uniform heat distribution along the evaporative area and more interactions with the incident particles [79], [80]. Furthermore, the additional heat transfer from latent heat allows the system to rely on smaller tubes but also leads to a reduction of the system mass since more heat per fluid mass is transported by the two-phase pumped loop systems.

2.3.2.1 HEP experiments

A single channel running all along the detector modules of the ALICE ITS SSD and SDD detectors is used with liquid deionized water to control the temperature [81]. The ALICE ITS SPD cooling system relies on two-phase C_4F_{10} in a duct with a hydraulic diameter of 2.6mm to refrigerate each stave [82]. An illustration of the stave is given in Figure 2.5(a). Similarly, evaporative CO_2 circulating in the central titanium pipe cools the staves of the ATLAS Insertable B-Layer (IBL), which cross-section is shown in Figure 2.5(b). The heat is evacuated from the silicon sensors and connected electronics through the carbon foam and a carbon structure, which host a titanium cooling pipe [83]–[85]. The staves were installed during phase 0 of the ATLAS upgrade (LS1, 2013-2014).

A new Inner Tracking System (ITS) was designed for the upgrade of ALICE during the LS2 (2018-present) [54]. This ITS baseline is an all-pixel silicon detector relying on a monolithic CMOS active pixel sensor called ALPIDE. The ITS consists of two distinct subsystems: the Inner Barrel (IB) and the Outer Barrel (OB), respectively shown in Figure 2.6(a) and (b).

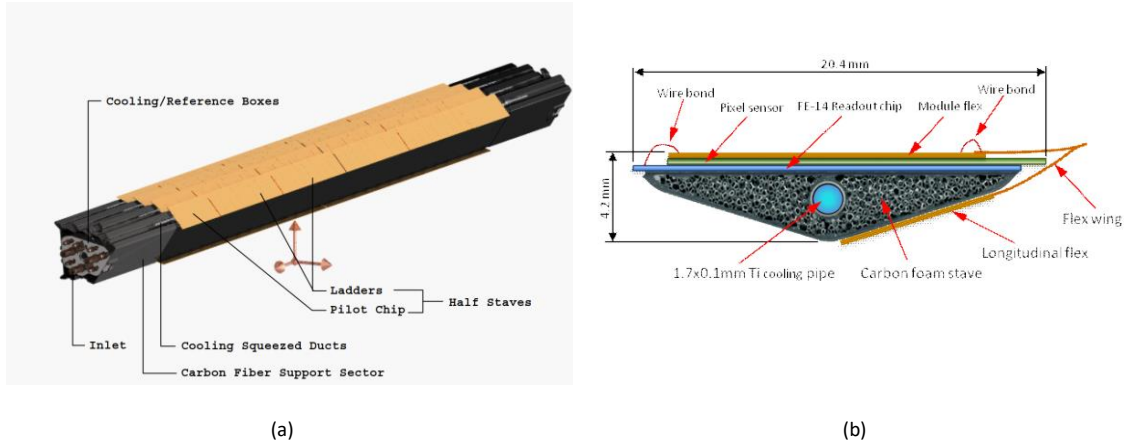


Figure 2.5. (a) ALICE SPD stave: the thermal connection between the squeezed cooling tubes, the sensors and the carbon support is done by thermal grease [86]. (b) ATLAS IBL stave cross-section [83]

The former is constituted of three layers of staves, while the latter is constituted of four. A complete IB stave measures 270mm in length and 15mm wide for only 25 grams. The OB ones are 875mm and 1475mm long and weight respectively 170g and 160g. Both rely on leak-less deionized water flow through encapsulated polyimide pipes. The cooling pipe for both types of staves of the ALICE ITS is encapsulated between two plies of carbon fleeces, a graphite foil and highly thermally conductive carbon fibres. Two alternatives cooling strategies to the carbon flees with embedded polyimide pipes were explored. Both alternatives relied on a microchannel cold plate. The microchannel section (2.3.3) contains more details about the alternatives.

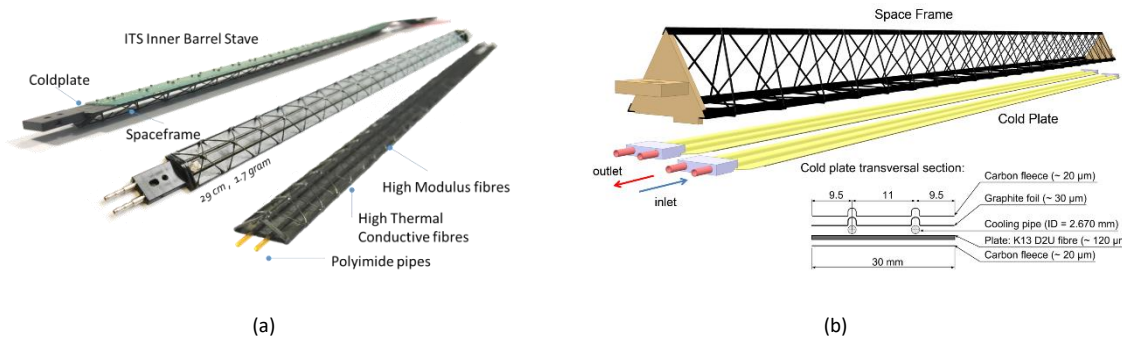


Figure 2.6. (a) ALICE ITS IB stave fully assembled [87] (b) Schematic layout of a stave of ALICE ITS OB (mechanical and cooling structure) [54].

In preparation of the HL-LHC, the Inner Tracker (ITk) of ATLAS was upgraded [55], [88], [89]. Light-weight structures support the chips, the electrical and thermal services. The heat generated by the front-end chips and the sensors is evacuated using two-phase flow CO_2 making the roundtrip along the tube of the staves. Unlike the ATLAS IBL concept where carbon foam fully encloses the pipe, the contact area between the pipe and base block is reduced in this case [90], [91]. The thermal interface also evolved, as shown in Figure 2.7: an aluminium-graphite cooling block and a pyrolytic graphite tile spread the heat from the bonded pixel modules. The cooling blocks transfer the heat to a thin-wall titanium cooling line through soldered aluminium-graphite base blocks. A pin-hole system guarantees the proper alignment of the cooling and base blocks.

2.3.2.2 Space applications

Pumped fluid loops are generally used only on larger spacecraft [92], [93], but recent investigations resulted in the integration of small pumps on-board small satellites. Single-phase systems

have proven their use in space on a limited number of applications. Two-phase pumped loop systems are a key technology for space exploration for both NASA and ESA; and therefore continuously under development [94]–[98].

The International Space Station (ISS) features a three-loop design architecture. The Internal Active Thermal Control System of the ISS uses water as working fluid while ammonia is mechanically pumped in the Photovoltaic Thermal Control System and the External Active Thermal Control System of the Space Station [99], [100]. The AlphaBus telecommunication platform also required the development of MPFL capable of dealing with high heat loads [101].

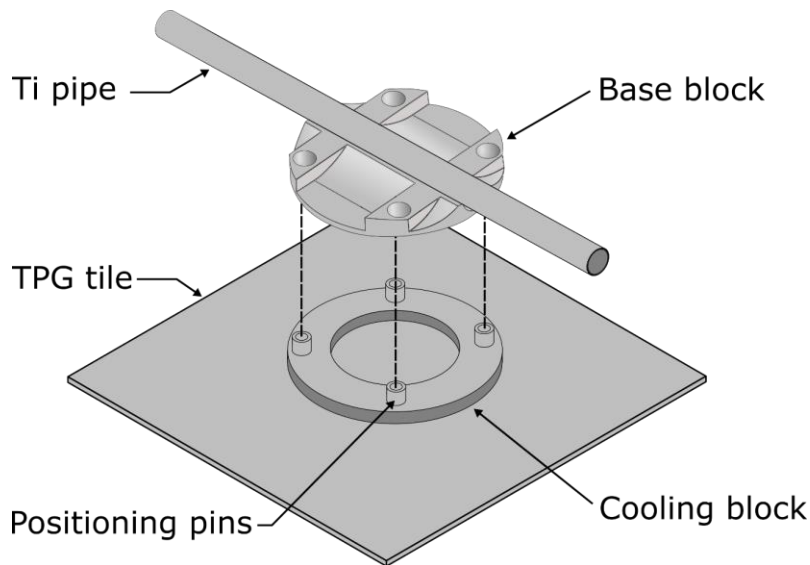


Figure 2.7. Design propositions for ATLAS ITK OB staves: schematic of the module connecting the pixel sensor to the evaporative CO₂ cooling line (adapted from [90], [91]).

During the explorations of the planet Mars, several spacecraft used single-phase mechanically pumped fluid loop [102]. Mars Pathfinder (MPF), Mars Exploration Rovers (MERs) *Spirit* (MER-A) and *Opportunity* (MER-B), relied on pumped CFC-11 loops to control the temperature during the cruising phase of their missions [103]. The tubes were brazed on-board MPF and glued on-board MERs [104].

Curiosity rover of the Mars Science Laboratory (MSL) [105]–[108] relied on two single-phase mechanically pumped loop with an external configuration that looks similar to the one used with the MPFL of *Opportunity* and *Spirit*. *Curiosity* is equipped with one cooling loop managing the heat from the Radioisotope Thermoelectric Generator (RTG), science instruments and electronics from the rover. During the cruising phase to Mars, while most instruments of the rover are off, the RTG continue to generate heat. The rover's MPFL controls the RTG's temperature, but it has to be linked to the second cooling loop located in the Cruise Stage to further evacuate the heat. The Cruise Stage is only operational from pre-launch to the entry in Mars environment, at which stage is jettisoned. The fluid circulating in tubes mounted on the outer shell of the RTG cools it. An additional aluminium hot plate is mounted around the RTG to further absorb the heat he generates. A sandwich panel separate the hot plate from the cold one. The tubes transferring the fluid between the two plates are glued on the panel with thermal epoxy. Additional aluminium thermal wedges are added between the cold plate and the tubes [109].

In 2010, at cross-road of HEP experiments and space systems, AMS-02 was successfully commissioned onboard the ISS [1], [2]. The device was designed to detect antimatter, lost matter and dark matter in space using silicon micro-strip track detectors. Among the subsystems designed for AMS-02, the TTCS (Tracker Thermal Control System) was designed to remove the 140W over the trackers front-end electronics' large surface, using a mechanically pumped two-phase CO₂ flow. The evaporator consisted of two parallel branches linked to the top and bottom of the tracker planes. Thermal bars drove the heat from the different tracker planes to the evaporator of the CO₂ loops. The large thermal interface drove the requirements, which led to a two-phase CO₂ cooling system, on which the temperature had to be even in all of the orbits' phases. The evaporator of the CO₂ loop was bolted to the evaporator bars with an Indium thermal gap filler.

2.3.3 Microchannels MPFL

In 1981, Tuckerman and Pease [110] introduced the concept of microchannel heat sinks possessing an array of narrow channels. This would guarantee sufficient cooling for high-power and high-density electronic devices by increasing the surface of heat exchange compared to macro-sized heat sinks. The small hydraulic diameter of the microchannels provides a high heat transfer coefficient. Moreover, the thin cold plate reduces the thermal path from heat source to the refrigerant. Their experiments demonstrated the possibility to cool up to 790 W/cm² with a laminar flow of water. These results motivated further studies on applications of single-phase and two-phase micro heat sink cooling [77], [80], [111], [112]. Special attention was given to the capacity to remove high heat fluxes, with passive features to improve the thermal performance, and two-phase microchannel heat sinks [78], [113]–[123]. Nowadays, microchannels cooling has proven its usefulness in a wide range of applications, from electronics as data centres and microchips, to fuel cells, energy conversion systems, photovoltaic modules [124]–[131] and automotive, as research is conducted on the integration of microchannels of 1020µm by 840µm embedded in CFRP plates to cool electric vehicle batteries [132].

In single-phase cooling, microchannels lead to a large pressure gradient, which can be decreased by reducing the flow length or designing several inlets and outlets. It has been demonstrated that microchannel cooling in single-phase can minimize the pumping power due to the reduced of flow rate and flow length [133], [134]. Using two-phase flow in microchannels provides a higher heat transfer coefficient coupled with a uniform temperature and requires lower pumping powers, at the expense of potential flow instabilities and complex designs and calculations [79], [80], [118].

2.3.3.1 HEP experiments

At present, two CERN experiments use silicon microchannel cold plates, namely the NA62 GiGaTraKer (GTK) and the LHCb VeLo upgrade [135], respectively visible in Figure 2.8 and Figure 2.9. Several additional experiments investigated on microchannel cooling solutions during their development, especially the ALICE experiment and BELLE II [136]–[138].

Silicon microchannels cooling plate used to control the temperature of the silicon detectors of NA62 pioneered the application of this technology in HEP experiments [139]–[141]. The system uses single-phase C₆F₁₄ passing through 154 parallel microchannels populating the 80x70 mm² silicon cold plate. The microchannels are 70µm deep and 200µm wide and separated by 200µm-thick walls. The thickness of the cold plate is reduced to 210µm in the central region

to decrease the material budget. Fluidic connection, visible in Figure 2.8(b), is achieved by four brazed capillary connections: two fluid inlets and two fluid outlets. Two manifold connectors, which are at the end of the capillary tubes, complete the fluidic connection. The sensor is glued on top of the cold plate, which provides it with structural support. The microchannel cooling plate aims to keep the $60 \times 38 \text{ mm}^2$ pixel sensor at -10°C while dissipating 2 W/cm^2 when in operation.

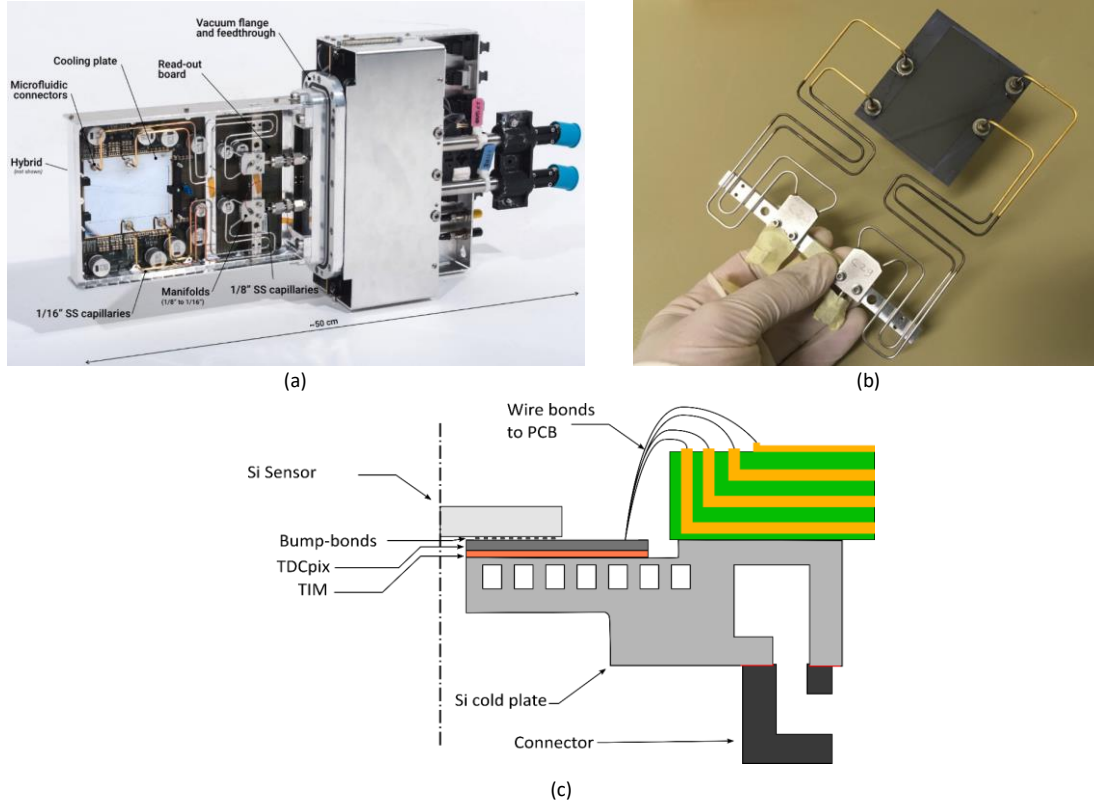


Figure 2.8. Picture of the (a) a NA62 GTK station [135] and (b) cooling plate alone, assembled with capillaries [142]. (c) Partial cross-section scheme of the cooling plate assembled to the silicon sensor.

The silicon cooling plates of the LHCb VeLo Upgrade detector are based on two-phase evaporative CO_2 circulating in microchannels [143]–[145]. The cooling plates exhibit a complex geometry (Figure 2.10 (c)) and larger footprint than the cooling plate used by NA62 to accommodate the four pixel sensors, two per side as illustrated in Figure 2.9(a), for an expected power dissipation of 13 W at the end-of-life. Unlike NA62 cooling plates, the fluidic connection of the LHCb VeLo Upgrade cooling plates is done by soldering to the cold plate a single connector containing the inlet and outlet manifold. Here, the total thickness of the cooling plate is $500 \mu\text{m}$. The microfabrication processes are compatible with the requirements coming from the use of high pressure CO_2 fluid loops qualified up to 200 bars . The cross-sections of the microchannels vary along their paths, featuring cross-section of $60 \times 60 \mu\text{m}^2$ at the inlet, and $120 \times 200 \mu\text{m}^2$ under the active area. These geometrical elements prevent back-flow phenomena and trigger the phase-change.

Two alternatives were also studied: (i) an aluminium nitride plate with a network of four stainless steel capillary tubes brazed to the ceramic, shown in Figure 2.10 (a); and (ii) a three-dimensionally printed titanium cold plate, displayed in Figure 2.10 (b), with embedded microchannels as small as $350 \times 350 \mu\text{m}^2$ [146], [147]. The two alternatives remained as backup solutions, since the silicon cold plate had no coefficient of thermal expansion (CTE) mismatch with the sensors and the ASIC, and passed all the qualifying tests.

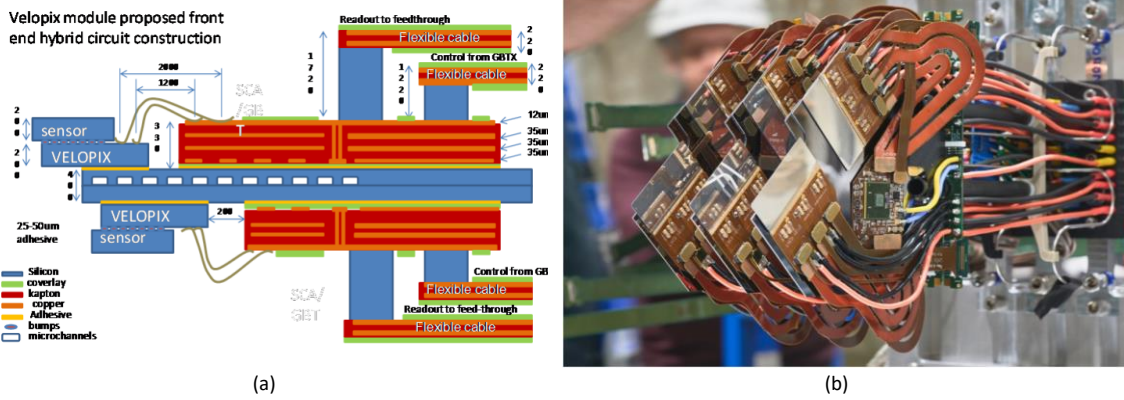


Figure 2.9. (a) Cross-section of the proposed VeLo module with front end hybrid circuit construction [147]. (b) Picture of three constructed VeLo module with the four sensors and the front end electronics assembled on each silicon plate [135]; here in the SPS test-beam.

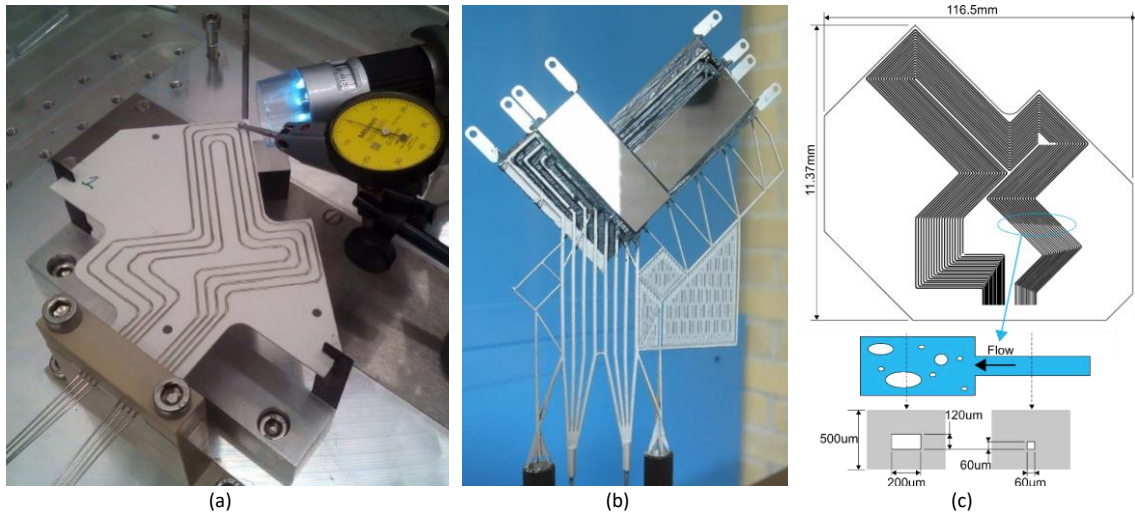


Figure 2.10. (a) AlN cooling plate with brazed capillaries and carbon supporting structures [146]. (b) Titanium 3D printed cooling plate with dummy heaters place on it, mimicking the heat load from the electronics and the sensors [147]. (c) Schematic of the layout of the silicon cold plate with the dimension of the restrictions and microchannels (adapted from [148]).

Beyond these two experiments, where microchannel cold plates are used, two options were developed in the frame of the upgrade of ALICE ITS [54]: one based on microchannels embedded in a PI cold plate [136] and another with microchannels embedded in interconnected silicon frames supporting the silicon sensors. Note that both solutions planned to use the same supporting *space frame*, shown in Figure 2.6, as adopted in the implemented solution for the staves [54]. The first alternative, illustrated in Figure 2.11, consists of a cold plate covering the whole surface of the silicon sensors with an array of 16 parallels microchannels with a cross-section of $800 \times 300 \mu\text{m}^2$ for each channel. Half of them circulates the fluid in one direction, from the inlet, while the second half serves to evacuate the heated fluid. In that way, the inlet and outlet are implemented from the same side of the stave.

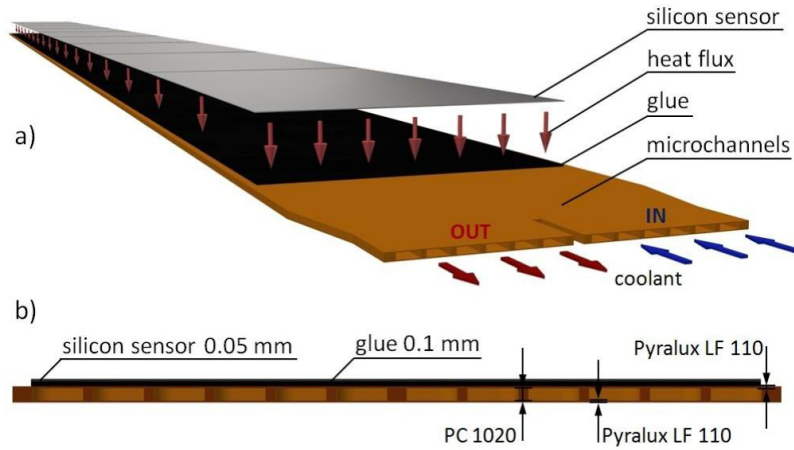


Figure 2.11. Polyimide micro-cooling system for silicon sensors [136]. (a) Sketch of in-going and out-going flows. (b) Cross-section of the microchannels.

The second option, the silicon frames, would also offer connection from one side, but the embedded microchannels cover only the perimeter of the sensors, the centre of the cooling frames are completely removed. Thus, the dissipation also relies on the thermal conductivity of the silicon substrate of the pixel sensors to control the temperature in the sensors. Each frame has two distinct fluidic loops with very distinct roles: the most external microchannels along the longer edges are devoted to supply cold liquid from the inlet to the second loop and the next interconnect frame. For this reason, they possess a larger hydraulic diameter. The second loop located on the inner perimeter of the frame integrates several microchannels with a smaller hydraulic diameter to cool the silicon, as depicted on Figure 2.12. The inner part of the frame has a thickness of $160\mu\text{m}$, whereas the thickness external area is $410\mu\text{m}$ [149].

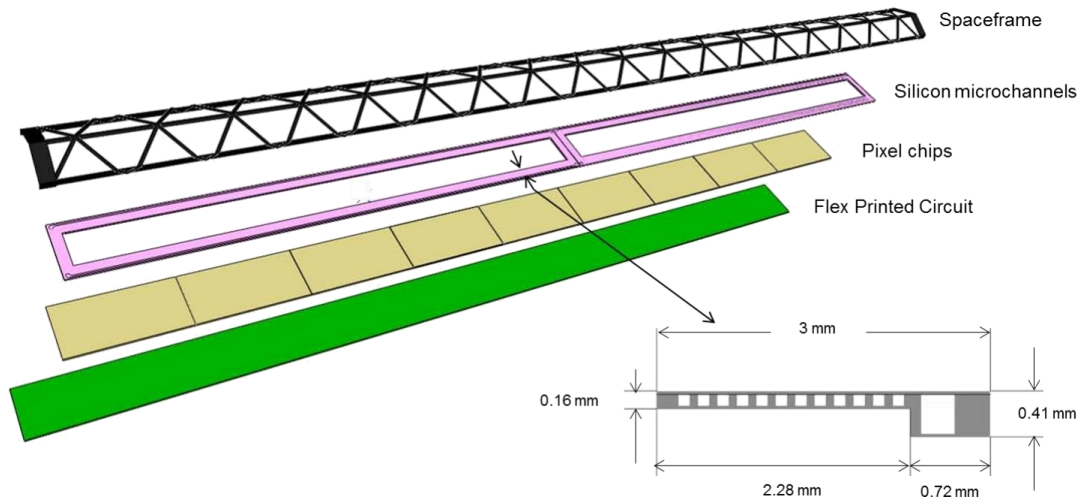


Figure 2.12. Concept of integration of silicon frames with microchannels into the staves for the Inner Layers of ALICE ITS [54].

Microchannels can also be integrated into silicon sensors used in HEP experiments in a different way. For the Belle II pixel detector, a monolithic all-silicon ladder with integrated microchannels was developed [67], [68], [138]. Two types of prototypes were developed: one with the cooling circuit only under the region of the ladder with the highest power density, the ladder's end; one

with an additional microchannel covering the rim of the ladder. An in-plane glued custom 3D-printed connector interfaces the microchannel manifold to the inlet and outlet capillaries.

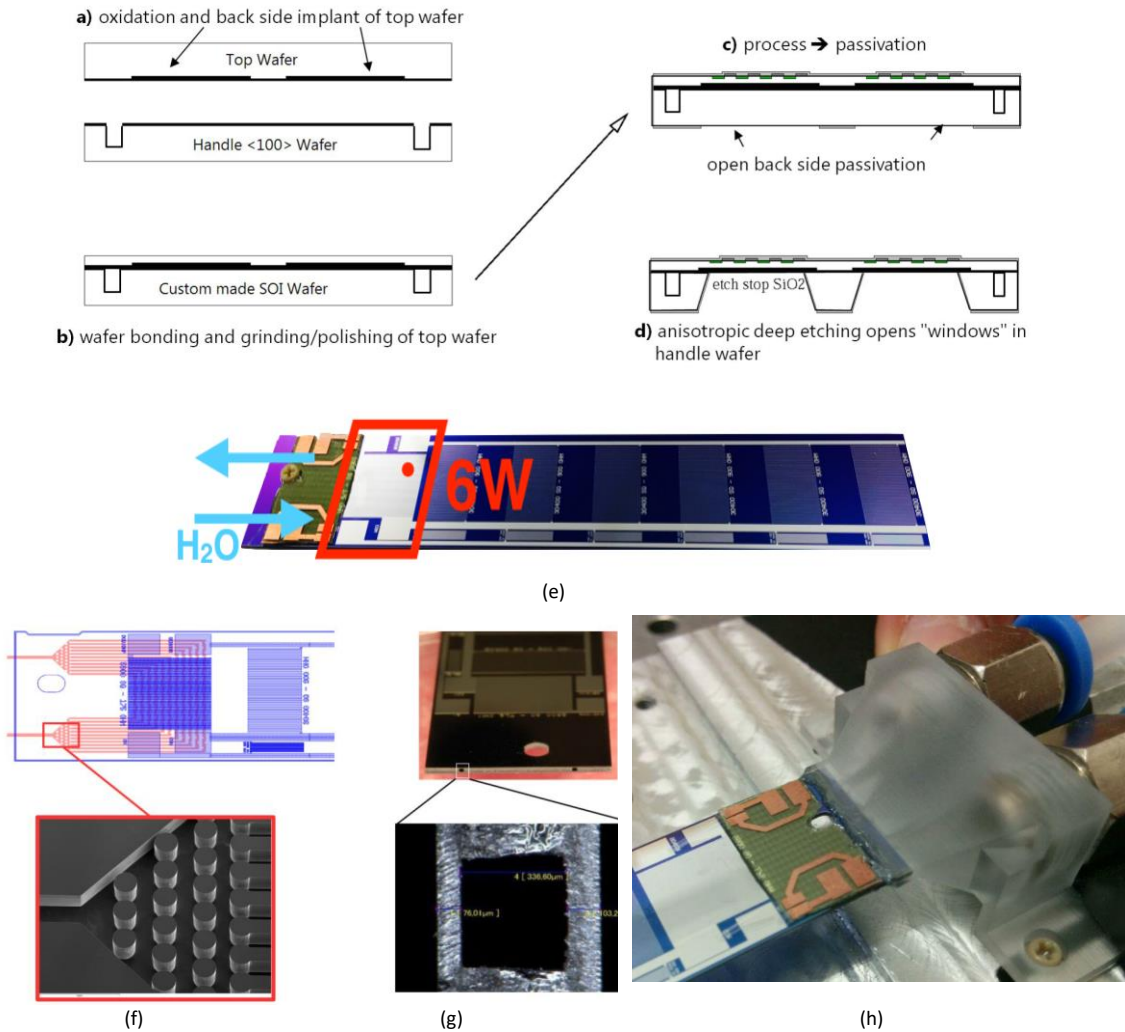


Figure 2.13. DEFPFET monolithic sensor of the BELLE II Vertex detector and the integrated ladder [138], [150], [151].

(a-d) Process flow of the production of the silicon ladder and embedded microchannels. (e) Illustration of one DEFPFET ladder with the inlet, outlet and main heat input locations. (f-g) Layout and SEM image of the pillars located at the inlet manifold. (d) Cross-section of the inlet and outlet microchannels. (h) 3D-printed connector glued to the silicon ladder and connected the fluidic lines.

Microchannels can also be directly integrated into the silicon dies. They are directly etched in the backside of the sensor as it was demonstrated with MATLTA chips [135], [152]. The CMOS-compatible process, developed at CERN and fabricated at the Center of Micro-Nanofabrication (CMi) at the Swiss Federal Institute of Technology (EPFL), relies on micro-trenches of $3 \times 10 \mu\text{m}^2$ etched in silicon. Bottoms of the trenches are then isotropically etched to create circular microchannels. A parylene layer then seals the top of the trenches and a 3D-printed connector provides the connection to the single-phase pumping system for testing purposes. Fluidic tests revealed that such microchannels can withstand 110 bars. Figure 2.14 shows the process flow and an SEM image of a cleaved sample. Kluba et al. [153] developed a similar process for high aspect ratio rectangular microchannels. Trenches and microchannels are etched through a SiO_2 mask using a single-step DRIE process. An additional PE-CVD SiO_2 layer is deposited over the existing mask and seals the top of the trenches.

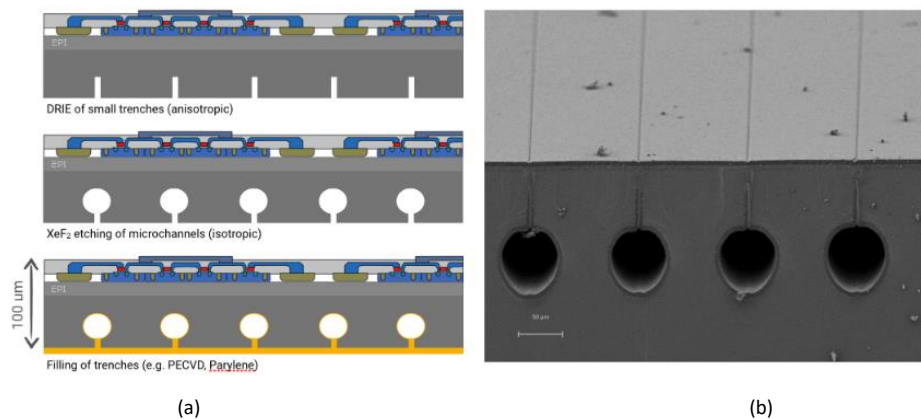


Figure 2.14. Buried microchannels [135]. (a) Schematic of the process flow. (b) SEM image of the cross section of buried micro channels in silicon.

2.3.3.2 Space applications

The relevant literature on the use of microchannel cooling systems in space is scarce, for both single or two-phase systems. Even taking into account the many advantages microchannel technology offers for cooling, research in this field has been mainly focussing on high heat flux devices [154]. In 2010, the draft version of the NASA Thermal Management Systems Roadmap Technology [94], the microchannels cold plates and heat exchangers were considered reaching a Technology Readiness Level (TRL) of 2-3, with the possibility of reaching TRL 6 by 2015. Unfortunately, newest versions of NASA roadmap, issued in 2015 [95] and 2020 [96] do not mention microchannels as cooling strategy. Already in 2001, the Jet Propulsion Laboratory (JPL) investigated the use of a MEMS-based cold plate for micro and nanosatellites [155]. The silicon cold plate was populated with 50 μ m-deep microchannels with widths ranging from 50 μ m to 100 μ m and deionized water was circulated inside. More recently, in 2010, the NASA Johnson Space Centre, partnering with the Pacific Northwest National Laboratories, developed a single-phase microchannel heat-exchanger in stainless steel [156]. The Defence Advanced Research Projects Agency (DARPA) initiated the Thermal Management Technology program in 2008 to pursue thermal management of aerospace high-performance semiconductor devices by improving through micro- and nanotechnologies. In this context, the DARPA started the Near Junction Thermal Transport and ICECool programs, respectively in 2011 and 2012. The latter program focused on microfluidic cooling, including fabricating micro-pores and microchannels directly into the chip (intra-chip approach) [157], or utilizing the gap between the three-dimensional stacked chips (inter-chip approach) [158]–[160]. The use of microchannels at chip level most of the time involved the use of silicon [161]. Within these two research programs, it was demonstrated that alternative substrates to silicon can be interesting: Bae et al. [162], [163] developed a silicon carbide manifold-microchannel cooling plate with high aspect-ratio channels for both single- and two-phase phases. They found that the use of silicon carbide substrate (SiC) significantly increased the thermal performance of the cooling system. However, the results obtained with microfabricated SiC are not on par with those for silicon.

While applying two-phase microchannel cooling in space, Robinson et al. [159] determined that one of the significant barriers to the use of such micro-cooling systems is the complex nature of the boiling flow, especially under reduced gravity, in particular as there was a limited amount of experimental data available. They reduced the complexity of parallel microchannels by using a

single, low aspect ratio channel, also called microgap. This configuration mitigates the flow instabilities and flow reversal as it enables the vapour to expand both downstream and spanwise [164]. Only a limited quantity of data and correlations are available for microgravity (μg), but as they are critical to put two-phase microchannels into use, research actively continues on the subject and takes place on ground and in reduced-gravity environment [84], [89]–[92].

2.3.4 Micro Heat Pipes (μ HPs)

Macro-scale heat pipes existed prior to the micro version, since the 1940s [165] and were preceded by the Jacob Perkins tube [166]. Nowadays, they are widely used in many industrial and automotive applications, as they are able to transfer heat by using the latent heat of vaporisation and the capillary properties of the working fluid. However, despite numerous studies on heat pipes for the last fifty years, the research continues as no predictive tool exists for their design, leading to a limitation in the diffusion of this technology due to the need of carefully design and testing for each application. During the last decade, studies tried to capture the complex nature of the two-phase flow occurring in heat pipes, notably by studying the effect of gravity, the effects of magnetic and electric fields, as well as the relationship between the start-up behaviour, the working fluid and the substrate's material [167], [168].

Macro scale heat pipes (μ HPs) are very attractive cooling components for spacecraft thermal control due to their low weight, high reliability and absence of maintenance needs. They are used in space for cooling electronics, sensors or structural elements [168]–[172]. The first experiments started in 1974 with the flight of the International Heat Pipe Experiment [173] and continued up to this day, ranging from conventional heat pipes to thermal diodes and sorption heat pipes, including loop and capillary pumped loop heat pipes [93], [169], [174].

Micro heat pipes appear to be one of the most promising solutions among the innovative and passive cooling technologies developed to provide highly efficient and compact thermal control solutions. They have attracted considerable attention since they were first introduced [77], [78], [112]. Proposed by Cotter in 1984 [175], the concept of micro heat pipe consists in one device “so small that the mean curvature of the vapour-liquid interface is necessarily comparable in magnitude to the reciprocal of the hydraulic radius of the flow channel”. Despite remaining only a conceptual description at the time, it paved the way to a series of investigations on the steady-state and transient behaviour of the liquid trapped in the device, but also to the development of a variety of micro-scale heat pipes.

2.3.4.1 Micro Grooved Heat Pipes (μ GHPs)

As said before, Cotter envisioned in 1984 the first micro heat pipes, today referred to as micro grooved heat pipes (μ GHP), Peterson validated the concept later in 1993 [176]. Initially, μ GHP's substrates integrated triangular or rectangular groove arrays, all linked by a common fluid line as illustrated in Figure 2.15. More complex shapes as star and rhombus micro-grooves [177], [178], or arteries are possible. Figure 2.16 illustrates the most common cross-sections of the μ GHPs. The presence of the micro grooves increases the effective thermal conductivity, which is highly influenced by the circulation capacity of the working fluid. The working principle residing behind μ GHP is the change of radii of curvature between the hot and cold parts, which forces the liquid

backflow to the evaporator. Arrays with triangular channels have a higher effective thermal conductivity than those with a rectangular cross-section as the former feature smaller interior angles.

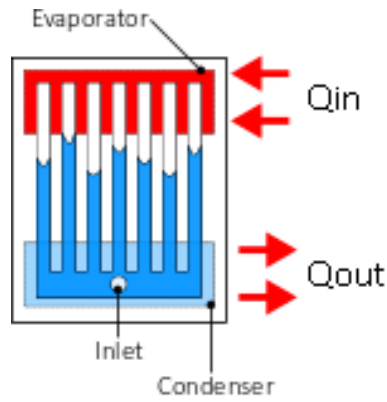


Figure 2.15. Schematic of an μ GHP with a channel which serves as common cold pool or just as charging channel.

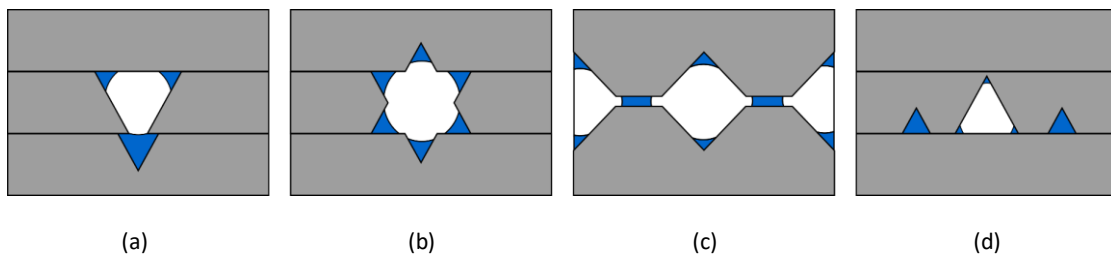


Figure 2.16. Cross-sections of complex channel geometries of μ GHPs. The substrate is in grey, the liquid phase in blue and the vapour in white. (a) Stacked triangular groove with triangular artery constituted of three layers. (b) Star groove constituted of three layers. (c) Rhombus groove layer. (d) Triangular groove with small return arteries in the same plane.

The resulting improvement, in term of thermal performance, ranges from none [179] to an improvement of 300% compared to similar substrates without micro-grooves [180]. Gillot et al. [181] proposed two μ GHP spreading the heat of electronics systems, one copper-based one and a silicon-based alternative. Luo et al. [182] designed a micro-GHP array with arteries and non-parallel cross-section resulting in ten-times higher maximum thermal conductivity than bulk silicon. Similarly, Kang et al. [183] demonstrated the advantages of incorporating arteries for an improved backflow of the liquid. Additional representative studies are summarized in Table 2-4.

Table 2-4. Non-exhaustive summary of studies on μ GHPs

Ref.	Working fluid	Substrate material	Cross section shape and width x depth (μm^2)	Channel number	Charging ratio [%]	Remarks
[176]	Methanol	Silicon	Triangular (120x80), rectangular (45x80)	39, Uniform and Parallel	-	At 4W of power input, an increase of thermal conductivity of 31% and 81% compared to plain silicon were observed
[177]	Methanol	Silicon	Star(662x326), rhombus (180x160 + 620x24)	31, Uniform and Parallel	0, 20, 40, 60, 80	The thermal conductivity reached 277.9W/m·K for star-shaped grooves and 289.4W/m·K for rhombus-shaped ones
[178]	DIW	Silicon	Rectangular (200x67), Trapezoidal-rectangular (200x85 - 70x30), Double rectangular (200x50 + 110x45)	40, Uniform and parallel	20, 40, 60	Three different cross-sections of microchannel were etched and then their thermal performance was compared. Based on the observation, an optimisation based on Box-Behnken design was performed and resulted in a thermal conductivity of 119W/m·K.
[184]	DIW	Silicon	Trapezoidal(350-700x162.5)	70, Expanding and radially distributed	30%, 53%, 70%	Temperature of the evaporator is decreased by 27% compared to bulk silicon.
[181]	DIW	Brass	Grooves: rectangular (200x400), chamber: rectangular (2000x9400)	-, Uniform and Parallel	-	Brass μ GHP possesses a thermal resistance of 0.5 K/W at best.
[181]	DIW	Silicon	Grooves: rectangular (90x100-300), Chamber: rectangular (500x9400)	-, Uniform and Parallel	-	The best performance achieved is 1.5 K/W using 300 μm wide grooves.
[180]	Ethanol	Silicon	Triangular (230x170)	55, Uniform and Parallel	6-66	Highest thermal conductivity reached is 133 W/m·K.

(Table continued next page)

Table 2-4 (continued)

Ref.	Working fluid	Substrate material	Cross section shape and width x depth (μm^2)	Channel number	Charging ratio [%]	Remarks
[180]	Methanol	Silicon	Triangular (230x170), Triangular (500x340) with triangular arteries (-)	25 (and 25 arteries), Uniform and Parallel	50	Improvement of 300% compared to empty heat pipe when triangular arteries are present
[185]	DIW	Copper	Rectangular (100x250)	-, Uniform and Parallel	30-50	Use wettability gradient and structure fabricated by laser to reach a thermal resistance of 0.0025W/K at 50W. Higher hydrophilicity leads to lower thermal resistance, with an optimal contact angle of 45°
[182]	DIW	Silicon	Grooves: rectangular (Parallel: 150x160, 230x160, Non-parallel: 150-100x160, 230-180x160), chamber: rectangular (10000x200)	-, Non-uniform, parallel and non-parallel.	35	Non-parallel and large grooves help with vapour return to the condenser which results in 743W/m·K at 3W (horizontal operation).
[183]	Ethanol	Silicon	Triangular (200x156) with triangular arteries (100x78)	9 (and 8 arteries), Uniform and parallel	90	Arteries effectively return the liquid to the evaporator section, limiting the onset or dry-out.

2.3.4.2 Micro Capillary Pumped Loops (μ CPLs) and Micro Loop Heat Pipes (μ LHPs)

Micro capillary pumped loops (μ CPLs) and micro loop heat pipes (μ LHPs) both use separate vapour and liquid lines to supply liquid to the evaporator and evacuate the generated vapour [186], [187]. By separating vapour and liquid phases of the working fluid, the shear force at the interface vanishes, maximizing the heat transport [188]. However, both of these types of micro heat pipes need wicking structures to operate, mainly located in the evaporator. The two designs share similar features: an evaporator, a condenser, a liquid reservoir and separate liquid/vapour transport arteries. The difference resides in the location of the reservoirs: μ CPLs possess a remote reservoir while it is directly integrated in the evaporator for μ LHPs and is called compensation chamber [189]. Conceptualized in 1999 by Kirshberg et al. [190], the first μ CPL used monoporous (single-scale pores) wick structures as grooves wicks, structural wicks, mesh and powder wick structures. The design of wicks evolved to be biporous, with two distinct pore and structure scales, to increase the heat transport capability [191], [192].

Integration of the μ CPLs and μ LHPs also evolved from 2D planar to 3D integrated structures [193]. The combination of both results in relatively heavy and thick devices. More recently, researches aimed to reduce the overall thickness of the micro devices [194], [195]. Notably, Fujitsu Laboratories developed a 0.6mm thick evaporator, which was aimed for consumer mobile electronics cooling [196]. Assembled from six 0.1mm-thick copper plates assembled by diffusion bonding, the device featured a three-dimensional mesh with staggered micro-holes as wick. The Table 2-5 summarizes the dimensions of several μ CPLs and μ LHPs, and their wicking structures.

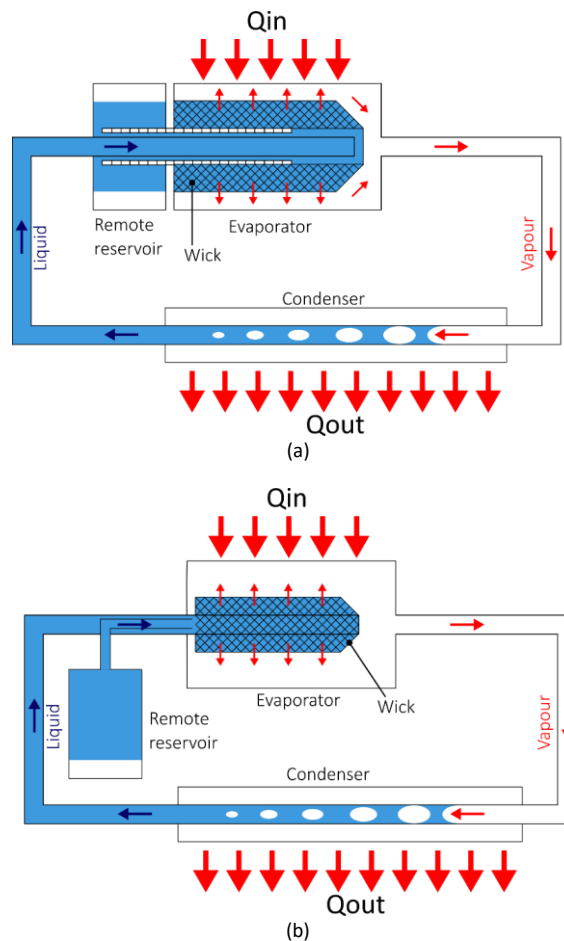


Figure 2.17. Schematics of (a) a μ LHP and (b) a μ CPL.

Table 2-5. Non-exhaustive summary of μ CPL and μ LHP researches.

Ref.	Working fluid (Charging ration %)	Substrate material	Evaporator / condenser area (μm^2)	Wick type and dimensions (size x depth, μm)	Remarks
[197]	FC-72 (50, 60, 70)	Silicon	24000x24000 / 24000x24000	Array of 56x56 cone shaped microgrooves at the condenser($\varnothing 55 \times 480$) and at the evaporator($\varnothing 250 \times 480$)	The CPL handled 6.22 W/cm^2 for the air-cooled condenser. 10 minutes were necessary to reach steady-state operation conditions. The relative height between the evaporator and the condenser influenced the heat transport capability.
[198]	DIW(-)	Silicon carbide	2000x1070 / 5070x7500	Parallel grooves at the evaporator (2000x22) and at the condenser (5070x22)	Tests demonstrated that larger widths of the vapour and liquid lines result to higher heat removal capability
[188]	DIW(-)	Silicon	9000x10000 / 10000x20000	167 two-staged parallel grooves only at the evaporator (20x60 + 20x200)	Two-staged grooves prevent back-flow and vapour accumulation at the evaporator. The thermal resistance reaches 6°C/W .
[192]	-(-)	Silicon (Quartz wool fibre for the stochastic secondary wick)	- / -	Coherent porous silicon ($\varnothing 2 @ 4 - 25\%$ porous, $\varnothing 5 @ 10 \mu\text{m} - 25\%$ porous and $\varnothing 5 @ 10 \mu\text{m} - 39\%$ porous) and stochastic secondary wick($\varnothing 8 - 92\%$ porous) at the evaporator	The coherent porous silicon separates the liquid and the vapour phases.
[196]	DIW	Copper	15000x15000 / 5600x110000	Staggered holes at the evaporator ($\varnothing 200 \times 400$)	Thermal resistance reaches 0.8 K/W

2.3.4.3 Micro Oscillating Heat Pipes (μ OHPs)

Oscillating heat pipes, also known as pulsating heat pipes, were introduced by Akachi in 1990 [199], [200]. They consist of a serpentine-arranged single-loop capillary channel in open or closed loop configuration. The motion of the fluid results from pressure difference between the evaporation and condensation of the alternating vapour plugs and liquid slugs. This type of heat pipe does not possess any wick structure, thus simplifying the fabrication process and reducing the fabrication cost.

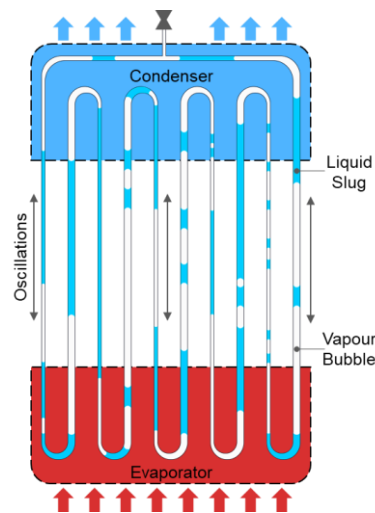


Figure 2.18. Schematic representation of a closed-loop μ OHP. The heat supplied vaporizes the liquid entering the area, while the vapour entering the condenser condenses and cools down.

Qu *et al.* [201]–[206] conducted the first experiments on μ OHP in silicon. The simultaneous flow visualisation and local temperature monitoring proved that the OHP can be translated to the micro scale and that the device is capable of sustaining oscillatory flow with good thermal performance. Several studies identified the relevant trends in thermal performance depending on materials and geometry of the devices, the working fluid, the heat input and the orientation of the device (gravity). These studies indicate that the highly chaotic two-phase flow pattern also influence the performance of the micro device [207], similar to what was observed with macro scale OHPs [208]–[210]. Considering the high flow resistance of microchannels, the driving potential of the working fluid has been found to be an important characteristic as it would ease the start-up and creates robust oscillatory flow. Thus, a fluid possessing a large saturation pressure gradient, $(dp/dT)_{sat}$, is favourable, as it would give an important pressure fluctuation for a small temperature change.

As the thermo-hydrodynamics are not well known, studies discussed the roles of the working fluids, the number of turns, the possible designs and influence of gravity, as well as the flows observed and the start-up characteristics. Properties of the working fluids largely influence the two-phase interface and the motion of the fluid, especially considering the increased flow resistance of the slug flow in the microchannels. The number of turns determines the length of the flow path, and consequently flow resistance. Besides the flow resistance, the number of turns also influences the role of the gravity: a higher number of turns reduces the influence of gravity on the thermal performance for different orientations. The literature tends to conclude that a minimum number of turns is required to operate horizontally or with the evaporator higher than the condenser. In addition, the integration of Tesla-type check-valves [211], [212], or asymmetric

microchannels [213], would increase the heat transfer while decreasing the role of gravity as the system would have a preferred direction of circulation of the flow [214].

From physics, it is known that the balance of forces between gravity and surface tension leads to the formation of bubbles. Therefore, Zhang and Faghri [215] proposed a value for the upper limit of the internal hydraulic diameter based on the ratio of these two forces, known as the Bond number, denoted Bo . This limit is expressed as:

$$Bo = D_{max} \sqrt{\frac{(\rho_l - \rho_g)g}{\sigma}} \leq 2 \text{ or } D_{max} \leq 2 \sqrt{\frac{\sigma}{(\rho_l - \rho_g)g}} \quad (2.3)$$

With D_{max} the maximal diameter, ρ the densities of the two phases, g the gravitational acceleration and σ the surface tension.

In a similar manner, a lower limit was proposed by Dobson and Harms [216] which is expressed as:

$$D_{min} \geq 0.7 \sqrt{\frac{\sigma}{(\rho_l - \rho_g)g}} \quad (2.4)$$

This lower limit prevents high flow resistance, which would hinder the start-up for the oscillations. Qu et al. [217] proposed a newer lower limit based not only on the two forces, but also on the operating characteristics and design of the μ OHP. The results showed that hydraulic diameters smaller than 300 μ m are usable with common refrigerants, this limit varies non-monotonically with the number of turns, the inclination, the temperature and the charging ratio. Table 2-6 summarizes recent and relevant papers on μ OHPs and mini-OHPs.

Table 2-6. Non-exhaustive summary of studies on μ OHPs and mini-OHPs.

Ref.	Working fluid	Substrate material	Cross section shape (top width (bottom width) x depth [μ m])	Channel distribution / number	Charging ratio	Remarks/Notes
[201]	FC-72	Silicon	Trapezoidal (820 (294)x303, 1020 (485)x303)	Uniform / 7,5	41-58%	No nucleation was observed over the start-up period. The μ OHPs sustained oscillations at an inclination angle ranging from 10° to 90° (bottom heating mode) with FC-72. Injection flow type only appeared in largest device.
[218]	Acetone	Aluminium	Rectangular (762x762)	Uniform / 15	73%	3D geometry proved to work in bottom heating mode with localized heat input up to 180W/cm ² . However, with very localized heat flux, fluid in the microchannels further away did not move.
[219]	DIW + Acetone	Copper	Rectangular (1175x1700)	Uniform/8		The investigated 3D design generally displayed a lower thermal resistance than the experiments conducted with smaller microchannels [218]. The average temperature oscillations depended on heating, channels' width, operating orientation and working fluid properties. Localized heating led to larger peak-to-peak temperature amplitudes in the evaporator.
[220]	Ethanol	Silicon	Rectangular (1000x400)	Uniform/5	50%	Liquid oscillations' frequency and amplitude were 0.67 Hz and 15 mm at the best thermal performance. Effective thermal conductivity reached 600W/m·K.
[221]	R113 + FC-72	Silicon	Trapezoidal (820 (294)x303)	Uniform/7	41-58%	A maximum reduction in evaporator's temperature of 34.9% were obtained with R-113 for 6.3W of power input. FC-72 led to smaller reduction of the temperature. The use of dielectrics fluids limits with good wetting properties of silicon limits the nucleation.
[202]	R113 + FC-72 + DIW + Ethanol	Silicon	Trapezoidal (266 (618)x201, 820 (294)x303) and (1020(485)x303)	Uniform/5,7 + 5	0-73%	Best thermal performance were obtain with filling ratios of 52%, 55% and 47% for the three μ OHPs, respectively, in bottom heating mode. Liquid film evaporation drove the pulsating two-phase flow.
[222]	DIW	Copper	Rectangular (2000x2000, 2000-1000x2000)	Uniform /8 and non-uniform/ 8	40%, 50%, 60%, 70%	Results linked the thermal resistance decreases to the increase of heating power by the rise of circulating speed. Inclinations increases decreased the thermal due to gravity effect. However, it appears that the uniform channel OHP were more sensitive to inclination especially when the inclination angles were small and it is not functional at a horizontal configuration.

(Table continued next page)

Table 2-6 (continued)

Ref.	Working fluid	Substrate material	Cross section shape (top width (bottom width) x depth [μm])	Channel distribution / number	Charging ratio	Remarks/Notes
[223]	HFE-7100	Silicon	Rectangular (uniform, 800x250; non-uniform, 1000x 250 and 600x250)	Uniform/4, non-uniform/4	uniform: 59.3%, non-uniform; 61.5%	Only alternate channel micro-OHP could start up and operated horizontally with power input of 7W at maximum. Vapour slug moved sine-like for both the uniform and alternate channel designs.
[224]	R245fa	Brass	Rectangular (1000x1000)	Uniform/1	20%, 40%, 60%, 80%	Latent heat is dominating the heat transfer process. Shear stress and gravity were determined as the only axial forces acting on the fluid, which supplied the impulse necessary to reverse the flow's sense.
[225]	FC-72	Copper tube	Circular (1100, 500)	Uniform/16	50%	The Model developed was compared to experiments of tubular OHP for 0g, 1g and 2g with less than 7°C of error. With a reduced hydraulic diameter, the thermal performance is hinder at all g-levels.
[226]	Ethanol + FC-72	Silicon	Rectangular ((1000–1800)x500 and (1000–200)x500)	Non-uniform/5	50%	The μOHP with dual-diameter channels operated independent of the orientation. They displayed better thermal performance than that with uniform channel. Effective thermal conductivity topped at 905W/m·K with five dual-diameter pairs.
[227]	DIW + methanol	Silicon	Rectangular (500x250 and 300x250)	Non-uniform/32	80%	Water-charged μOHPs failed to operate, whereas the methanol-charged ones with non-uniform channel operated with better thermal performance.
[228]	Ethanol	Silicon	Rectangular (1000x500)	Uniform/5, 10, 15 20	50%	With more than five turns, closed-end μOHP had higher effective thermal conductivity than that of the closed-loop one. Besides, the former's performance is more orientation-independent than the latter.

(Table continued next page)

Table 2-6 (continued)

Ref.	Working fluid	Substrate material	Cross section shape (top width (bottom width) x depth [μm])	Channel distribution / number	Charging ratio	Remarks/Notes
[229]	FC-72 + Ethanol	Stainless steel	Rectangular (1000-500x500)	Non-uniform/ 7	FC-72: 20%, 55%, 67%, Ethanol: 20%, 40%, 53%	The thermal conductivity of the stainless steel μOHP filled with FC-72 is higher than that by ethanol. An optimum filling ratio was found around 55% and 40% for FC-72 and ethanol, respectively. The corresponding thermal conductivities are respectively 276 and 158W/m·K.
[230]	Ace-tone	Silicon	Rectangular (878x400)	Uniform/5	40%, 53%, 58%, 61%, 64% and 74%	The μOHP experienced intermittent periods of stop-over, small-oscillation and large-oscillation. Operating ranges of heat load and filling ratio expand as the inclination angle increases (30° to 90°) signifying. Gravity had a non-negligible positive function in the flow dynamics and thermal performance of the μOHP , despite low Bond number ($\text{Bo}=0.314$).
[231]	HFE-7000	Silicon	Rectangular ((1000-1500)x500)	Uniform/5 (randomized layout)	50%	The channel layout affects the thermal performance under local heating condition: up to 32% higher thermal performance with randomized layout.
[232]	R141b	Silicon	Rectangular(285.7(226.5-365)-285.7)	Uniform/16, Non-uniform/ 16	50%	Expanding channels led to better thermal performance but achieved ephemerally circulation flow. Straight channels experienced intermittently localized slug-plug oscillations and intermittent stop-overs. Thus, expanding channels are beneficial for realizing robust oscillating motions of larger amplitudes for heat transfer enhancement.
[233]	Liquid Nitrogen	Copper	Rectangular (2000x2000)	Uniform/9	60%	The device operated normally even in the horizontal orientation. Effective thermal conductivity decreased by 20.4% on the average.
[234]	HFE-7000	Copper + polyimide	Rectangular (1500(500)x500)	Non-uniform/15		The flexible μOHP thermal performance reaches 1070W/m·K in bottom heating mode. At other orientation or when bent, the performance decreases.
[235]	FC-72	Silicon	Rectangular (3250-1550x300)	Non-uniform/8	50%	The asymmetric OHP possesses better thermal performance at all orientation than supported graphite. The performance is not uniform over all orientations: it decreases when the action of gravity on the fluid is reduced.

2.3.4.4 Micro Vapour Chambers (μ VCs)

In general, micro vapour chambers (μ VCs) possess similar wick structures as evaporators in the μ LHP and μ CPL. But, unlike them they can spread the heat in two directions, as highlighted by Peterson *et al.* [236]. μ VCs, also known as micro flat heat pipes, consist of closed containers with inner walls covered in wicking structures. In a general manner, the evaporating area is smaller than the condensing one, while the two are located at opposite side, as illustrated in Figure 2.19

The capillary limitation is a primary point of focus of the studies as it is, with the orientation-dependence and gravitational environment, one of the major impact parameters on the heat transfer of the μ VCs [194], [237]. For this reason, various wick sizes and designs were investigated to increase the handled heat flux while lowering the superheat, including micro- and nano- hierarchical capillary wicks. Cai *et al.* [238] based their silicon vapour chamber on fine and coarse pillared wicks for the evaporator and condenser, respectively. The design of the 3mm-thick device allowed reaching an exceptionally high thermal conductivity of 2500W/m.K with low orientation dependence when filled with ethanol. While being at the same scale, the use of the two wicks benefits to the thermal performance. Ding *et al.* [239] used a hierarchical wick for the μ VC. In this special case, the heat and cold source were placed on the same side of the device. The base material was titanium and the wicking pillars had a diameter of 5 μ m with a square pitch of 10 μ m and a height of 50 μ m. Oxidized titanium formed a nano-structured titania, 200nm hair-like, secondary wicking structure on the pillars. The 600 μ m-thick device was filled with DIW and displayed a thermal conductivity of 350 W/m.K.

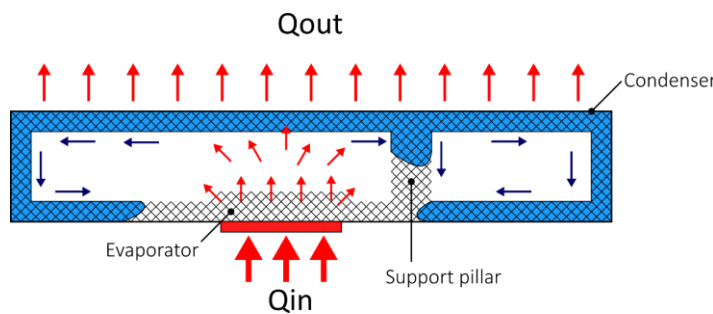


Figure 2.19. Schematic of a μ VC. The heat is spread by evaporation of the fluid on one side and condensation on the opposite side. The wicking structures along the edges of the chamber help to liquid to return to the evaporator and for structural resistance, support pillars might be integrated with, or without, capillary role.

The presence of wicking structures increases the risk of flow blockage after a long period of use and the generation of non-condensable gases [240]. Kumar *et al.* removed the wicks and used a surface-active ionic liquid to mitigate these issues [241]. The return of the condensed liquid did not rely on wicks but on gravity, limiting the potential orientation independence of the device, without speaking the potential application in environment subject to micro-gravity. More examples are summarized in Table 2-7.

Table 2-7. Non-exhaustive summary of investigations on μ VCs.

Ref.	Material	Working fluid	Wick	Wick dimensions (width x depth) [μm^2]	Remarks
[242]	Copper and sintered copper particles	DIW	Thin evaporator wick, multilayer screen condenser wicks connected by the 12 capillary arteries and porous support ports	Evaporator: $2 \times 3.5 \text{ cm}^2$ with particle of $60 \mu\text{m}$ of diameter Condenser: $12 \times 7 \text{ cm}^2$ Support post with $150 \mu\text{m}$ particles	The evaporator wick extends beyond the heater area (1 cm^2). No wick is used outside this area, thus liquid delivery is through the permeable arteries to the evaporator wick. The device handled a heat flux of 380 W/cm^2 for a thermal resistance of $0.05 \text{ K}\cdot\text{cm}^2/\text{W}$.
[243]	Silicon	DIW	Round pillar array, rectangular wick structures on the wall of the cell	Pillars: 100×250 Wall wick: 50×150	Hexagonal cell withstanding up to 300 W/cm^2 with a superheat of 35°C when heated on a $2 \times 2 \text{ mm}^2$ area.
[239]	Titanium	DIW	Micro pillar arrays with surface nanostructured with hair like titania	Pillars: $\varnothing 5 \times 5$ Titania: 200 nm	The effective thermal conductivity reached $350 \text{ W/m}\cdot\text{K}$ at 7.2 W
[238]	Silicon	DIW and Ethanol	Coarse square micro pillars array at the condenser Fin cylindrical micro pillar array at the evaporator	Cylindrical pillars: $\varnothing 10 \times 220$ Square pillars: 200×300 Posts: 2000×2000	A heat transfer of $2500 \text{ W/m}\cdot\text{K}$ was achieved at 10 W using ethanol, at several orientation and in high gravity environment.

2.3.4.5 *Micro Heat Pipes in Space*

Micro heat pipes are used in a number of terrestrial applications ranging from smartphone to computer [194]. However, due to the complexity of development, the use in space mission is scarce to not existent. With the exception of Ando et al. [244], and the on-orbit demonstration of μ OHP, the long flight test of μ OHPs onboard the Boeing X-37 [245] and a mini heat pipe onboard the GSAT-19 satellite from ISRO, the studies are limited to short period of microgravity flying with sounding rockets or parabolic flights. Table 2-8 summarizes the recent studies on mini and micro heat pipes.

Operating independently of the orientation of the heat pipe on Earth is not sufficient for space uses and an actual low gravity demonstration has to be conducted. The access to testing under microgravity conditions is limited. Parabolic flights and sounding rockets allow access at a reasonable price, however reduced gravity time is from second to minutes. To reach a high μg quality for an extended period three alternatives exists: experiments on boards ISS, experiments flying on a satellite or experiment flying in an orbital vehicle. There is a long waiting list for ISS use, and the last options implied a specific scientific payload.

Ground-based facilities simulating microgravity are either based on the clinostat principle, on the magnetic levitation principle or on the random position principle [246]. It is worthy to mention that most of experiments conducted within these facilities lack of comparison point with real microgravity and the difference can be noticeable between the simulated and the real microgravity. Drop towers, such as the on Bremen Drop Tower of ZARM, offer microgravity for a period in the order of a few seconds.

Table 2-8. Summary table of recently conducted studies on mini and micro heat pipe for microgravity.

Ref.	Type	Working fluid	Substrate	Cross section and dimension (top width (bottom width) x depth) [μm^2]	Microgravity platform
[245]	μOHP	Butane + R134a	-	Rectangular (1000x1000)	Boeing X-37
[247]	Hybrid Closed Loop Thermosiphon/PHP (SPHP concept)	FC-72	aluminium	Circular (3000)	Parabolic flight
[248]	HP	DIW + DIW/alcohol mix	Copper	Circular (8000, wickless; 4000 composite wick)	Parabolic flight
[198]	μOHP	R134a	Stainless steel	Circular (800)	Satellite
[202]					
[250]	Hybrid Closed Loop Thermosiphon / PHP (SPHP concept)	FC-72	Aluminium	Circular (1700, 3000)	Sounding rocket
[251]	OHP	Acetone	Aluminium	Rectangular(1300x1300)	Parabolic flight
[252]	OHP	FC-72	Copper	Circular (1100)	Parabolic flight
[253]	OHP	FC-72	Copper	Circular (1100)	Parabolic flight
[254]	OHP	Ethanol	Titanium & Molybdenum	Rectangular(3000x2500)	Parabolic flight
[255]	Hybrid GHP with sintered particle at the evaporator	Methanol	Copper	Circular (1270)	Sounding Rocket
[256]	OHP	R114	Teflon	Circular (1600)	Parabolic flight
[257]	μOHP	R134a	Aluminium	Rectangular (1000x1000)	Parabolic flight
[258]	Hybrid Closed Loop Thermosiphon/PHP (SPHP concept)	FC-72	Aluminium	Circular (3000)	Parabolic flight
[259]	OHP	FC-72	Copper	Rectangular(1600x1700)	Parabolic flight
[260], [261]	Hybrid Closed Loop Thermosiphon/PHP (SPHP concept)	FC-72	Copper	Rectangular (2500x2500)	Parabolic flight

2.3.5 Thermal Straps

In some applications, the heat can be removed without the use of micro channel cold plate or fluid loops, by relying on the thermal conductivity of the material alone to transport and control the heat of the device through the mounting system. This heat removal system is called a thermal strap. Thermal straps create an additional heat transfer path, and they can consist of simple pieces of highly thermally conductive materials. This approach has been used for decades. On some occasions, mechanical compliance is needed. Thus, flexible thermal straps are employed to avoid stress resulting from a mismatch of the coefficient of thermal expansion of the materials. The flexible thermal straps either consist of thin foils, slit or not, braids or wire attached at both end to the heat source and heat sink [262].

Thermal straps are commonly constructed from copper or aluminium due to their high capacity to transfer heat and low production costs. Advanced solutions are also used to reach increased thermal transport and handling capacity, for example, silicon carbide or supported graphite. Encasing graphite in a matrix material such as aluminium or copper, or simply adding layers on top of the metal thermal straps, drastically increases the thermal conductivity of the thermal straps [263], [264]. As the out-of-plan thermal conductivity of the graphite is low, thermal vias are incorporated under the hot spots to increase the diffusion of the heat and thus benefit from all the thickness of the annealed pyrolytic graphite (APG) present. This technology is used for the spine of the end-cap module of ATLAS [265]. The spine supports silicon ASIC-hybrids on both side and has to provide them structural supports and heat transfer. It consist of sandwiched TPG between aluminium nitride plates. The ATLAS ITk OB depends also on TPG to evacuate the heat from the sensors, complemented by an evaporative mini-channel cooling line [55], [90]. Additionally, thin-film coatings, or encapsulation, of diamonds or carbon nano-tubes, both highly thermally conductive materials, are potential candidates to further increase the heat transport of thermal straps [264], [266]–[268].

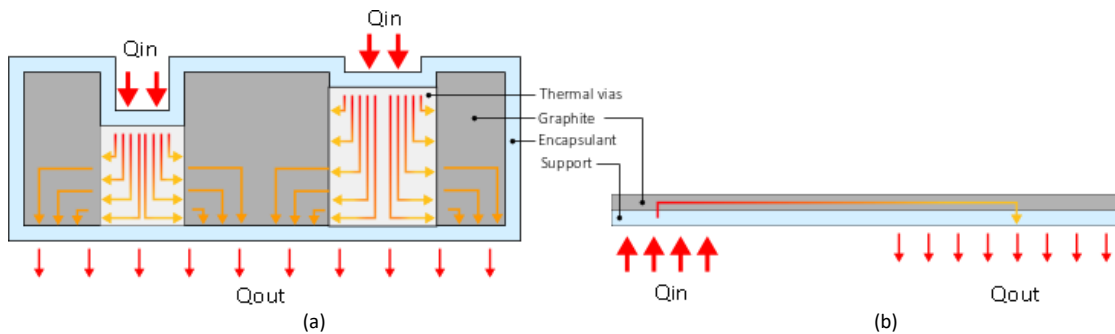


Figure 2.20. (a) Schematic of encapsulated graphite, which adapts several heat source with different heights and locations. (b) Schematic of supported graphite

Graphite appears as a high-end, low mass, low-stiffness and high performance material for flexible thermal straps. Graphite is a likely candidate due to its superior thermal conductivity compared to copper and aluminium. It found its use in several fields as cryocooling, telescopes, antennas and electronics. Moreover, the space sector used graphite thermal straps in some spacecraft as it was the case on-board JAXA's satellite ASTRO-H and its Soft X-Ray Spectrometer (SXS) [33], [269], [270]. The SXS relied on a graphite thermal strap to be the primary heat transfer part of the cryocooler, without compromising the vibration isolation system implemented. A model of the SXS and the thermal straps is shown in Figure 2.21. The satellite was unfortunately lost

briefly after launch, but other space missions, such as Orion and Spice, carried graphite thermal straps. As for graphite, highly thermally conductive carbon fibres can be used as flexible thermal straps [271]. The ExoMars rover relies on carbon fibre flexible thermal straps [272]. Each strap consists of several K1100 carbon fibre bundles, each wrapped in a thin polyester wire and each carbon fibre bundle is constituted of 20 000 individual fibres. Both graphite and carbon are subject to fracturing and fraying, generating in micro- and nano- foreign objects [273]. For this reason, both are usually encapsulated using a conformal layer or an aluminized Mylar sheeth to avoid the scattering of the particles generated.

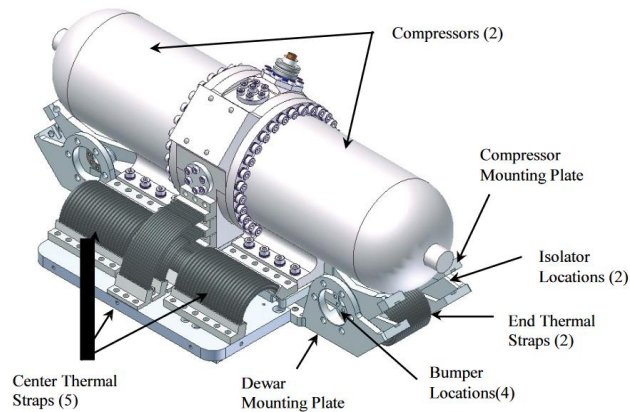


Figure 2.21. Model of the thermal straps used to control the temperature of the SXS on board JAXA's ASTRO-H [270].

Graphene is used similarly to graphite and carbon fibres for flexible thermal straps, with even higher thermal conductivity [274], [275]. Furthermore, layered and nanostructured cross-linked graphene is not subject to the splintering or fracture like graphite and carbon thermal straps. Thus, no encasing or encapsulation is required [276].

Chapter 3 A Two-circuit Cooling Approach Based on Micro Oscillating Heat Pipes

In the previous chapter, different technologies for the cooling of HEP experiment and space missions were reviewed, as well as the current state of studies on micro heat pipes. This chapter present a new approach based on micro oscillating heat pipes. The proposed cooling scheme relies on two fluidic loops; one consists of a pumped fluid loop and the second of a μ OHP. The design thereof of this second loop is shown.

3.1 Beyond the Used Single-loop Scheme

Thermal management at the system level is tackled by adequate conventional cooling schemes. However, cooling at chip level remains a major challenge to the performance and reliability of electronics and optoelectronics [277], [278]. Furthermore, the management of the generated heat in HEP experiments and space missions remains a challenge considering the constraints emanating from the harsh environmental conditions encountered and the very nature of both applications. Due to recent advances in micro-engineering, HEP experiments already benefit from miniaturized, efficient cooling devices based on single and two-phase flows. Similarly, the continuous effort to develop more performant solutions will likely lead to the first applications of micro-cooling systems in spacecraft.

Although silicon-based microchannels mechanically pumped fluid loops (MPFL) represent the state-of-the-art for chip-level cooling, they are based on a single loop scheme in which the pumped fluid directly circulates close to the heat source. Even though this represents an efficient solution, it has several drawbacks that hamper their applications, namely:

- i) The lack of appropriate interconnections between cooling plates or between cooling plates and the piping used in the rest of the MPFL. Despite the diversity of techniques to connect tubing to the microfabricated cold plate, obtaining a reliable connection remains challenging. The volume occupied by the connectors and their material can be problematic for integration, either being too bulky or being incompatible with the material budget for the applications. Occasionally, the connections turn out to be fragile, either due to weak adhesion to the substrate or the thermal stresses induced during their processing or in operation.

- ii) The brittle nature of single crystal silicon limits the pressure resistance of the silicon micro-channels. When part of the mechanically-pumped fluid loop, the micro-channels must withstand the internal pressure imposed by the requirements of the application and the working fluid. Increasing the pressure resistance of the cold plates can be achieved by increasing their thickness, with the consequent mass and material penalty. Furthermore, the brittle nature of silicon often leads to catastrophic failure of the system with crack growing on one or two sides of the cold plate. Careful consideration must be taken when optimising the mechanical design of the silicon cold plates.
- iii) Integration and packing difficulties for cooling large surfaces. The size of the cold plate is limited by the available raw material and processing capabilities. Whilst joining multiple cooling plates in series may help to overcome this limitation, it poses severe difficulties from the interconnection standpoint, as discussed in (i).

A cooling scheme relying on two independent fluidic loops would help to overcome the limitations of MPFL featuring cold plates with embedded microchannels. The two cooling loops, referred to as the primary cooling loop (PCL) and the secondary cooling loop (SCL) respectively, are connected through thermal and mechanical interfaces, but they do not share any fluidic interface. Both circuits work together to remove heat and control the temperature of the electronic components to be cooled. The SCL transfers the heat generated at the source to the PCL, which transports it further away and dissipates it to the environment, as depicted in Figure 3.1(a). As only thermo-mechanical interfaces are required between the two loops, several SCLs could be connected to the same PCL, allowing to cool large structures with multiple heat sources (e.g. HEP staves) without complex fluidic interconnections. As illustrated in Figure 3.1(b), the SCLs would be mounted in series to homogenously cool several sensors with a single PCL.

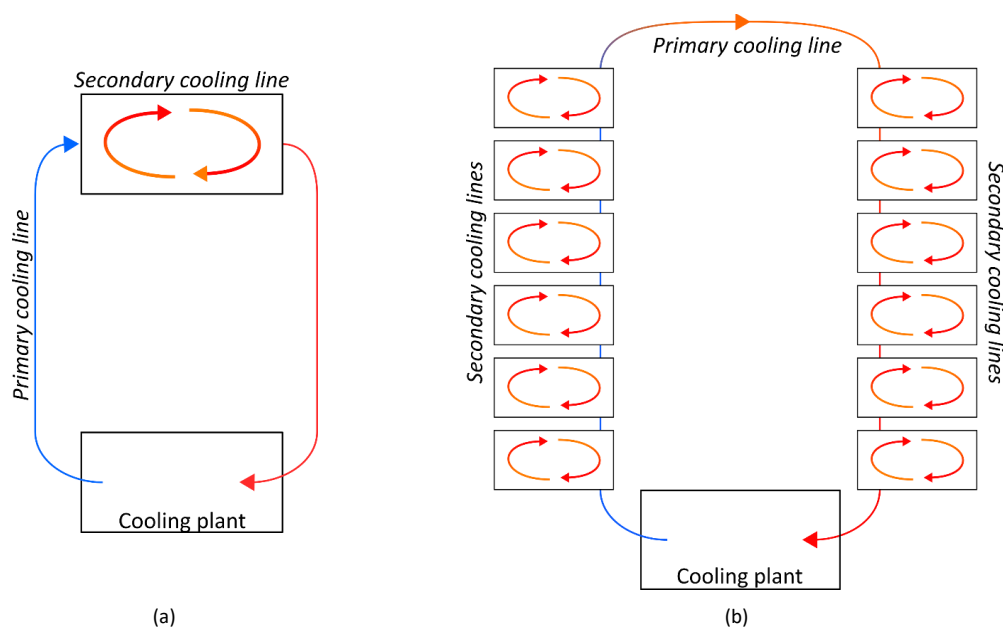


Figure 3.1. Cooling schemes for (a) a single heat source from which the SCL removes the heat and transfers it to the PCL. (b) Several heat sources connected to independent SCLs while the PCL remove the heat from the cold side of the SCLs.

The μ OHPs offer the best characteristics to be incorporated as SCL. They present several advantages over other types of heat pipes:

- High thermal performance
- Potential orientation-independent operation
- Integration on silicon possible (no CTE mismatch, high radiations hardness and low particle interaction)
- Low thickness
- Low mass
- Reliable
- Self-actuated
- Absence of wicking structures and ease of fabrication

The high thermal performance is achieved through the evaporation of the fluid in microchannels' hot section and condensation in the cold one. μ OHPs are capable of working with distributed heat load but also hot spots. Furthermore, among other types of devices reviewed, μ OHPs could operate along several orientations without wicking structures. The absence of wicking structures benefits the low thickness: wicking structures tend to limit the vapour space volume that restricts thermal performance. The integration of μ OHPs in silicon permits obtaining a device with a reduced mass and thickness that benefits the particle interaction, which makes them ideal for HEP experiments. They could even be integrated on the backside of the modules during their manufacturing process.

3.2 μ OHP Design for the SCL

This section describes the design of the μ OHP used in this work. It was designed not based on any specific experiment or space mission, but as proof of concepts to evaluate the impact of various parameters on its performance.

A silicon-based device is designed to comply with the following objectives: (i) high thermal performance for a heat load ranging from $0.25\text{W}/\text{cm}^2$ to $3\text{W}/\text{cm}^2$, (ii) orientation-independent thermal performance, (iii) low mass and (iv) material budget.

The μ OHPs used silicon as substrate, as it is the same material as the elements targeted for cooling, thus reducing the thermal stress resulting from a mismatch of CTE. Furthermore, it is suited for microchannels etching. Its high thermal conductivity makes it also appropriate to have increased fin-like efficiency for heat transfer between the fluids and the walls of the microchannels.

The evaporator's size of the μ OHPs was fixed to $20\times 20\text{mm}^2$, which is comparable to the dimensions of the front-end chips developed for the RD53 collaboration for ATLAS and CMS upgrades [279]–[282], but also to the size of several silicon sensors used in space applications. The targeted

power range is derived from the same applications. The size of the condensing area was fixed to $20 \times 20 \text{ mm}^2$ for symmetry.

The ability of the devices to operate independently of their orientation is of high importance. Thus, the design approach was to include dual-diameter pairs of microchannels. Alternating the hydraulic diameter between adjacent microchannels allows operations in most orientations without altering the thermal performance, since this arrangement creates an additional capillary pumping force.

An eleven-turn dual-diameter μ OHP with microchannel possessing a rectangular cross-section was designed in this scope. The overall dimensions were fixed to 60mm for the length and 20mm for the width (see Figure 3.3). Figure 3.2 illustrates the cross section of the microchannels, the dimensions of which are summarised in Table 3-1.

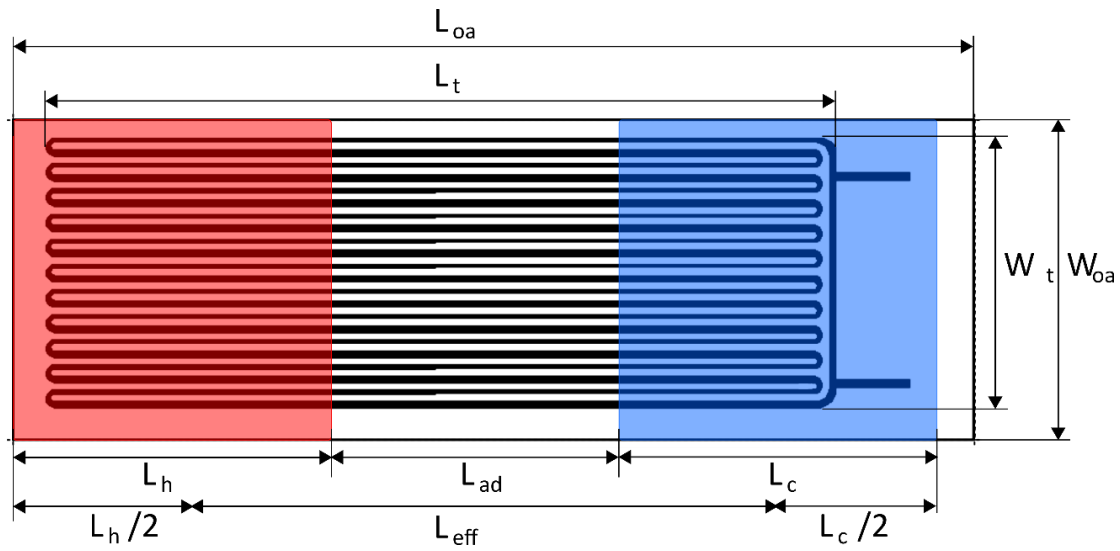


Figure 3.2. Schematic representation of a μ OHP with eleven turns, with the evaporative and condensing area represented in red and blue respectively. The values of the different parameters used in this thesis are summarised in Table 3-1.

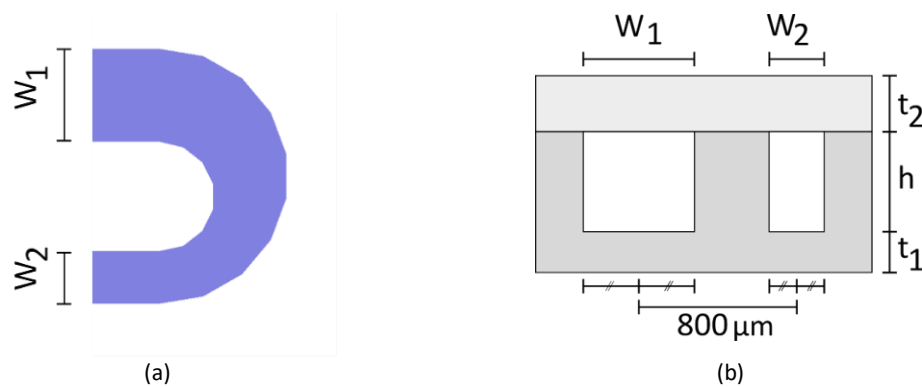


Figure 3.3. Schematic representation of (a) a U-turn with two different diameters with a faceted perimeter, (b) the cross-section for a dual-diameter pair of microchannels.

Table 3-1. Selected design parameters of the tested geometry.

Abbreviation	Descriptions	Value	Units
L_{oa}	Overall length	59.6	[mm]
L_h	Heater length	20	[mm]
L_c	Condenser length	20	[mm]
L_{ad}	Adiabatic length	16.6	[mm]
L_{eff}	Effective length	35	[mm]
W_{oa}	Overall width	19.6	[mm]
W_1	Width of large microchannel	400	[μm]
W_2	Width of small microchannel	225	[μm]
h	Microchannel height	400	[μm]
L_t	Length of microchannel area	49.4	[mm]
W_t	Width of microchannel area	16.85	[mm]
t_2	Cover wafer thickness	500	[μm]
t_1	Material thickness at the bottom of the channels	225	[μm]

The dimensions and cross-sectional shape of the microchannels are determining for the orientation-independent operation and the start-up and dry-out points of the μOHPs . The difference of width was estimated based on the Figure of Merit M_{php} proposed by Kwon and Kim [226], [283] :

$$M_{php} = \frac{N \rho_l \sigma \left(\frac{1}{w_2} - \frac{1}{w_1} \right)}{\mu_l C_f \left[N \left(\left(1 + \frac{h}{w_1} \right)^4 + \left(1 + \frac{h}{w_2} \right)^4 \right) + (N_t - N) \left(1 + \frac{h}{w} \right)^4 \right]} \quad (3.1)$$

Where N and N_t are the number of pairs of dual-diameter microchannels and the total number of microchannels respectively, and C_f is the coefficient of friction. The equation is detailed in Appendix F.

The choice of hydraulic diameters was also constrained by the limits imposed by the operation principle of the μOHPs . Table 3-2 summarizes the calculated limits for the hydraulic diameter according to the proposition from Zhang and Faghri¹ [215], Dobson and Harms² [216], and Harirchian and Garimella³ [284]. The selected values for the depth and widths of μOHP were set below the static limit. Nevertheless, Qu et al. [217] proposed a newer definition for the lower limit, described in appendix F, which encompasses the hydraulic diameters used for the μOHP .

¹ $D_{max}^{Bo} = 2 \sqrt{\frac{\sigma}{g(\rho_l - \rho_v)}}$, defined as the upper static limit as no dynamic effect is considered.

² $D_{min}^{Bo} = 0.7 \sqrt{\frac{\sigma}{g(\rho_l - \rho_v)}}$, defined as the lower static limit as no dynamic effect is considered.

³ $D_{max}^{Ga} \leq \sqrt{\frac{160 \mu_l}{\rho_l U_l} \sqrt{\frac{\sigma}{g(\rho_l - \rho_v)}}}$, definier as upper dynamic limit as dynamic effects are considered.

Table 3-2. Critical diameters, static and dynamic, for different fluids on ground and in microgravity conditions. The critical bond number in microgravity is not included as the values are unrealistic.

Liquid	$D_{max}^{Ga} [\mu m]$	$D_{max}^{Ga} [\mu m]$	$D_{min}^{Bo} [\mu m]$	$D_{max}^{Bo} [\mu m]$
	$g = 9.81 \text{ m/s}^2$ $U_l = 0.5 \text{ m/s}$	$g = 0.01 \text{ m/s}^2$ $U_l = 0.5 \text{ m/s}$	$g = 9.81 \text{ m/s}^2$ (static)	$g = 9.81 \text{ m/s}^2$ (static)
C ₄ F ₁₀	642.6	3596.2	6.1	17.4
C ₆ F ₁₄	323.4	1809.9	600.5	1715.8
Novec 649	326.3	1826.0	582.8	1665.2
Isopropyl alcohol	1186.3	6639.0	1187.2	3392.1
Acetone	457.4	2560.1	1225.8	3502.4
CO ₂	1290.5	7222.5	674.2	1926.2
Ammonia	466.0	2608.1	1296.7	3704.8
R236fa	266.0	1488.9	684.1	1954.5
R245fa	328.1	1836.2	736.4	2104.0
Water	846.2	4736.0	1843.0	5265.6
Ethanol	905.3	5066.4	1179.2	3369.1

3.3 Test Device Overview

3.3.1 Device Microfabrication

Two sets of devices were fabricated using MEMS techniques. The first set was composed of microchannels etched in silicon wafers with glass wafers capping the channels. It was used to test the thermal performance. Glass allowed to observe the flow patterns, which could be linked to the thermal performance. The second set was constituted only of silicon. The microfabrication steps for both sets are addressed in the fifth chapter. In this chapter, the resistance of the cavities of both sets was also reported. Tests used a standardized test specimen from CERN.

3.3.2 Device Sealing

The test version of the device, in silicon and glass, relied on an Invar connector, as shown in Figure 3.4. It provided the device with an easy charging and purging solutions to change fluids. Capillary tubing and valves completed the connectors in this goal. The set in silicon was designed with a permanent sealing solution in mind, which is described in Chapter 7.

3.3.3 Tested Parameters

The test device was used for testing thermal performance for different fluids, orientations, charging ratios and power inputs. The resulting thermal performance and observed flow patterns are presented in Chapter 6.

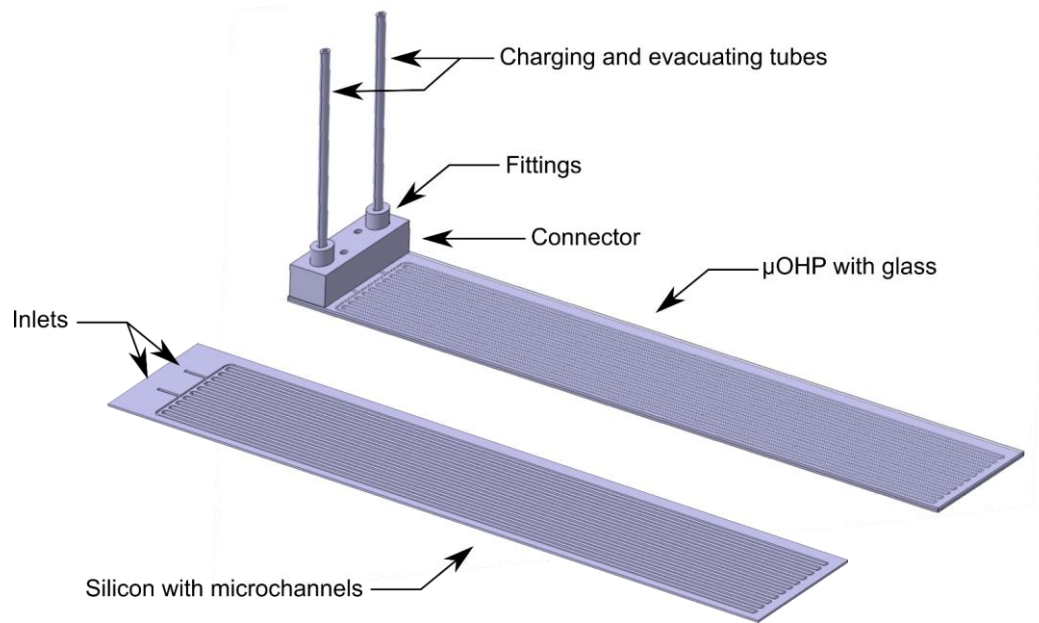


Figure 3.4. 3D Representation of the μ OHP with the connector.

3.4 Summary

This chapter describes a two-fluidic circuit concept to meet the thermal management needs for future HEP experiments and space missions. This approach combines a primary, mechanically pumped fluidic circuit with a series of secondary circuits. Micro-oscillating heat pipes made in silicon have been identified as the best solution for the secondary circuit. The design of such a device is described in more detail. Merging a downsized version of a well-established type of heat transfer devices and a new cooling approach for HEP experiments opens new possibilities for thermal management of fragile and critical silicon sensors in harsh environments. The designed μ OHP satisfies the theoretical limits to operate at all orientations with an evaporator and condenser, both measuring $20 \times 20 \text{ mm}^2$.

The next chapter describes the testing methods used to characterise the mechanical and thermal performance of such device.

Chapter 4 Methods & Experimental Apparatus

This chapter describes the methods and tools used for the assessment of the thermal performances of micro oscillating heat pipes described in Chapter 3. The methods used to characterise the mechanical resistance of wafer bond of the devices is also covered.

4.1 Thermal Performance Test Setup

A test setup was designed and assembled to assess the thermal performance of the μ OHPs.

The test setup consisted of a hermetically sealed micro heat pipe, a fan with a radiator connected to a thermoelectric module acted as the cold source, and a polyamide thin-film heater. Temperature sensors linked to a data acquisition system (DAQ) and power supplies complete the test setup.

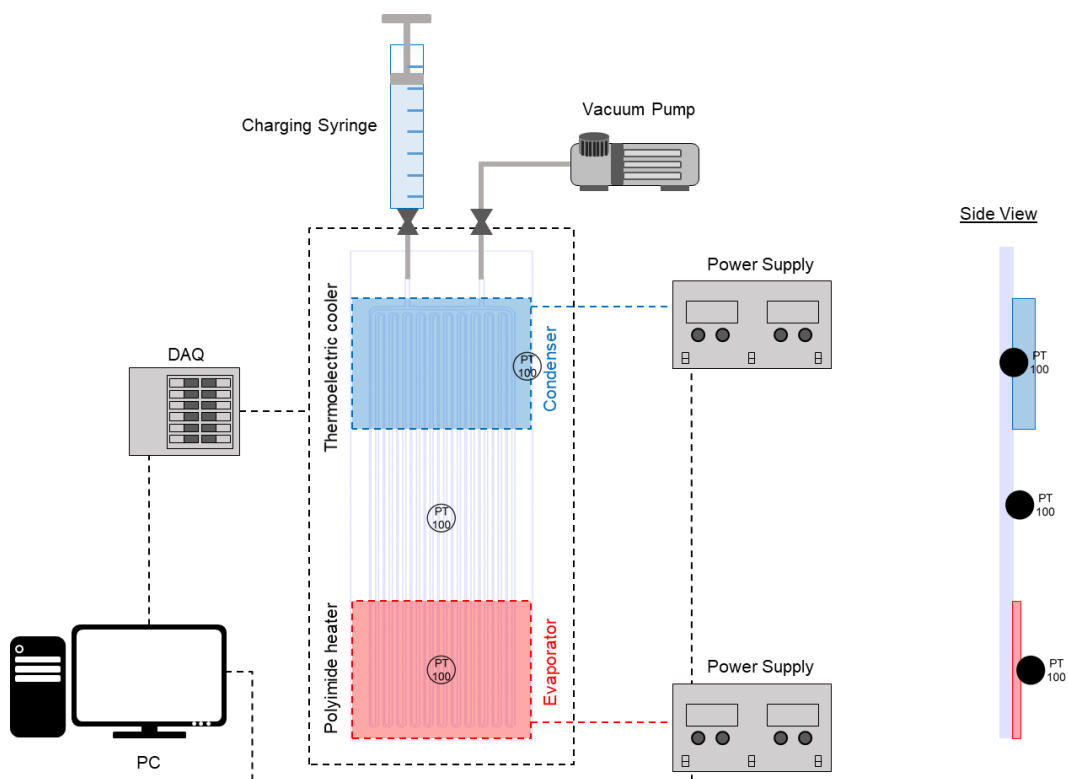


Figure 4.1. Schematic representation of the experimental setup with the connected instruments.

4.1.1 μ OHP Test-Section

A test setup was built to evaluate the thermal performance of the μ OHP described in Chapter 3. The device under test was mounted on a platform to evacuate the heat using a TEC module and a fan. The platform itself is contained in a box with dedicated opening for air intake and exhaust to avoid forced convection, as illustrated in Figure 4.2. The box's orientation was changed using blocks, or by laying the box on its flat faces. The inclination angles α , accordingly to the Figure 4.3, were referred to as:

- Top heating mode: $\alpha = -90^\circ$
- Bottom heating mode: $\alpha = 90^\circ$
- Horizontal mode: $\alpha = 0^\circ$

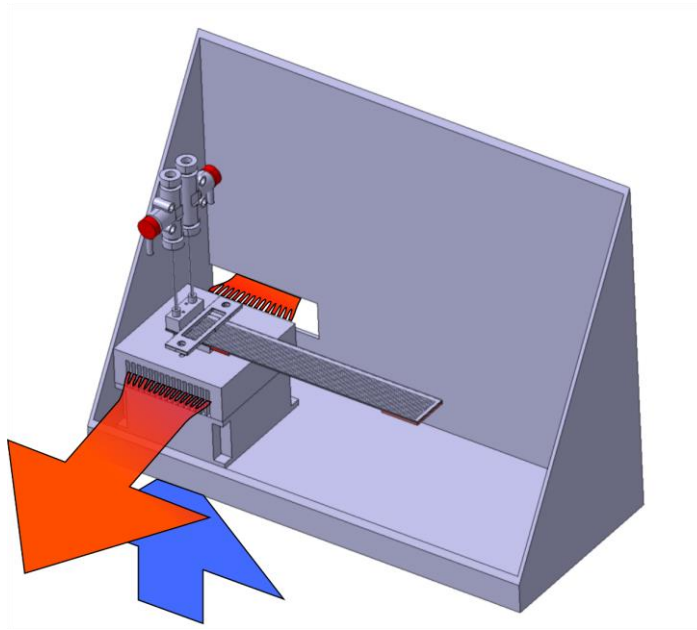
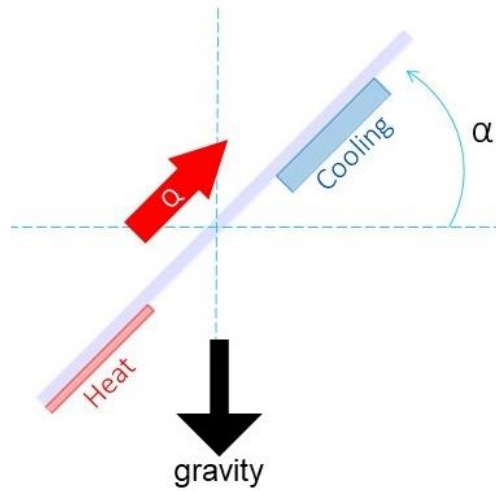
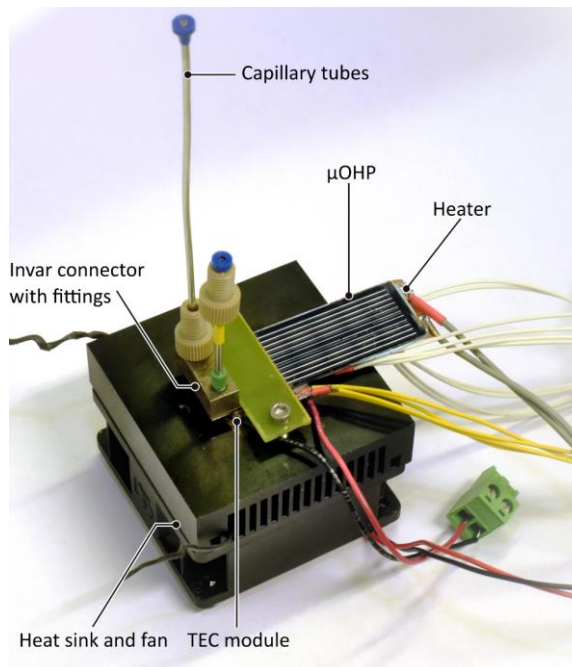


Figure 4.2. CAD view of the μ OHP test section with cold air intake and hot air exhaust.

For those devices where the silicon channels were closed using a glass wafer, the flow was visualised using a high speed camera.

The internal volume of the μ OHPs was 178mm^3 , including the inlet microchannels, with 31mm^3 additional dead volumes for the tubing and valves. Due to the small volume of fluid required, care was taken to remove non-condensable gases and avoid leaks. Leak-testing of the setup was done by simultaneously spraying the surfaces with Helium (He) and pumping vacuum. The He intake rate was monitored. The assembly and connections were considered operational if the helium leak rate did not exceed $10^{-7}\text{mbar}\cdot\text{l/s}$. The evaluation of the devices' thermal performance was conducted directly after the charging and not more than twenty hours later. It was done to ensure that non-condensable gases (NCG) in the fluid are low. After this time, the fittings' permeability may allow enough NCG to enter the microchannels, disrupting the operations of the μ OHP.

Figure 4.3. Illustration of the orientation angle α .Figure 4.4. μ OHP mounted on the heat sink and TEC module.

4.1.2 Working Fluid

The thermal characterisation of the device was conducted with three fluids:

- C_6F_{14} , also known as 3M™ Fluoinert™ Electronic Liquid FC-72, is a common low temperature refrigerant. Already used in some HEP experiments, C_6F_{14} is widely used as a working fluid for OHP and μ OHP as evidenced by the literature review.
- Isopropyl alcohol (IPA), while not being a common refrigerant, was selected for its low value of M_{php} and could be used to validate the threshold for the figure of merit.
- Acetone is a known working fluid for heat pipes. While studies on μ OHP rarely use it, acetone has a good potential as working fluid for μ OHP

Their relevant physical properties are summarised in Table 4-1.

Table 4-1. Main properties of working fluids.

Property	Units	C ₆ F ₁₄	IPA	Acetone
μ_l	[Pa · s]	$6.40 \cdot 10^{-4}$	$2.04 \cdot 10^{-3}$	$2.95 \cdot 10^{-4}$
σ	[N/m]	0.0120	0.0221	0.0237
ρ_l	[kg/m ³]	1680	786	790
ρ_v	[kg/m ³]	18.0	2.49	2.20
c_p	[J/(kg · K)]	1050.0	2680.00	2160.00
h_{fg}	[J/kg]	$8.80 \cdot 10^4$	$7.45 \cdot 10^5$	$5.52 \cdot 10^5$
K_l	[W/(m · K)]	0.0570	0.137	0.181
$\left(\frac{dP}{dT}\right)_{sat}$	[Pa/K]	0.046	-	0.0627

Before the test, the amount of fluid for each test condition was calculated based on Antoine's equations [285] to reach the working fluid's targeted amount. Once the leak tightness of the device was confirmed, the fluids were charged.

The fluids were degassed before every charging. A gas chromatography syringe was charged with the required amount of fluid, and sealed with a microfluidic PEEK valve. This valve was then connected to the charging line tube on the μ OHP. A second PEEK valve was used on the vacuum line of the μ OHP. The vacuum pump was then connected to a microfluidic circuit and trapped air was evacuated for two hours. The valve connected to the evacuation line was closed and the fluid injected into the microchannels. Once the fluid flashed inside the channels, the remaining quantity of working fluid was injected. Pictures of the liquid inside the microchannels served to verify the amount of liquid present, as exemplified by Figure 4.5.



Figure 4.5. Picture a μ OHP charged with acetone ($\varphi = 50\%$). Acetone is distinguishable inside the microchannels.

4.1.3 TEC Module

A thermoelectric cooling (TEC) module (Adaptive™ ET-071-10-13) absorbed the heat in the condensing section of the μ OHP. The module uses electricity to transfer heat. This is possible due to

the contribution of three thermoelectric effects, namely the Seebeck, the Peltier and the Thomson effects, which describe the thermodynamically reversible interactions linking the heat and charge carriers. The TEC module measured $20 \times 20 \text{ mm}^2$ for a thickness of 3.6 mm.

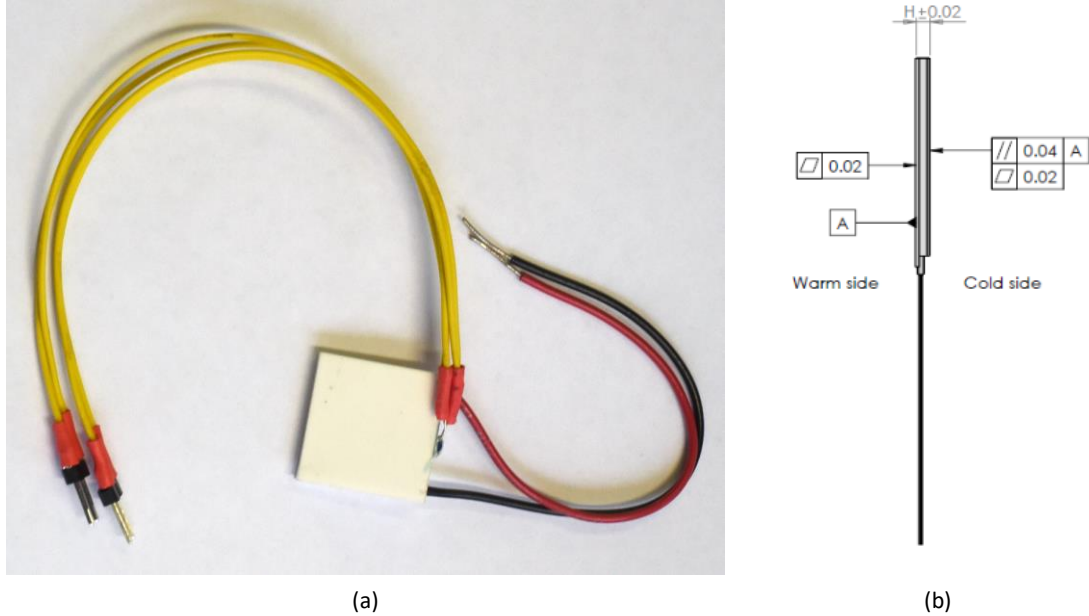


Figure 4.6. TEC module. (a) Picture of the Adaptive™ ET-071-10-13, here with a PT100 temperature sensor mounted on the cold side. (b) Geometrical tolerances of the TEC module from the datasheet of the manufacturer.

Table 4-2. Properties of the TEC module

I_{\max}	3.9 [A]	ΔT_{\max}	74 [°C]
V_{\max} (DC)	8.8 [V]	P_{\max}	18.7 [W]

The cold side of the TEC module was linked to a $60 \times 60 \times 30 \text{ mm}^3$ heat sink equipped with a fan to evacuate the heat. High-density polysynthetic silver thermal compound (Arctic Silver® 5) bridged the gap between (i) the TEC module and the heat sink and (ii) the TEC module and the condensing area of the μOHP .

4.1.4 Heating

A polyimide thin-film heater was used to replica the heat source. CERN EP-DT-DD Micro-Pattern Technologies group produced the custom-made thin-film heaters depicted in Figure 4.7.

The power was computed from the voltage and current supplied. A thermally conductive two-part epoxy (Electrolube® TBS20S) was used to join the thin-film heater to the μOHP . The glue layer included $300 \mu\text{m}$ thick glass beads to obtain a uniform and controlled thickness.

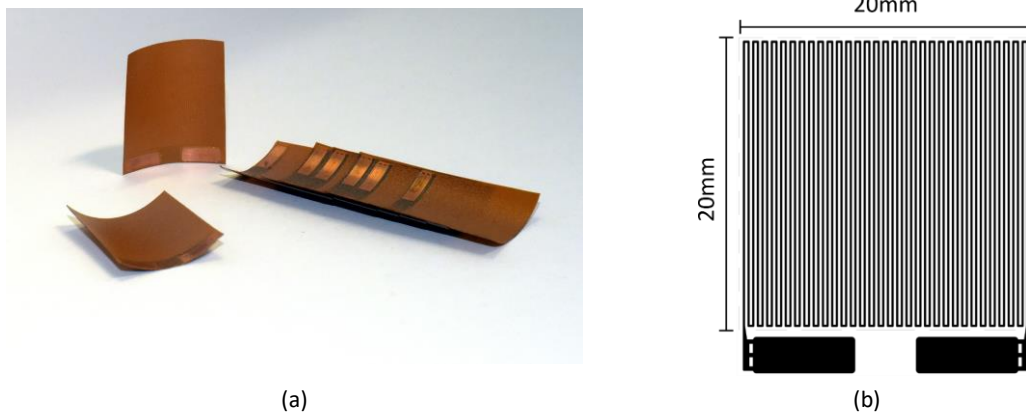


Figure 4.7. (a) Picture of the polyimide thin-film heaters produced at CERN. (b) Scheme with dimensions of the heaters.

4.1.5 Instruments & Data Acquisition

4.1.5.1 Instruments

The temperature data was acquired by the mean of PT100 resistance temperature detector (TE-Connectivity PTFCO-160 platinum thin-film, type 3851, silver wires) in 4-wire configuration. The footprint of the element was 2mm by 2.3mm. The lengths of the cables connecting the PT100 to the National Instrument (NI) 9216 card were identical for all RTDs. Off-the-shelves calibration results in a precision of $\pm 0.3^\circ\text{C}$ from -50°C to 600°C .

As illustrated in Figure 4.8, the temperature at the evaporator was acquired by one sensor located at the centre of the area. The temperature sensor located in the adiabatic section is centred accordingly to the overall dimensions of the device and the condenser's temperature sensor is centred over the length of the condenser, but positioned on the side due to the presence of the TEC module.

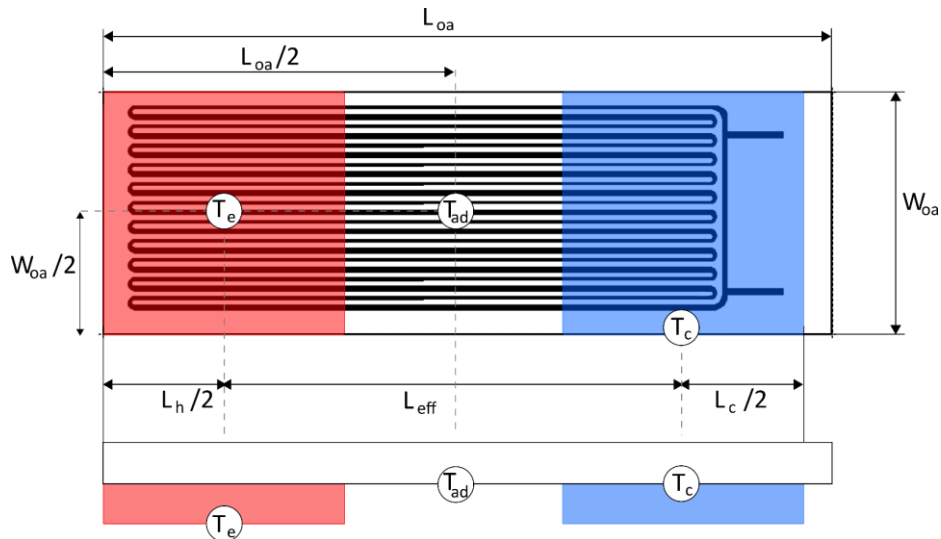


Figure 4.8. Schematic of the position of the temperature sensors used.

4.1.5.2 Data Acquisition

The data from three sources were acquired and processed through a connected computer. The power supplies were connected using a GPIB cable and the data is fed to the computer using a

National Instrument GPIB-to-USB controlling card (GPIB-USB-HS). The thermal measurements relied on a National Instrument CompactDAQ, a 9216 temperature input module from the same company and PT100 temperature sensors. The NI-9216 module provides eight analogue input channels with a sampling rate up to 400Hz per channel. Each four-wire channel was filtered and then sampled by a 24-bit delta-sigma ADC. The module's internal excitation current was set a 1mA per channel and the module set in the high-resolution mode. The data generated by the power supplies were stored at 1Hz using the internal measurement system featuring a 12-bit ADC. PSUs' current and voltage values were monitored at 4Hz to control the different subsystems.

4.1.5.3 *Control of the Setup*

The fan, the thin film heater and the TEC module were controlled by a 4Hz-loop using NI LabVIEW software package, while the temperature was read at 20Hz for specific purpose.

Details on the software are given in Appendix C.

4.1.6 Experiment Validation and Protocol

The preparatory work included estimating the energy balance and computation of the samples' frequency measurements.

4.1.6.1 *Energy Balance and Losses*

The energy balance between the heat removed by the TEC module and the heat supplied by the heater was monitored at 10W during the test. Based on the current and voltage measurements and the temperature at the hot and cold sides of the TEC module and its intrinsic characteristics.

The experiment experienced environmental losses during the test from natural convection and radiation. The loss through natural convection was calculated for a flat plate locally heated from the bottom in an enclosure, resulting in approximatively 6% of losses. It was calculated based on the experimental results of the empty devices ($\varphi = 0\%$), which ranged from 0W to 10W. The estimated losses and the energy balance matched. But the losses were not used to correct the measurement discussed in the next chapters. A passively thermally corrected vacuum chamber could be implemented to minimise these losses.

4.1.6.2 *Protocol*

The main objective was to characterise the thermal performance of the μ OHP for under different operating conditions for different working fluids. The relation between the flow patterns and thermal behaviour was also of interest. Therefore, visual and thermal data were extracted from experiments. Flow visualisations were conducted to observe the two-phase flow patterns, while the thermal data extracted served to determine the apparent thermal conductivity.

A protocol to prepare the device before the experiment was established to reduce the uncertainties induced by the preparation:

1. The system was cleaned using IPA before any test to remove unwanted fluid residues or dust.
2. The system, the tested device and lines were evacuated for two hours.

3. The μ OHP was charged at the predetermined charging ratio and sealed. The level of charged fluid was then verified optically.
4. The device was operated by setting the temperature of the condenser T_c to 20°C, unless specified otherwise. The heat load at the evaporator was gradually increased. For each power level, a steady state was maintained for six minutes.

At the end of each test run, the quantity of fluid was again optically controlled to check for potential leaks.

Each data point corresponds to a particular set of power input, orientation, temperature measurements and flow pattern. High-speed videos were acquired during specific sets of conditions.

4.1.7 Data Reduction

4.1.7.1 Thermal Data

The apparent thermal conductivity k_{app} of the μ OHP was computed based on device's external geometry, the power input and the temperature difference between the evaporator and condenser ΔT .

$$k_{app} = \frac{Q_{in} L_{eff}}{A_{cs} \Delta T} \left[\frac{W}{m \cdot K} \right] \quad (4.1)$$

Where Q_{in} is the uncorrected input power, L_{eff} is the distance between the centres of the evaporator and the condenser of the μ OHP ($L_{eff} = L_{adb} + (L_e + L_c)/2$), as illustrated in Figure 3.2, and is A_{cs} the cross section of the device including the silicon or glass cover.

4.1.7.2 Time-strip from Video Sequence

Time-strip technique was employed with the video captured. It resulted in a spatiotemporal representation of the evolution of the flow regimes [286], [287]. The high-speed sequences were utilised to obtain a 2D space-time representation, known as time-strip, of the flow of each pair of asymmetric channels, as illustrate by Figure 4.9. The frame space-time dimension was first reduced by straightening the U-turn's centreline to create 1D stripes. Each pair of channels is represented by one straight line of pixels with the middle of the U-turn on the evaporator side located at the centre of the resulting image. The two-phase flow distribution along the centre line is extracted for each frame along the channel centre line to build the time-strip. The extracted greyscale lines of pixels are plotted versus time.

The intensity of a pixel results from the light attenuation caused by the different fluid phases combined with the reflection and refraction at the liquid-vapour interfaces. The time-strip allowed extracting quantitative information from the flow, as the interface trajectories and velocities.

The pixel intensity identifies the phases and interfaces. Due the incoming illumination from the dedicated light sources and the ones from the experiment's surroundings, the subsequent reflections generate artefacts in the time-strip. A post-processing step can be applied to address this matter: an initial low pass-filter was applied, followed by a threshold step. A Laplace edge detection algorithm was applied to determine the interface profiles. The interfaces were tracked in order to characterize the displacement of the liquid slugs and vapour plugs. The centre of mass

of the liquid, defined as the middle point between two liquid-gas interfaces, was used to compute the velocity and the displacement of the corresponding liquid slug.

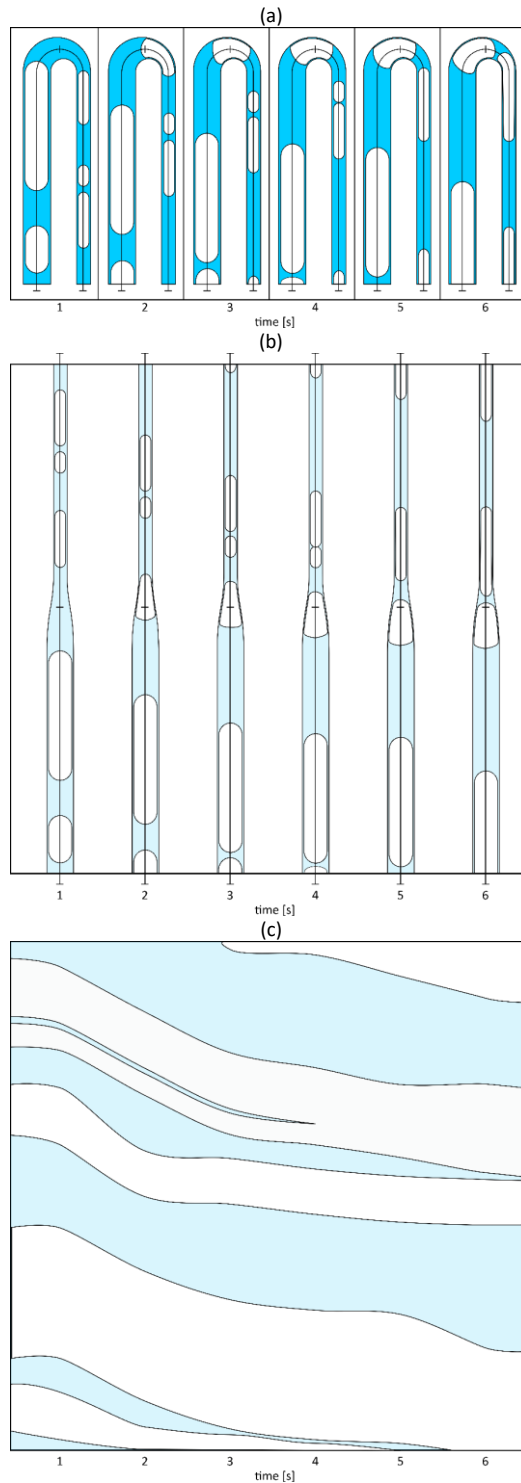


Figure 4.9. Schematics of a frame sequence capture and transformed in a time strip. (a) Slug-plug flow in the evaporator, (b) straightened microchannel on the central axis and (c) corresponding time strip.

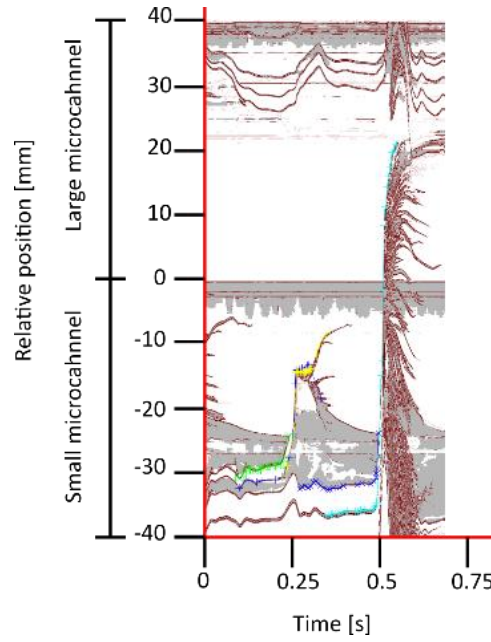


Figure 4.10. Illustration of the extraction of the position of the liquid-gas interfaces.

The liquid-vapour interface moving quasi unidirectionally was manually tracked using the open-source software Engauge. The velocities were then computed as the time derivatives from the displacement profiles.

4.2 Evaluation of the Wafer Bond Quality

This section describes the method used to assess the quality and pressure resistance of the bonded interfaces of the wafers.

Wafer bonding techniques are widely used in the MEMS industry and the bond's strength is one of the most important characteristics. For devices having cavities, the pressure test method, also known as blister test method, is sometimes used. It consists of pressurizing an internally sealed volume. The pressure initiating the fracture at the bond is used as an estimate of the bond's strength. The fracture energy can be expressed in case of pure mode I fracture, based on the geometrical properties of the microchannels and by considering the structure as bulging plates [288], [289], as:

$$G_{IC} = \frac{3p^2 r^4 (1 - \nu^2)}{32Et^3} \left(1 + \frac{8\alpha_s t^2}{3r^2 (1 - \nu^2)} \right) \quad (\text{circular membrane}) \quad (4.2)$$

$$G_{IC} = \frac{p^2 a^4 (1 - \nu^2)}{24Et^3} \left(1 + \frac{6\alpha_s t^2}{a^2 (1 - \nu^2)} \right) \quad (\text{rectangular membrane}) \quad (4.3)$$

Where p is the applied pressure, ν the Poisson's ratio, t the thickness of the bulging membrane, E the Young's modulus and α_s the shear coefficient; r and a are respectively the radius and the width of the structures. Blom et al. [288] observed two failures modes in the case of brittle materials. The first mode corresponded to the appearance and propagation of cracks in the cover wafer (t_2 in Figure 4.12), at the etched channels' edge. The second mode is related to the delamination starting at the junction of the two wafers and deviating in the bulk of the material. The

high pressure separated the wafers until one of the two failed, completely removing the membrane due to its brittleness.

Vallin et al. [290] reviewed the most used bond adhesion test methods. Among them, the pressure test method offered the advantages of low data scattering due to the homogenous load, with repeatability and reproducibility superior to other methods originating from the use of off-the-shelves parts with no influence from the operator. The pressure test method adopted in this work is based on destructive tests and dedicated test structures were included in the layout used for the production of the μ OHP to control the bond.

The CERN EP-DT standard pressure test setup for silicon devices with microchannels [291] used for the pressure resistance measurements is visible in Figure 4.11. It consisted of a manual pump developing up to 700bars connected to a pressure sensor, continuously monitored. The pressure signal was recorded and stored while the pressure progressively increases, up to sample's membrane's failure.

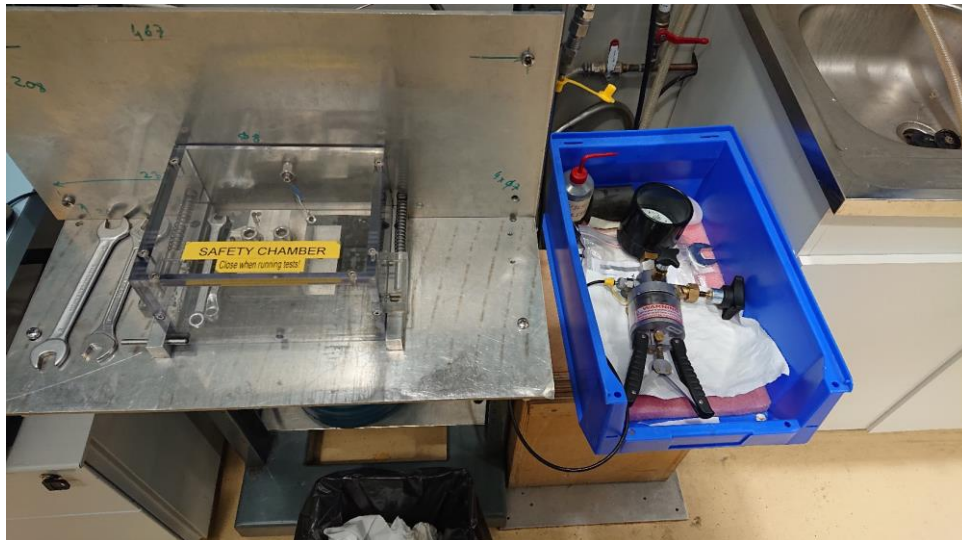


Figure 4.11. CERN EP-DT standard pressure test setup for silicon device Manual pressure pump (right) and safety chamber (left) with the dedicated clamping inside.

4.2.1 Standardized Test Structures

The test structures, illustrated in Figure 4.12, were based on the same design with variations of the dimensions of the microchannels (i.e. the width and the thickness of the bottom and the top covers, identified as W , t_1 and t_2). Varying these parameters allowed studying the bond strength under different configurations.

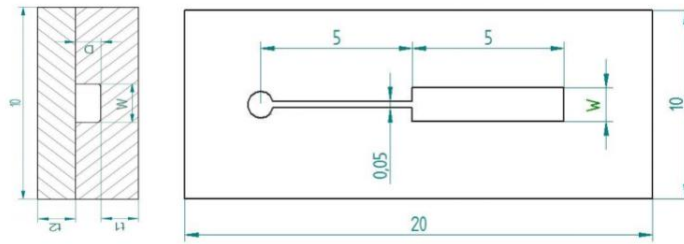


Figure 4.12. Drawing of the standardized design for pressure tests of microchannels (Design by CERN)

Additional circular test structures were included in the layout of the wafers. These test structures reuse the same inlet and entering restriction as the sample illustrated in Figure 4.12. They present a circular end-cavity instead of a rectangular one, as illustrate in Figure 4.13.

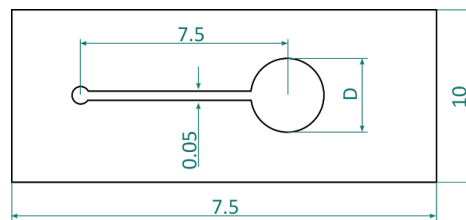


Figure 4.13. Drawing of a pressure test sample with circular cavity.

4.3 Summary

This chapter describes the methods used to characterise the thermal performance of the designed devices, as well as the method to establish the pressure resistance of the interfaces created during wafer bonding. The thermal characterisation relies on temperature measurements at various conditions. Pressurized water using a CERN setup allows to measure the pressure resistance of the test structures. A time-strip technique to process the images acquired during the test was also presented.

Chapter 5 μ OHPs Microfabrication

This chapter presents the process flows used to produce the two sets of μ OHPs, the obtained devices and the bond methods' pressure resistance. A brief review of CMOS-compatible wafer bonding techniques introduces the two bonding techniques used. After reviewing the two processes followed to obtain the proof-of-concept devices and prototypes, the pressure resistance of the thermocompressed interface is analysed.

5.1 Wafer Bonding Techniques Review

Silicon as a substrate for μ OHPs offers the advantage of a good thermal conductivity combined with a coefficient of thermal expansion matching the sensor modules' one, reducing the thermally induced mechanical stress. Fabrication techniques for MEMS are well established.

While microchannels etching using deep reactive ion etching (DRIE) process is considered as established, the wafer bonding step must be overviewed for each use case. The fabrication of silicon-based micro heat pipes includes a bonding step, either with a wafer with CMOS electronics in the case of direct integration or with a blank wafer for embedded or stand-alone μ OHP. Therefore, considering the limiting case, a CMOS-compatible and hermetic bonding process is required. The complete CMOS or CMOS-like structures must keep the characteristics during the bonding and pre-treatment steps and the possible post-bonding treatments. Thus, the elaboration of the bonding process has to consider the following points:

- The bonding temperature should not exceed 450°C to prevent changes in aluminium metallization, as this metal is one of the most commonly used in CMOS technology.
- Thermal budget in the 200-400°C range to minimize the degradation of the doping profiles or metals (diffusion-based changes).
- Limit the use of treatments based on strong acids for surface activation before the bonding step, as the wet chemical treatment would attack open metal areas.
- Avoid electrical discharges during the bonding or the plasma treatment for surface activation.
- Prevent trapping of charges in the bonding interface's neighbourhood, which would alter the charge characteristics of the CMOS detector.
- Introduction of mobile ions, such as sodium, potassium or gold, must be minimized in the CMOS device's structures.
- The residual mechanical stress characteristic of the active layers emerging from the bonding process must not change, particularly when considering symmetric circuitries.
- Avoid the introduction of parasitic effects (parasitic capacitance, ohmic current leakage, short circuits)

High-temperature bonding processes, such as direct or fusion bonding, cannot be used. Table 5-1 compares different bonding techniques. The selection of the process for the bonding step is application-dependent. Thus, it has to be reconsidered each time.

Table 5-1. Summary table of wafer bonding techniques

Bonding methods	Advantages	Drawbacks
Direct	<ul style="list-style-type: none"> • Strong bonds • Hermetic • CMOS-compatible (low temperature) 	<ul style="list-style-type: none"> • High demands in roughness and surface geometry • Not topography tolerant • Not CMOS-compatible (high temperature)
Anodic	<ul style="list-style-type: none"> • Strong bonds • Narrow bond lines • Hermetic • $T < 450\text{ }^{\circ}\text{C}$ • CMOS-compatible 	<ul style="list-style-type: none"> • Low Δ CTE in bonded materials • Requires planarity • Requires voltage and current • Possible ion contamination
Activated insulating intermedia layer	<ul style="list-style-type: none"> • Low process temperature: RT–$300\text{ }^{\circ}\text{C}$ • Low induced stress • Strong bonds • Hermetic • Insulating bonding interfaces w/o oxides • CMOS-compatible 	<ul style="list-style-type: none"> • High vacuum level (10^{-4}–10^{-7} Pa) • Not topography tolerant
Glass frit	<ul style="list-style-type: none"> • Hermetic • Strong bond • Topography tolerant • CMOS-compatible 	<ul style="list-style-type: none"> • Large bond lines • $T \sim 440^{\circ}\text{C}$
Adhesive	<ul style="list-style-type: none"> • Simple and low cost process • $T \leq 200\text{ }^{\circ}\text{C}$ • No electric voltage and current • Topology tolerant • CMOS-compatible 	<ul style="list-style-type: none"> • Moisture penetration • No long-term stability • Limited operating temperature • Bond thickness variance • Low bond strengths
Eutectic	<ul style="list-style-type: none"> • Low induced stress • Hermetic • Low demands on surface topography and roughness • Strong bonds • Narrow bond lines 	<ul style="list-style-type: none"> • CTE mismatch of wafer and alloy • Technological procedures to prevent oxidation of silicon surface • Possible contamination of CMOS structures
Thermocompression	<ul style="list-style-type: none"> • Localized heating • Rapid cooling • Strong bond • Bonding interface without oxide • Hermetic • $T < 400^{\circ}\text{C}$ • CMOS-compatible 	<ul style="list-style-type: none"> • Extensive preparation (Al, Cu) • Not topography tolerant

Anodic bonding is a logical choice for the set of μ OHPs involving silicon and glass, as it provides a strong hermetic bond between glass and silicon without requiring an additional intermediate layer. The set based on silicon for the microchannels and the capping wafer used thermocompression of gold thin-films as the bonding method.

5.2 Microfabrication of the Prototypes

The prototypes aimed to provide an insight into encountered flow patterns, as well as thermal performance. Therefore, visual access was required, in addition to the possibility to easily charge and discharge the fluids in the tested microfabricated device. A glass capping wafer provides the visual access required, and anodic bonding between the glass and the silicon wafers is a standard process. Thermocompression of a connector fill the need for an easy and reliable connection from the silicon-glass chip to the two microfluidic lines for the charging and evacuating tubing. However, it requires holes in the glass wafers for evacuating and charging the μ OHP.

5.2.1 Layout

The layout presented in Figure 5.1 represents a 6in (150mm) wafer containing twenty pressure test samples and five μ OHPs of different overall lengths of 60mm, 100mm and 140mm.

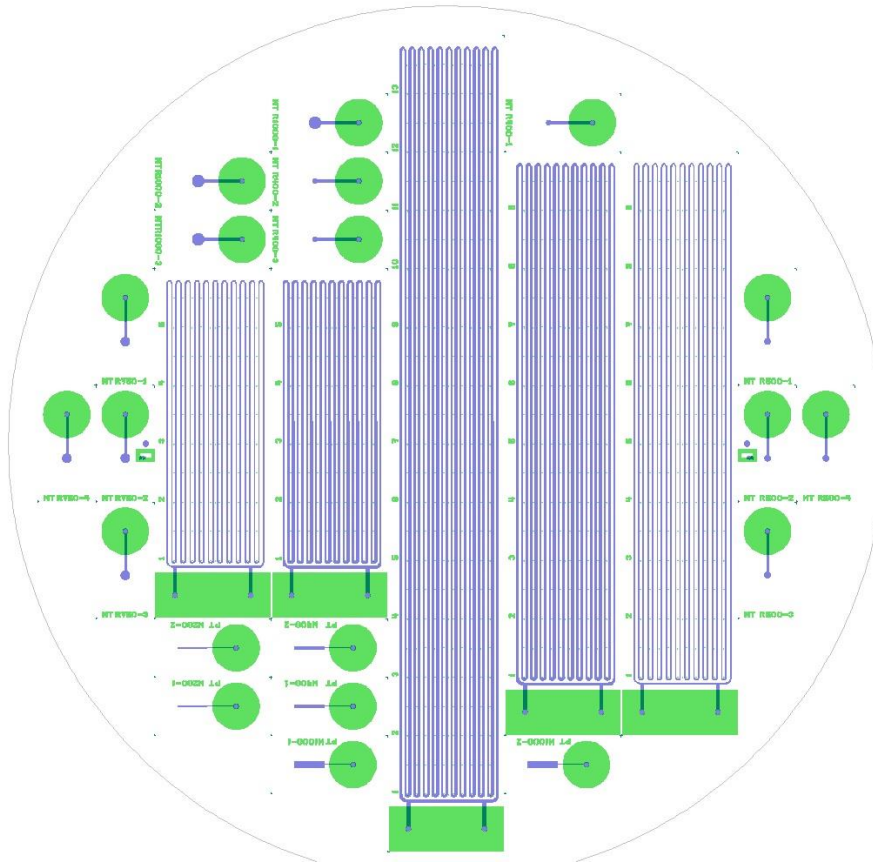


Figure 5.1. Layout for 6in wafers for the test vehicles. The etched microchannels are in blue. The green areas are covered by titanium and gold.

5.2.2 Fabrication Process Flow

The layout was transferred on 7in quartz masks using the *Heidelberg* VPG200. These masks then served to pattern the photoresist on the silicon wafers before etching the microchannels, while the holes in the glass wafers were machined with diamond drill bits.

Appendix D.1 details the process flow for the silicon and glass devices.

5.2.2.1 Silicon Microchannels

Silicon microchannels were processed on 6in wafers using photoresist and silicon oxide masks with DRIE process. Double-side polished 625 μ m-thick silicon wafers were initially cleaned before going through wet oxidation of their surfaces. The photoresist was deposited on one face and patterned. The oxide was used as a mask after being patterned through the deposited photoresist mask. Both the photoresist and the silicon oxide partially masked the silicon's surface that would constitute the walls of the microchannels. The DRIE process etched the silicon vertically. The alternatively pulsed gases used in the aforementioned process left a wavy profile on the walls, called scalloping. Thus, after removing the remaining photoresist and oxide, a new layer of oxide was formed and removed to reduce any scalloping present.

5.2.2.2 Glass Wafer Micro-machining

The inlets and outlets required by the μ OHPs were prepared before in the 500 μ m-thick borosilicate glass wafers. Each μ OHP required two inlets/outlets, and each pressure sample one. Thus, a total of 30 holes with a diameter of 0.8mm were micro-machined in the glass. Wax was used to attach the glass wafer to a carrier and to limit the chipping at the edges of the machined holes.

5.2.2.3 Anodic Bonding

The glass and silicon wafers were joined by anodic bonding. This step required an additional preparation of the wafers by cleaning them in a Piranha solution (H_2SO_4 , H_2O_2) to remove all impurities from the surfaces, which would result in a bonding defect. The holes present in the glass wafers served as alignment points with the two targets etched in the silicon wafers using a *Süss Microtec MA/BA6* aligner combined with the *SB6L* bonder from the same brand. The bonding parameters were set accordingly to values in Table 5-2.

Table 5-2. Bonding parameters used for the anodic bonding on the *Süss Microtec SB6L*.

Parameters	Value	Units
Applied force	1100	[N]
Temperature	400	[°C]
Voltage	700	[V]

The current was monitored to estimate the end of the bond process. When the voltage was applied to the stack, a peak value of current was observed, and the measured value decreases over time. When the current reached 10% of its peak value, the voltage was removed, and the bonding process was considered completed. Visual inspections provided a good qualitative estimate of the bonding quality since the defects between the two wafers are visible in Figure 5.2. Figure 5.2(a) shows defects visible on the bonded wafers' periphery and at several locations between the structures and over a μ OHP. The wafers presented in Figure 5.2(b) shows bonding defects on the periphery only, which is a sign of better cleaning and bonding.



Figure 5.2. Images of two bonded pairs of wafers with etched μ OHPs. Defects are visible on the image (a) on the periphery of the wafers and several locations over the etched microchannels, whereas (b) only show defects on the periphery.

5.2.2.4 Metallic Layers Deposition

Once the bonding was completed, one of the last steps was the deposition of metallic layers to connect the required tubing. The deposition relied on a 150 μ m-thick stainless steel stencil mask to obtain the desired patterns: markings to identify the pressure test samples and the connectors' pads.



Figure 5.3. Laser-cut stainless steel stencil used to pattern the metal layers on 6in wafers

The stencil (see Figure 5.3) was manually aligned to the wafer with a microscope, and Polyimide tape holds the stencil on top of the wafer. The first metallic layer was a titanium-tungsten alloy (TiW) and served as a diffusion barrier. A thin titanium (Ti) layer used as an adhesion layer was deposited before the gold (Au) layer. Table 5-3 summarizes the thickness of the deposited layers and tools used. A change in the tool occurred between the TiW and Ti layer, meaning breaking the vacuum and possible contamination during the transfer from one tool to another. However, contamination of the surfaces did not seem to have affected these layers.

Table 5-3. Layer deposition thicknesses and tools.

Layer		Thickness [nm]	Deposition method and tool
Titanium tungsten	TiW (10%/90%)	300	Sputtering – <i>Oerlikon</i> LLS-EVO
Titanium	Ti	30	E-Beam evaporation – <i>Leybold</i> Univex 500
Gold	Au	500	E-Beam evaporation – <i>Leybold</i> Univex 500

5.2.2.5 Dicing

The dicing step concluded the microfabrication process of the device to separate each component from the others. As the dicing relies on a circular saw blade revolving at high speed to cut the hard materials. The bonded wafers are glued to an adhesive tape to hold them while they are diced. Dicing marks are present on the wafers' surface and serve as reference points to align the saw and perform the cut.

5.2.2.6 Thermocompressed Connector

The reliable and compact connection of microchannels remains a challenging point to address. The method adopted to connect the μ OHPs presents the advantages of being fluxless and solderless at the expense of more complicated manufacturing and higher tolerances during surface preparation and connection. An Invar connector is machined and partially covered in Parylene. Gold is then electrodeposition and polished to obtain a flat and smooth surface, as illustrated in Figure 5.4. An adhesive film protects the surface and will be removed just before de deposition.

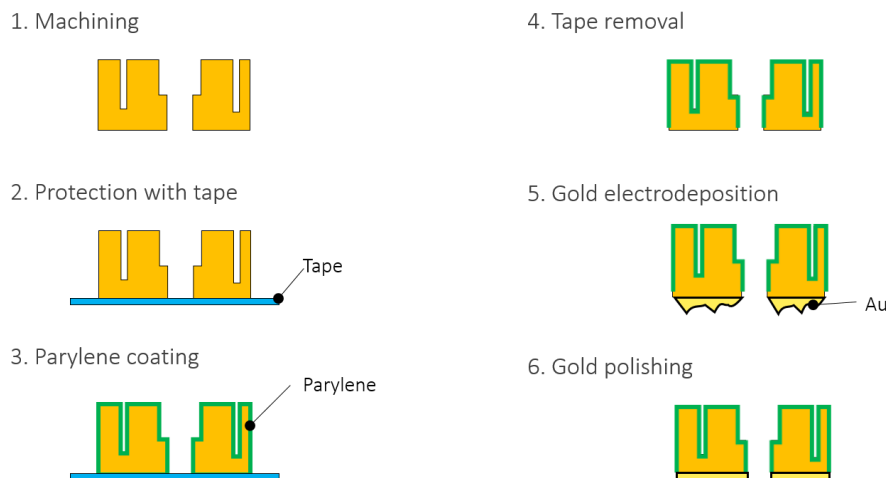
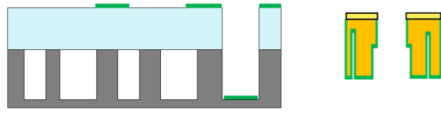


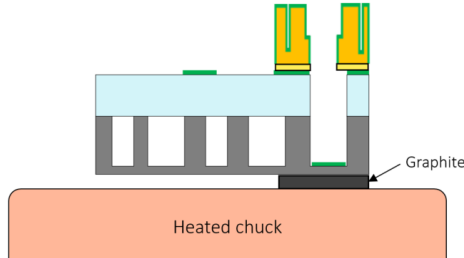
Figure 5.4. Schematic process of the preparation of the connector.

The thermocompression is depicted in Figure 5.5. The gold surfaces of the connector and the silicon and glass chip are prepared by the mean of a Piranha bath. They were then aligned on top of a graphite pad on a chuck. A second chuck is used to compress both parts together while heat is provided at the same time.

1. Gold surface cleaning



2. Alignment and stacking



3. Thermocompression

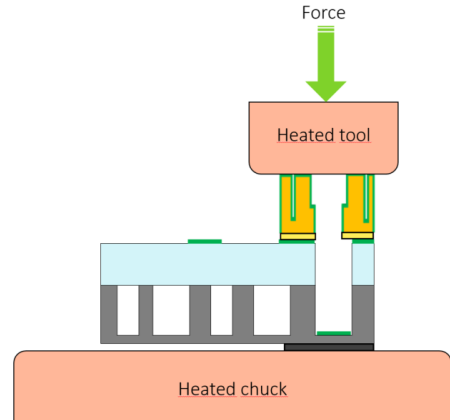


Figure 5.5. Schematic of the thermocompression of the connector by the mean of a dedicated tool with heated chuck.

A graphite layer of 0.5mm was placed between the silicon and the heated chuck in order to compensate for the inhomogeneity. The pressure applied to the gold surfaces was 10MPa with the temperature profile set according to Figure 5.6. The pressure was applied from the beginning of the heating to the end of the cool down.

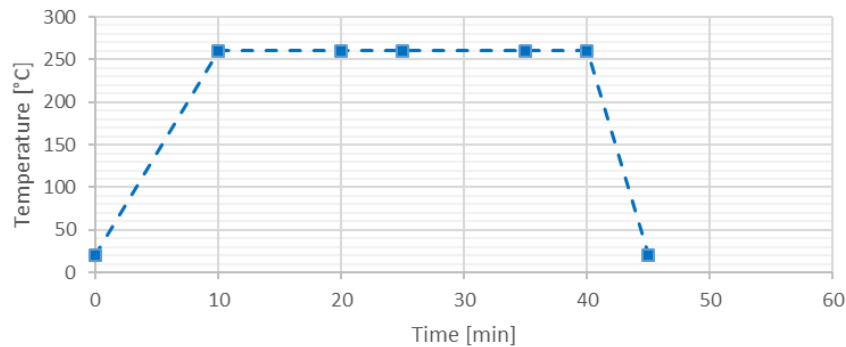


Figure 5.6. Temperature profile for the thermocompression of the connector.

The connector was designed to accommodate fittings with a flat-bottom port and the corresponding ferrules. Two threaded ports accommodated UNF#6-40 fittings, and two M1.6 threaded holes were used to connect the wires for the gold deposition and fix the connector during the polishing of the deposited gold.

5.2.3 Results

The resulting device is displayed in Figure 5.7, and an SEM cross-section is visible in Figure 5.8.



Figure 5.7. μ OHP with a connector. The device presented here measures 60mm by 20mm.

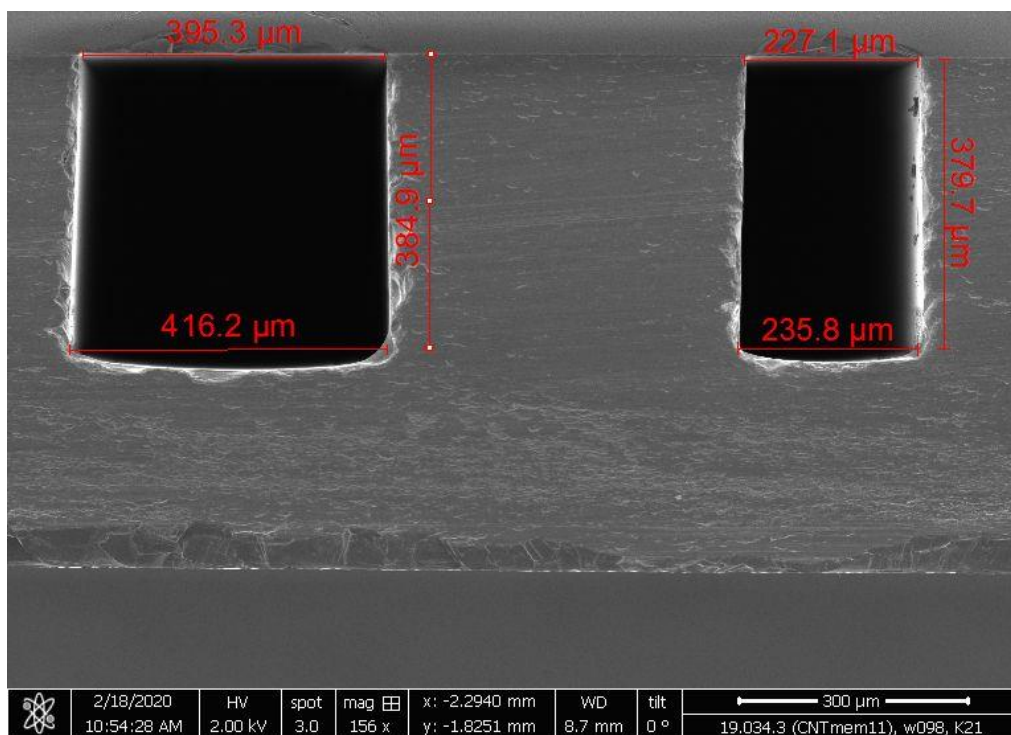


Figure 5.8. SEM cross-section of the microfabricated μ OHPs in silicon capped by a glass (top of the SEM image).

Each pair of bonded wafers was tested. Figure 5.9 gathers the results of the pressure tests conducted with the rectangle samples, and Figure 5.10, the results for the circular membrane.

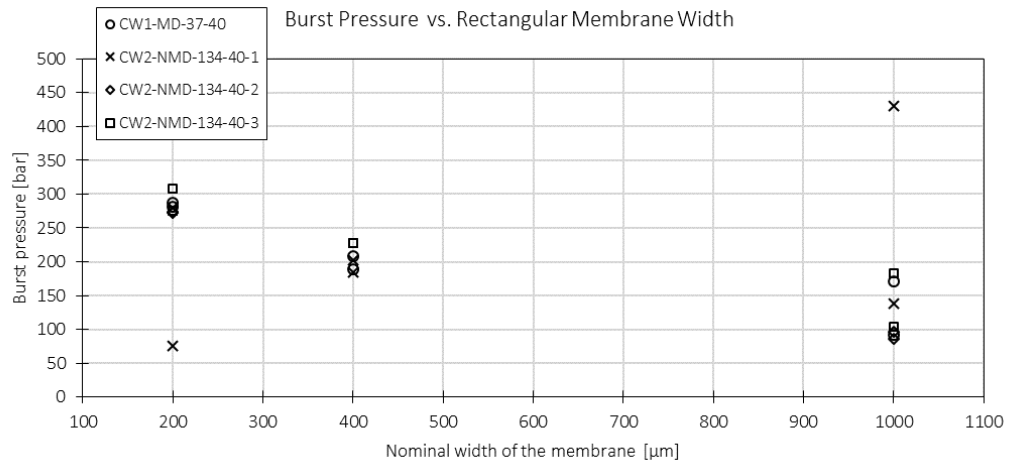


Figure 5.9. Burst pressure of the pressure test samples from four pairs of wafers.

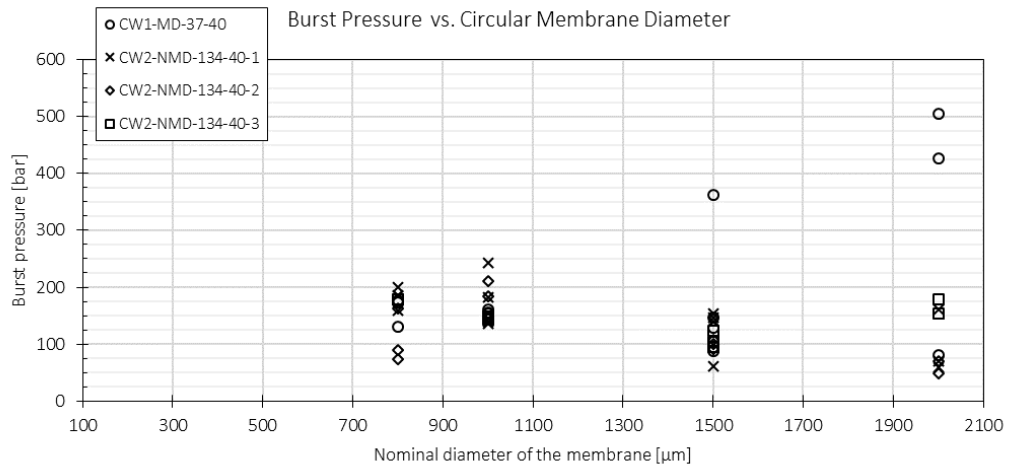


Figure 5.10. Burst pressure of the pressure test samples from four pairs of wafers.

At the exception of the two samples from the pair CW2-NMD-134-40-1 at 200 μm and 1mm, the samples follow the $1/a^2$ trend, with an increasing deviation.

The bonding quality of the μ OHPs was also verified. The pressure was applied to the device using the same test stand as used previously. The bonding was considered to be sufficient if the μ OHP could withstand 15bar of pressure. None of them failed.

5.3 Microfabrication of the Proof-Of-Concept Demonstrator

Gold thermocompression was used to realise the proof-of-concept demonstrators, which used silicon as capping material. This method is a variation of generic diffusion bonding processes involving the simultaneous application of pressure and heat to form bonds. Gold, among other ductile materials, exhibits advantageous properties as low yield point, oxidation resistance and electrical conductivity, in addition to providing a hermetic interface.

5.3.1 Layout

The layout was designed for 6in wafers and comprises eight μ OHPs and twenty pressure samples. Figure 5.11 illustrates the layout of the 6in wafers.

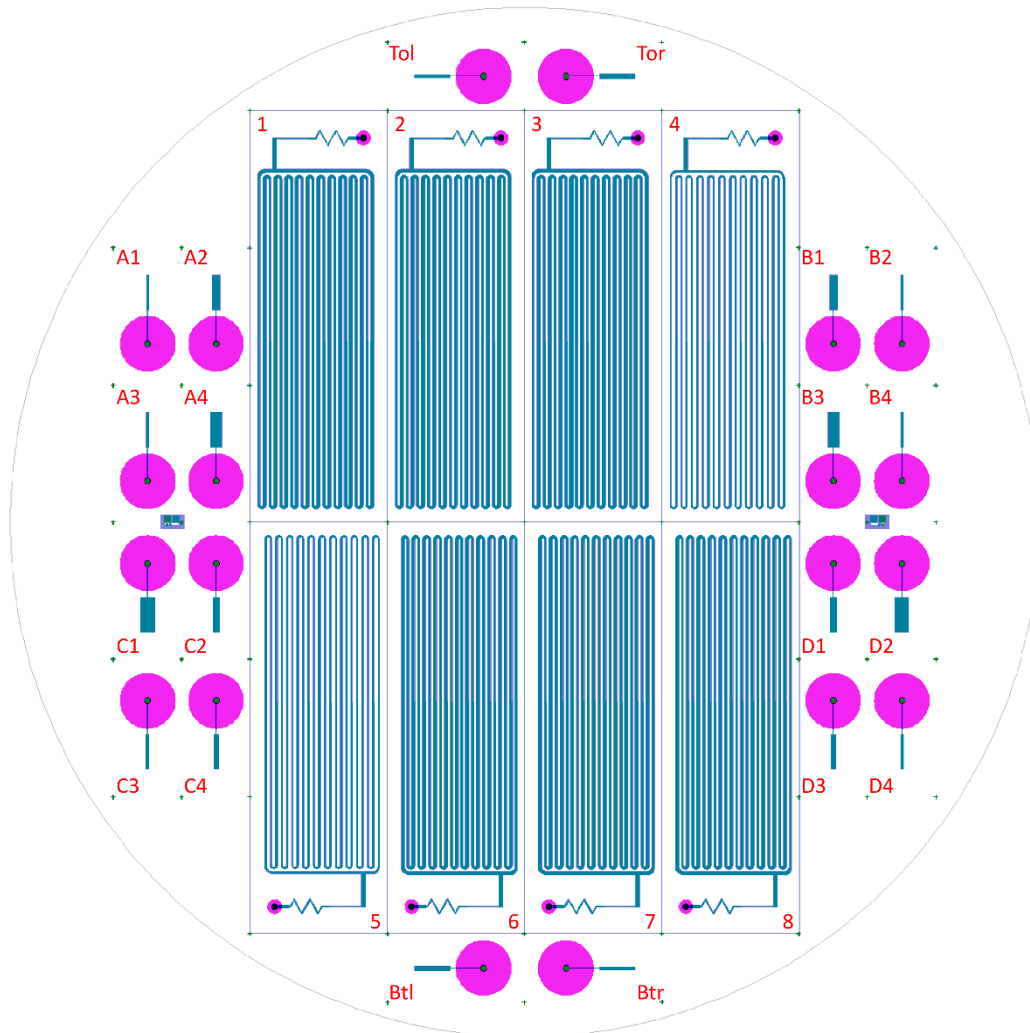


Figure 5.11. Layout on 6in wafers for the end-product devices. Blue and green areas represent the etching area for the microchannels. The magenta areas delimit the deposition of the titanium and gold layers deposited after the bonding. The red identifiers of the samples and μ OHPs are present only for reference.

5.3.2 Fabrication Process Flow

The microchannels' processing was done on 625 μ m-thick silicon wafers for the microchannels, while 380-thick silicon wafers capped the etched microstructures.

The process involved the deposition and patterning of gold before the etching of silicon. Carefully attention was given to create the microchannels without gold on microchannels' bottom and walls but with gold on each inlet wall.

Appendix D.2 details the process flow for the silicon devices.

5.3.2.1 Silicon Microchannels and Inlets Etching

The microchannels and the inlet were integrated into the same 6in silicon wafer with two etching steps. The process flow is detailed in Appendix D. The gold used for bonding is deposited before the DRIE etching steps. Titanium layers are used as adhesion layers between silicon oxide and gold layers. An aluminium layer was deposited on the wafers' backside to protect the tools' chucks during the inlets' etching.

A safety margin was kept between the gold layer and the etching masks of the microchannels to limit the risk of etching the gold during the microchannels' etching steps. The margin is illustrated in Figure 5.12 and visible in Figure 5.23.



Figure 5.12. Illustration of the safety margin kept to avoid exposition of gold during the silicon and silicon oxide etching steps. The etching layout for gold is in purple and the one of Si and SiO_2 in teal.

5.3.2.2 Capping Wafers

The capping wafers were processed in parallel to the ones with the microchannels, except for the etching steps. The two types of wafers were then separated for the etching step until the titanium had to be removed from the top of the gold layer.

5.3.2.3 Gold Thermocompression Bonding

The wafers were joined by thermocompression of intermediate gold layers. Although the exposed gold layer does not oxide under standard conditions, both wafers were soaked before bonding in a Piranha cleaning solution, rinsed in DIW and dried. The two 500nm-thick gold layers were aligned after the cleaning. As the critical elements were all processed on the same wafer, only a coarse alignment was performed. After the vacuum pumping the bond chamber, the wafers were subject to heat and mechanical pressure to perform the bonding. The bonding parameters used were the following:

- Temperature: 270° (top and bottom chucks)
- Force: 25 kN
- Time: 60min

5.3.3 Results

The μ OHPs obtained with the pair of pilot wafers of the batch are presented in Figure 5.13.

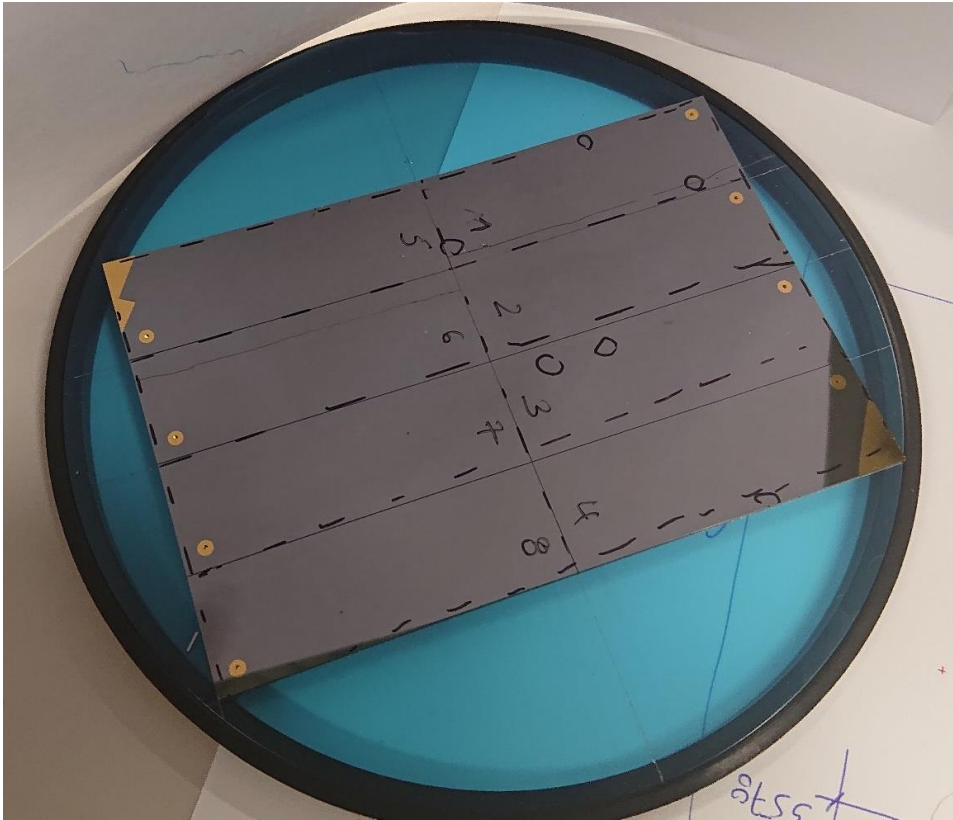


Figure 5.13. μ OHPs after dicing remaining on the dicing frame and tape. Fractures are visible on the μ OHPs no.1 and no.6.

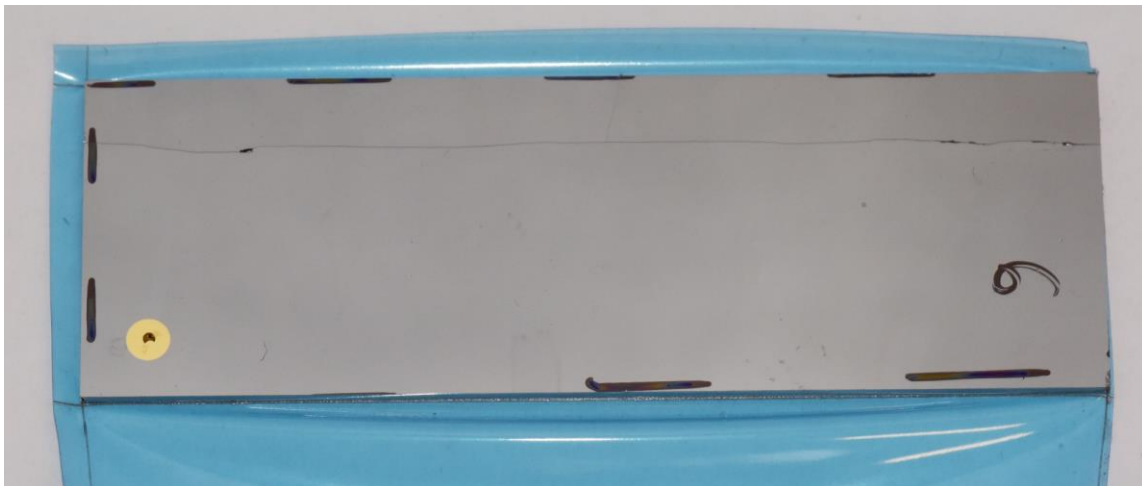


Figure 5.14. Close view of the fracture on μ OHP no.6. Fracture are visible on the top surface and tends to favour a path parallel to the microchannels.

5.3.4 Pressure Resistance

Similarly to wafers obtained by anodic bonding, the bonding quality of the thermocompressed wafers is tested with pressure samples. The pressure samples were thinned as the capping wafer's initial thickness prevented the membrane from breaking under pressure. Twelve samples were thinned down at three different levels. Figure 5.15 and Table 5-4 summarize the results obtained for the different thicknesses and widths.

The observed fracture modes differ from the ones observed with silicon and glass in the precedent pressure tests or with the data gathered by CERN EP-DT over the different projects. In this specific case, the fracture of the interface can be classified as:

- Fracture of t_2 : the membrane above the cavity is completely removed, with or without delamination of the interface (see Figure 5.16).
- Partial fracture of t_2 : the membrane is partially fractured. The fracture is visible near the microchannels, but the membrane remains in position (see Figure 5.17).
- Leaks from sides of the sample: the membrane remains unbroken, but leaks appear at the samples' edges. The interface is locally de-bonded (see Figure 5.18).

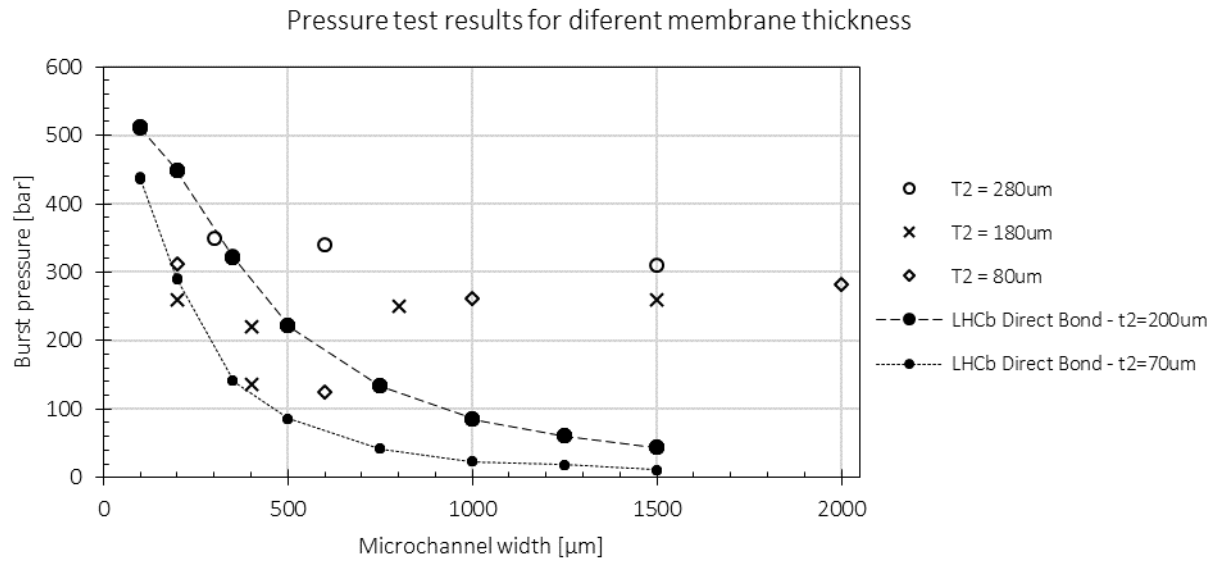


Figure 5.15. Burst pressure of rectangular microchannels microfabricated by gold thermocompression with different membrane thickness t_2 . Direct bonding values for comparison[292].

Table 5-4. Summary of pressure samples with thinned thickness t_2 , burst pressure and the corresponding fracture mode observed (illustrated in Figure 5.16 to Figure 5.18)

Sample ID	W [μm]	t_2 [μm]	Burst pressure [bar]	Fracture mode
A1	200	180	260	Leak from side interface
A2	1000	80	261	Fracture of t_2
A4	1500	180	260	Partial fracture of t_2
B2	200	80	312	Partial fracture of t_2
B3	1500	280	310	Partial fracture of t_2
B4	300	280	350	Partial fracture of t_2
C1	2000	80	283	Leak from side interface
C4	600	280	340	Fracture of t_2
D1	800	180	250	Partial fracture of t_2
D4	400	180	220	Leak from side interface
Btl	600	180	125.5	Fracture of t_2
Btr	400	80	137	Partial fracture of t_2

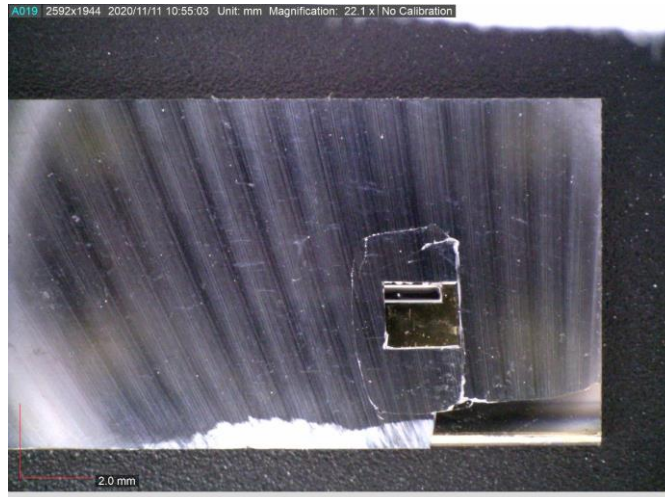


Figure 5.16. Sample BtI – Fracture of the membrane. The microchannel is visible. A part of the membrane remained attached despite the fracture, while two distinct parts detached entirely from the sample.

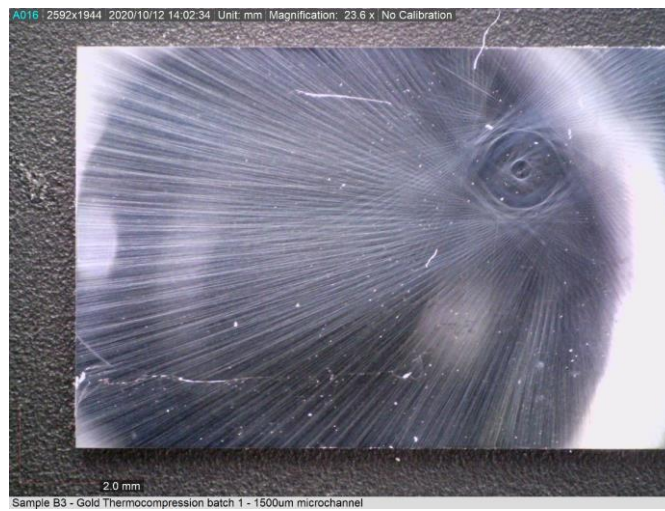


Figure 5.17. Sample B3 – Partial fracture of the membrane above a 1.5mm-wide channel. The fracture is visible on the left, top and bottom sides of the sample. It did not propagate to the right side.



Figure 5.18. Sample C1 – A deformation of the membrane above the microchannel is visible, but leaks appeared at the edges of the sample.

The samples A2, B4 and C1, each one exemplifying one of the observed fracture modes, were diced accordingly to the scheme in Figure 5.19. The goal was to observe the failure modes of the interfaces. Two failure modes exist for bonded interface with gold: cohesive and adhesive failures [293], [294]. The first mode involves a breakdown of the intermolecular links in gold layers formed during bonding; the second one describes the adhesion's failure to the substrates.

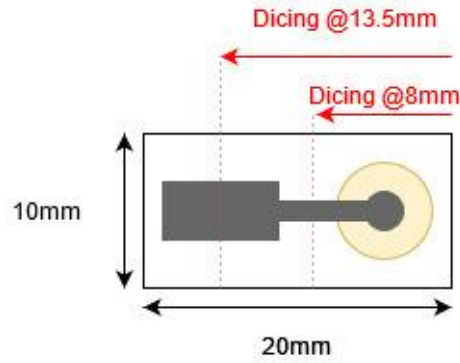


Figure 5.19. Dicing scheme for samples for SEM

5.3.4.1 Sample A2

The sample A2 was subject to complete fracture of the membrane t_2 . The sample was diced along the second cutline to investigate the fracture modes. The fracture of the sample A2 is depicted in Figure 5.20, with an illustration of the two cross-sections observed.

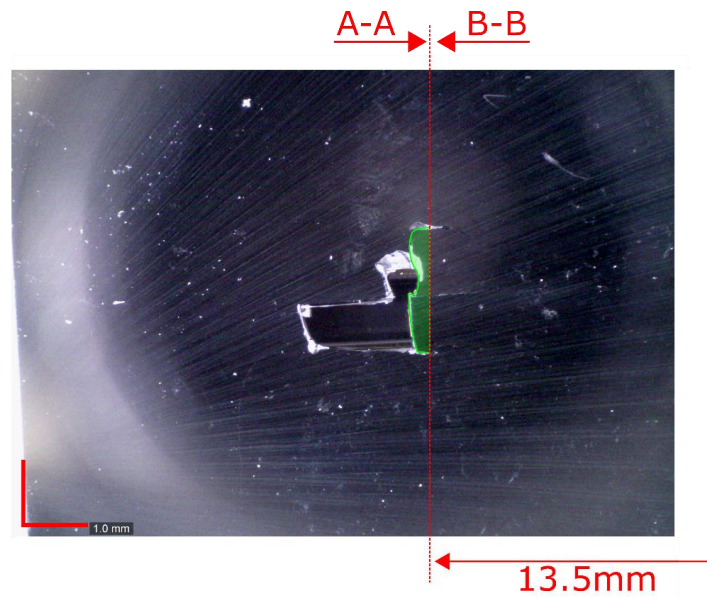


Figure 5.20. Sample A2 - Dicing and cross sections. The green area represent the part of the membrane t_2 that disappeared during the dicing

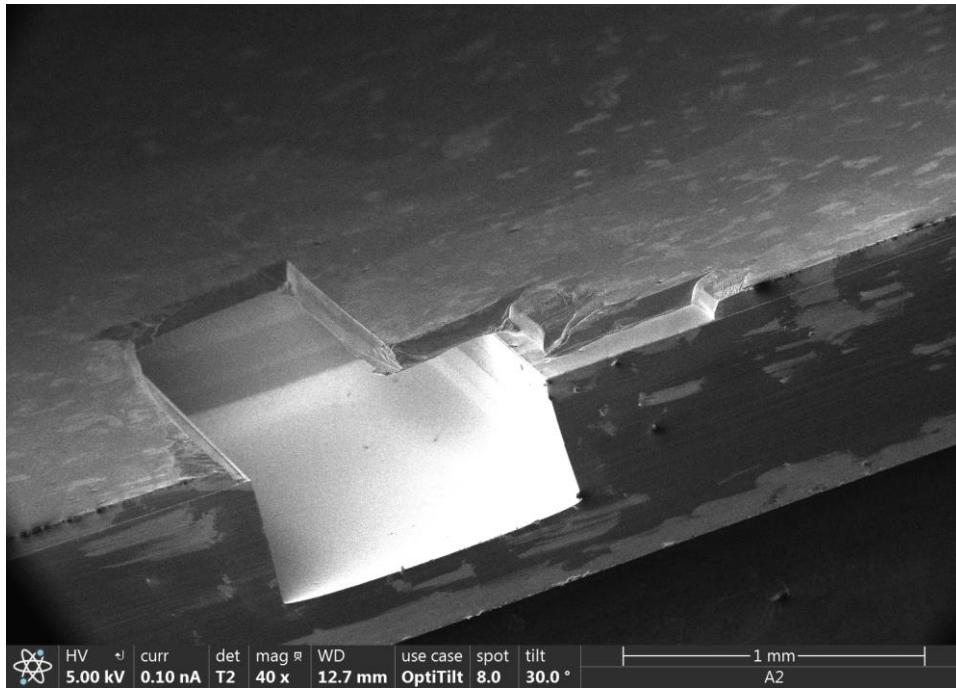


Figure 5.21. Sample A2 (B-B) – SEM image of the fractured membrane and microchannel.

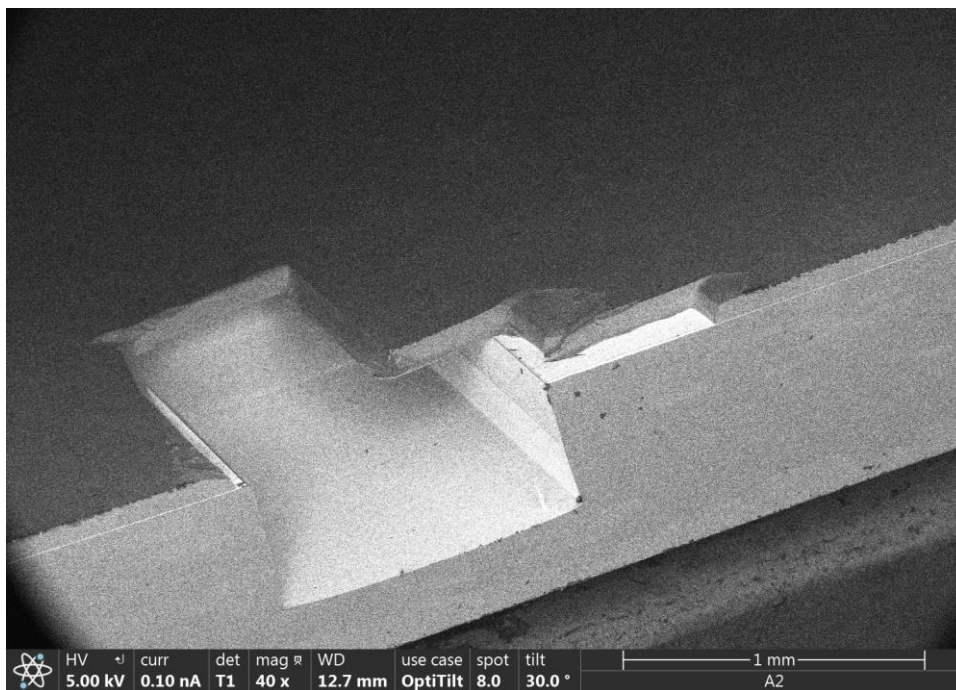


Figure 5.22. Sample A2 (B-B) – EDS image of the fractured membrane and microchannel.

Figure 5.21 and Figure 5.22 display the fracture of the membrane of the sample A2. An overhanging part of the membrane remains visible. The complex shape of the missing part of the membrane suggests that the unbounded gold on the capping wafer above the microchannel participates in the crack propagation's energy dissipation, potentially deviating the propagation path of initiated crack. The EDS image shows elements with high Z number remain on the ledges of the microchannels.

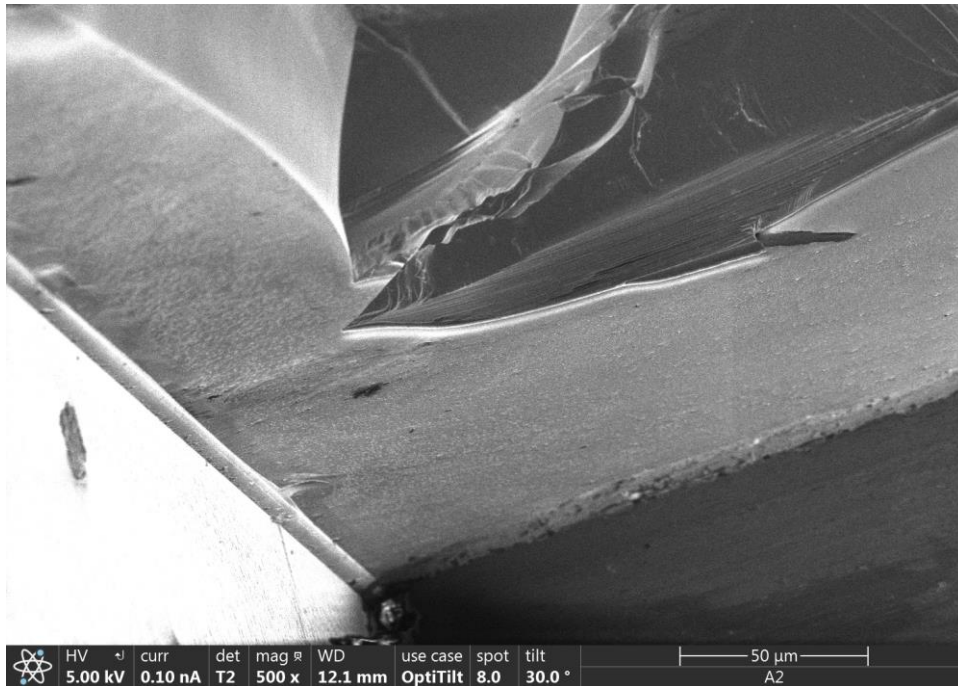


Figure 5.23. Sample A2 (B-B) – Zoomed SEM image on the ledge of channels. The gap between the etched micro-channel and gold is visible. Roughness on the gold covered area is visible.

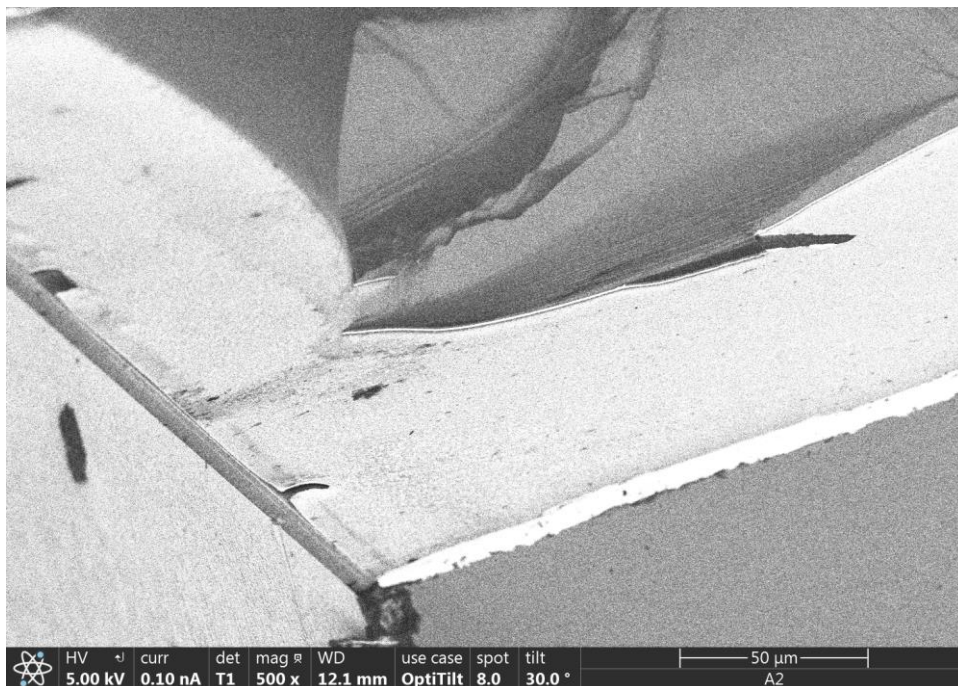


Figure 5.24. Sample A2 (B-B) – EDS image of the fractured membrane and microchannel. Partial delamination of the titanium and gold layers from the Si-SiO₂ substrate is visible on several locations at the ledge of the microchannel.

Figure 5.23 shows the ledge of the microchannels with the recess in the gold layer near the edge. Partial adhesive failure of the bonding layers is visible close to the recess. The EDS image (Figure 5.24) of the adhesive failures' locations allows concluding that nor does gold or titanium remain on the failing areas. Furthermore, the roughness of the gold layer, visible in the SEM image, disappears near the edge of the Ti-Au layers, hinting at a mix of adhesive and cohesive failure.

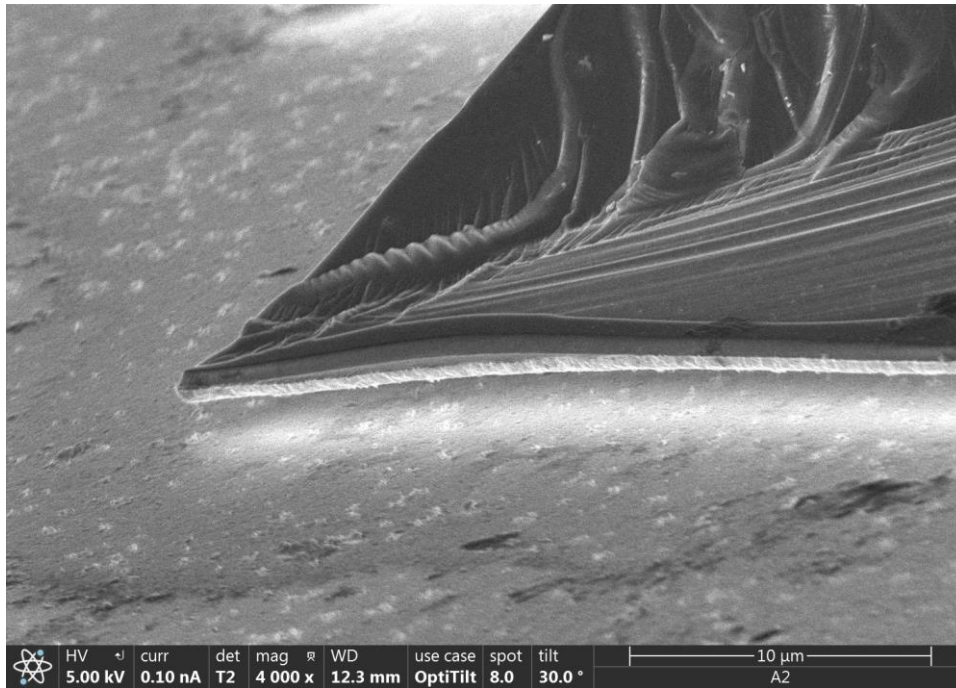


Figure 5.25. Sample A2 (B-B) – SEM image of the silicon tip. Roughness is visible on the gold layer. A gap between the tip and the substrate is noticeable.

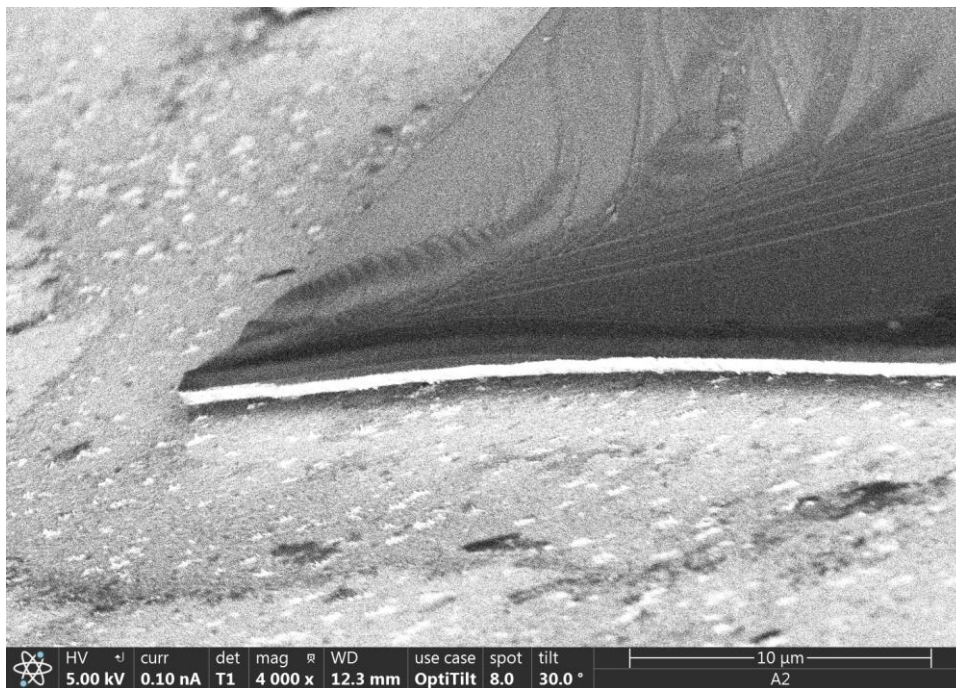


Figure 5.26. Sample A2 (B-B) – EDS image of the silicon tip. Gold and titanium remains are visible on the lower edge of the tip.

Figure 5.25 and Figure 5.26 highlight the cohesive fracture mode as the roughness resulting from the voids and cones formation due to the ductile interface's cohesive failure [295]. However, dark spots originating from adhesive failure are also visible. The EDS image suggests the presence of titanium and gold on the hidden side of the tip.

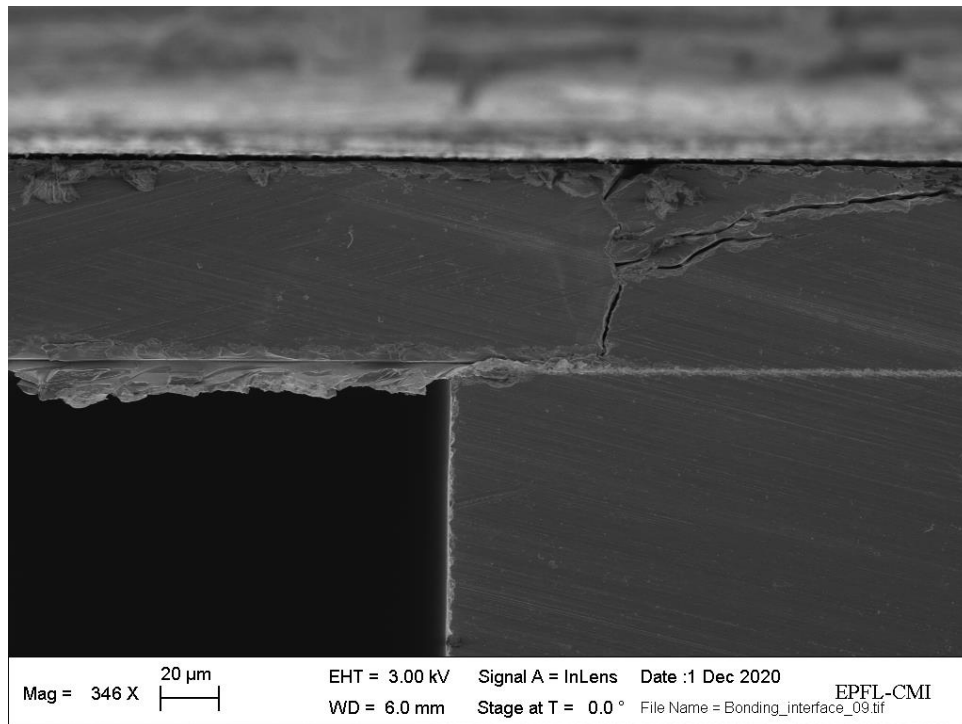


Figure 5.27. Sample A2 (A-A). SEM image of a fracture of the interface that changed path through the t_2 membrane.

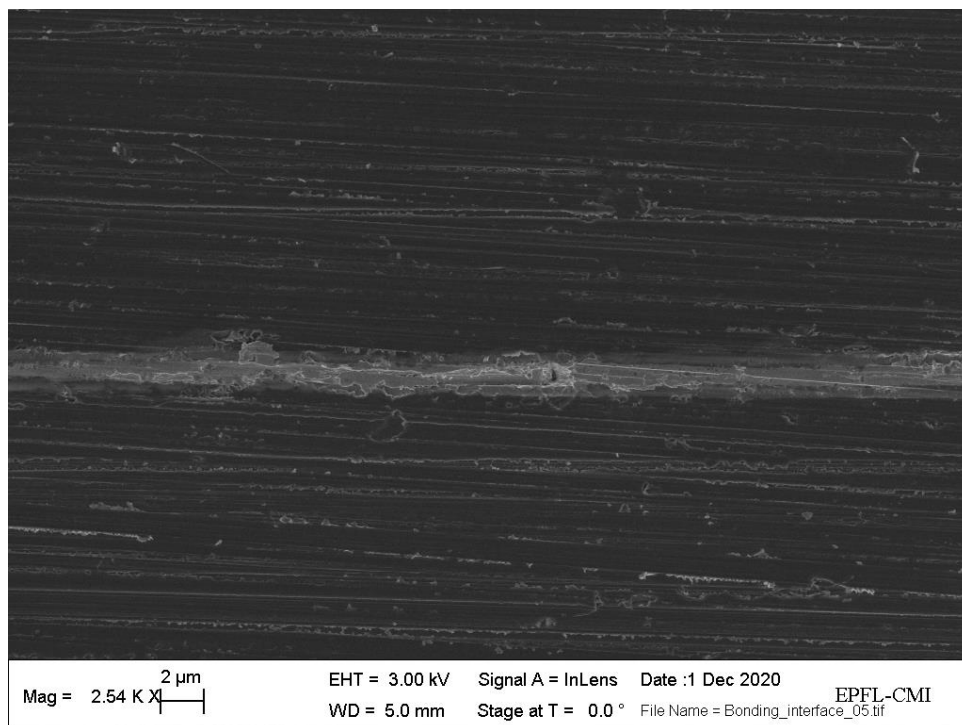


Figure 5.28. Sample A2 (A-A) – SEM image of a cohesive failure 130 μ m from the wall of the microchannels.

Local fracture propagations through silicon can be observed by the mean of the perpendicular views of the cross-section, as visible in Figure 5.27. However, the possibility to determine the failure mode is deterred as the ductile gold is deformed by the dicing saw but can occasionally be visible, as in Figure 5.28.

5.3.4.2 Samples B4

The sample B4 was subject to partial fracture of the membrane t_2 , as visible in Figure 5.29. The membrane delaminated partially, keeping the membrane attached and intact in some locations. The sample was diced along the second cutline to investigate the fracture modes.

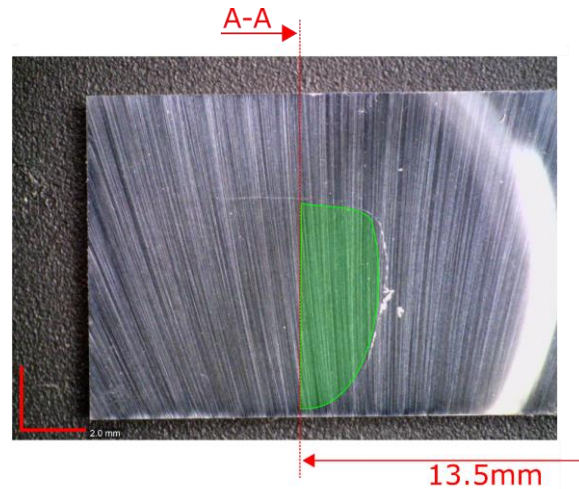


Figure 5.29. Samples B4 - Dicing and cross section. The green area represent the part of the membrane t_2 that disappeared during the dicing.

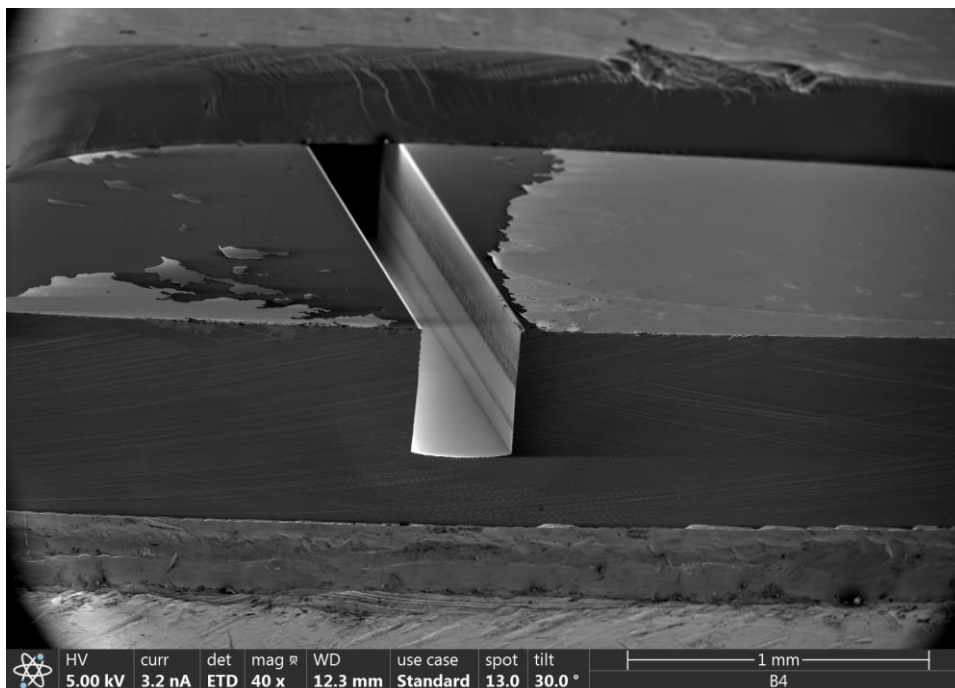


Figure 5.30. Samples B4 (A-A) – SEM image of the 300μm-wide microchannel. Gold and titanium adhesive failure is visible on both sides of the microchannel.

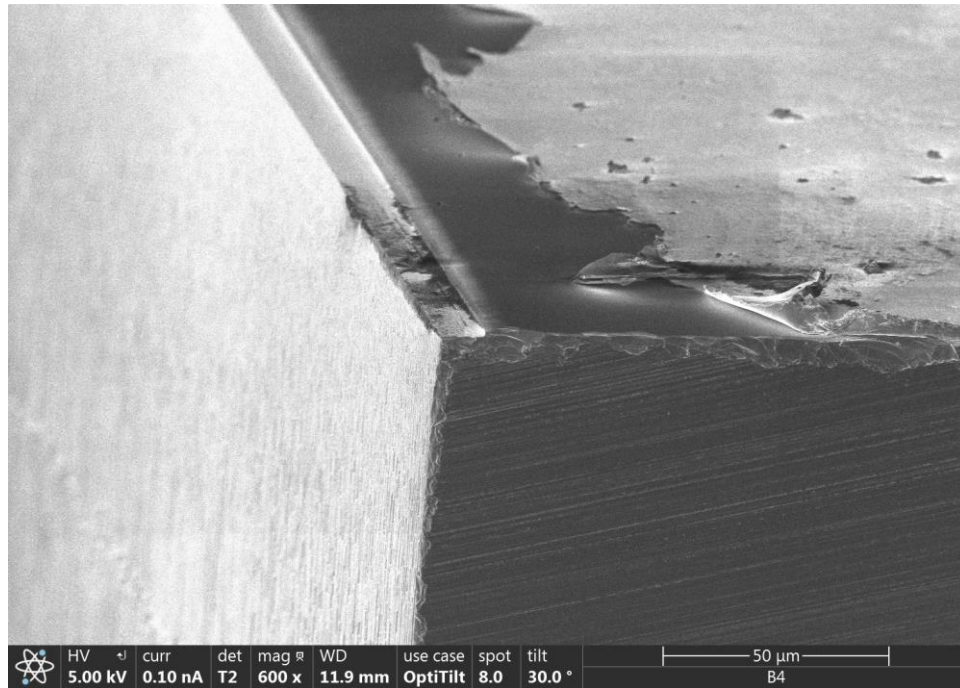


Figure 5.31. Samples B4 (A-A) – SEM image of the top of the wall of the microchannel. Ti-Au layers are seen to roll on them-self.

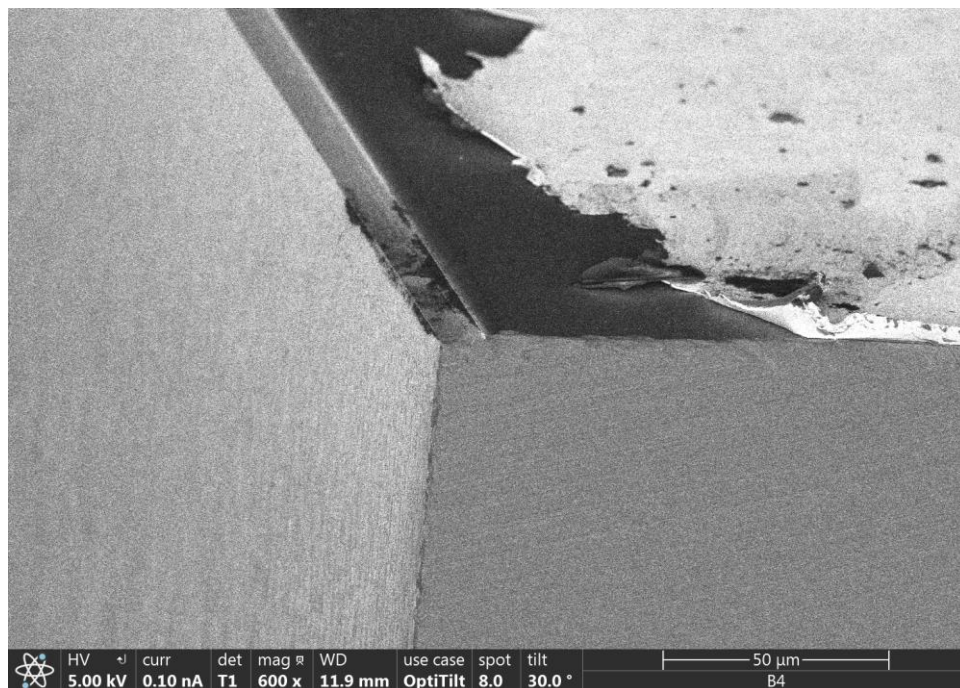


Figure 5.32. Samples B4 (A-A) – EDS image of the top of the wall of the microchannel. Titanium or gold are absent from the ledge of the channel. They are seen further away on the right (clear areas).

Figure 5.30 depicts a large adhesive failure area on both sides of the channels. In Figure 5.31 and Figure 5.32, small cones and voids suggest a failure of the gold-to-gold bond. Thus, the adhesive failure was mixed to a cohesive failure. A part of the membrane was lost during the dicing, suggesting that the lost part was completely detached from the substrate after the pressure test.

5.3.4.3 Samples C1

Sample C1 was subject to leaks from the sample's sides. This particular sample displays a deformation of membrane t_2 . The sample was diced along the second cutline, as illustrated in Figure 5.33. The dicing removed a part of the membrane.

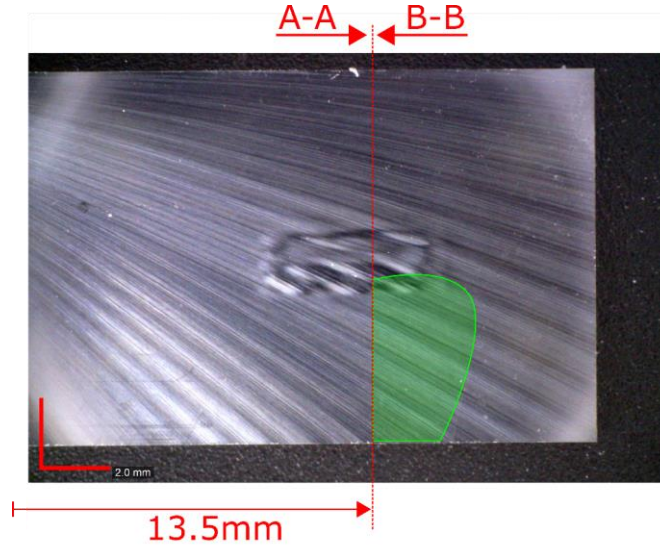


Figure 5.33. Samples C1 - Dicing and cross section. The green area represent the part of the membrane t_2 that disappeared during the dicing.

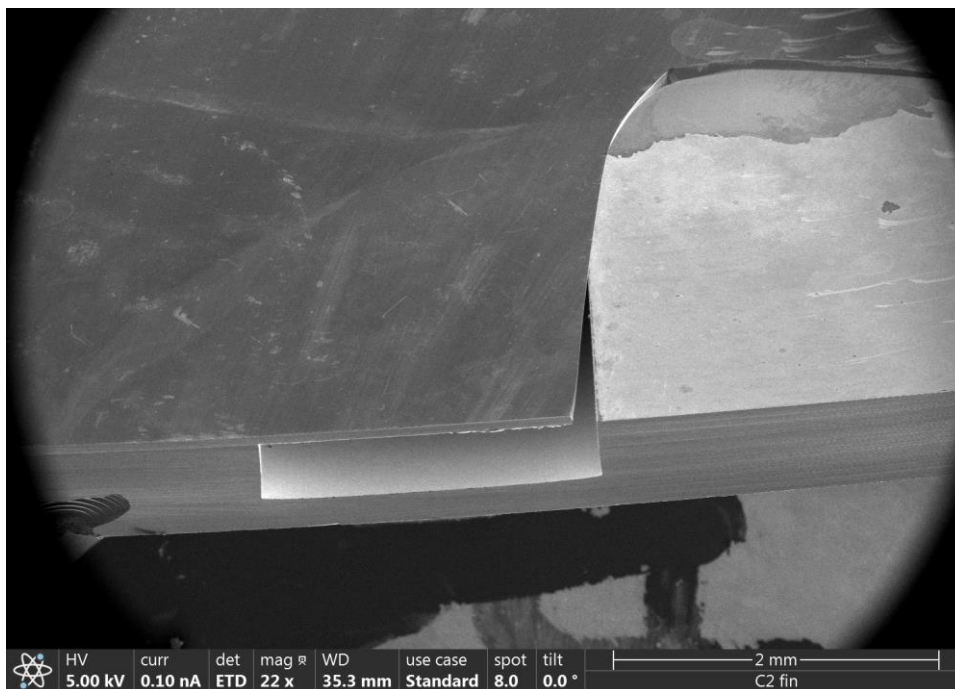


Figure 5.34. Sample C1 (A-A) – SEM image of the fractured membrane and microchannel. The right side of the membrane is missing and a default in the t_1 membrane at the bottom left is revealed by the SEM picture.

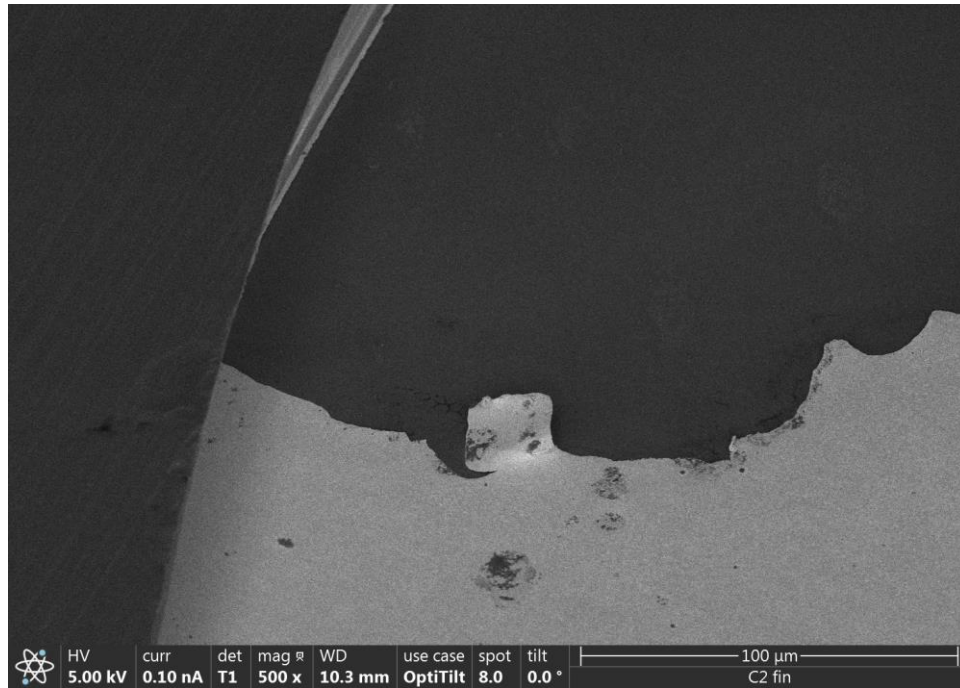


Figure 5.35. Samples C1 (A-A) – EDS image of the releveled gold. Adhesive failure is deductible as the Ti-Au layers are missing locally.

The sample C1 was prone to a mix of cohesive and adhesive failures, as visible in Figure 5.34 and Figure 5.35. In this particular case, the stress generated by the pressure did not reach the substrate's fracture toughness but was sufficient to break the bonds of the interface.

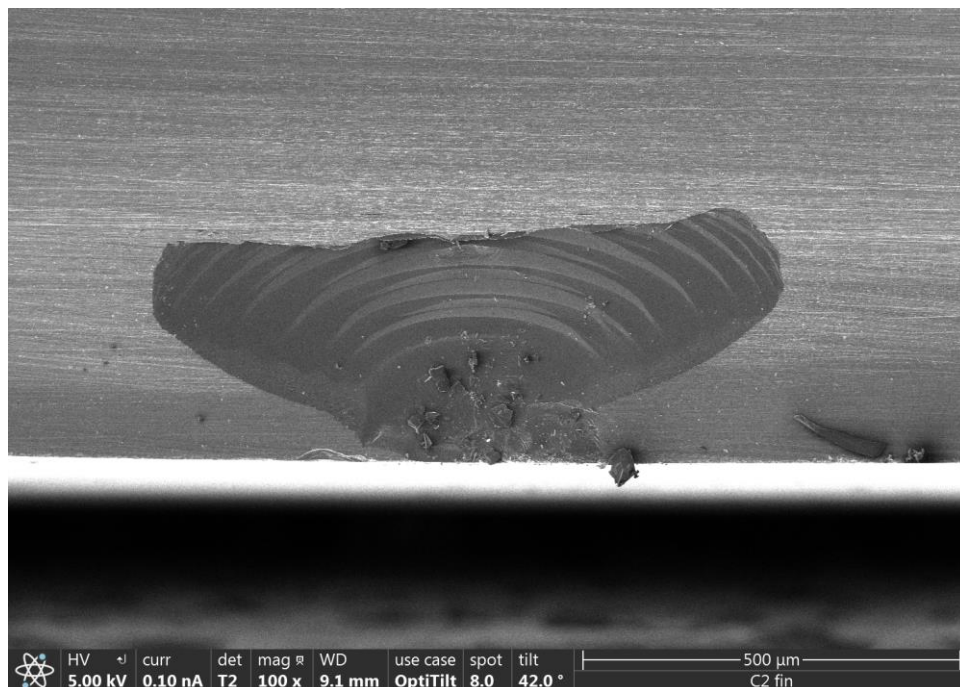


Figure 5.36. Sample C1 (A-A). Detailed SEM image of the default in the membrane t_1 .

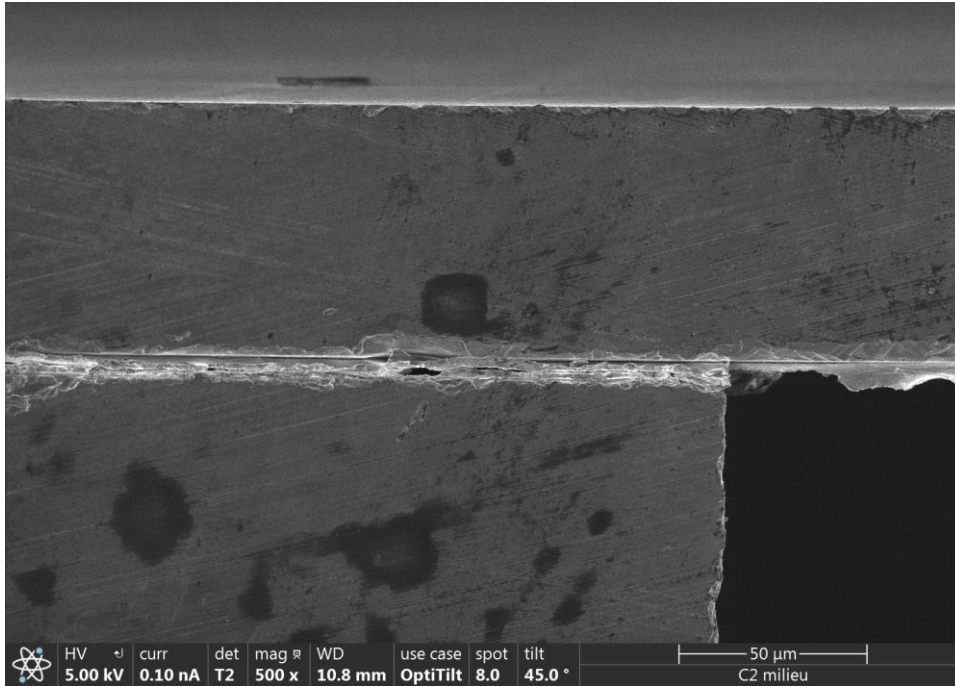


Figure 5.37. Sample C1 (B-B) – SEM image of the microchannel wall and the capping membrane t_2 . The deformation of t_2 remains invisible when observed with an SEM. Cohesive failure is distinguishable.

Despite the visible deformation in Figure 5.33, sample C1 was not subject to a membrane failure only the interface failed. The propagation path of the fracture did not deviate in the membranes' bulk, and both cohesive and adhesive failures were observed.

5.3.5 Discussion

The analyses of the sample A2, B4 and C1 conclude to a mix of adhesive and cohesive failures in the samples. The bond toughness and the failure modes depend on several parameters, such as the bonding temperature, the force used and the surfaces' cleanliness. The deposition process of the gold does not influence the bond. However, thickness, temperature and pressure do, as creep and diffusion have an exponential dependency on the temperature. The flatness and the bow of the substrate also influence the resulting bond. High bond energy would lead to the observation of cohesive failure mode as the predominant mode [294], [296], [297]. Therefore, the bonding procedure could be improved.

Considering that the area etched for the microfabrication of the μ OHPs, including the pressure samples, but excluding the dicing marks and alignment marks, represents a total of 4199mm^2 and a 6in wafers possesses a total surface of approximately 17670mm^2 , the pressure exerted on the gold layers during the thermocompression is 1.85MPa . Spearing et al. [297], and Charlot et al. [296] reported contact pressures from 5.8MPa to 120MPa for similar bonding approaches. In their cases, higher pressures led to higher bond strength. Therefore, an increase in force could lead to a higher bond strength than the one observed in this work. Besides, the increase in temperature would also contribute to create a strong bond, as it would modify the malleability of the gold layers and limit strain-hardening. In bonded systems with ductile materials, energy can be

dissipated in the surrounding material by plastic deformation. More energy is required to propagate the crack when plasticity is involved, whereas the plastic deformation contribution is negligible with brittle material.

Figure 5.15 summarises burst pressures of the samples from the pilot pair alongside the ones of direct-bonded samples obtained during the evaluation of the bond quality for the LHCb VeLo's cooling plates [292]. Direct bonding of silicon wafers results in a decreasing resistance with the increasing microchannel's width. Thermocompressed wafers' pressure samples display a resistance with strong variation at the lower widths, but high-pressure resistance for large microchannels. The sample A2 ($t_2 = 80\mu m$, $w = 1000\mu m$) withstood 260bar whereas sample with the same with obtained by direct bonding broke at 85.6bar. Au-Au interface's ductile deformation could explain this difference as it would dissipate more energy than direct-bonded ones. The bonding strength and quality could be increased by changing the bonding parameters, as the temperature and force.

The role of the thickness of the membrane t_2 on the resistance of the microchannels to the pressure cannot be established from the tested samples. Decreasing the thickness t_2 did not reduce the burst pressure in each case.

One potential disadvantage of the thermocompression is the interaction with the particles since gold and titanium have high Z numbers, which result in a radiation length of 0.33cm for gold and 0.54cm for titanium. However, layers' total thickness mitigates this potential issue as a total of 100nm of Ti and $1\mu m$ of Au were deposited. The material budget resulting from the thermocompression remains low. Furthermore, decreasing the thickness of the gold layers would reduce the material budget while keeping the bonding strength acceptable [298].

Alternatively, wafer bonding with an intermediate insulating layer is possible and could even further reduce the material budget. Sahoo et al. [299] proposed a process based on Al_2O_3 (alumina) thin-films to bond homogenous and heterogeneous wafers. Alumina has a radiation length of 7.04cm, and the bonding can be performed with film thickness ranging from 3nm to 50nm. This hints at a low material budget solution for wafer bonding.

Silicon carbide (SiC) could be used as a substrate for the μ OHPs instead of silicon. It would offer a higher thermal conductivity compared to silicon. However, the coefficient of thermal expansion of the SiC does not match the CTE of silicon. Furthermore, the added cost for such a high-thermally conductive substrate led to the selection of silicon as base-material for this work.

5.4 Conclusions

Two sets of μ OHPs were microfabricated using the two methods presented. They possess the advantage of bonding silicon wafers at low-temperature and being CMOS-compatible.

The SEM observations of the thermocompressed samples led to the conclusion that gold layers are subject to a mix of cohesive and adhesive failures. This mix-mode led to a variation in the pressure resistance of the samples. Gold thermocompression is a promising solution for the realization and integration of microchannels subject to high pressure or wide channels. However, this solution could be further optimized to reduce the material budget and the variation in adhesion strength.

Chapter 6 Flow Patterns & Thermal Performance

This chapter presents the flow observations and resulting thermal performance of the microfabricated proof-of-concept devices. The effects of the working fluids, charging ratios and orientations on the performance of the device are discussed.

Thermal performance, and consequently the operation of the μ OHPs, depends on the geometry, the temperature conditions, the working fluid and the pattern of the two-phase flow in the microchannels. For these reasons, the identification of the major trends in the flow pattern, but also on the transitions on different patterns, may help to determine the optimal parameters for the design of such devices. The glass cover used in part of the μ OHPs allowed monitoring the flow patterns through visual inspection and analysis of the time-strips. This chapter reports the observed flow patterns and thermal performance obtained for three working fluids as a function of the charging ratio and the orientation of the devices.

6.1 Flow Patterns

The flow patterns fall into the five categories, in order of apparition with increasing power input: low amplitude oscillations, oscillations, unstable oscillations with circulation and direction reversals, and unidirectional flow circulation. Figure 6.1 illustrates the flow dynamics observed during the tests, which are briefly described here-under.

No oscillation. The liquid slugs and vapour plugs are randomly distributed in the channel before starting the operations of the μ OHPs. Before reaching a sufficient power to initiate any fluid reaction, no oscillation is observed beside minor nucleation and vapour plug growth in the evaporator.

Low amplitude oscillations. The restricted pumping action generated by the low heat input creates low amplitude oscillations of the slugs around a mean position. This flow pattern is mainly observed at low power inputs.

Unstable oscillations with slow circulation. Larger amplitudes driven by the increased power inputs occasionally force to the liquid slugs and vapour plugs to pass into adjacent channels. Their passage prompts the slugs and plugs present in the microchannel section to advance, generating a slow circulating motion with stopovers accompanied by local oscillations.

Oscillations. The amplitude of the oscillations increases and is equivalent to the length of the channel. The liquid sweeps through the evaporator and the condenser, resulting in an increased heat transfer.

Unstable oscillation with circulation. The velocity of the generated oscillations increases, and circulation occurs in one direction. Flow reversal, a change in the flow direction, is also observed. Additionally, an annular-like flow is formed at the evaporator's outlets yielding higher thermal performance.

Unidirectional flow circulation. The flow follows the same arbitrary direction of circulation in the microchannels. A train of slugs and plugs or a fully developed annular flow can be observed leaving the evaporator while slug-plug flow enters it. Unidirectional flow circulation corresponds to the operational state with the highest thermal performance until the heat load dries out the liquid films on the walls, and the performance decreases.

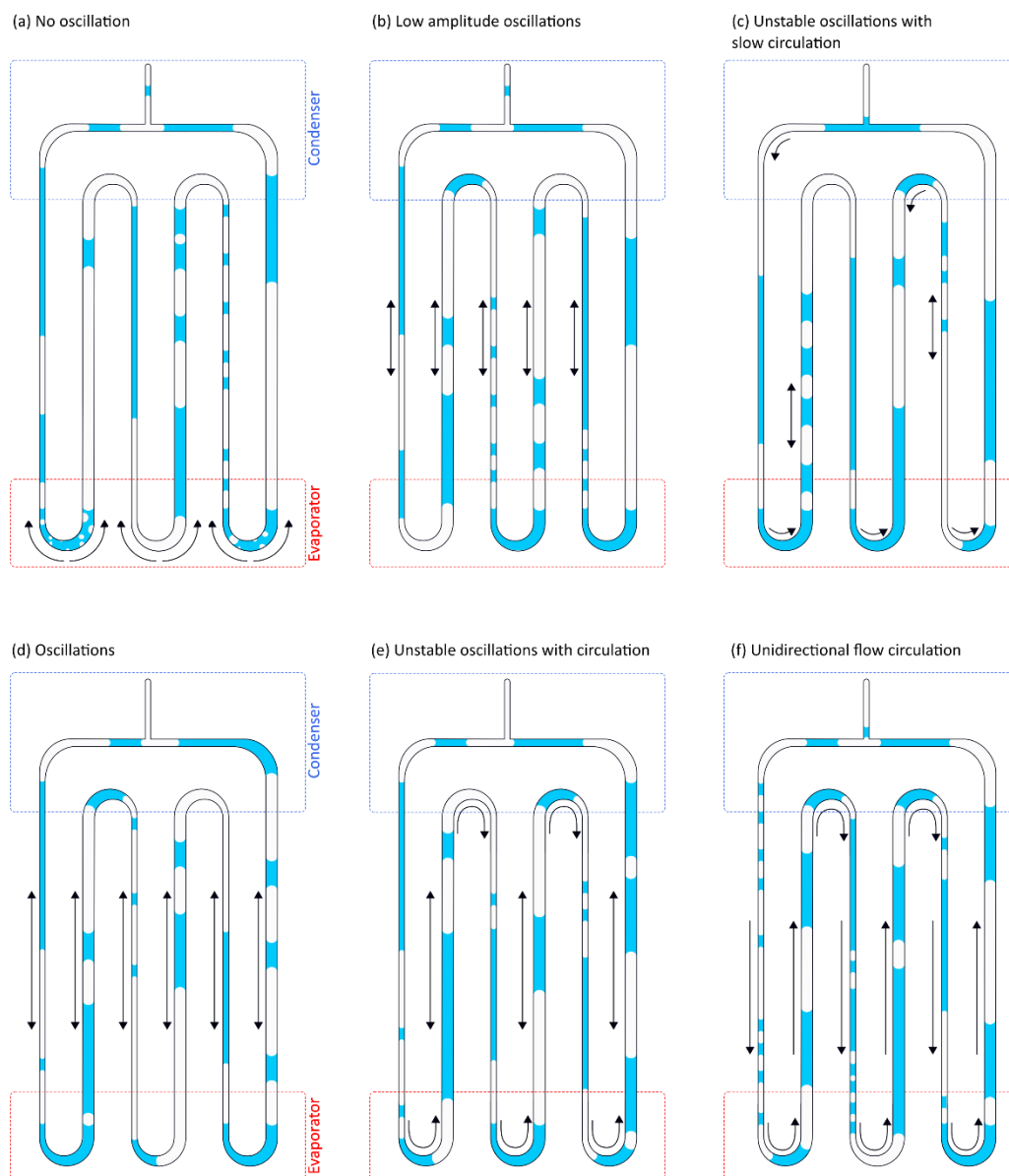


Figure 6.1. Illustration of the different flow patterns occurring in a μ OHP and OHP.

Khandhekar et al.[214], [300] highlighted the evidence of the non-linear complexity involved in the transport phenomena of a μ OHP. Multiple-quasi steady phase states can coexist for the same operating condition due to the high numbers of degrees of freedom in the system. Furthermore, flow perturbations, internal or external, can trigger the transition of the flow pattern between these states for the same set of operating parameters, leading to a change of thermal performance.

The flow pattern maps are shown in Figure 6.2, Figure 6.3 and Figure 6.4 and summarize the visual observations of the different operating conditions. The influences of the charging ratio, heating power and device's orientation on the two-phase flow are made visible by these flow pattern maps. These maps underline the stochastic non-linear behaviour of the flow. No transition boundaries could be comprehensively defined based on the tests. It is paramount to identify the operating condition range producing each flow patterns for efficient applications, as each flow pattern possesses its thermal performance. The thermal performance of unidirectional flow circulation is the highest among all the flow patterns, and therefore is the preferred operation mode for all OHP, μ OHP included [253], [301].

6.1.1 Acetone

The flow patterns observed for Acetone do not transition by a steady-state oscillating flow. Additionally, the heat load starting the operations increases with the increasing fluid charging ratio ϕ . In agreement with the literature results, the flow circulation was attained at higher heat loads. A flow transition trend was observed at all charging ratios: the flow transitioned from unstable oscillation with slow circulation to unstable oscillations with circulation and finally flow circulation.

However, some exceptions have been observed during the vertical tests ($\alpha = -90^\circ$) with charging ratios of $\phi = 50\%$ and $\phi = 30\%$. In the first case, the system transitioned from unstable oscillation with slow circulation to a circulating flow and then to dry-out before experiencing a unidirectional flow circulation again at higher power input. At the lowest charging ratios ($\phi = 30\%$), the system sustained unstable oscillations with slow circulation at low power inputs and stopped when the heat load was increased. On one occasion, a unidirectional flow circulation was observed with 4.5W of heat input before stopping and transitioning to unstable oscillations with circulation. The unstable oscillations stopped before transitioning to unidirectional flow circulation with the increased power inputs. Low amplitude oscillations were observed only during horizontal orientation ($\alpha = 0^\circ$) with a charging ratio of $\phi = 50\%$.

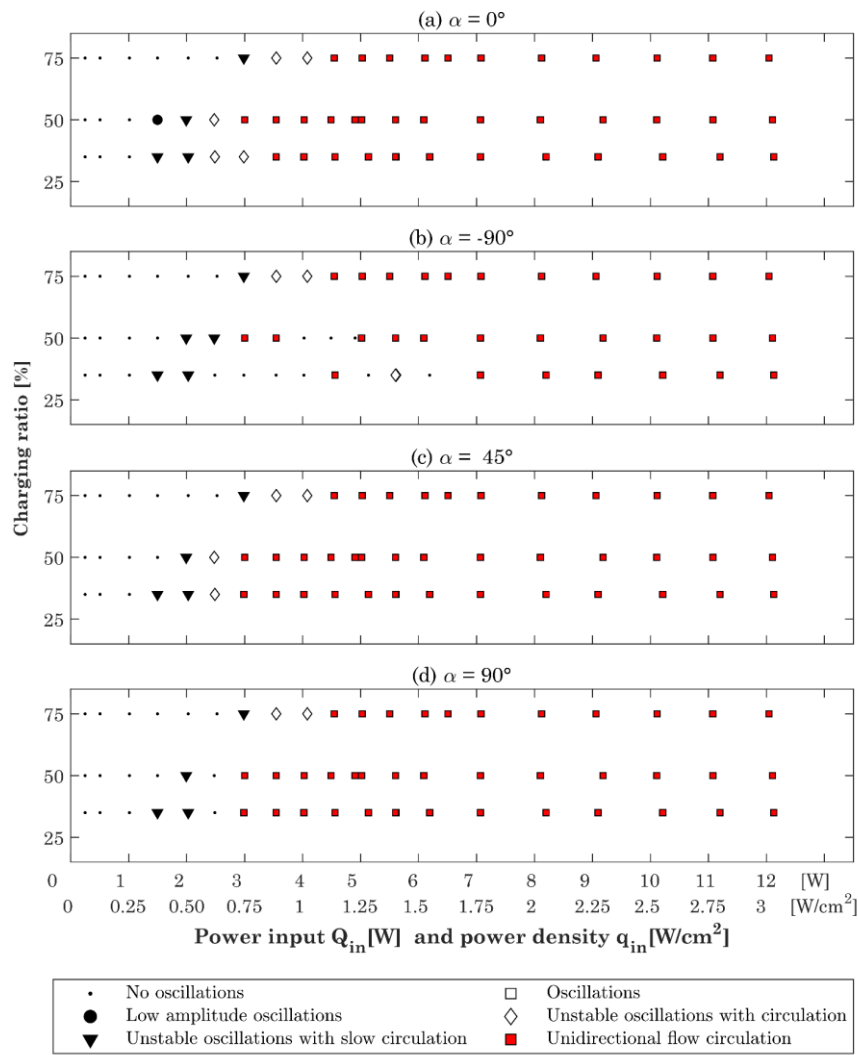


Figure 6.2. Flow pattern map of the μ OHP charged with Acetone and operating at (a) $\alpha = 0^\circ$, (b) $\alpha = -90^\circ$, (c) $\alpha = 45^\circ$ and (d) $\alpha = 90^\circ$.

6.1.2 Isopropyl Alcohol

Unidirectional flow circulation was reached at all orientation with a charging ratio of $\phi = 50\%$ but only at one specific power input. Low amplitude oscillations were present at low power inputs, shifting to unstable oscillation with low circulation and then oscillations before reaching circulating flow. The system turned back to unstable oscillations with circulation, followed by oscillations when the heat load was increased. With the least quantity of fluid, the flow was subject to low amplitude oscillations, oscillations and unstable oscillations with slow circulation, in increasing order of power inputs. The heat load required to generate oscillations was higher when the fluid charging ratio was $\phi = 75\%$ than for lower charging ratios. The observed flow patterns were similar at all orientations except for the operations conducted in top heating mode ($\alpha = 90^\circ$) with $\phi = 75\%$. In this specific case, the oscillatory motion stopped at a lower input than for other orientations. Unstable oscillations with slow circulation were always observed at high charging ratios of $\phi = 75\%$, except when inclined at $\alpha = -90^\circ$. In this case, the flow pattern changed from unstable oscillations with slow circulation to low amplitude oscillations before reaching a dry-out state.

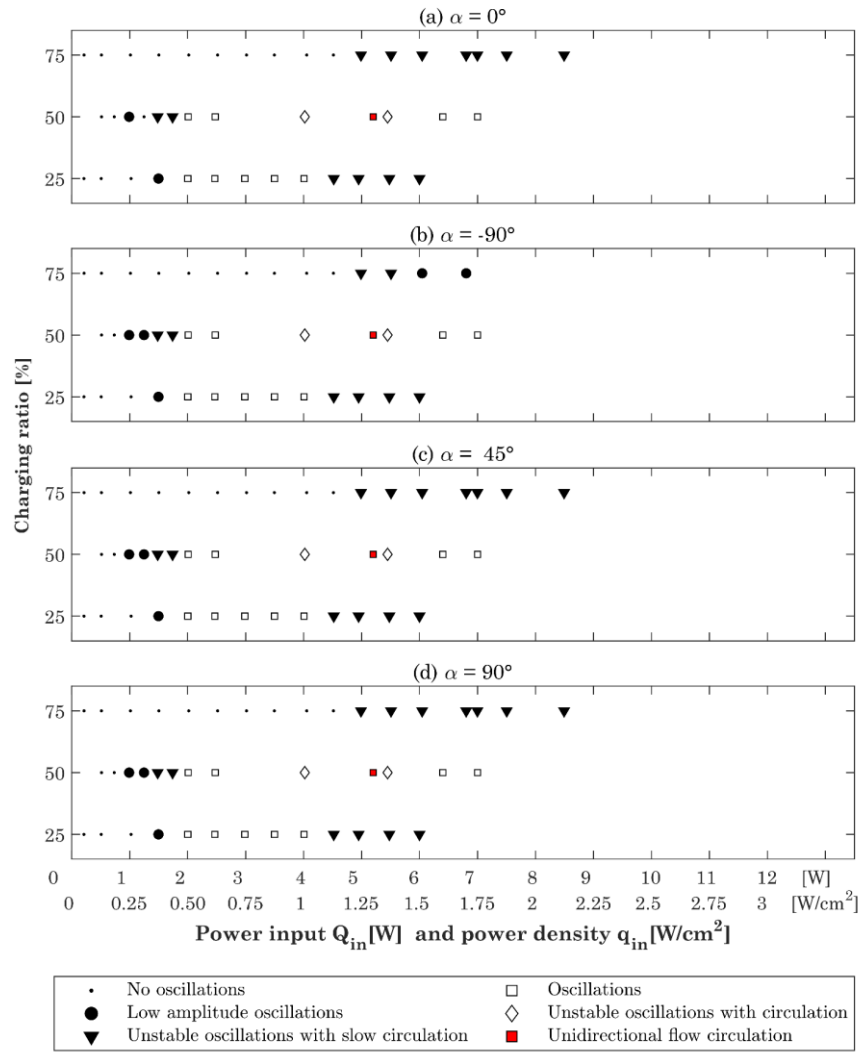


Figure 6.3. Flow pattern map of the μ OHP charged with IPA and operating at (a) $\alpha = 0^\circ$, (b) $\alpha = -90^\circ$, (c) $\alpha = 45^\circ$ and (d) $\alpha = 90^\circ$.

6.1.3 C₆F₁₄

In line with acetone, the unidirectional flow circulation was reached at higher heat loads. One exception to note with the evaporator up ($\alpha = -90^\circ$) and a charging ratio of $\phi = 50\%$, unidirectional flow circulation was observed at a particular power input while no circulation was observed around this specific power input. In this case, flow circulation was observed again at higher heat loads, appearing from no prior circulation. With a charging ratio of $\phi = 25\%$, unstable oscillations with low circulation, followed by low amplitude oscillations, were observed. Unidirectional flow circulation was also observed before the evaporator dried-out.

A flow transition trend is visible with the exception mentioned above: low amplitude and unstable oscillations with slow circulation were observed at low power input as the first oscillatory motions of the flow and were often alternating with the increased power input. The flow shifted from this point to either unidirectional flow circulation or unstable oscillations with circulation followed by circulation flow.

The tested orientations, exception for $\alpha = -90^\circ$, showed oscillatory flow patterns resulting from the expansion of the vapour bubbles following their nucleation, as well as the evaporation through the thin-film formed at the front of the meniscus.

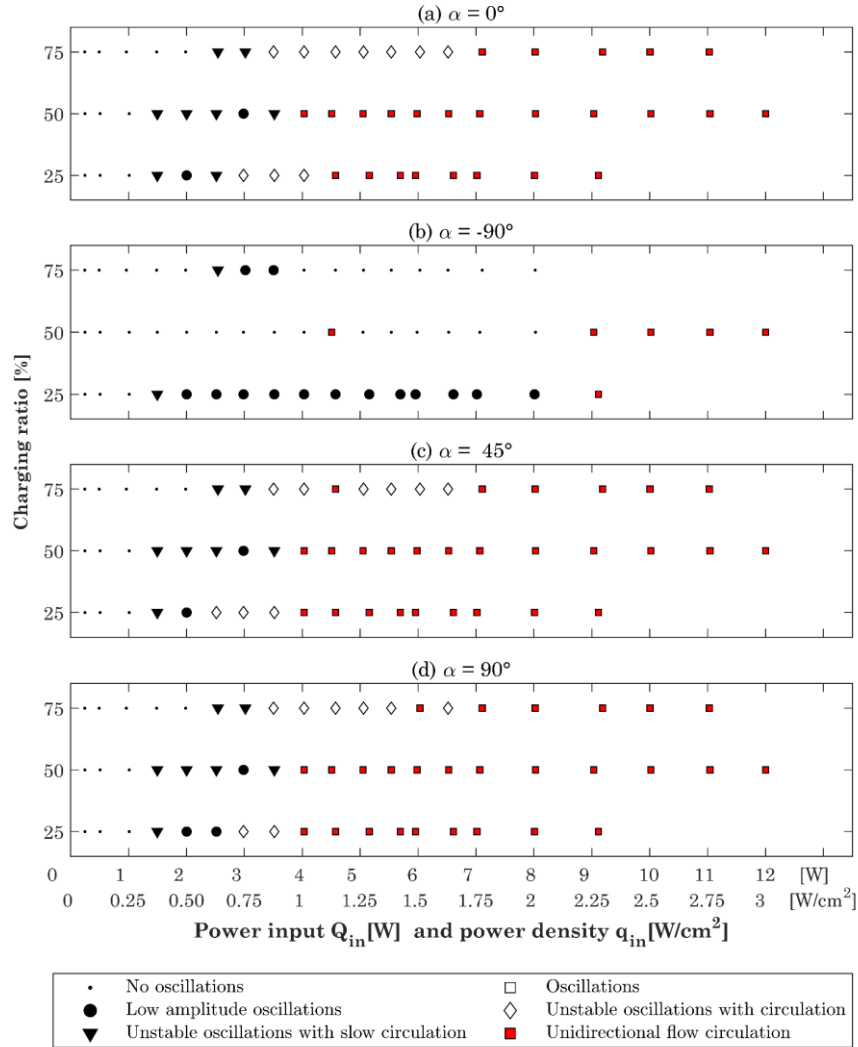


Figure 6.4. Flow pattern map of the μOHP charged with C_6F_{14} and operating at (a) $\alpha = 0^\circ$, (b) $\alpha = -90^\circ$, (c) $\alpha = 45^\circ$ and (d) $\alpha = 90^\circ$.

The μOHPs operated below the diameter limits based on the Bond number for all the three fluids used, as calculated in Table 3-2, but above the lower limit proposed by Qu et al. in equation (F.26) [217]. For flow speed of $U_l = 0.5 \text{ m/s}$, C_6F_{14} operates above the transitional limit based on the Garimella number (equation F.18, [284]), estimated for a two-phase flow, whereas IPA and acetone operated below this transitional limit. The time-strip analysis conducted on the horizontal μOHP at a heat load of 11W with C_6F_{14} ($\phi = 75\%$) and Acetone ($\phi = 50\%$), illustrated by two examples in Figure 6.5, shows that the speed of the liquid slugs, accelerated by the rapid expansions of the bubbles, extent faster than the speed used for $D_{\text{max}}^{\text{Ga}}$. During the sudden expansions illustrated in Figure 6.5, the flow reached 1.47m/s for C_6F_{14} , whereas it ranged from 1.6m/s to 3.6m/s for acetone. The resulting Weber number exceeded the unit, revealing that the fluid's inertial force exerted overcomes the surface tension. The inertia of the expanding bubbles broke the liquid slug meniscus, resulting in a churn, semi-annual or annular flow, corroborated by the

time-strip observations reported in Appendix G. The broken meniscus resulted in local mist flow, a type of flow with low heat transfer. Nevertheless, the resulting thermal performance remained high, as described in the next section.

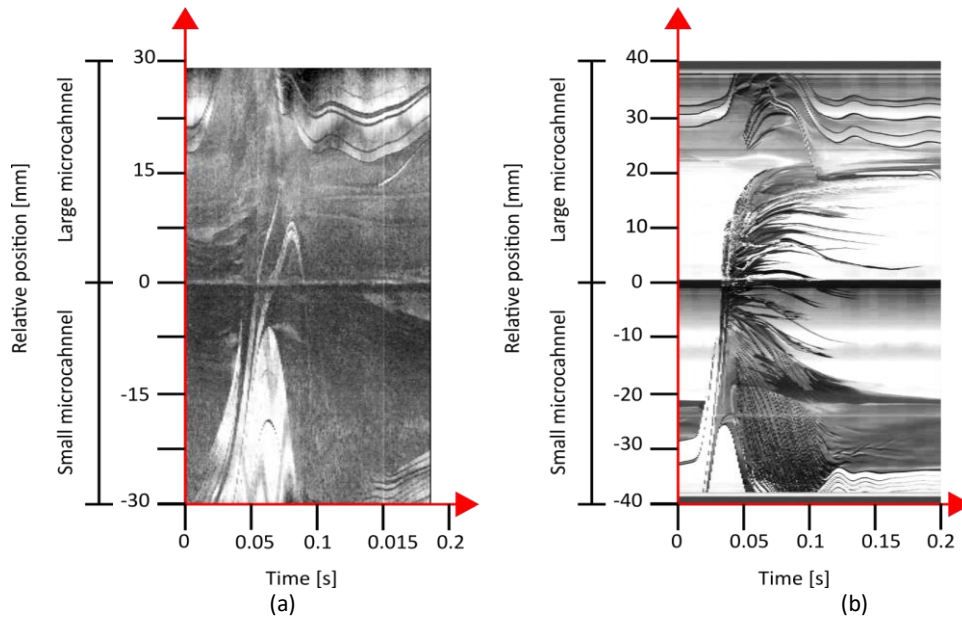


Figure 6.5. Time-strip obtained at 11W in horizontal position for (a) C_6F_{14} ($\phi = 75\%$, 10th U-turn) and (b) Acetone ($\phi = 50\%$, 3rd U-turn).

6.2 Thermal Performance

The apparent thermal conductivity k_{app} was chosen as the metric for evaluating of the thermal performance as a function of the inclination angle, fluid and charging ratio. As defined in (4.1), it is expressed by the following equation:

$$k_{app} = \frac{Q_{in}}{A_{cs}} \frac{L_{eff}}{\Delta T} \left[\frac{W}{m \cdot K} \right] \quad (4.1)$$

Where Q_{in} is the uncorrected input power, L_{eff} is the distance between the centres of the evaporator and the condenser of the μ OHP. Figure 6.6 illustrates the position of the temperature sensors for the calculation of temperature gradient ΔT between the evaporator and the condenser.

The temperature of the condenser was set to 20°C for all the test, unless specified otherwise. The heat load resulted in an increasing evaporator's temperature. The temperatures reached are illustrated in Figure 6.7 for one charged μ OHP, the same device but empty and a copper strip.

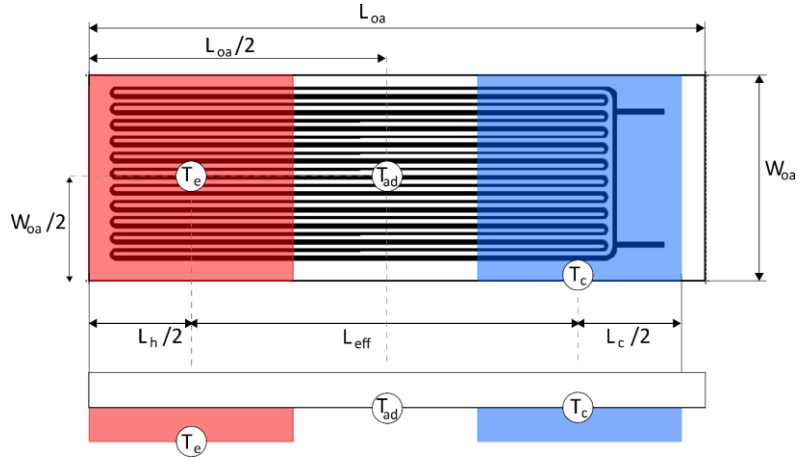
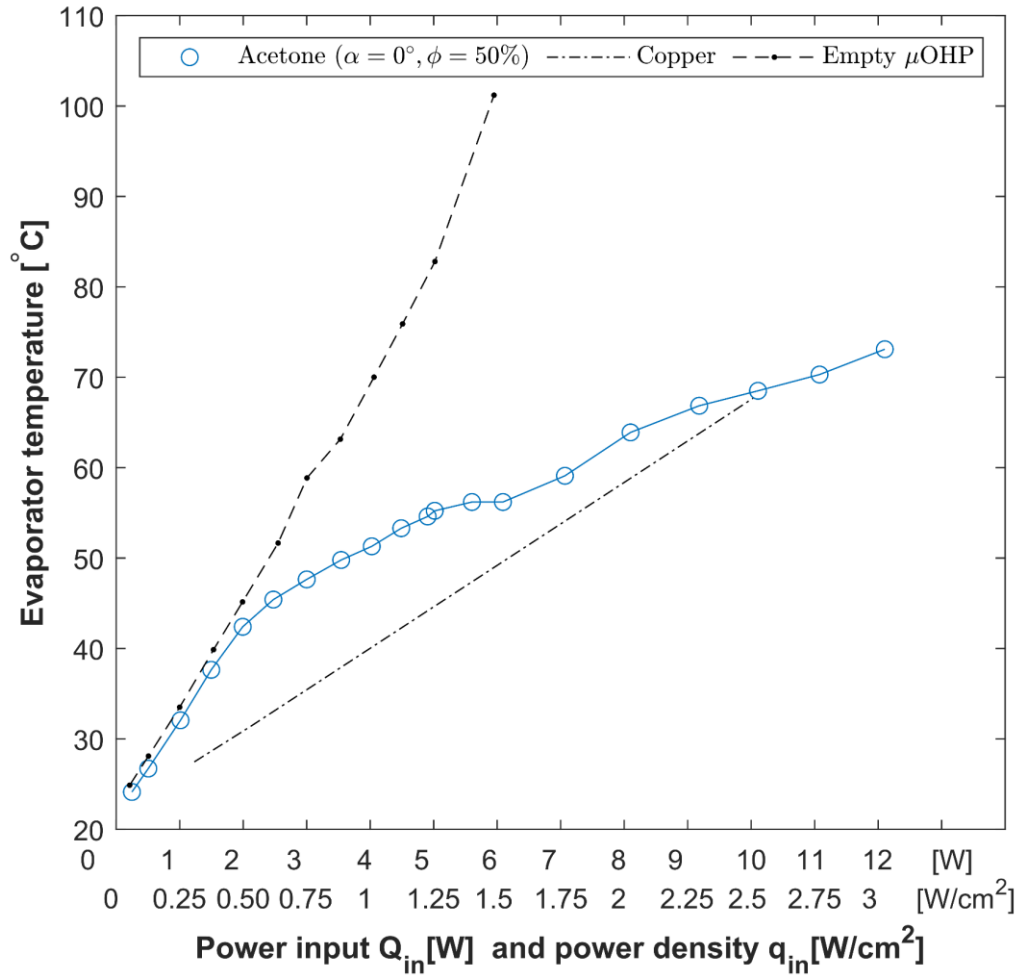


Figure 6.6. Schematic of the position of the temperature sensors used.

Figure 6.7. Evaporator's temperature T_e for acetone, an empty μ OHP and a copper thermal strap. The empty device and the copper display quasi-linear rising temperatures, while an inflection is visible for acetone.

High values for k_{app} , indicate better thermal performance of the μ OHP. The effects of the two-phase flow within the heat pipe are compared to the values obtained by pure conduction of an empty device and a copper thermal strap with the same dimensions.

The following general trends were observed:

- The apparent thermal conductivity increased with the increasing heat input, leading to unidirectional flow circulation.
- For a given heat input and orientation, the thermal performance decreases as the charging ratio increases.
- A lower charging ratio decreases the thermal performance at high heat loads as the segregation of the two phases eventually results in a local dry-out at the evaporator.
- Thermal performance measured in top heating mode ($\alpha = -90^\circ$) are generally lower than the thermal performance at other orientations for similar heat input and charging ratio.

6.2.1 Acetone

Figure 6.8 shows the apparent thermal conductivity as a function of the heat load, charging ratio and orientation for the acetone-charged μ OHP.

Positive orientations ($\alpha = 45^\circ, \alpha = 90^\circ$) are observed to have similar trends at all charging ratios. At the low charging ratio of $\phi = 30\%$, unstable oscillations with slow circulation appeared at 1.5W at both orientations. Increasing the power input to 3W, the thin-film evaporation and bubble nucleation produced an unidirectional flow circulation. Liquid slugs entered the evaporator, and bubble nucleation within the slug separated the slug into two or more slugs. In parallel, the evaporation increased the pressure gradient on both sides of the slugs, generating a directional circulation due to the different hydraulic diameters of the microchannels. The liquid slugs and vapour plugs in adjacent microchannels moved gradually in the condenser, pushing further the slugs and plugs from the condenser to the evaporator. With rewetted walls in the evaporator, the evaporation and bubble nucleation continued, and circulation was established, increasing the heat transfer.

At higher charging ratios, the thermal performance increased in a similar manner. However, the early onset of the oscillations was delayed, as shown in Figure 6.2, with later transitions into unidirectional circulation flow mode. The delay induced by the larger charging ratio corresponds to the delayed thermal performance improvements compared to the substrate alone, as visible in Figure 6.8.

Horizontally positioned μ OHP ($\alpha = 0^\circ$) leads to similar observations for the flow pattern and the thermal performance when positively oriented:

- Decreased charging ratios lead to earlier start-ups;
- Unidirectional flow circulation coincides with the improvement of thermal performance.

However, with only 30% of liquid acetone ($\alpha = 0^\circ$), the unidirectional flow yielded a slightly lower thermal performance than at positive orientations, particularly between 3.5W and 8W, as visible in Figure 6.8(c). The force that gravity exerts on the liquid slugs and liquid thin-film was

non-existent for this orientation, limiting the liquid supply to the evaporator as a result. Nevertheless, the evaporation is sufficient to provide the pressure gradient for the oscillations and circulation to take place.

In top heating mode ($\alpha = -90^\circ$), the tests conducted with the highest charging ratio ($\phi = 75\%$) show a negligible gravity influence. However, at lower charging ratios, gravity influences the thermal performance and flow patterns as it decreases the thermal performance. In both cases ($\phi = 30\%$, $\phi = 50\%$), the presence of oscillations or circulation does not coincide with increases of thermal performance until 7W. Above this threshold heat input, the apparent thermal conductivity reaches values obtained at the three other orientations. An inflexion in the apparent thermal conductivity curves is visible for $\phi = 30\%$ at 12W. This suggests an onset of the dry-out stage, which would be first experimented with the least quantity of liquid.

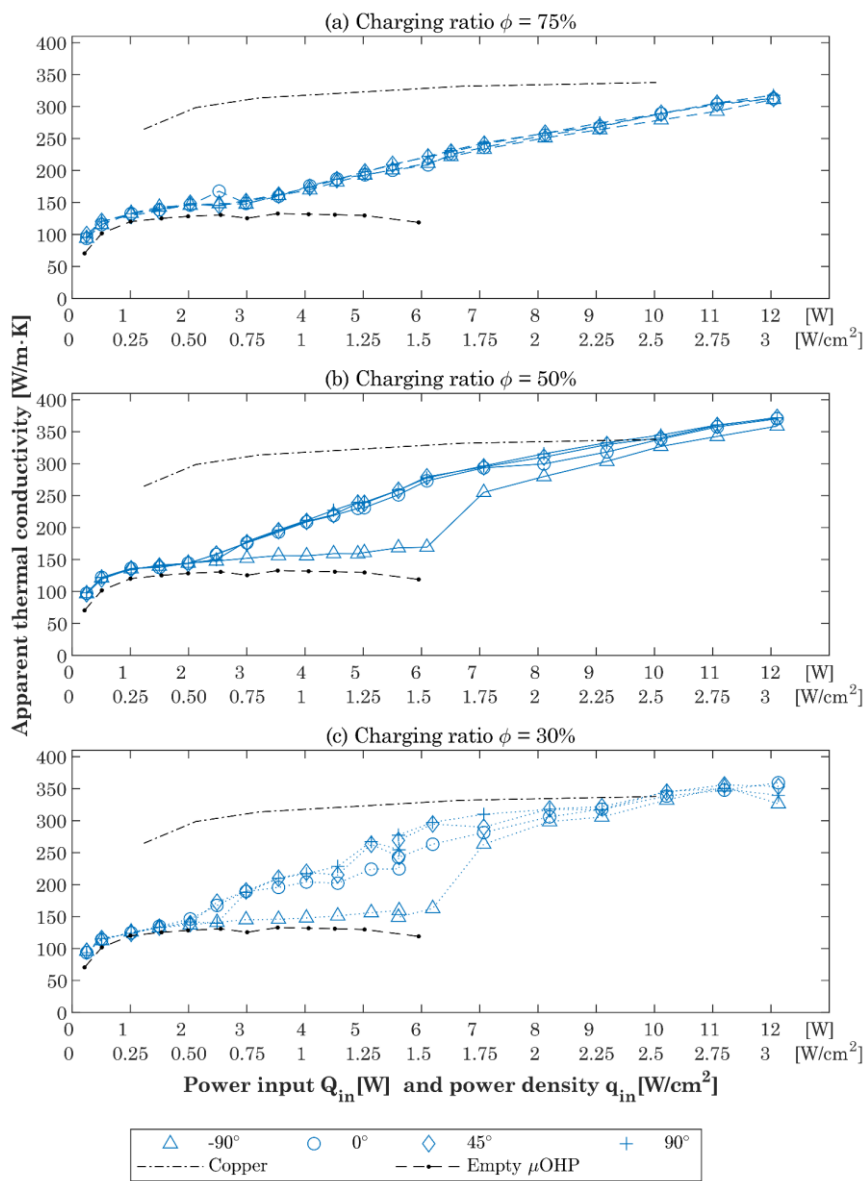


Figure 6.8. Apparent thermal conductivity as a function of the heat input of μ OHP charged with acetone for different orientations and charging ratios. Values for an empty μ OHP and a copper thermal strap with the same length and cross section are given for comparison.

6.2.2 Isopropyl Alcohol

Figure 6.9 shows the apparent thermal conductivity as a function of the heat load, fluid charging ratio and orientation for an IPA-charged μ OHP.

The effects of the orientation on the thermal performance were negligible for all power inputs and quantity of working fluid tested. Increases in thermal performance are negligible, compared to an empty μ OHP, when this last is charged with 25% of liquid IPA, despite the presence of oscillations and slow circulation. The test was stopped at 6W to preserve the integrity of the test setup. The tests conducted with a charging ratio of 75% lead to the same outcomes but at 8.5W. The only exception is observed at a charging ratio of $\phi = 50\%$. The apparent thermal conductivity increased between 4W and 5.5W with a maximum at 5W. This improvement in the thermal performance coincides with the acceleration of the flow since unstable oscillations with circulation and unidirectional flow circulation are observed in this range.

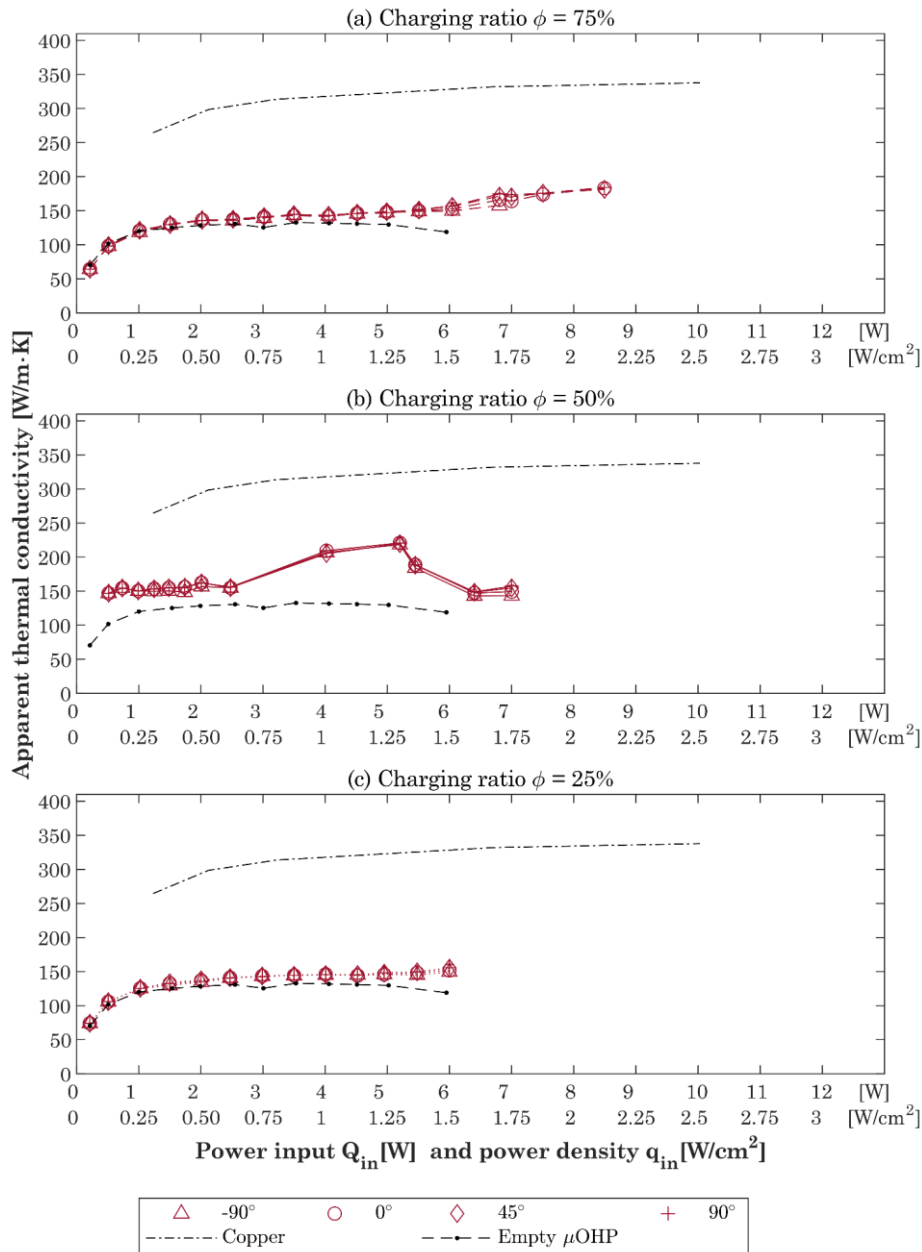


Figure 6.9. Apparent thermal conductivity as a function of the heat input of IPA-charged μ OHP for different orientations and charging ratios. Values for an empty μ OHP and a copper thermal strap with the same length and cross section are given for comparison.

6.2.3 C₆F₁₄

Figure 6.10 shows the apparent thermal conductivity as a function of the heat load, fluid charging ratio and orientation for a μ OHP charged with C₆F₁₄.

In bottom heating mode ($\alpha = 90^\circ$) and positive inclination at $\alpha = 45^\circ$, the role of gravity had a comparable impact on the thermal performance independently of the fluid quantity. Unstable oscillations with slow circulation appeared at 1.5W for $\phi = 25\%$ and $\phi = 50\%$. With the smallest fluid charging ratio ($\phi = 25\%$), the circulation accelerated at 3W to achieve unstable oscillations with flow circulation, which increased the thermal performance. At 4W, unidirectional flow was observed with liquid slug and plugs entering the evaporator and stopped at 9W as dry-out

occured above that heat load, as visible in the slope change in Figure 6.10(c). With $\phi = 50\%$, the flow transition in both cases from unstable oscillations to unidirectional flow circuit at 4W. The change of the flow and, consequently, the evaporator's wetting, resulted in an increasing apparent thermal conductivity. The first slow, unstable oscillations appeared at 2.5W with $\phi = 75\%$ for both $\alpha = 45^\circ$ and $\alpha = 90^\circ$. At both orientations, the working fluid flowed in a unidirectional way from 7W to 11W. Additionally, this flow was occasionally observed at 4.5W for $\alpha = 45^\circ$ and 6W for $\alpha = 90^\circ$.

In horizontal position ($\alpha = 0^\circ$), the flow patterns observed are comparable to those observed at positive orientations barring two exceptions. Firstly, unstable oscillations circulating in the microchannel did not develop into a unidirectional flow for $\phi = 75\%$. Secondly, unstable, circulating oscillations for $\phi = 25\%$ were present at 4W with a horizontal μ OHP. The ensuing thermal performance was on par with the one mentioned before, except for the test conducted with the lowest quantity of IPA in the microchannel ($\phi = 25\%$). For this specific case, apparent thermal conductivity only increased when the unidirectional flow circulation was observed.

For C_6F_{14} , top heating mode ($\alpha = -90^\circ$) perturbs the flow enough to see severe thermal performance degradation compared to other orientations. For $\phi = 25\%$, the oscillations begin at 1.5W, which is similar to the other orientations. From 2W to 8W, only low amplitude oscillations are observed. The liquid part of the fluid accumulates in the condenser's U-turns. A thin film of liquid is formed on the walls of the microchannels in the adiabatic part. The adiabatic temperature rises with the evaporator's one, generating vapour through the thin-films and the meniscus of the liquid slugs. The resulting pressure gradient is sufficient to generate low amplitude oscillations. Above 9W, pressure gradient generates a unidirectional flow circulation. However, the thermal performance gain remains minimal due to the low charging ratio insufficiently wetting the evaporator. Dry-out occurs at higher heat loads. When half-charged, only unidirectional flow circulation happens: specifically at 4.5W and within the 9W to 12W range. Thermal performance with this flow pattern reaches the values observed at other orientations whenever the flow circulates. The flow behaviour for $\phi = 75\%$, at $\alpha = -90^\circ$ is only active from 2.5W to 3.5W. However, the impact of the moving fluid on the apparent thermal conductivity is negligible. Above 3.5W, the evaporator only experiences dry-out, which does not yield any improvement of the thermal performance.

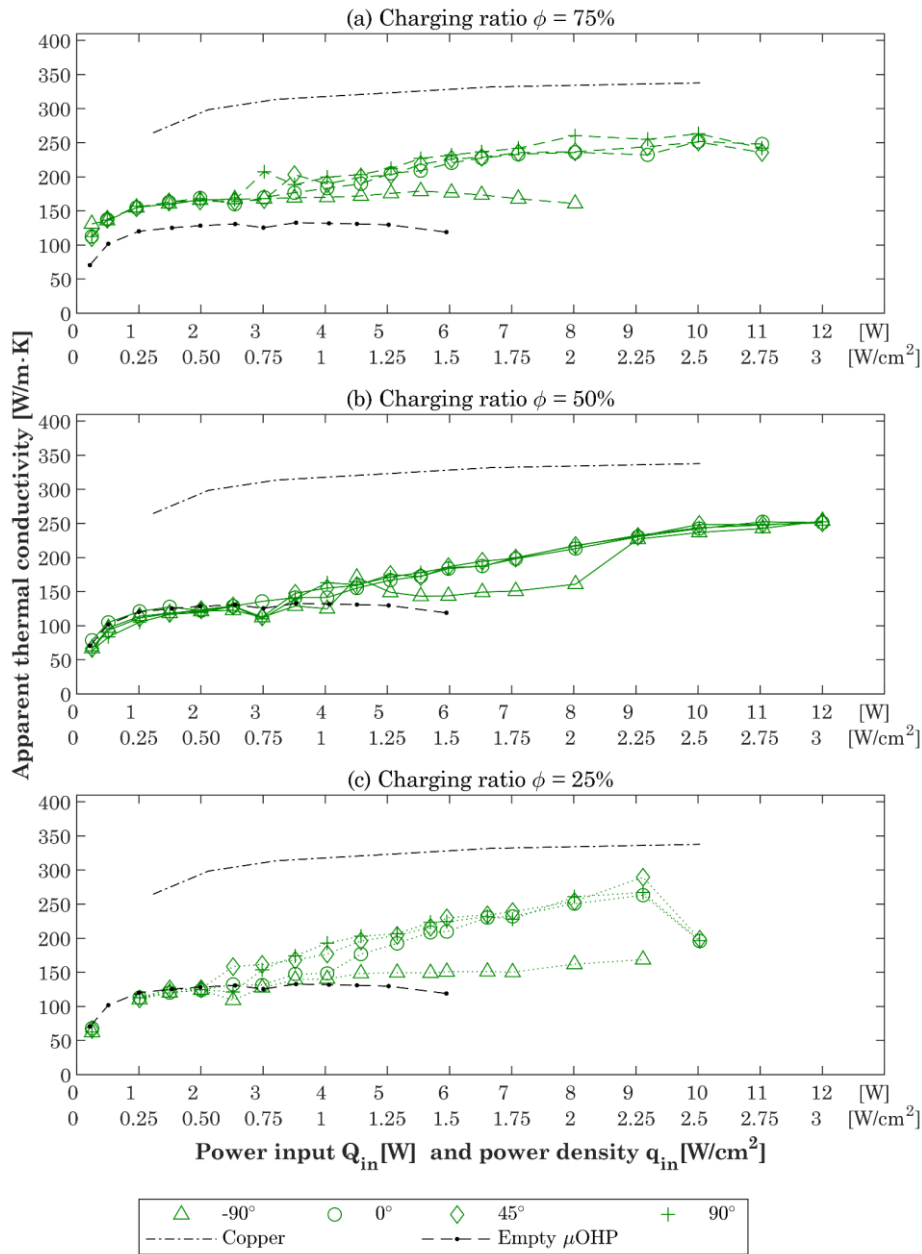


Figure 6.10. Apparent thermal conductivity as a function of the heat input of μ OHP charged with C_6F_{14} for different orientations and charging ratios. Values for an empty μ OHP and a copper thermal strap with the same length and cross section are given for comparison.

6.3 Discussion

Among the three tested fluids, acetone filled μ OHP performed the best, especially for high heat loads. The effect of the inclination angles on the performance of the system is noticeable for C_6F_{14} and acetone. Top heating mode ($\alpha = -90^\circ$) degrades the thermal performance unless specific conditions are met. Nevertheless, the bottom heating mode ($\alpha = 90^\circ$) shows low to no improvement of the thermal performance compared to the horizontal orientation. Considering the gravitational force's role on the liquid slugs and the thin-films, the gravity modifies the evaporator's wetting by changing the liquid's return in the region. Therefore, operating horizontally prevents it.

Additionally, the temperature of the condenser plays a role in the performance of the device. Investigations on the impact of its variation were conducted with acetone and C₆F₁₄. These additional measurements highlight the thermal performance dependencies on the saturation pressure gradient $(dP/dT)_{sat}$. The partial derivative is the driving force of the fluid motion and increases non-linearly. Therefore, increasing the temperature at the condenser shifts the equilibrium. This shift results in an increase in the temperature in the evaporator for the same heat load. Nevertheless, due to the non-linear behaviour of $(dP/dT)_{sat}$, the temperature gradient is reduced. The increase in thermal performance also depends on fluid charging ratio. Apparent thermal conductivity with increased condenser's temperature are visible in Table 6-1.

Table 6-1. Apparent thermal conductivity for different heat loads and condenser's temperatures for acetone and C₆F₁₄. ^(a)Linear interpolation of nearest neighbouring values.

Acetone	$Q_{in} = 4[W] \text{ (or } 1[W/cm^2])$ $T_c = 20[^\circ C]$					
	Charging ratio	$\phi = 30\%$	$\phi = 50\%$	$\phi = 75\%$	$T_c = 39.3[^\circ C]$	
	$K_{app} [W/m \cdot K]$	204	208.8	176.2	367.8	263.6
Acetone	$Q_{in} = 6.5[W] \text{ (or } 1.625[W/cm^2])$ $T_c = 20[^\circ C]$					
	Charging ratio	$\phi = 30\%$	$\phi = 50\%$	$\phi = 75\%$	$T_c = 36.8[^\circ C]$	
	$K_{app} [W/m \cdot K]$	269.5 ^(a)	281.6 ^(a)	225.2	379.8	293.7
Acetone	$Q_{in} = 8[W] \text{ (or } 2[W/cm^2])$ $T_c = 20[^\circ C]$					
	Charging ratio	$\phi = 30\%$	$\phi = 50\%$	$\phi = 75\%$	$T_c = 40[^\circ C]$	
	$K_{app} [W/m \cdot K]$	263.1	299.5	255.2	431.3	334.2
Acetone	$Q_{in} = 9[W] \text{ (or } 2.25[W/cm^2])$ $T_c = 20[^\circ C]$					
	Charging ratio	$\phi = 30\%$	$\phi = 50\%$	$\phi = 75\%$	$T_c = 42[^\circ C]$	
	$K_{app} [W/m \cdot K]$	317.9	318.1	268.4	453.4	370.6
C ₆ F ₁₄	$Q_{in} = 4[W] \text{ (or } 1[W/cm^2])$ $T_c = 20[^\circ C]$					
	Charging ratio	$\phi = 25\%$	$\phi = 50\%$	$\phi = 75\%$	$T_c = 39.3[^\circ C]$	
	$K_{app} [W/m \cdot K]$	148.4	141.3	183.3	253.3	199.7
C ₆ F ₁₄	$Q_{in} = 6.5[W] \text{ (or } 1.625[W/cm^2])$ $T_c = 20[^\circ C]$					
	Charging ratio	$\phi = 25\%$	$\phi = 50\%$	$\phi = 75\%$	$T_c = 36.8[^\circ C]$	
	$K_{app} [W/m \cdot K]$	230	187.6	227.5	293.7	263.8
C ₆ F ₁₄	$Q_{in} = 8[W] \text{ (or } 2[W/cm^2])$ $T_c = 20[^\circ C]$					
	Charging ratio	$\phi = 25\%$	$\phi = 50\%$	$\phi = 75\%$	$T_c = 40[^\circ C]$	
	$K_{app} [W/m \cdot K]$	250.8	213.1	235.9	341.2	290.4
C ₆ F ₁₄	$Q_{in} = 9[W] \text{ (or } 2.25[W/cm^2])$ $T_c = 20[^\circ C]$					
	Charging ratio	$\phi = 25\%$	$\phi = 50\%$	$\phi = 75\%$	$T_c = 42[^\circ C]$	
	$K_{app} [W/m \cdot K]$	236	230.4	232.3	355.6	298.7

With a μ OHP charged with acetone, the increase in thermal performance depends on the working fluid quantity present. For a temperature of 20°C at the condenser (T_c), both quantities of fluid $\phi = 30\%$ and $\phi = 50\%$ result in similar apparent thermal conductivity. The increases are significantly higher for $\phi = 50\%$: an increase of 20°C ($T_c = 40^\circ\text{C}$) at 8W, leads to an increase in thermal conductivity of 66.3%. In comparison, the increases are 40.9% and 30.9% for $\phi = 30\%$ and $\phi = 75\%$, respectively. The maximum apparent thermal conductivity reached was 545W/m·K at 9W.

The dual-diameter design stimulates the circulation of the two-phase flow in one direction, as illustrated by the observed flow patterns. The figure of merit M_{PHP} for the tested fluids and geometry is visible in Figure 6.11. The value of the figure of merit M_{PHP} should exceed the threshold of $2 \cdot 10^5$ fixed to guarantee operations independent of the device's orientation [226]. The Figure of Merit values for acetone remain above the threshold for a charging ratio ranging from 10% to 60%. However, the observed flow patterns and apparent thermal conductivity obtained at $\phi = 75\%$ contradict the threshold's value to operate independently of the orientation. Furthermore, the two other charging ratios, which result in values of M_{PHP} above the threshold, only operate independently of the orientation above 6W. In the case of C_6F_{14} , orientation-independence operations were observed only above 8W for $\phi = 50\%$. In other cases, while no significant variation in apparent thermal conductivity from horizontal position to bottom heating mode was observed at other charging ratios, top heating mode led to reduced thermal performance. On the other hand, isopropyl alcohol possesses low values of M_{PHP} but displays an orientation-independent performance.

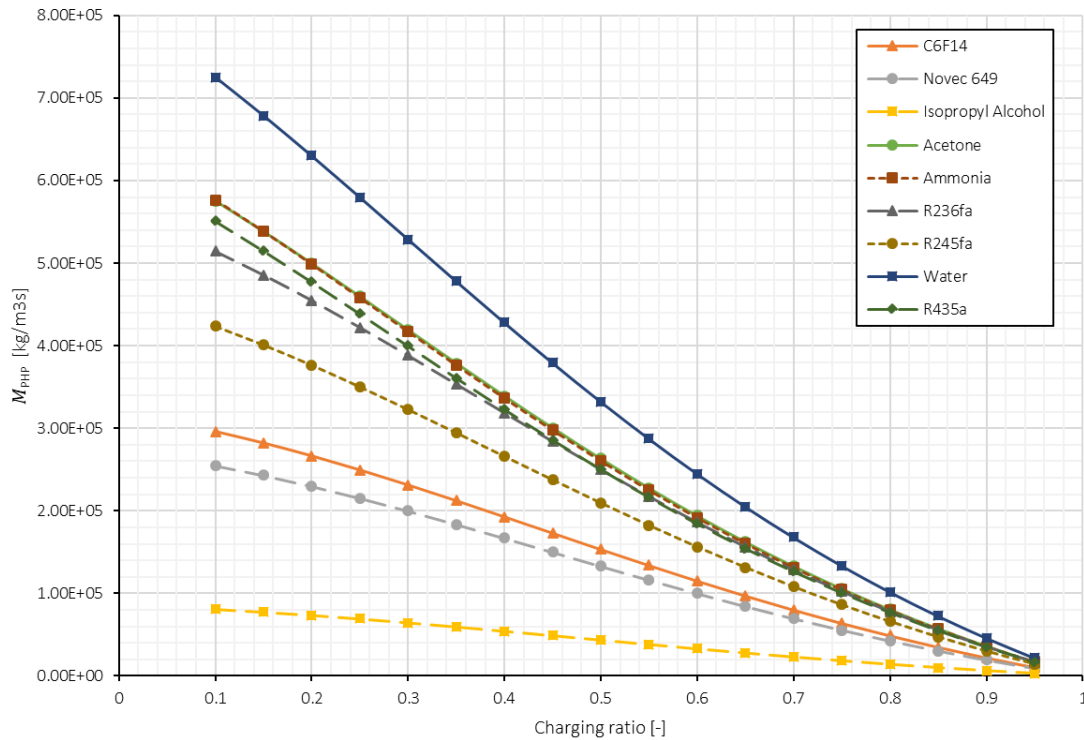


Figure 6.11. Effects of the charging ratio on the figure of merit M_{PHP} for several working fluids with the following parameters for the microchannel: $w_1 = 400\mu\text{m}$, $w_2 = 255\mu\text{m}$ and $h = 400\mu\text{m}$; with a total of eleven dual-diameter pairs and no symmetric microchannel pairs ($N_t = N = 11$).

Nevertheless, the resulting thermal performance is low. However, the values obtained for each fluid match qualitatively the respective thermal performance. Acetone, which possesses the highest values compared to C_6F_{14} and IPA, also shows the highest apparent thermal conductivity values. Follows, in the order, C_6F_{14} and IPA. Therefore, the Figure of Merit M_{PHP} can be used to analyse the potential working fluids qualitatively.

Figure 6.12, Figure 6.13 and Figure 6.14 represent the ranges where the μ OHPs offer an advantageous thermal conductivity over for the three fluids, respectively IPA, C_6F_{14} and acetone. It highlights the conditions increasing the apparent thermal conductivity compared to the empty device.

The start-up heat fluxes estimated in Table 6-2, based on models of Qu and Ma [302], when compared to the observed values, shows large discrepancies that can be attributed to the lack of nucleation sites present in silicon microchannels. The smoothing step included in the processing of the test devices, reduced the surface roughness of the etched microchannels [303]. Avoiding this step and reducing the optimisation of the DRIE process for smooth walls would increase the nucleation sites on the walls. Hence, it might reduce the required start-up heat load. The high wettability on silicon substrate by the working fluids and microchannels' small dimensions reduces the bubble generation phenomena, leading to high wall superheat for the boiling process to occur. Thus, larger heat fluxes than estimated were observed.

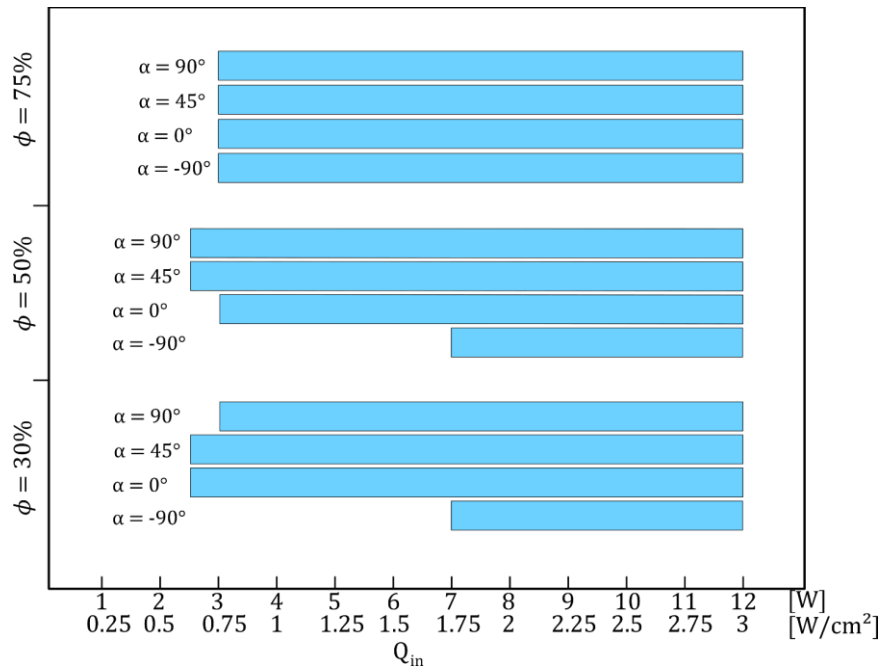


Figure 6.12. Operational map for Acetone in all tested conditions.

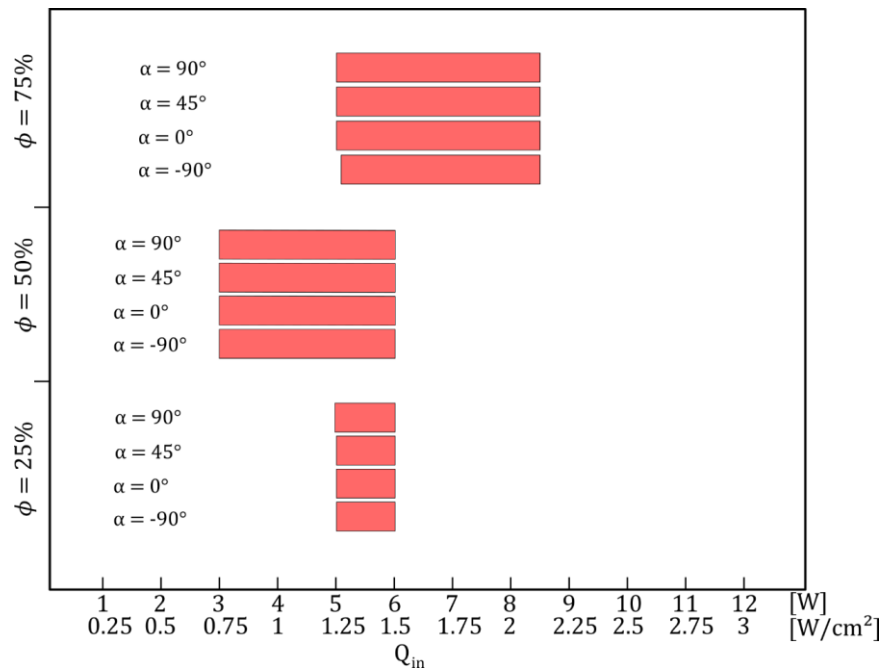
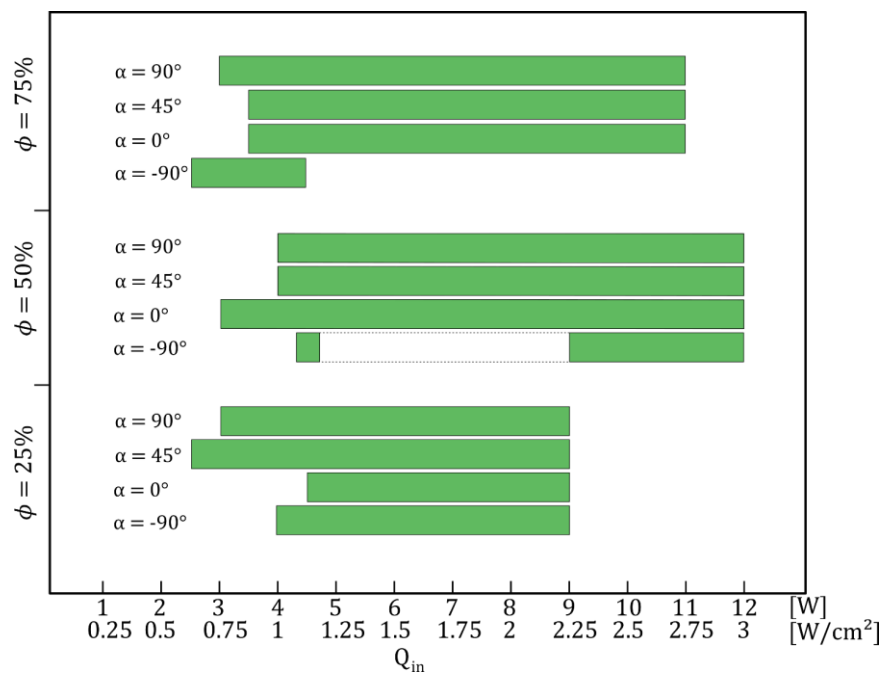


Figure 6.13. Operational map for IPA in all tested conditions.

Figure 6.14. Operational map for C_6F_{14} in all tested conditions.

The maximal heat fluxes estimated with the relation established by Lee and Kim [304] were also underestimated. While dry-outs occurred for both C_6F_{14} and IPA, they occurred above $2W/cm^2$ and $1W/cm^2$, respectively. Higher values could result from the flow propensity, dictated by de-

sign, to follow unidirectional circulation. Thus, limiting the oscillations, which locally thin the trailing liquid film when changing the direction. Appendix F details both approaches to estimate the minimal and maximal heat fluxes.

Table 6-2. Calculated value for the heat flux for start-up and dry-out for the selected working fluids.

Liquid	$q''_{min} [W/cm^2]$ [302]	$q''_{max} [W/cm^2]$ [304]
C ₆ F ₁₄	0.0545	0.747
Isopropyl alcohol	0.0205	0.434
Acetone	0.0442	2.25

Other fluids, operating at lower temperatures as R236fa, ammonia or CO₂, could replace the tested working fluids. While the first one represents an alternative easy to implement, ammonia and CO₂ possess the advantages of the pressure gradient and lower operating temperatures. Nevertheless, both come with disadvantages of the higher pressure at room temperature. Furthermore, ammonia is a liquid that requires additional precautions as it can pose safety and health concerns. Furthermore, C₆F₁₄ possesses a high global warming potential, as most fluorocarbon refrigerants, and alternatives should be favoured. Nevertheless, knowledge on the radiation hardness and the by-products creation remains scarce, and additionally research on this topic would be needed.

Mass is a crucial element for the envisioned applications. At the exception of acetone above 10W for $\phi = 30\%$ and 50%, μ OHP displays a lower apparent thermal conductivity than the copper strip for a condenser temperature of 20°C over the whole heat load range, as illustrated in Figure 6.8, Figure 6.9 and Figure 6.10. Nevertheless, the copper thermal strap's mass is 11.3g, compared to the 3.1g of the μ OHP charged with fluids. The ratio of the apparent thermal conductivity highlights the potential of the μ OHP as a low mass and highly thermally conductive solution. When operating with acetone ($\phi = 50\%$) at 4W, μ OHP reaches a ratio value of 68.7W/m·K·g, compared to 29.9W/m·K·g for the copper strip. The advantage of the μ OHP over copper thermal strap is even more marked at 10W. At this heat load, the ratio is 108.7 for the acetone-filled μ OHP. Furthermore, the material budget for both thermally conductive solutions points toward the use of μ OHP. The material lengths X_0 are 1.4 and 9.37 for pure copper and silicon, respectively. Hence, μ OHP would interact less with the incident particle while transporting the energy.

To put this work in perspective with the existing devices, the obtained results were compared to representative example issued from Table 2-6. Kwon and Kim [226] designed several μ OHPs with different pairs of widths, noticeably two devices: one with a 1300 μ m-700 μ m wide microchannels pair and one with a 1500 μ m-500 μ m wide microchannels pair. They tested their devices with C₆F₁₄ from $\alpha = 0^\circ$ to $\alpha = 90^\circ$. They observed apparent thermal conductivities of 225 W/m·K and 300 W/m·K at 5W (2.7W/cm²) respectively for the mentioned devices when considering glass in the calculation and at all the tested orientation. At 10W (5.4 W/cm²), the devices displayed thermal conductivities of 400W/m·K and 300W/m·K, respectively. The μ OHPs they tested had larger hydraulic diameters than the one designed in this thesis. Nevertheless, the tested devices showed comparable thermal performance despite the increased pressure drop for similar power

densities. The thermal performance reached with acetone in the presented tests were slightly over Kwon and Kim's results at $2.7\text{W}/\text{cm}^2$.

Jang et al. [235] proposed several devices with single and dual-diameter design. They compared their optimal devices, with alternating diameters of 1.55mm and 3.25mm for $300\mu\text{m}$ of depth, to a supported graphite sheet. Once charged with C_6F_{14} , the device displayed higher thermal conductivity than the graphite strip for the three orientation tested, equivalent to the angles $\alpha = -90^\circ$, 0° and 90° used in this work. The gravity negatively impacted the operation in top heating mode ($\alpha = -90^\circ$); it decreased the performance by a factor higher than 2, unlike the device tested here under specific conditions.

Compared to the tested device, the work of Jang et al. resulted in thermal performance comparable with the one from acetone in this work. But the start-up heat load density was as low as $0.22\text{W}/\text{cm}^2$ compared to the minimum of $0.5\text{W}/\text{cm}^2$ required by the μOHP presented here.

In comparison with the single-diameter μOHPs presented by Liu et al. ($878\mu\text{m}$ by $400\mu\text{m}$) [230] and Lee and Kim ($D_h = 390\mu\text{m}$) [304], the dual-diameter μOHP experienced start-up at lower power densities than their single-diameter counterparts, all charged with C_6F_{14} . Liu et al.'s device started oscillating at $1.7\text{W}/\text{cm}^2$; Lee and Kim's one started at $1\text{W}/\text{cm}^2$.

Additionally, at equivalent hydraulic diameter, the dual-diameter μOHP experienced dry-out at higher heat loads than the μOHP with a single hydraulic diameter, $2\text{W}/\text{cm}^2$ for the μOHP presented by Lee and Kim. Jang et al. [235] and Kwon and Kim [226] experienced dry out at higher heat loads with C_6F_{14} than the present work due to the larger hydraulic diameters.

A larger hydraulic diameter usually leads to delayed start-up but higher operating limit and orientation dependency. Nevertheless, the work of Jang et al. [235] presented start-up at lower heat flux than the μOHP tested in this thesis despite the larger channels. Two possible explanations: the walls' surface was smoothed, which could lead to delayed start-up due to the lack of nucleation sites and reduced heat transfer [302], [303], [305], [306]; and the possibility to have remaining gases trapped in the fluid despite the outgassing step, as they would increase the system's total pressure [307]. As hinted before, one solution to the walls' smoothness is to modify the microfabrication process. Using a more efficient outgassing process for the fluid could further remove the NCG from the fluid.

6.4 Conclusion

A novel investigation was carried on dual-diameter μOHP charged with acetone, C_6F_{14} and isopropyl alcohol at three different charging ratios. The orientation was varied from top heating mode to bottom heating mode. The thermal performance was assessed and the flow patterns identified for each test case. The theoretical limits of the hydraulic diameters and heat fluxes were discussed, concluding that the limits should be used for designing, but experimental testing is required to define the correct operational conditions of the μOHPs .

The designed device operated with similar thermal performance as reported studies: better considering the operation independence, but worse considering the start-up heat flux required. Leads to improve this last point were proposed.

Chapter 7 Lightweight Sealing Solution for Leak-tight Charging Port

This chapter describes the new packaging solution developed for micro heat pipes. The method relies on Indium's capacity to cold weld to metalized surfaces. A small volume of this metal is compressed in the inlet to seal it and glue mechanically reinforces the formed seal.

As discussed in Chapter 6, the charging ratio has a major impact on the operation of the μ OHP. Hence, ensuring a correct sealing of the inlet port after the charging step is paramount to guarantee a sustained performance throughout the entire service life of the device. Furthermore, the seal also has to prevent external gasses from entering the device and interacting with the working fluid. Such gasses, which are often non-condensable, can perturb the operation of the heat pipe [308], [309].

Various solutions reported in the literature to achieve the sealing of the charging power are reviewed in Appendix H. Dhillon and Pisano [193], [310], as well as Li et al. [311], [312], developed an intricate fill-hole system based on melting metal alloys. Their solutions involve induction heating with a molten alloy that is hard to control or a complex structure to flow an important volume of metallic alloy. Both approaches are not satisfying for the HEP and space applications targeted by this work: either the proposed solutions rely on large quantities of metallic material with visible leak paths or embedded magnetic heating elements. Therefore, a new packaging solution is proposed to seal the micro heat pipes.

7.1 Working Principle of the Proposed Sealing Method

The method explored in this work uses Indium as sealing material. Indium is employed in cryogenic applications to create leak-tight seals [313], [314]. It is also used in the manufacturing and assembly of MEMS and electronics [315], [316]. Its low processing temperature and malleability reduce the stress caused by CTE mismatch with the substrates, as it would accommodate large plastic strains. Additionally, Indium possesses good wettability and adhesion to many surfaces. It can be used as solder or thermocompressed intermediate layers or bumps to provide an electro-mechanical connection, but Indium would continuously flow under constant stress. Besides, its high thermal conductivity makes it an attractive material for thermal interface [317].

Indium possesses the unique ability to cold weld at room temperature. However, pressure needs to be applied to the Indium preform for it to deform and seal the charging point. A simple procedure was developed to obtain a leak-tight seal. An Indium preform is compressed in the charging port after a liquid has been added to a cavity. Figure 7.1 illustrates the procedure. A clamping system compresses a flat gasket, which would provide a leak-tight connection between the chip and the tube's tip. Once the connection established and the needle tip introduced in the orifice,

the liquid is injected, and the tube's tip is lowered to deform the Indium located at the bottom of the inlet. Once the charging tube and clamping system removed, the glue can be added to reinforce mechanically the Indium at the charging port. The adhesive would prevent the Indium to continuously flow and, ultimately break the leak-tightness.

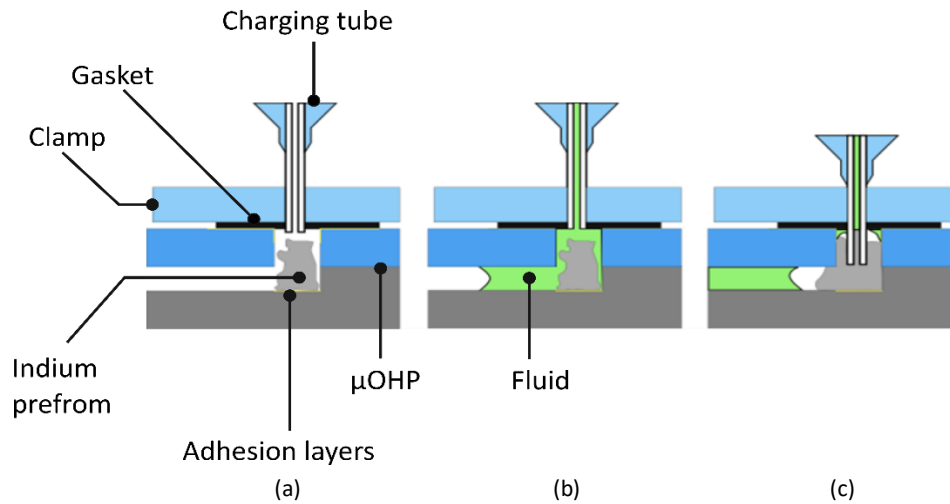


Figure 7.1. Schematic view of the procedure used for the initial Indium cold welding. (a) Tube's tip inserted through the flat gasket. (b) Fluid injection. (c) Indium deformation.

7.2 Sealing Setup

A dedicated sealing apparatus has been developed to implement the proposed solution for the charging and subsequent sealing of the inlet port. This setup delivers the working fluid after purging the μ OHP and the other charging lines. It also controls the relative position of the tube used to deliver the working fluid in the microchannels and then to compress the Indium preform.

Figure 7.2 displays the setup and Figure 7.3 illustrates the design apparatus and specifies the labels associated with each part in its description.

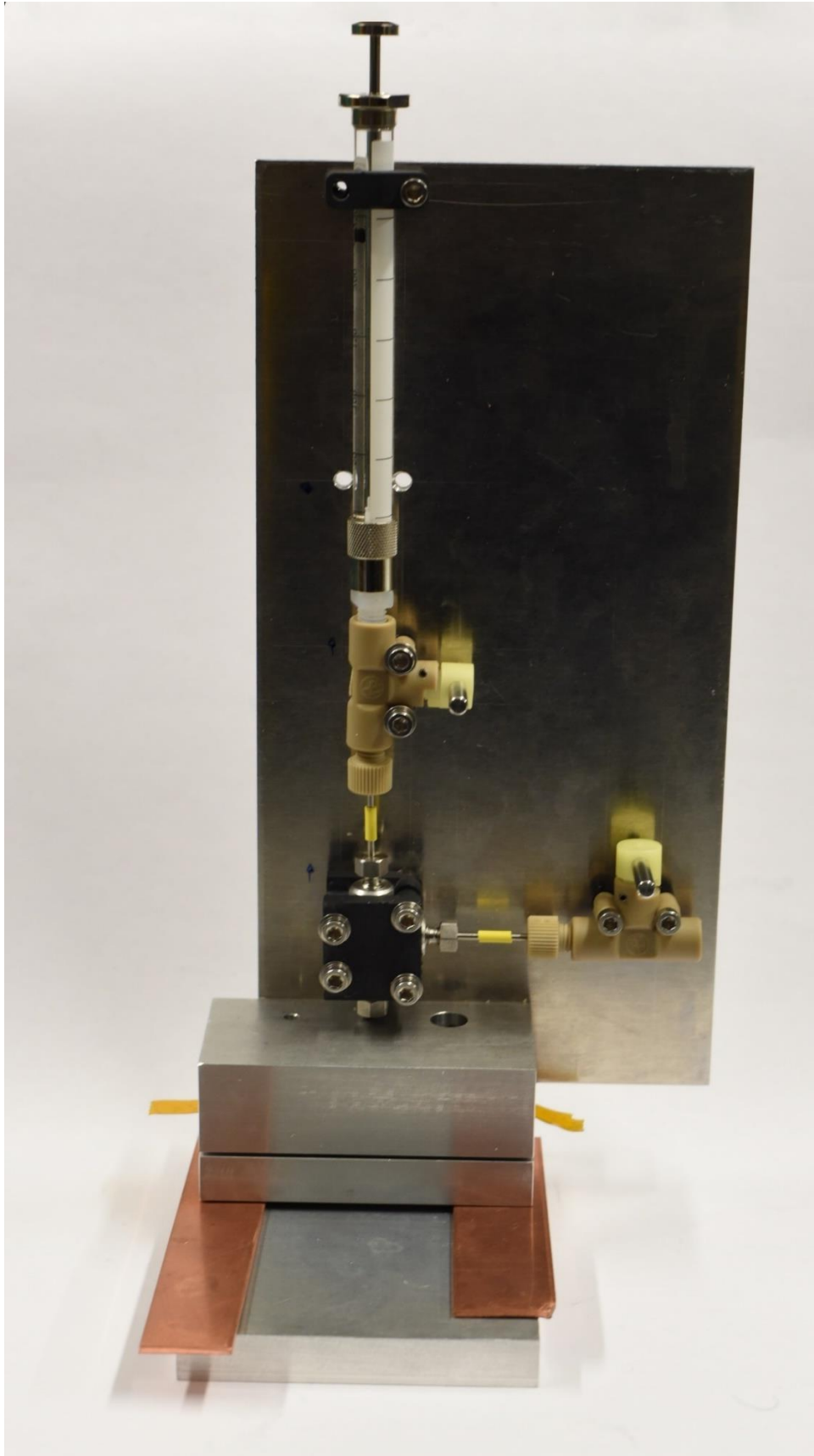


Figure 7.2. Charging and sealing system with the shims placed between the different blocks. Here without silicon micro heat pipe.

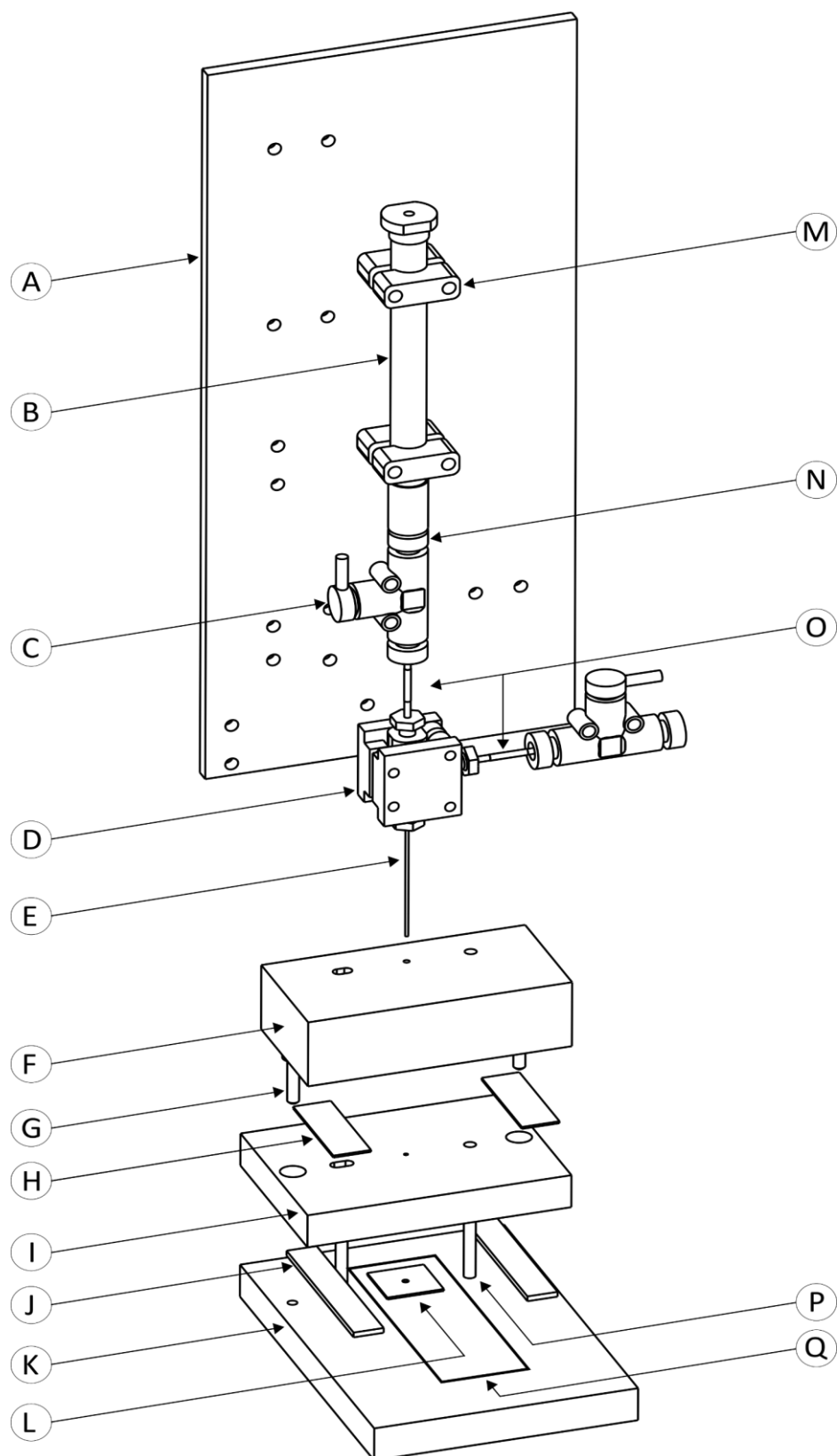


Figure 7.3. Exploded CAD view of the charging and sealing apparatus used to seal inlets by Indium cold welding. (A) Support back plate. (B) Gas chromatography syringe. (C) Manual shut-off valve. (D) High pressure low dead volume T connector and supports. (E) Stainless steel tube 1/32"OD – 100µm ID. (F) Syringe alignment support. (G) M3 screws (ISO4762). (H) Spacer – Tip travel. (I) Gasket clamp with syringe pass-through. (J) Spacer – Gasket clamp. (K) Base plate. (L) Flat gasket. (M) Syringe supports. (N) Syringe-to-valve adapter. (O) Stainless steel tube 1/16inOD – 500µm ID. (P) 3mm pins. (Q) Silicon device.

The charging and sealing procedure follows the steps:

1. Indium is preformed through a reflow step. At first, a thin wire is inserted in the charging port and enters the microchannel. Indium is then pressed in the inlet port around the wire using a pair of dedicated syringe needles with a diameter of 300 μm . Once the Indium was compressed around the wire, at the same level as the top of the port, it was set in an oven to reflow it.
2. Optical alignment of the gasket **L** and the clamping blocks **F** and **I** is performed through the syringe needle's pass-through to ensure that the needle will enter the charging port.
3. Clamping of the gasket and silicon chip is done using two M3 screws **G**. The clamp **I** is progressively compressing the gasket **L** on the chip **Q**.
4. The working fluid is outgassed. The syringe **B** is connected to the valve **C**, but not connected to the rest of the system, is progressively charged up to the required quantity. Possible bubbles are evacuated through the valve before closing it. The syringe **B** and valve **C** are then connected to the rest of the system.
5. The tube **E** is inserted in the gasket **L**, passing through **F** and **I**. The shims **H** are placed between **F** and **I**, while the rest of the system, attached to the back plate **A** is progressively lowered to insert the tube **E**.
6. The vacuum is pumped in the system to evacuate all NCGs of the microchannels and tubing.
7. Closing of the vacuum line using the valve **C** not directly connected to the syringe.
8. The charging of the fluid is done by opening the valve **C** connected to the syringe and injection of the working fluid in the device **Q**.
9. Indium is compressed by removing the spacer **H**. The clamping block **F**, and all the system it is supporting, slide down under their own weight until the block **H** and **I** are in contact.
10. The system is removed, including the clamping block **I** and the gasket **L**, is removed.
11. The deformed Indium preform is reinforced with an adhesive to prevent Indium from continuously flowing under the stress from the pressure gradient between the inside and outside of the sealed cavity.

More details about specific parts are given in the following subsections.

7.2.1 Indium Pre-shaping

Indium needs to be pre-shaped in the inlet to ensure that the correct quantity of material is present. A low amount of Indium results in a partially unobstructed inlet which leads to a leaking charging point. On the other hand, if the volume of Indium placed at the inlet is too high, the channel is sealed during the gasket's compression or the insertion of the tube through the gasket before charging fluids. Therefore, the amount of Indium needs to be controlled to avoid any failure during its compression.

Before pre-shaping the Indium, a wire is inserted in the charging port and the microchannels linking it. The wire's goal is to prevent Indium from clogging the port before the fluid charging, by keeping an open path in the Indium. The used wire had an outer diameter of 150 μm and was made of tinned

copper. After the insertion of the wire, a flat strip of Indium of approximately 32mg is carefully pressed in the charging port and levelled to the to the surface of the chip. The assembly is introduced in an oven and it is heated up to 180°C for one minute. After the hot cycle, the silicon device with the protruding wire is let to cool down at room temperature. The wire is carefully pulled out of the inlet with the help of tweezers. It leaves an open microchannel in the Indium, ready for evacuating the air and charging the working fluid. Reflowing Indium spreads it evenly in the inlet but also the adjacent microchannel, clogging it. The proposed solution to avoid this issue is to insert a wire in the microchannel at the inlet, which would prevent Indium from entering the microchannels of the μ OHP and shape a passage inside the Indium when removed.

The inlets of the two types of devices produced are depicted in Figure 7.4(a) and (b). The inlets of the silicon and glass devices present a circular cavity of 800 μ m of diameter linked to a 500 μ m-wide microchannel in the silicon, for a depth of 400 μ m. The glass possess a hole of 1mm of diameter, which creates a step at the inlet, as shown in Figure 7.4(a). The step and the width of the microchannel make the sealing more complicated for the displacement of the tip, the deformation of Indium and the sealing of the microchannel. The silicon demonstrators feature a microchannel with a reduced width of 100 μ m and a depth of 400 μ m. No step is present along the inlet. In one hand, it eases the sealing. In the other hand, the reduced width increases the criticality and complexity of preforming Indium.

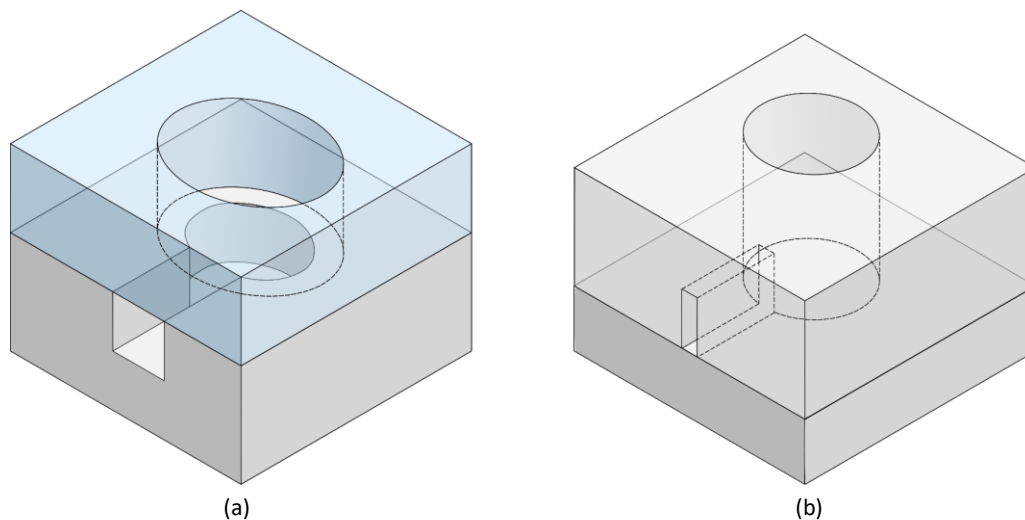


Figure 7.4. Schematics (Not to scale) of the two inlets for (a) the prototypes, glass on top and silicon on the bottom) and (b) the proof of concept demonstrators (silicon for both top and bottom).

Figure 7.5 shows the results obtained after the reflow, once with the wire and once with the wire removed. The hole left by the wire would not be centred in Figure 7.5(a), but correctly formed otherwise. A correctly formed Indium preform is visible in Figure 7.5(b) without the wire.

When two charging ports are present, as it is the case with the silicon and glass devices, one of the two ports have to be closed with Indium and a reinforcing adhesive before preparation of the second one for charging and sealing. No issue occurred during the two consecutive sealing steps, one for each inlet.

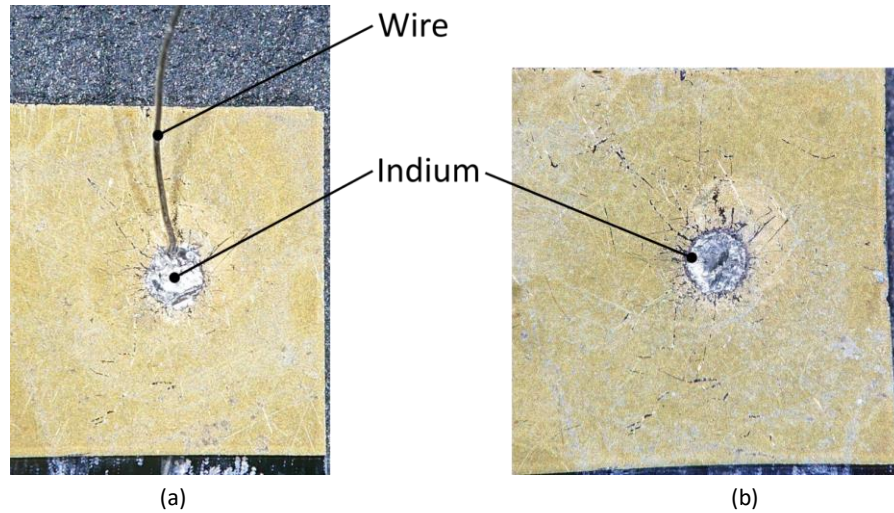


Figure 7.5. Inlet filled with Indium. (a) Result of the reflow process. Surface tension moved the wire from the centre of the inlet. (b) Correctly formed Indium preform, wire removed.



Figure 7.6. μ OHP after Indium reflow. Protruding wire is visible on the right side of the device. The inlet at the top is sealed, while the bottom one will remain unobstructed once the wire is removed.

7.2.2 Flat Gasket

The flat gaskets **L** guarantee the leak tightness during the different steps of the process. Two screws guarantee the constant compression of the gasket. The compression between the silicon device **Q** and the block **I** adds compression to the gasket around the tube when it is inserted.

The material used for the trials was Viton® A, a fluoropolymer elastomer. The gaskets were hand-cut, and a central hole was punched in each gasket. Two different punch tools with outer diameter 0.5mm and 0.7mm were tested. The smaller punched holes prevented the tube from passing through the hole once the gasket was compressed, hence the larger diameter was used for the charging and sealing tests. Additionally, two different thicknesses of gasket were evaluated: 0.3mm and 0.6mm. The thinner gaskets did not provide an appropriate sealing during the injection of the working fluid. Thus, the 0.6mm-thick gaskets were used for the devices.

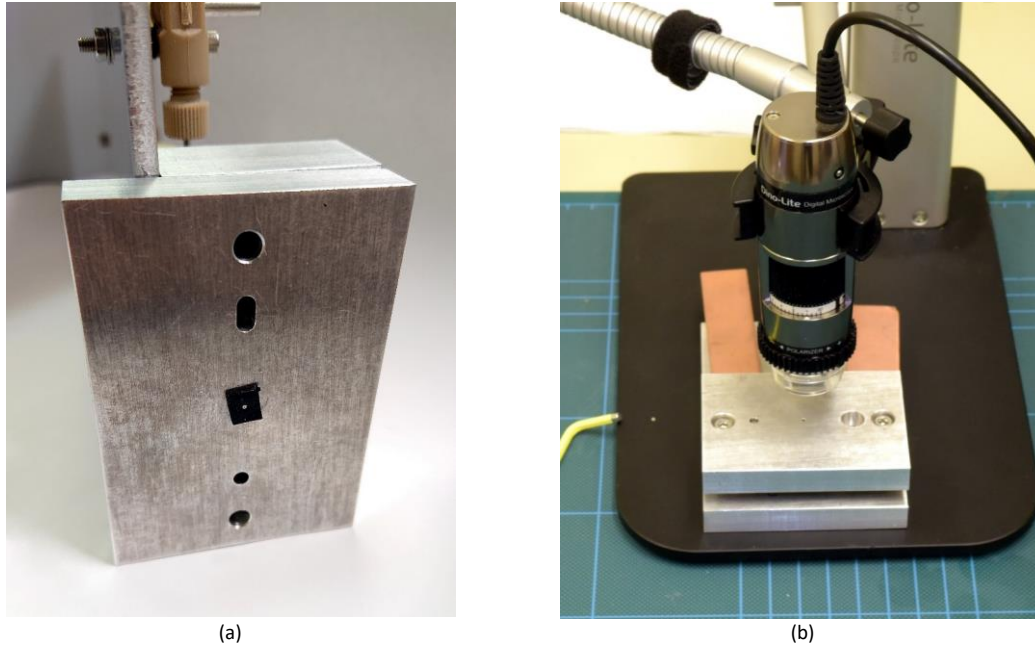


Figure 7.7. (a) Flat gasket positioned on the tip of tube **E** that pass-through the block **I**. (b) Setup of the setup used to align a μ OHP with the gasket and the clamping Al block though using a microscope

7.2.3 Alignment of the Charing Port

The aluminium blocks rely on dowel pins and holes alignment. In addition, they feature a precise hole guides the tube to access the inlet port of the silicon μ OHP. The alignment of the inlet port and the gasket with the through-hole in part **I** is done optically. A Dino-Lite digital microscope, shown in Figure 7.7(b), is placed over the aluminium parts. The centre of the tube-guiding hole serves as a reference point on the microscope, and the gasket and the inlet of the silicon device are subsequently aligned with respect to the centre of reference before clamping the assembly. The 3mm dowel pins, going from **K** to **F** through a hole and a slot, guide the different parts. The 0.8mm tube **O** is guided by small holes in the different aluminium blocks.

7.2.4 Vertical Displacement Control

Calibrated shims control the relative position of the different parts. The shims labelled **J** in Figure 7.3 are used to fix the compression distance of the gasket. The shims labelled **H** are placed between parts **F** and **I**. The combination of these shims determines the distance between the tip of the tube and the inlet's bottom. They also determine the travel distance for the compression of the Indium preform. Thus, shims need to be tailored for each type of device. Figure 7.8 shows the stacked shims used for the tests.

The height of the shims (t_H), referenced in Figure 7.8, was determined in function of needed travel distance required to compress the Indium. It was estimated that this length had to be comprised between the diameter of the wire and the depth of the charging port. The proposed value for thickness t_h is equivalent to the material thickness above the microchannels

The length t_{tip} is determined by the actual length of the tube and the relative position of the three way connectors. The initial position of the tip of the tube is at the same level as the compressed gasket, as illustrate in Figure 7.8. Hence, the thickness of the block **I** (t_I) is fixed by the shims **H**'s thickness (t_H) and the thickness of the compressed gasket **L** (t_L^{cmp}).

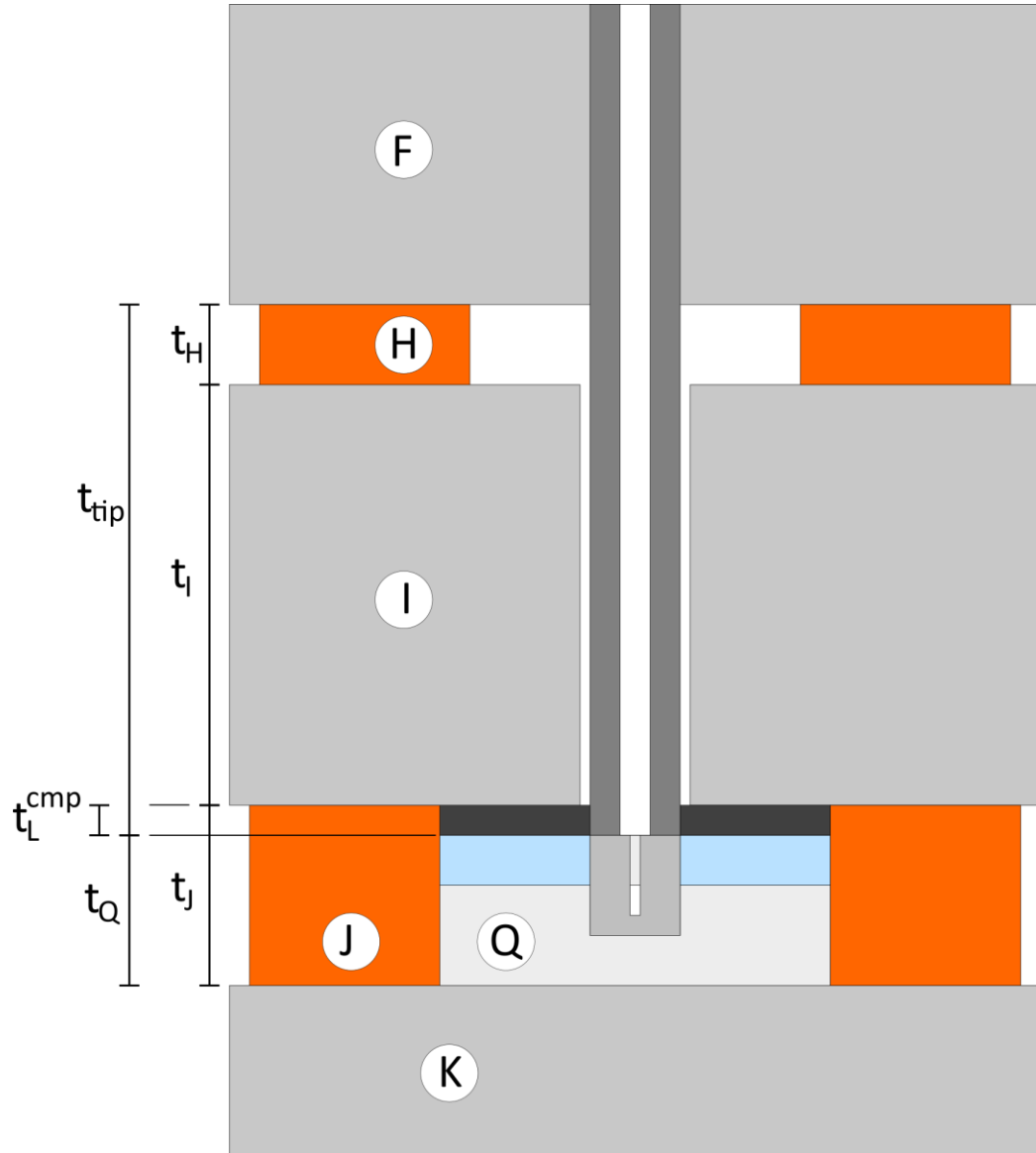


Figure 7.8. Schematic cross section of the setup for charging and sealing with labels and corresponding thicknesses.

Shims **J**'s thickness is determined by the thickness of the device (t_Q) and the thickness of the compressed gasket (t_L^{cmp}).

For the prototypes, the shims' thicknesses were 0.5mm and 1.7mm, respectively for t_H and t_J . The proof-of-concept devices required two sets of shims **H** to avoid changes of the thickness of the clamping block **I** and keep the tube's tip flush to the gasket level. The shims **H**'s thickness were 0.25mm and 0.5mm. The thicker ones needed to be removed to compress Indium, while the thinner ones remained in place to limit the travel to 250 μ m. The thickness of the shims **J** was 1.5mm.

7.2.5 Adhesive Reinforcement of the Indium

Indium is known to continuously flow under stress. Therefore, the oscillating motion inside the μ OHP and the oscillating pressure would progressively alter the Indium without reinforcement.

The adhesive used was Araldite 2011. This epoxy resin is already in use at CERN. It possesses a good radiation hardness [37], in addition to reliable mechanical properties [318]. The viscosity of Araldite 2011 (30-45Pa·s) limited the spread of the glue around the inlet.

7.3 Results and Discussion

At first, tests were conducted on unused pressure samples before using μ OHP. The different elements were aligned, evacuated and charged following the method described previously. Once the shims **H** were removed, the block **F** and the tube slide down under their own weight ($\sim 460\text{g}$), compressing the Indium and sealing the inlet. Figure 7.9 shows a sealed charging port from different angles. Figure 7.10 shows the adhesive over the Indium. It has visibly spread around the inlet.

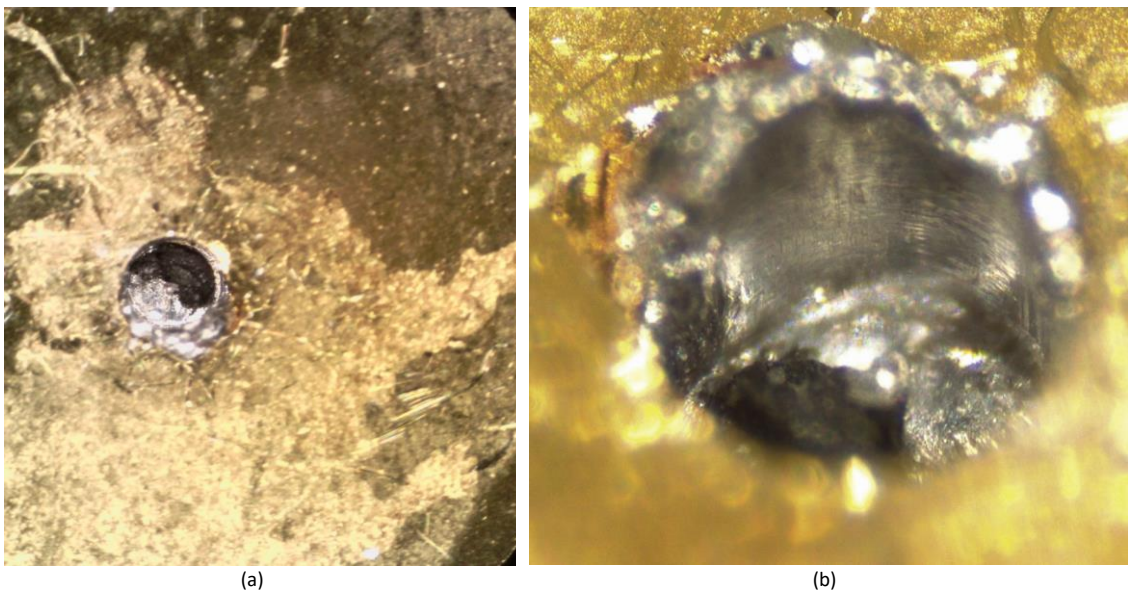


Figure 7.9. (a) View from above of a sealed charging port with Indium. The diameter of the inlet is $800\mu\text{m}$. (b) Detailed view of the inlet at 45° . The microchannel is hidden by the visible Indium (grey).



Figure 7.10. Glue deposited on a freshly sealed μ OHP. The central deformation of Indium, with deformation on the wall is visible through the glue.

The pressure resistance of the seal was evaluated in similar manner as the pressure sample by using the CERN standard pressure test setup with a dedicated clamping tool, illustrated in Figure 7.11. A seal was realized at the end of a microchannel, while the other side was pressurized. The

same sample and clamping system were used to determine the leak-tightness of the developed sealing method.

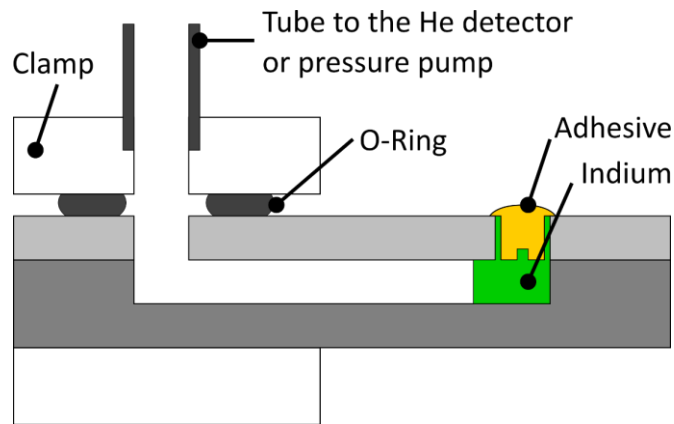


Figure 7.11. Scheme of a clamped seal sample used for leak-tightness test and pressure resistance.

The leak-tightness peaked at $1.8 \cdot 10^{-8} \text{ mbar} \cdot \text{l/s}$ when spraying helium around the clamped sample. When helium was carefully sprayed around the sealed charging port using a syringe needle, the leak-tightness results slightly improved. The short distance between the O-ring and the charging port and the fitting used to connect the tube to the clamps are source of errors for this measurement. Nevertheless, the worst value observed, $1.8 \cdot 10^{-8} \text{ mbar} \cdot \text{l/s}$, is kept. The maximal pressure measured was 44.8 bar. The seal port did not show any leak, but the test was stopped due to leak appearing at the O-Ring.

For charged devices with visual access, an additional verification of the effectiveness of the sealing can be performed directly by removing the tube from the inlet. The biphasic system evolving inside the meandering microchannel depends on the pressure equilibrium inside the microchannel. Any variation of this pressure leads to a perturbation of this equilibrium, thus to a rapid evolution of the two-phase state of the fluid. Therefore, a seal wrongly prepared would perturb the biphasic system's equilibrium. If visual verification cannot be performed, the sealing's effectiveness can be assessed by verification of the increased apparent thermal conductivity of the device. Any leak, when operating, leads to a rapid loss of the working fluid. Thus, decreased thermal performance. After verifying the seal effectiveness, glue is applied to the inlet to reinforce the seal mechanically, as Indium would continuously flow under stress. A sealed μOHP prototype can be seen in Figure 7.12.

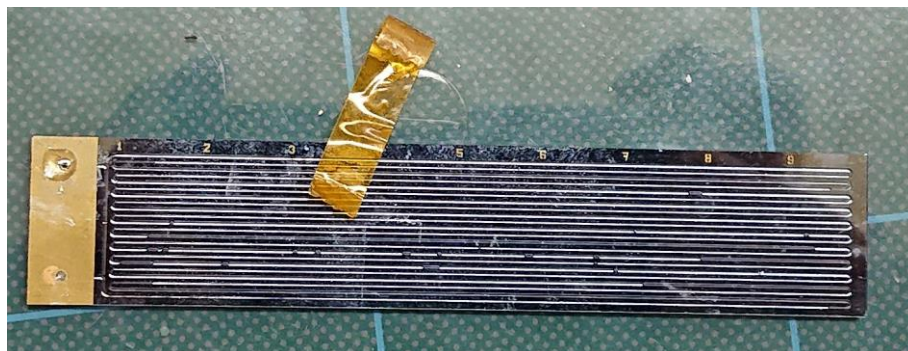


Figure 7.12. μOHP after sealing. The two charging ports blocked by Indium and glue are visible on the left side.

The propensity of the adhesive to flow unevenly around the inlet could be mitigated by structuring a circular recess around it to pin the flow of the uncured resin.

The melting point of Indium limits this solution. If Indium melts, it cannot fulfil its role as sealing material, and only the adhesive would remain. The pressure of the fluid could break the Indium seal once the compression performed if no reinforcement is present around the Indium.

7.4 Conclusion

An innovative charging and sealing technique was proposed. The proposed sealing method simplify one major challenge of the micro heat pipe. Sealing micro heat pipes by compressing Indium on gold-covered surfaces provides a hermetic seal without the need to apply additional heat after the charging of the working fluid. This heat could trigger the evaporation of the fluid, which would perturb the Indium and prevent the channels' sealing. The pressure variations induced by the fluid pushed vapour and liquid through the inlet. Furthermore, compressing Indium is not a time-critical process. The sealing procedure does not have to follow timed steps, which further ease the process.

Nevertheless, a key factor for this process to seal a μ HP is to have the correct amount of Indium beforehand. A low volume would prevent Indium from blocking the inlet. On the contrary, too much Indium may cause it to seal the inlet before charging the working fluid.

Chapter 8 Conclusions

8.1 Summary

This study deals with the design, fabrication, experimental testing and integration of micro oscillating heat pipes fabricated using MEMS techniques. The proposed μ OHPs intend to pave the way to new cooling schemes for thermal management of electronic components for HEP experiments and space applications. Thermal-related failures are predominant among all failures of semiconductor devices, as estimated by NASA. The existing cooling solutions adopted in HEP experiments and space applications to mitigate thermal related issues involve some challenges (i) the lack of appropriate interconnections for long silicon staves, (ii) the brittle nature of silicon and the (iii) integration and packaging difficulties. The proposed cooling scheme involves two separate fluid loops, alleviating some of the challenges and enabling new opportunities.

The results of this research can be summarised as:

- Silicon-based μ OHPs were realized by two methods: anodic bonding and gold thermo-compression (chapter 5). Promising results were obtained for the thermocompressed wafer. The burst pressures reached with this method exceed the ones from direct bonding. Burst pressures above 260bar were observed for 1.5mm-wide microchannels closed by thermocompression. In comparison, microchannels obtained by direct bonding typically burst below 100bar.
- The μ OHP's apparent thermal conductivity was measured and correlated with the observed flow patterns for three fluids at different orientation and with different quantities of fluids (chapter 6). Acetone, as working fluid, yielded the best thermal performance of the three tested fluids. It reached the apparent thermal conductivity of the copper strip at 10W - a charging ratio ϕ of 50% - and exceeded it above this heat load. On the other hand, IPA was the least efficient of the three fluids.
- The role of dual-diameter design was investigated in gravitationally adverse conditions for a range of charging ratios (chapter 6). Orientation-independent operations were achieved. IPA-charged device showed a uniform apparent thermal conductivity that did not depend on the orientation. C_6F_{14} - and acetone-charged devices have seen their thermal performance vary with the orientation depending the charging ratio and the heat load, except for the device filled at 75% with acetone.
- A new packaging technique based on Indium for micro heat pipes was investigated and implemented to seal permanently the devices without protruding elements (chapter 7). It allowed to seal micro heat pipes with a limited amount of metals in a low-volume and without the need of heat. A leak-tightness of $1.8 \cdot 10^{-8}$ mbar/l·s was reached when tested with Helium and it withstood a pressure of 44.8bar without failing.

The successful operations of the device demonstrate that the μ OHPs are a promising solution to be integrated in silicon for thermal management. The relative ease of fabrication and high thermal conductivity advocates in favour of μ OHP, despite the complex internal flow behaviour.

Five distinct flow patterns were observed when the orientation, charging ratio and heat inputs varied. Unidirectional flow circulation appeared as the predominant flow patterns for both C_6F_{14} and acetone, whereas IPA was mostly subject to unstable oscillations with slow circulation. However, no universal transition criterion could be determined. Orientation affected the flow patterns: in top heating mode the transition to unidirectional flow circulation happened at higher heat load. Low quantities of fluid led to early start-ups of the fluid motion, while high quantities delayed the process, with the advantage of handling higher heat fluxes.

The analysis of the apparent thermal conductivity coupled with the flow patterns' observations correlated the effects of the unidirectional flow circulation on the system performance. In a consistent manner with the literature, the emergence of unidirectional flow led to an improved thermal performance. The liquid inventory directly influenced the thermal performance. Low charging ratios yielded high apparent thermal conductivity, as observed for medium charging ratio. Higher quantities of liquids resulted in reduced thermal performance but higher maximal heat inputs than with less fluid.

Micro heat pipes are generally aimed for high power devices' thermal management. The foreseen use case remains a particular application of this technology. Nevertheless, devices showed promising results.

The summarizing tables (Table 2-4 to Table 2-8) created for micro heat pipe technology comparison could have an extended use to estimate future designs using a machine learning approach. Complementary data would be required to depict each experimental set. A collective and open database could be implemented for that purpose.

Non-invasive sealing system proposed and implemented provided an efficient solution to enclose low-temperature fluids. This solution reduced the footprint of the sealing systems of micro heat pipes, enhancing the integration of such systems in field.

8.2 Future Work

Within this study's scope, a novel microchannel fabrication method was tested, showing potential improvement and simplification over the direct-bonding technique. In particular, the wafer bonding by thermocompression of gold thin-films withstood higher pressure at equivalent width than directly bonded samples. The transition to cohesive failure with the higher bond quality would allow numerical studies of the interfaces. Therefore, this bonding process needs improvements, mainly to reduce the variations in the results.

The question of the thermal performance and flow patterns of the device in microgravity remains open, as even if operating horizontally and against gravity, no proof exists that dual-diameter μ OHPs could efficiently work in this conditions. Numerical simulations could hint at an answer, but experimental results remain nonetheless necessary. Additional interrogations arise on the ability of the device to cope with small accelerations and vibrations typical from an operating

satellite. Furthermore, a critical angle might be identified for the transition from not operating devices to an operating one.

Additionally, the long term reliability of these devices, particularly when considering the foreseen radiation doses of the future accelerators, should be investigated. The thermal performance of these devices could be subject to change when exposed to high radiation doses. The fluid's molecular structure, under radiations, might evolve. Furthermore, the leak tightness of the seal should be verified after radiation exposure and over years of use.

To succeed the research, it would be necessary to experiment more on fluids and design variations. Two or three more years would be required to test the varying devices with the additional fluids at all orientations. Refining the increments of the charging ratio, but also the orientation and the heat load could be useful to determine a critical transition at which gravity dominates the flow regime.

References

- [1] R. Battiston and AMS Collaboration, "The Anti Matter Spectrometer (AMS-02): a particle physics detector in space," Pune, 2005, p. 22.
- [2] Johannes van Es *et al.*, "AMS02 TRACKER THERMAL CONTROL SYSTEM OVERVIEW AND SPIN-OFF FOR FUTURE SPACECRAFT COOLING SYSTEM DEVELOPMENTS (IAC-09.C2.7.1)," presented at the 60th International Astronautical Congress 2009 (IAC 2009), Daejeon, Republic of Korea., 2009, Accessed: Mar. 24, 2021. [Online]. Available: https://ams.nasa.gov/Documents/AMS%20in%20The%20News/IAC-09.C2.7.1_Paper_AMS02_TTCS_J_van_Es_IAC_Space_Vehicles_iss04.pdf.
- [3] P. Cooper, M. Harrington, T. Starke, C. Stirling, N. Stockham, and C. Beck, "Developments and trends in thermal management technologies – a mission to the USA," GLOBAL WATCH MISSION REPORT, Dec. 2006. Accessed: Mar. 03, 2021. [Online]. Available: <http://www-eng.lbl.gov/~ecanderssen/STAR/Beam%20Pipe%20Info/Thermal%2520Management.pdf>.
- [4] M. Ikonen, "Power cycling lifetime estimation of IGBT power modules based on chip temperature modeling," PhD Thesis, Lappeenranta Univeristy of Technology, 2012.
- [5] M. Ciappa, "Selected failure mechanisms of modern power modules," *Microelectronics Reliability*, vol. 42, no. 4, pp. 653–667, Apr. 2002, doi: 10.1016/S0026-2714(02)00042-2.
- [6] M. Krammer and H. Frank, "Silicon Detectors," presented at the CERN Official Schools - Detectors and Instrumentation in HEP - Silicon strips and pixels technologies - part 1, CERN, 2015, [Online]. Available: <https://indico.cern.ch/event/124392/contributions/1339904/attachments/74582/106976/IntroSilicon.pdf>.
- [7] D. Bortoletto, "How and why silicon sensors are becoming more and more intelligent?," *J. Inst.*, vol. 10, no. 08, pp. C08016–C08016, Aug. 2015, doi: 10.1088/1748-0221/10/08/C08016.
- [8] N. Wermes, "Pixel Detectors ... where do we stand?," *Nuclear Instruments and Methods in Physics Research Section A: Accelerators, Spectrometers, Detectors and Associated Equipment*, vol. 924, pp. 44–50, Apr. 2019, doi: 10.1016/j.nima.2018.07.003.
- [9] R. Mendicino *et al.*, "3D trench-electrode sensors for charged particle tracking and timing," *Nuclear Instruments and Methods in Physics Research Section A: Accelerators, Spectrometers, Detectors and Associated Equipment*, vol. 927, pp. 24–30, May 2019, doi: 10.1016/j.nima.2019.02.015.
- [10] F. Hartmann, *Evolution of Silicon Sensor Technology in Particle Physics*, vol. 275. Cham: Springer International Publishing, 2017.
- [11] A. Gligorova *et al.*, "Comparison of Planar and 3D Silicon Pixel Sensors Used for Detection of Low Energy Antiprotons," *IEEE Trans. Nucl. Sci.*, vol. 61, no. 6, pp. 3747–3753, Dec. 2014, doi: 10.1109/TNS.2014.2368591.
- [12] Yu. K. Akimov, "Silicon radiation detectors (Review)," *Instrum Exp Tech*, vol. 50, no. 1, pp. 1–28, Feb. 2007, doi: 10.1134/S0020441207010010.

-
- [13] G. Dearnaley and D. C. Northrop, *Semiconductor counters for nuclear radiations*. Wiley, 1963.
 - [14] N. Wermes, "Pixel detectors for particle physics and imaging applications," *Nuclear Instruments and Methods in Physics Research Section A: Accelerators, Spectrometers, Detectors and Associated Equipment*, vol. 512, no. 1, pp. 277–288, Oct. 2003, doi: 10.1016/S0168-9002(03)01905-3.
 - [15] N. Wermes, "Pixel Detectors for Tracking and their Spin-off in Imaging Applications," *Nuclear Instruments and Methods in Physics Research Section A: Accelerators, Spectrometers, Detectors and Associated Equipment*, vol. 541, no. 1–2, pp. 150–165, Apr. 2005, doi: 10.1016/j.nima.2005.01.052.
 - [16] G. F. Knoll, *Radiation Detection and Measurement*. John Wiley & Sons, 2010.
 - [17] S. Seidel, "Silicon strip and pixel detectors for particle physics experiments," *Physics Reports*, vol. 828, pp. 1–34, Oct. 2019, doi: 10.1016/j.physrep.2019.09.003.
 - [18] G. L. Miller, B. M. Foreman, L. C. L. Yuan, P. F. Donovan, and W. M. Gibson, "Application of Solid State Detectors to High Energy Physics," *IRE Transactions on Nuclear Science*, vol. 8, no. 1, pp. 73–78, Jan. 1961, doi: 10.1109/TNS2.1961.4315802.
 - [19] C. J. S. Damerell *et al.*, "A vertex detector for SLD," *Nuclear Instruments and Methods in Physics Research Section A: Accelerators, Spectrometers, Detectors and Associated Equipment*, vol. 275, no. 3, pp. 484–493, Mar. 1989, doi: 10.1016/0168-9002(89)90735-3.
 - [20] P. Weilhammer, "Experience with Si Detectors in NA32," CERN, "New Solid-State Devices for High Energy Physics" Berkley 1985, CERN-Ep/86-54, 1986. Accessed: Jul. 13, 2020. [Online]. Available: <http://cds.cern.ch/record/167535/files/198606216.pdf>.
 - [21] P. Allport, "Supplement Information to Applications of silicon strip and pixel-based particle tracking detectors," *Nat Rev Phys*, vol. 1, no. 9, pp. 567–576, Sep. 2019, doi: 10.1038/s42254-019-0081-z.
 - [22] P. Allport, "Applications of silicon strip and pixel-based particle tracking detectors," *Nature Reviews Physics*, vol. 1, no. 9, Art. no. 9, Sep. 2019, doi: 10.1038/s42254-019-0081-z.
 - [23] J. R. Wertz and W. J. Larson, *Space mission analysis and design*, Springer Netherlands. Microcosm, 1999.
 - [24] C. Dubois, M. Avignon, and P. Escudier, *Observing the Earth from space: Space data - social and political stakes*. Dunod, 2014.
 - [25] Shen-En Qian, *Hyperspectral Satellites and System Design*, CRC Press. 2020.
 - [26] C. T. Russell, *The Cassini-Huygens Mission: Volume 1: Overview, Objectives and Huygens Instrumentarium*. Springer Science & Business Media, 2013.
 - [27] S. P. George *et al.*, "Very high energy calibration of silicon Timepix detectors," *J. Inst.*, vol. 13, no. 11, pp. P11014–P11014, Nov. 2018, doi: 10.1088/1748-0221/13/11/P11014.
 - [28] X. Llopart, R. Ballabriga, M. Campbell, L. Tlustos, and W. Wong, "Timepix, a 65k programmable pixel readout chip for arrival time, energy and/or photon counting measurements," *Nuclear Instruments and Methods in Physics Research Section A: Accelerators, Spectrometers, Detectors and Associated Equipment*, vol. 581, no. 1, pp. 485–494, Oct. 2007, doi: 10.1016/j.nima.2007.08.079.
 - [29] M. Campbell *et al.*, "PARTICLE DETECTION AND IMAGING USING THE MEDIPIX AND TIMEPIX CHIPS," presented at the SÉMINAIRE DE PHYSIQUE CORPUSCULAIRE, Ecole de physique, Genève, 2017.

-
- [30] R. Gaza, M. Kroupa, R. Rios, N. Stoffle, E. R. Benton, and E. J. Semones, "Comparison of novel active semiconductor pixel detector with passive radiation detectors during the NASA Orion Exploration Flight Test 1 (EFT-1)," *Radiation Measurements*, vol. 106, pp. 290–297, Nov. 2017, doi: 10.1016/j.radmeas.2017.03.041.
 - [31] Lucas Tlustos, "Timepix in Space," presented at the EP-ESE Seminar, CERN, Jun. 23, 2020, Accessed: Jun. 23, 2020. [Online]. Available: <https://indico.cern.ch/event/876028/attachments/2062000/3459212/20200623-ESE.pdf>.
 - [32] C. Granja *et al.*, "Miniaturized Radiation Monitorspacecraft platform for GEO telecommunications satellites," Nov. 2018, Accessed: Jun. 17, 2020. [Online]. Available: <https://linkinghub.elsevier.com/retrieve/pii/S0168900218309586>.
 - [33] T. Takahashi *et al.*, "The ASTRO-H X-ray Astronomy Satellite," *arXiv:1412.1356 [astro-ph]*, p. 914425, Jul. 2014, doi: 10.1117/12.2055681.
 - [34] J.-L. Autran, D. Munteanu, and D. Munteanu, *Soft Errors : From Particles to Circuits*. CRC Press, 2017.
 - [35] B. G. Kumar, R. P. Singh, and T. Nakamura, "Degradation of Carbon Fiber-Reinforced Epoxy Composites by Ultraviolet Radiation and Condensation:," *Journal of Composite Materials*, Jul. 2016, doi: 10.1177/002199802761675511.
 - [36] R. L. Clough, "High-energy radiation and polymers: A review of commercial processes and emerging applications," *Nuclear Instruments and Methods in Physics Research Section B: Beam Interactions with Materials and Atoms*, vol. 185, no. 1, pp. 8–33, Dec. 2001, doi: 10.1016/S0168-583X(01)00966-1.
 - [37] F. Guarino, M. Tavlet, and C. Hauviller, "Compilation of radiation damage test data, part IV: adhesives," CERN, CERN-2001-006, 2001. doi: 10.5170/CERN-2001-006.
 - [38] H. Schönbacher and A. Stolarz-Izycka, "Compilation of radiation damage test data, part I: cable insulating materials," CERN, HS-RP-038-YR-PARTI, 1979. doi: 10.5170/CERN-1979-004.
 - [39] M. Tavlet and H. Schönbacher, "Compilation of radiation damage test data, part I (2nd edition): Halogen-free cable-insulating materials," CERN, CERN-89-12, 1989. doi: 10.5170/CERN-1989-012.
 - [40] H. Schönbacher and A. Stolarz-Izycka, "Compilation of radiation damage test data, part II: thermosetting and thermoplastic resins.," CERN, HS-RP-038-YR-PARTII, 1979. doi: 10.5170/CERN-1979-008.
 - [41] M. Tavlet, A. Fontaine, and H. Schönbacher, *Compilation of radiation damage test data, part II (2nd edition): thermoset and thermoplastic resins, composite materials*, 2nd ed. Geneva: CERN, 1998.
 - [42] P. Beynel, H. Schönbacher, and P. Maier, "Compilation of radiation damage test data, part III: materials used around high-energy accelerators," CERN, HS-RP-093, 1982. doi: 10.5170/CERN-1982-010.
 - [43] A. Holmes-Siedle and L. Adams, "Handbook of radiation effects," 1993, Accessed: May 28, 2020. [Online]. Available: http://inis.iaea.org/Search/search.aspx?orig_q=RN:26063911.
 - [44] C. Cristiano and G. Umberto, *Rad-hard Semiconductor Memories*. River Publishers, 2019.
 - [45] D. Kiselev, "Activation and radiation damage in the environment of hadron accelerators," *CERN Document Server*, Mar. 27, 2013. <https://cds.cern.ch/record/1533024> (accessed Jun. 03, 2020).

-
- [46] M. A. Xapsos *et al.*, "Inclusion of Radiation Environment Variability in Total Dose Hardness Assurance Methodology," *IEEE Trans Nucl Sci*, vol. 64, no. 1, pp. 325–331, Jan. 2017, doi: 10.1109/TNS.2016.2607021.
 - [47] J.R. Srour and J.W. Palko, "A Framework for Understanding Displacement Damage Mechanisms in Irradiated Silicon Devices - IEEE Journals & Magazine," *IEEE Transactions on Nuclear Science*, vol. 53, no. 6, Dec. 2006, doi: 10.1109/TNS.2006.885796.
 - [48] M. Bagatin and S. Gerardin, *Ionizing Radiation Effects in Electronics: From Memories to Imagers*. CRC Press, 2018.
 - [49] C. Poivey, "TNID Total Non Ionizing Dose or DD Displacement Damage," presented at the Radiation environment and its effects in EEE components and hardness assurance for space applications, CERN-ESA-SSC workshop, Oct. 05, 2017.
 - [50] M. Poizat, "TID Total Ionizing Dose," presented at the Radiation environment and its effects in EEE components and hardness assurance for space applications, CERN-ESA-SSC workshop, Oct. 05, 2017.
 - [51] H. Evans, "Space Environment Basics & Calculation methods," presented at the ESA Internal Course, EEE Component Radiation Hardness Assurance Tutorial, ESTEC, ESA, ESTEC, Nov. 04, 2016.
 - [52] H. R. Shea, "Radiation sensitivity of microelectromechanical system devices," *JM3*, vol. 8, no. 3, p. 031303, Jul. 2009, doi: 10.1117/1.3152362.
 - [53] P. Kuijer, "The ALICE silicon strip detector system," *Nucl. Instrum. Methods Phys. Res., A*, 2000. <http://cds.cern.ch/record/783069> (accessed Mar. 20, 2018).
 - [54] B. Abelev *et al* and The ALICE Collaboration, "Technical Design Report for the Upgrade of the ALICE Inner Tracking System," *J. Phys. G: Nucl. Part. Phys.*, vol. 41, no. 8, p. 087002, Aug. 2014, doi: 10.1088/0954-3899/41/8/087002.
 - [55] Diego Álvarez, "Prototyping of large structures for the Phase-II upgrade of the pixel detector of the ATLAS experiment," presented at the 2017 IEEE NSS and MIC, Atlanta, Oct. 26, 2017, [Online]. Available: <https://cds.cern.ch/record/2291042/files/ATL-ITK-SLIDE-2017-929.pdf>.
 - [56] M. Hamer and ATLAS ITk Community, "Phase-II Upgrade of the ATLAS Pixel Detector," in *Proceedings of The 27th International Workshop on Vertex Detectors — PoS(VERTEX2018)*, MGM Beach Resorts, Muttukadu, Chennai, India, Sep. 2019, p. 020, doi: 10.22323/1.348.0020.
 - [57] A. Abada *et al.*, "FCC-hh: The Hadron Collider," *Eur. Phys. J. Spec. Top.*, vol. 228, no. 4, pp. 755–1107, Jul. 2019, doi: 10.1140/epjst/e2019-900087-0.
 - [58] Michael Moll, "Radiation damage in silicon particle detectors: Microscopic defects and macroscopic properties - INSPIRE," Hamburg University, 1999.
 - [59] C. A. Heusch, A. G. Holodenko, and H. G. Moser, "Measurements of Silicon Detector Thermal Runaway," CERN-ATL-INDET-99-015, 1999.
 - [60] M. T. Brunetti *et al.*, "Leakage current and capacity variation with temperature in silicon detectors of a space calorimeter," *Nuclear Instruments and Methods in Physics Research Section A: Accelerators, Spectrometers, Detectors and Associated Equipment*, vol. 302, no. 2, pp. 362–367, Apr. 1991, doi: 10.1016/0168-9002(91)90423-N.
 - [61] M. L. Rieger, "Retrospective on VLSI value scaling and lithography," *JM3*, vol. 18, no. 4, p. 040902, Nov. 2019, doi: 10.1117/1.JMM.18.4.040902.

-
- [62] M. Ohadi, K. Choo, S. Dessiatoun, and E. Cetegen, "Emerging Applications of Microchannels," in *Next Generation Microchannel Heat Exchangers*, M. Ohadi, K. Choo, S. Dessiatoun, and E. Cetegen, Eds. New York, NY: Springer, 2013, pp. 67–105.
 - [63] W. Nakayama, "Evolution of Hardware Morphology of Large-Scale Computers and the Trend of Space Allocation for Thermal Management," *J. Electron. Packag.*, vol. 139, no. 1, Mar. 2017, doi: 10.1115/1.4035019.
 - [64] A. L. Moore and L. Shi, "Emerging challenges and materials for thermal management of electronics," *Materials Today*, vol. 17, no. 4, pp. 163–174, May 2014, doi: 10.1016/j.mat-tod.2014.04.003.
 - [65] G. Contin *et al.*, "The STAR MAPS-based PiXeL detector," *Nuclear Instruments and Methods in Physics Research Section A: Accelerators, Spectrometers, Detectors and Associated Equipment*, vol. 907, pp. 60–80, Nov. 2018, doi: 10.1016/j.nima.2018.03.003.
 - [66] H. H. Wieman *et al.*, "STAR PIXEL detector mechanical design," *J. Inst.*, vol. 4, no. 05, p. P05015, 2009, doi: 10.1088/1748-0221/4/05/P05015.
 - [67] T. Abe *et al.*, "Belle II Technical Design Report," *arXiv:1011.0352 [hep-ex, physics:physics]*, Nov. 2010, Accessed: Jul. 01, 2020. [Online]. Available: <http://arxiv.org/abs/1011.0352>.
 - [68] Valerio Bertacchi, "Development and performance of the trackfinder for the Belle II Vertex Detector," Università di Pisa, 2017.
 - [69] N. Berger *et al.*, "Ultra-low material pixel layers for the Mu3e experiment," *J. Inst.*, vol. 11, no. 12, pp. C12006–C12006, Dec. 2016, doi: 10.1088/1748-0221/11/12/C12006.
 - [70] "The International Linear Collider Technical Design Report, Volume 4: Detectors," ILC, 000, 2013. Accessed: Jul. 13, 2020. [Online]. Available: <https://ilchome.web.cern.ch/sites/ilchome.web.cern.ch/files/images/pdf/Detectors.pdf>.
 - [71] S. Spannagel, "Silicon Vertex & Tracking Detectors for the Compact Linear Collider," presented at the 28th International Workshop on Vertex Detectors, Lopud, Croatia, Jun. 2019, Accessed: Jul. 13, 2020. [Online]. Available: <http://cdsweb.cern.ch/record/2703588/files/CLICdp-Conf-2019-013.pdf>.
 - [72] N. A. Tehrani *et al.*, "CLICdet: The post-CDR CLIC detector model," CLICdp-Note-2017-001 (Rev. 05 Apr. 2019), Feb. 2018.
 - [73] G. Blanchot, D. Dannheim, and C. Fuentes, "Power-pulsing schemes for vertex detectors at CLIC," *J. Inst.*, vol. 9, no. 01, pp. C01005–C01005, Jan. 2014, doi: 10.1088/1748-0221/9/01/C01005.
 - [74] H. Aihara *et al.*, "The International Linear Collider. A Global Project," *arXiv:1901.09829 [hep-ex, physics:physics]*, Jan. 2019, Accessed: Jun. 08, 2020. [Online]. Available: <http://arxiv.org/abs/1901.09829>.
 - [75] Marcel Vos, "LC Vertex Detector Workshop," presented at the AWLC17, SLAC, Ringberg, Jun. 2017, [Online]. Available: https://agenda.linearcollider.org/event/7507/contributions/39319/attachments/31755/47875/ringberg_summary.pdf.
 - [76] B. Avram, *Encyclopedia Of Thermal Packaging, Set 3: Thermal Packaging Applications (A 3-volume Set)*. World Scientific, 2018.
 - [77] J. B. Marcinichen, J. A. Olivier, N. Lamaison, and J. R. Thome, "Advances in Electronics Cooling," *Heat Transfer Engineering*, vol. 34, no. 5–6, pp. 434–446, Jan. 2013, doi: 10.1080/01457632.2012.721316.

-
- [78] S. V. Garimella *et al.*, “Thermal Challenges in Next-Generation Electronic Systems,” *IEEE Transactions on Components and Packaging Technologies*, vol. 31, no. 4, pp. 801–815, Dec. 2008, doi: 10.1109/TCAPT.2008.2001197.
 - [79] A. Agrawal, H. M. Kushwaha, and R. S. Jadhav, *Microscale Flow and Heat Transfer: Mathematical Modelling and Flow Physics*. Cham: Springer International Publishing, 2020.
 - [80] Satish Kandlikar, Srinivas Garimella, Dongqing Li, Stephane Colin, and Michael R. King, *Heat Transfer and Fluid Flow in Minichannels and Microchannels*. Elsevier, 2005.
 - [81] M. P. Dos Santos, “ALICE SSD and SDD cooling system,” Technical Report 490537, 2004. [Online]. Available: <https://edms5.cern.ch/document/490537/1>.
 - [82] A. Pepato *et al.*, “The mechanics and cooling system of the ALICE silicon pixel detector,” *Nuclear Instruments and Methods in Physics Research Section A: Accelerators, Spectrometers, Detectors and Associated Equipment*, vol. 565, no. 1, pp. 6–12, Sep. 2006, doi: 10.1016/j.nima.2006.04.093.
 - [83] B. Verlaat *et al.*, “The ATLAS IBL CO₂ cooling system,” *Journal of Instrumentation*, vol. 12, no. 02, pp. C02064–C02064, Feb. 2017, doi: 10.1088/1748-0221/12/02/C02064.
 - [84] M. Capeans *et al.*, “ATLAS Insertable B-Layer Technical Design Report,” Technical Design Report ATLAS-TDR-19, CERN-LHCC-2010-013, 2010.
 - [85] D. Attree *et al.*, “The evaporative cooling system for the ATLAS inner detector,” *J. Inst.*, vol. 3, no. 07, p. P07003, 2008, doi: 10.1088/1748-0221/3/07/P07003.
 - [86] ALICE Collaboration, “ALICE Technical Design Report of the Inner Tracking System (ITS),” TDR CERN / LHCC 99–12; ALICE TDR 4, Jun. 1999. Accessed: Jul. 10, 2020. [Online]. Available: https://edms.cern.ch/ui/file/398932/1/ITS_TDR.pdf.
 - [87] Panos Charitos, “The ALICE ITS upgrade: Pixels for quarks | EP Department newsletter,” *CERN Website*, Sep. 19, 2019. <https://ep-news.web.cern.ch/content/alice-its-upgrade-pixels-quarks> (accessed May 20, 2020).
 - [88] The ATLAS Collaboration, “Technical Design Report for the ATLAS Inner Tracker Pixel Detector,” CERN-LHCC-2017-021 ATLAS-TDR-030, Jun. 2018. [Online]. Available: <https://cds.cern.ch/record/2285585/files/ATLAS-TDR-030.pdf>.
 - [89] Pierre Barroca, “Modelling CO₂ cooling of the ATLAS ITkPixel Detector,” PhD Thesis, Université de Grenoble Alpes, Grenoble, 2019.
 - [90] Diego Álvarez, Christophe Bault, Jordan Degrange, Alexandre Pascal Perez, Ricardo Rego, and Krzysztof Sliwa, “Design Overview of Global Mechanics and Integration for the ITk Pixel Outer Barrel,” CERN, CERN, Technical ATLAS AT2-IP-EN-0022, 2020. [Online]. Available: https://edms.cern.ch/ui/file/2438127/1/ITk_Pixel_Outer_Barrel_Global_Mechanics_Design_and_Integration_VR1.0_04122020.pdf.
 - [91] Diego Álvarez, “Mechanics & Cooling Challenges for the ATLAS ITk Upgrade for HL-LHC,” presented at the 28th International Workshop on Vertex Detectors (VERTEX2019), Lafodia Sea Resort, Lopud Island, Croatia, Oct. 17, 2019, Accessed: Jun. 16, 2021. [Online]. Available: <https://indico.cern.ch/event/806731/contributions/3503818/>.
 - [92] “State of the Art Small Spacecraft Technology,” NASA Ames Research Center, Small Spacecraft Systems Virtual Institute, Moffett Field, California, Technical Publication NASA/TP—2018–220027, 2018. [Online]. Available: https://www.nasa.gov/sites/default/files/atoms/files/soa2018_final_doc.pdf.

-
- [93] J. Meseguer, I. Pérez-Grande, A. Sanz-Andrés, and G. Alonso, "Thermal Systems," in *The International Handbook of Space Technology*, M. Macdonald and V. Badescu, Eds. Berlin, Heidelberg: Springer, 2014, pp. 371–395.
 - [94] Scott A. Hill, Christopher Kostyk, Brian Motil, William Notardonato, Steven Rickman, and Theodore Swanson, "DRAFT Thermal management Systems Roadmap Technology Area 14," National Aeronautics and Space Administration, Nov. 2010. Accessed: Jan. 05, 2020. [Online]. Available: https://www.nasa.gov/pdf/501320main_TA14-Thermal-DRAFT-Nov2010-A.pdf.
 - [95] "NASA Technology Roadmaps TA 14: Thermal Management Systems," National Aeronautics and Space Administration, Jul. 2015.
 - [96] "2020 NASA Technology Taxonomy," National Aeronautics and Space Administration, 2020. Accessed: May 26, 2020. [Online]. Available: https://www.nasa.gov/sites/default/files/atoms/files/2020_nasa_technology_taxonomy_lowres.pdf.
 - [97] P. Zhang, X. Wei, L. Yan, H. Xu, and T. Yang, "Review of recent developments on pump-assisted two-phase flow cooling technology," *Applied Thermal Engineering*, vol. 150, pp. 811–823, Mar. 2019, doi: 10.1016/j.applthermaleng.2018.12.169.
 - [98] E. Sunada *et al.*, "A Two-Phase Mechanically Pumped Fluid Loop for Thermal Control of Deep Space Science Missions," Jul. 2016, Accessed: May 20, 2020. [Online]. Available: <https://ttu-ir.tdl.org/handle/2346/67545>.
 - [99] "Active Thermal Control System (ATCS) Overview," Boeing IDS Business Support, Communications and Community Affairs. Accessed: Jun. 02, 2020. [Online]. Available: https://www.nasa.gov/pdf/473486main_iss_atcs_overview.pdf.
 - [100] J. Raetz and J. Dominick, "Space Station External Thermal Control System Design and Operational Overview," SAE International, Warrendale, PA, SAE Technical Paper 921106, Jul. 1992. doi: 10.4271/921106.
 - [101] R. C. van Benthem, W. de Grave, J. van Es, J. Elst, R. Bleuler, and T. Tjptahardja, "Development of a Mechanically Pumped Fluid Loop for 3-6 kW Payload Cooling," National Aerospace Laboratory NLR, Executive summary, Mar. 2010. Accessed: Jun. 02, 2020. [Online]. Available: <https://reports.nlr.nl/bitstream/handle/10921/251/TP-2009-459.pdf?sequence=1>.
 - [102] J. van Es, H. J. van Gerner, R. C. van Benthem, S. Lapensée, and D. Schwaller, "Component Developments in Europe for Mechanically Pumped Loop Systems (MPLs) for Cooling Applications in Space," 2016, vol. ICES-2016, p. 14.
 - [103] Pradeep Bhandari, "Mechanically Pumped Fluid Loops for Spacecraft Thermal Control: Past, Present and Future," presented at the 15th Annual Thermal & Fluid Analysis Workshop, Pasadena, CA, 2004, [Online]. Available: <https://tfaws.nasa.gov/TFAWS04/Website/program/Speakers/TFAWS2004PresentationonMechLoops-v1.pdf>.
 - [104] G. B. Ganapathi, G. C. Birur, G. T. Tsuyuki, P. L. McGrath, and J. D. Patzold, "Active Heat Rejection System on Mars Exploration Rover — Design Changes from Mars Pathfinder," in *AIP Conference Proceedings*, Jan. 2003, vol. 654, pp. 206–217, doi: 10.1063/1.1541296.
 - [105] P. Bhandari, B. Dudik, G. Birur, P. Karlmann, D. Bame, and A. Mastropietro, "Design of Accumulators and Liquid/Gas Charging of Single Phase Mechanically Pumped Fluid Loop Heat Rejection Systems," presented at the 42nd International Conference on Environmental Systems, San Diego, California, Jul. 2012, doi: 10.2514/6.2012-3515.
 - [106] P. Bhandari *et al.*, "Performance Of The Mechanically Pumped Fluid Loop Rover Heat Rejection System Used For Thermal Control Of The Mars Science Laboratory Curiosity Rover

-
- On The Surface Of Mars,” presented at the 43rd International Conference on Environmental Systems, Vail, CO, Jul. 2013, doi: 10.2514/6.2013-3323.
- [107] Gajanana C. Birur, “Thermal Control of MSL Rover Curiosity using an Active Fluid Loop,” presented at the 29th International Symposium on Space Technology and Science, Nagoya, Japan, Jun. 2013, Accessed: Jun. 02, 2020. [Online]. Available: https://trs.jpl.nasa.gov/bitstream/handle/2014/44150/13-1750_A1b.pdf.
- [108] G. C. Birur, P. Bhandari, M. Prina, D. P. Bame, A. H. Yavrouian, and G. A. Plett, “Mechanically Pumped Fluid Loop Technologies for Thermal Control of Future Mars Rovers,” *SAE Transactions*, vol. 115, pp. 95–103, 2006.
- [109] A. J. Mastropietro *et al.*, “Design and Preliminary Thermal Performance of the Mars Science Laboratory Rover Heat Exchangers,” presented at the 40th International Conference on Environmental Systems, Barcelona, Spain, Jul. 2010, doi: 10.2514/6.2010-6194.
- [110] D. B. Tuckerman and R. F. W. Pease, “High-performance heat sinking for VLSI,” *IEEE Electron Device Letters*, vol. 2, no. 5, pp. 126–129, mai 1981, doi: 10.1109/EDL.1981.25367.
- [111] S. G. Kandlikar and A. V. Bapat, “Evaluation of Jet Impingement, Spray and Microchannel Chip Cooling Options for High Heat Flux Removal: Heat Transfer Engineering: Vol 28, No 11,” *Heat Transfer Engineering*, vol. 28, no. 11, pp. 911–923, Nov. 2007, doi: 10.1080/01457630701421703.
- [112] B. Agostini, M. Fabbri, J. E. Park, L. Wojtan, J. R. Thome, and B. Michel, “State of the Art of High Heat Flux Cooling Technologies,” *Heat Transfer Engineering*, vol. 28, no. 4, pp. 258–281, Apr. 2007, doi: 10.1080/01457630601117799.
- [113] Girish Upadhyaya, Mark Munch, Peng Zhou, James Hom, Douglas Werner, and Mark McMaster, “Micro-scale liquid cooling system for high heat flux processor cooling applications,” in *Semiconductor Thermal Measurement and Management Symposium, 2006 IEEE Twenty-Second Annual IEEE*, 2006, pp. 116–119, Accessed: Apr. 10, 2017. [Online]. Available: <http://ieeexplore.ieee.org/abstract/document/1625215/>.
- [114] N. H. Naqiuddin, L. H. Saw, M. C. Yew, F. Yusof, T. C. Ng, and M. K. Yew, “Overview of micro-channel design for high heat flux application,” *Renewable and Sustainable Energy Reviews*, vol. 82, pp. 901–914, Feb. 2018, doi: 10.1016/j.rser.2017.09.110.
- [115] P. Smakulski and S. Pietrowicz, “A review of the capabilities of high heat flux removal by porous materials, microchannels and spray cooling techniques,” *Applied Thermal Engineering*, vol. 104, pp. 636–646, Jul. 2016, doi: 10.1016/j.applthermaleng.2016.05.096.
- [116] M. A. Ebadian and C. X. Lin, “A review of high-heat-flux heat removal technologies,” *Journal of heat transfer*, vol. 133, no. 11, p. 110801, 2011.
- [117] H. Hirshfeld, I. Silverman, A. Arenshtam, D. Kijel, and A. Nagler, “High heat flux cooling of accelerator targets with micro-channels,” *Nuclear Instruments and Methods in Physics Research Section A: Accelerators, Spectrometers, Detectors and Associated Equipment*, vol. 562, no. 2, pp. 903–905, Jun. 2006, doi: 10.1016/j.nima.2006.02.104.
- [118] Avram Bar-Cohen, Ed., *Encyclopedia of thermal packaging, Set 1: Thermal packaging techniques, Volume 1: Microchannel Heat Sinks for Electronics Cooling*, vol. 1, 6 vols. Singapore ; London: World Scientific, 2013.
- [119] A. Bar-Cohen, K. Matin, N. Jankowski, and D. Sharar, “Two-Phase Thermal Ground Planes: Technology Development and Parametric Results,” *J. Electron. Packag*, vol. 137, no. 1, pp. 010801–010801–9, Nov. 2014, doi: 10.1115/1.4028890.

-
- [120] Jaeseon Lee and I. Mudawar, "Low-Temperature Two-Phase Microchannel Cooling for High-Heat-Flux Thermal Management of Defense Electronics," *IEEE Transactions on Components and Packaging Technologies*, vol. 32, no. 2, pp. 453–465, Jun. 2009, doi: 10.1109/TCAPT.2008.2005783.
 - [121] Nina Zuzanna Wojtas, "Microfluidic Thermoelectric Heat Exchangers for Low-Temperature Waste Heat Recovery," PhD Thesis, ETH ZURICH, 2014.
 - [122] K. W. Jung *et al.*, "Microchannel cooling strategies for high heat flux (1 kW/cm²) power electronic applications," in *2017 16th IEEE Intersociety Conference on Thermal and Thermomechanical Phenomena in Electronic Systems (ITherm)*, May 2017, pp. 98–104, doi: 10.1109/ITHERM.2017.7992457.
 - [123] S. Szczukiewicz, N. Borhani, and J. R. Thome, "Two-phase flow boiling in a single layer of future high-performance 3D stacked computer chips," in *Thermal and Thermomechanical Phenomena in Electronic Systems (ITherm), 2012 13th IEEE Intersociety Conference on*, 2012, pp. 597–605, Accessed: Apr. 21, 2017. [Online]. Available: <http://ieeexplore.ieee.org/abstract/document/6231483/>.
 - [124] Nicolas LAMAISON, "Dynamic Modeling and Experimental Evaluation of a Controlled Two-Phase On-Chip Cooling System Designed for High Efficiency Datacenters," Ecole Polytechnique Fédérale de Lausanne, 2014.
 - [125] X. Wei, Y. Joshi, and M. K. Patterson, "Experimental and Numerical Study of a Stacked Microchannel Heat Sink for Liquid Cooling of Microelectronic Devices," *J. Heat Transfer*, vol. 129, no. 10, pp. 1432–1444, Oct. 2007, doi: 10.1115/1.2754781.
 - [126] Y. Joshi and X. Wei, "MICRO AND MESO SCALE COMPACT HEAT EXCHANGERS IN ELECTRONICS THERMAL MANAGEMENT-A REVIEW," p. 18.
 - [127] A. Y. M. Ali, E. M. Abo-Zahhad, M. F. Elkady, S. Ookawara, A. H. El-Shazly, and A. Radwan, "Temperature uniformity enhancement of densely packed high concentrator photovoltaic module using four quadrants microchannel heat sink," *Solar Energy*, vol. 202, pp. 446–464, May 2020, doi: 10.1016/j.solener.2020.03.106.
 - [128] Y. Joshi and P. Kumar, *Energy Efficient Thermal Management of Data Centers*. Springer Science & Business Media, 2012.
 - [129] N. Gernert, K. Wert, G. Baldassarre, and M. J. Wilson, "Pumped Liquid Cooling System for Desktop Computers," presented at the 38th, International symposium on microelectronics; IMAPS 2005, 2005.
 - [130] R. Van Erp, G. Kampitsis, and E. Matioli, "Efficient Microchannel Cooling of Multiple Power Devices with Compact Flow Distribution for High Power-Density Converters," *IEEE Transactions on Power Electronics*, pp. 1–1, 2019, doi: 10.1109/TPEL.2019.2959736.
 - [131] R. van Erp, G. Kampitsis, and E. Matioli, "A manifold microchannel heat sink for ultra-high power density liquid-cooled converters," in *2019 IEEE Applied Power Electronics Conference and Exposition (APEC)*, Mar. 2019, pp. 1383–1389, doi: 10.1109/APEC.2019.8722308.
 - [132] S. J. Pety, M. H. Y. Tan, A. R. Najafi, P. R. Barnett, P. H. Geubelle, and S. R. White, "Carbon fiber composites with 2D microvascular networks for battery cooling," *International Journal of Heat and Mass Transfer*, vol. 115, pp. 513–522, Dec. 2017, doi: 10.1016/j.ijheatmasstransfer.2017.07.047.
 - [133] E. Cetegen, "FORCE FED MICROCHANNEL HIGH HEAT FLUX COOLING UTILIZING MICRO-GROOVED SURFACES," 2010.

-
- [134] M. M. Ohadi, K. Choo, S. Dessiatoun, and E. Cetegen, *Next Generation Microchannel Heat Exchangers*. New York: Springer-Verlag, 2013.
 - [135] A. Mapelli, "Microfabricated silicon substrates for pixel detectors assembly and thermal management a.k.a. Silicon Microchannel Cooling Plates," *Nuclear Instruments and Methods in Physics Research Section A: Accelerators, Spectrometers, Detectors and Associated Equipment*, vol. 958, p. 162142, Apr. 2020, doi: 10.1016/j.nima.2019.04.096.
 - [136] G. Fiorenza, C. Pastore, V. Manzari, I. Sgura, M. Torresi, and C. Gargiulo, "An innovative polyimide microchannels cooling system for the pixel sensor of the upgraded ALICE inner tracker," in *5th IEEE International Workshop on Advances in Sensors and Interfaces IWASI*, Jun. 2013, pp. 81–85, doi: 10.1109/IWASI.2013.6576065.
 - [137] A. FRANCESCON *et al.*, "Development of interconnected silicon micro-evaporators for the on-detector electronics cooling of the future ITS detector in the ALICE experiment at LHC," presented at the 4th Micro and Nano Flows Conference, UCL, London, UK, Sep. 2014, [Online]. Available: http://bura.brunel.ac.uk/bitstream/2438/9402/1/FinalPaper_AF.pdf.
 - [138] L. Andricek *et al.*, "Integrated cooling channels in position-sensitive silicon detectors," *J. Inst.*, vol. 11, no. 06, pp. P06018–P06018, Jun. 2016, doi: 10.1088/1748-0221/11/06/P06018.
 - [139] G. Romagnoli *et al.*, "Silicon micro-fluidic cooling for NA62 GTK pixel detectors," *Microelectronic Engineering*, vol. 145, pp. 133–137, Sep. 2015, doi: 10.1016/j.mee.2015.04.006.
 - [140] Giulia Romagnoli, "Micro-fabricated Silicon Devices for Advanced Thermal Management and Integration of Particle Tracking Detectors," PhD Thesis, Università degli Studi di Genova, Genova, 2016.
 - [141] A. Mapelli *et al.*, "Low material budget microfabricated cooling devices for particle detectors and front-end electronics," *Nuclear Physics B-proceedings Supplements - NUCL PHYS B-PROC SUPPL*, vol. 215, pp. 349–352, Jun. 2011, doi: 10.1016/j.nuclphysbps.2011.04.050.
 - [142] G. A. Rinella *et al.*, "The NA62 GigaTracker: a low mass high intensity beam 4D tracker with 65 ps time resolution on tracks," *J. Inst.*, vol. 14, no. 07, pp. P07010–P07010, Jul. 2019, doi: 10.1088/1748-0221/14/07/P07010.
 - [143] J. Buytaert *et al.*, "Micro channel evaporative CO2 cooling for the upgrade of the LHCb vertex detector," *Nuclear Instruments and Methods in Physics Research Section A: Accelerators, Spectrometers, Detectors and Associated Equipment*, vol. 731, pp. 189–193, Dec. 2013, doi: 10.1016/j.nima.2013.03.069.
 - [144] A. Nomerotski *et al.*, "Evaporative CO2 cooling using microchannels etched in silicon for the future LHCb vertex detector," *Journal of Instrumentation*, vol. 8, no. 04, pp. P04004–P04004, Apr. 2013, doi: 10.1088/1748-0221/8/04/P04004.
 - [145] O. A. de A. Francisco *et al.*, "Evaporative CO2 microchannel cooling for the LHCb VELO pixel upgrade," *J. Inst.*, vol. 10, no. 05, pp. C05014–C05014, May 2015, doi: 10.1088/1748-0221/10/05/C05014.
 - [146] O. A. De Aguiar Francisco and LHCb VELO and CERN PH-DT collaborations, "Microchannel Cooling techniques at LHCb," in *Proceedings of The 26th International Workshop on Vertex Detectors — PoS(Vertex 2017)*, Las Caldas, Asturias, Spain, Nov. 2018, p. 024, doi: 10.22323/1.309.0024.
 - [147] O. A. De Aguiar Francisco, "Microchannel cooling techniques for the LHCb VELO Upgrade," presented at the 26th International Workshop on Vertex Detectors, Las Caldas, Asturias,

- Spain, Dec. 09, 2017, Accessed: Jan. 23, 2018. [Online]. Available: https://indico.cern.ch/event/627245/contributions/2676731/attachments/1522197/2378533/3.-170912_VELOUpgradeCooling_v5.pdf.
- [148] O. A. De Aguiar Francisco, W. Byczybski, and J. Buytaert, "Microchannel CO₂ cooling for the VELO Upgrade," presented at the The 9th International Workshop on Semiconductor Pixel Detectors for Particles and Imaging, (PIXEL2018), Taipei, Taiwan, Dec. 2018, [Online]. Available: <https://indico.cern.ch/event/669866/contributions/3226465/>.
- [149] Alessandro Mapelli, "Low mass integrated cooling," in *PoS (Vertex 2013)*, Lake Starnberg, Germany, 2014, p. 046, doi: 0.22323/1.198.0046.
- [150] G. Vidal, "Status of activities in ValenciaMicro-Channels & Forward Tracking Disks," presented at the AID2020, Oxford, UK, Apr. 02, 2019, Accessed: Jul. 09, 2020. [Online]. Available: https://indico.cern.ch/event/773447/contributions/3376221/attachments/1822433/2981426/Status_of_the_activities_in_Valencia.pdf.
- [151] Marcel Vos, "DEPFET active pixel detectors with integrated support and cooling," presented at the CEPC workshop, IHEP, Beijing, Nov. 2018, Accessed: Jul. 09, 2020. [Online]. Available: <https://indico.ihep.ac.cn/event/7389/session/10/contribution/30/material/slides/0.pdf>.
- [152] R. Cardella, "CMOS detector and system developments for LHC detector upgrades," PhD Thesis, University of Oslo, 2019.
- [153] M. Kluba, A. Arslan, R. Stoute, J. Muganda, and R. Dekker, "Single-Step CMOS Compatible Fabrication of High Aspect Ratio Microchannels Embedded in Silicon," *Proceedings*, vol. 1, no. 4, p. 291, Aug. 2017, doi: 10.3390/proceedings1040291.
- [154] I. Mudawar, "Two-Phase Microchannel Heat Sinks: Theory, Applications, and Limitations," *Journal of Electronic Packaging*, vol. 133, no. 4, p. 041002, 2011, doi: 10.1115/1.4005300.
- [155] G. C. Birur, T. W. Sur, A. D. Paris, P. Shakkottai, A. A. Green, and S. I. Haapanen, "Micro/nano spacecraft thermal control using a MEMS-based pumped liquid cooling system," in *Microfluidics and BioMEMS*, Sep. 2001, vol. 4560, pp. 196–206, doi: 10.1117/12.443059.
- [156] E. Hawkins-Reynolds, H. Le, and R. Stephan, "Development, Fabrication, and Testing of a Liquid/Liquid Microchannel Heat Exchanger for Constellation Spacecrafts," presented at the 40th International Conference on Environmental Systems, Barcelona, Spain, Jul. 2010, doi: 10.2514/6.2010-6137.
- [157] L. P. Yarin, A. Mosyak, and G. Hetsroni, *Fluid Flow, Heat Transfer and Boiling in Micro-Channels*. Berlin Heidelberg: Springer-Verlag, 2009.
- [158] A. Bar-Cohen, F. L. Robinson, and D. C. Deisenroth, "Challenges and opportunities in Gen3 embedded cooling with high-quality microgap flow," in *2018 International Conference on Electronics Packaging and iMAPS All Asia Conference (ICEP-IAAC)*, Mie, Japan, Apr. 2018, p. K-1-K-12, doi: 10.23919/ICEP.2018.8374353.
- [159] F. Robinson and A. Bar-Cohen, "Gravity effects in microgap flow boiling," in *2017 16th IEEE Intersociety Conference on Thermal and Thermomechanical Phenomena in Electronic Systems (ITherm)*, Orlando, FL, May 2017, pp. 480–491, doi: 10.1109/ITHERM.2017.7992513.
- [160] F. L. Robinson and A. Bar-Cohen, "Orientation Effects in Two-Phase Microgap Flow," *J. Electron. Packag*, vol. 141, no. 3, Sep. 2019, doi: 10.1115/1.4043483.
- [161] A. Bar-Cohen, J. J. Maurer, and D. H. Altman, "Embedded Cooling for Wide Bandgap Power Amplifiers: A Review," *J. Electron. Packag*, vol. 141, no. 4, Dec. 2019, doi: 10.1115/1.4043404.

-
- [162] D. Bae, R. Mandel, and M. Ohadi, "Effect of Bonding Structure and Heater Design on Performance Enhancement of FEEDS Embedded Manifold-Microchannel Cooling," p. V001T02A024, Aug. 2017, doi: 10.1115/IPACK2017-74158.
 - [163] D. G. Bae *et al.*, "Embedded two-phase cooling of high heat flux electronics on silicon carbide (SiC) using thin-film evaporation and an enhanced delivery system (FEEDS) manifold-microchannel cooler," in *2017 16th IEEE Intersociety Conference on Thermal and Thermo-mechanical Phenomena in Electronic Systems (ITherm)*, May 2017, pp. 466–472, doi: 10.1109/ITHERM.2017.7992511.
 - [164] T. Alam, P. S. Lee, and L.-W. Jin, *Flow Boiling in Microgap Channels: Experiment, Visualization and Analysis*. New York: Springer-Verlag, 2014.
 - [165] Amir Faghri, "HEAT PIPES: REVIEW, OPPORTUNITIES AND CHALLENGES," *Frontiers in Heat Pipes*, vol. 5, no. 1, Apr. 2014, doi: 10.5098/fhp.5.1.
 - [166] J. Perkins, "UK Patent No. 7059."
 - [167] S. Lips, V. Sartre, F. Lefevre, S. Khandekar, and J. Bonjour, "OVERVIEW OF HEAT PIPE STUDIES DURING THE PERIOD 2010-2015," *Interfacial Phenomena and Heat Transfer*, vol. 4, no. 1, pp. 33–53, 2016, doi: 10.1615/InterfacPhenomHeatTransfer.2016016345.
 - [168] N. Blet, S. Lips, and V. Sartre, "Heats pipes for temperature homogenization: A literature review," *Applied Thermal Engineering*, vol. 118, pp. 490–509, May 2017, doi: 10.1016/j.applthermaleng.2017.03.009.
 - [169] K. N. Shukla, "Heat Pipe for Aerospace Applications—An Overview," *Journal of Electronics Cooling and Thermal Control*, vol. 05, no. 01, pp. 1–14, 2015, doi: 10.4236/jectc.2015.51001.
 - [170] M. Marengo, "Novel Hybrid Heat Pipes for Space and Ground Applications (HyHP)," presented at the HyHP Kick-off meeting, Apr. 04, 2017, [Online]. Available: <https://cpb-euw2.wpmucdn.com/blogs.brighton.ac.uk/dist/e/2879/files/2017/04/Introduction-skmgcq.pdf>.
 - [171] F. Belfi, F. Iorizzo, C. Galbiati, and F. Lepore, "Space Structures With Embedded Flat Plate Pulsating Heat Pipe Built by Additive Manufacturing Technology: Development, Test and Performance Analysis," *J. Heat Transfer*, vol. 141, no. 9, Sep. 2019, doi: 10.1115/1.4042082.
 - [172] A. Faghri, "Review and Advances in Heat Pipe Science and Technology," *J. Heat Transfer*, vol. 134, no. 12, pp. 123001-123001–18, Oct. 2012, doi: 10.1115/1.4007407.
 - [173] McIntosh R., Ollendorf S., and Harwell W., "The International Heat Pipe Experiment," N76-32374 23–31, 1976. Accessed: Jun. 03, 2020. [Online]. Available: <https://ui.adsabs.harvard.edu/abs/1976hepi.rept..589M/abstract>.
 - [174] J. van Es and H.J. van Gerner, "Benefits and Drawbacks of Using Two-Phase Cooling Technologies in Military Platforms," Executive summary, 2011. Accessed: May 26, 2020. [Online]. Available: <https://core.ac.uk/download/pdf/53033946.pdf>.
 - [175] Cotter, T.P., "PRINCIPLES AND PROSPECTS FOR MICRO HEAT PIPES," 1984, Accessed: Mar. 19, 2018. [Online]. Available: <http://permalink.lanl.gov/object/tr?what=info:lanl-repo/lareport/LA-UR-84-0120>.
 - [176] G. P. Peterson, A. B. Duncan, and M. H. Weichold, "Experimental Investigation of Micro Heat Pipes Fabricated in Silicon Wafers," *J. Heat Transfer*, vol. 115, no. 3, pp. 751–756, Aug. 1993, doi: 10.1115/1.2910747.

-
- [177] S.-W. Kang and D. Huang, "Fabrication of star grooves and rhombus grooves micro heat pipe," *J. Micromech. Microeng.*, vol. 12, no. 5, pp. 525–531, Jun. 2002, doi: 10.1088/0960-1317/12/5/303.
 - [178] M. Hamidnia, Y. Luo, X. Wang, and G. Jing, "Thermal performance optimization of Si micro flat heat pipes by Box–Behnken design," *Microsystem Technologies*, Mar. 2018, doi: 10.1007/s00542-018-3829-y.
 - [179] B. Badran, F. M. Gerner, P. Ramadas, T. Henderson, and K. W. Baker, "Experimental Results for Low-Temperature Silicon Micromachined Micro Heat Pipe Arrays Using Water and Methanol as Working Fluids," *Experimental Heat Transfer*, vol. 10, no. 4, pp. 253–272, Oct. 1997, doi: 10.1080/08916159708946547.
 - [180] M. L. Berre, S. Launay, V. Sartre, and M. Lallemand, "Fabrication and experimental investigation of silicon micro heat pipes for cooling electronics," *J. Micromech. Microeng.*, vol. 13, no. 3, pp. 436–441, Mar. 2003, doi: 10.1088/0960-1317/13/3/313.
 - [181] C. Gillot, Y. Avenas, N. Cezac, G. Poupon, C. Schaeffer, and E. Fournier, "Silicon heat pipes used as thermal spreaders," *IEEE Transactions on Components and Packaging Technologies*, vol. 26, no. 2, pp. 332–339, Jun. 2003, doi: 10.1109/TCAPT.2003.815092.
 - [182] Y. Luo, G. Liu, L. Zou, B. Yu, and X. Wang, "Thermal behavior investigation of silicon-Pyrex micro heat pipe," *AIP Advances*, vol. 4, no. 3, p. 031305, Feb. 2014, doi: 10.1063/1.4861209.
 - [183] J. Kang, X. Fu, W. Liu, and P. Dario, "Investigation on Microheat Pipe Array with Arteries," *Journal of Thermophysics and Heat Transfer*, vol. 24, no. 4, pp. 803–810, 2010, doi: 10.2514/1.49913.
 - [184] S.-W. Kang, S.-H. Tsai, and H.-C. Chen, "Fabrication and test of radial grooved micro heat pipes," *Applied Thermal Engineering*, vol. 22, no. 14, pp. 1559–1568, Oct. 2002, doi: 10.1016/S1359-4311(02)00085-6.
 - [185] X. Xie, Q. Weng, Z. Luo, J. Long, and X. Wei, "Thermal performance of the flat micro-heat pipe with the wettability gradient surface by laser fabrication," *International Journal of Heat and Mass Transfer*, vol. 125, pp. 658–669, Oct. 2018, doi: 10.1016/j.ijheatmasstransfer.2018.04.110.
 - [186] J. T. Dickey and G. P. Peterson, "Experimental and analytical investigation of a capillary pumped loop," *Journal of Thermophysics and Heat Transfer*, vol. 8, no. 3, pp. 602–607, 1994, doi: 10.2514/3.584.
 - [187] R. R. Riehl, H. V. R. Camargo, L. Heinen, and E. Bazzo, "Experimental Investigation of a Capillary Pumped Loop Towards Its Integration on a Scientific Microsatellite," Jun. 2008, pp. 101–106, doi: 10.1115/IMECE2002-33557.
 - [188] Seok-Hwan Moon and Gunn Hwang, "Development of the micro capillary pumped loop for electronic cooling," in *2007 13th International Workshop on Thermal Investigation of ICs and Systems (THERMINIC)*, Sep. 2007, pp. 72–76, doi: 10.1109/THERMINIC.2007.4451750.
 - [189] M. Nikitkin and B. Cullimore, "CPL and LHP Technologies: What are the Differences, What are the Similarities?," *SAE Transactions*, vol. 107, pp. 400–408, 1998, doi: 10.2307/44735762.
 - [190] J. Kirshberg and K. L. Yerkes, "Micro-Cooler for Chip-Level Temperature Control," Apr. 1999, pp. 1999-01–1407, doi: 10.4271/1999-01-1407.

-
- [191] T. Semenic and I. Catton, "Experimental study of biporous wicks for high heat flux applications," *International Journal of Heat and Mass Transfer*, vol. 52, no. 21, pp. 5113–5121, Oct. 2009, doi: 10.1016/j.ijheatmasstransfer.2009.05.005.
 - [192] D. Cytrynowicz, M. Hamdan, P. Medis, H. T. Henderson, and F. M. Gerner, "Test Cell for a Novel Planar MEMS Loop Heat Pipe Based on Coherent Porous Silicon," *AIP Conference Proceedings*, vol. 654, no. 1, pp. 227–238, Jan. 2003, doi: 10.1063/1.1541298.
 - [193] N. S. Dhillon, "Micro-Columnated Loop Heat Pipe: The Future of Electronic Substrates," PhD Thesis, University of California, Berkley, 2012.
 - [194] H. Tang *et al.*, "Review of applications and developments of ultra-thin micro heat pipes for electronic cooling," *Applied Energy*, vol. 223, pp. 383–400, Aug. 2018, doi: 10.1016/j.apenergy.2018.04.072.
 - [195] G. Zhou, J. Li, and L. Lv, "An ultra-thin miniature loop heat pipe cooler for mobile electronics," *Applied Thermal Engineering*, vol. 109, pp. 514–523, Oct. 2016, doi: 10.1016/j.applthermaleng.2016.08.138.
 - [196] T. Shioga and Y. Mizuno, "Micro loop heat pipe for mobile electronics applications," in *2015 31st Thermal Measurement, Modeling Management Symposium (SEMI-THERM)*, Mar. 2015, pp. 50–55, doi: 10.1109/SEMI-THERM.2015.7100139.
 - [197] J.-Y. Jung, H.-S. Oh, D. K. Lee, K. B. Choi, S. K. Dong, and H.-Y. Kwak, "A capillary-pumped loop (CPL) with microcone-shaped capillary structure for cooling electronic devices," *Journal of Micromechanics and Microengineering*, vol. 18, no. 1, p. 017002, Jan. 2008, doi: 10.1088/0960-1317/18/1/017002.
 - [198] L. Meyer *et al.*, "A silicon-carbide micro-capillary pumped loop for cooling high power devices," in *Nineteenth Annual IEEE Semiconductor Thermal Measurement and Management Symposium, 2003.*, Mar. 2003, pp. 364–368, doi: 10.1109/STHERM.2003.1194386.
 - [199] H. Akachi, "Structure of a Heat Pipe," US4921041, 1990.
 - [200] H. Akachi, "Structure of Micro-Heat Pipe," US5219020, 1993.
 - [201] J. Qu and H. Wu, "Flow visualization of silicon-based micro pulsating heat pipes," *Sci. China Technol. Sci.*, vol. 53, no. 4, pp. 984–990, Apr. 2010, doi: 10.1007/s11431-009-0391-y.
 - [202] J. Qu, H. Wu, and P. Cheng, "Start-up, heat transfer and flow characteristics of silicon-based micro pulsating heat pipes," *International Journal of Heat and Mass Transfer*, vol. 55, no. 21–22, pp. 6109–6120, Oct. 2012, doi: 10.1016/j.ijheatmasstransfer.2012.06.024.
 - [203] J. Qu, X. Li, Q. Wang, F. Liu, and H. Guo, "Heat transfer characteristics of micro-grooved oscillating heat pipes," *Experimental Thermal and Fluid Science*, vol. 85, pp. 75–84, Jul. 2017, doi: 10.1016/j.expthermflusci.2017.02.022.
 - [204] J. Qu and Q. Wang, "Experimental study on the thermal performance of vertical closed-loop oscillating heat pipes and correlation modeling," *Applied Energy*, vol. 112, pp. 1154–1160, Dec. 2013, doi: 10.1016/j.apenergy.2013.02.030.
 - [205] Q. Sun, J. Qu, J. Yuan, and Q. Wang, "Operational characteristics of an MEMS-based micro oscillating heat pipe," *Applied Thermal Engineering*, vol. 124, pp. 1269–1278, Sep. 2017, doi: 10.1016/j.applthermaleng.2017.06.109.
 - [206] Qin Sun, Jian Qu, Jianping Yuan, and Hai Wang, "Start-up characteristics of MEMS-based micro oscillating heat pipe with and without bubble nucleation," *IJHM*, vol. 122, pp. 515–528, Jul. 2018.

-
- [207] H. B. Ma, M. A. Hanlon, and C. L. Chen, "An investigation of oscillating motions in a miniature pulsating heat pipe," *Microfluid Nanofluid*, vol. 2, no. 2, pp. 171–179, Mar. 2006, doi: 10.1007/s10404-005-0061-8.
 - [208] P. Charoensawan, S. Khandekar, M. Groll, and P. Terdtoon, "Closed loop pulsating heat pipes Part A: parametric experimental investigations," *Applied Thermal Engineering*, 2003.
 - [209] S. Khandekar, P. Charoensawan, M. Groll, and P. Terdtoon, "Closed loop pulsating heat pipes Part B: visualization and semi-empirical modeling," *Applied Thermal Engineering*, vol. 23, no. 16, pp. 2021–2033, Nov. 2003, doi: 10.1016/S1359-4311(03)00168-6.
 - [210] S. Khandekar, M. Schneider, P. Schäfer, R. Kulenovic, and M. Groll, "Thermofluid Dynamic Study of Flat-plate Closed-loop Pulsating Heat Pipes," *Microscale Thermophysical Engineering*, vol. 6, pp. 303–317, 2002.
 - [211] S. F. de Vries, D. Florea, F. G. A. Homburg, and A. J. H. Frijns, "Design and operation of a Tesla-type valve for pulsating heat pipes," *International Journal of Heat and Mass Transfer*, vol. 105, pp. 1–11, Feb. 2017, doi: 10.1016/j.ijheatmasstransfer.2016.09.062.
 - [212] S. M. Thompson, H. B. Ma, and C. Wilson, "Investigation of a flat-plate oscillating heat pipe with Tesla-type check valves," *Experimental Thermal and Fluid Science*, vol. 35, no. 7, pp. 1265–1273, Oct. 2011, doi: 10.1016/j.exptthermflusci.2011.04.014.
 - [213] K. H. Chien, Y. R. Chen, Y. T. Lin, C. C. Wang, and K. S. Yang, "The Experimental Studies of Flat-Plate Closed-Loop Pulsating Heat Pipes," 2011, p. 5.
 - [214] S. Khandekar, A. P. Gautam, and P. K. Sharma, "Multiple quasi-steady states in a closed loop pulsating heat pipe," *International Journal of Thermal Sciences*, vol. 48, no. 3, pp. 535–546, Mar. 2009, doi: 10.1016/j.ijthermalsci.2008.04.004.
 - [215] Y. Zhang and A. Faghri, "Advances and Unsolved Issues in Pulsating Heat Pipes," *Heat Transfer Engineering*, vol. 29, no. 1, pp. 20–44, Jan. 2008, doi: 10.1080/01457630701677114.
 - [216] R. Dobson and T. Harms, "Lumped parameter analysis of closed and open oscillatory heat pipes," presented at the 11th International heat pipe Conference, 1999.
 - [217] J. Qu, Q. Wang, and Q. Sun, "Lower limit of internal diameter for oscillating heat pipes: A theoretical model," *International Journal of Thermal Sciences*, vol. 110, pp. 174–185, Dec. 2016, doi: 10.1016/j.ijthermalsci.2016.07.002.
 - [218] S. M. Thompson and H. B. Ma, "Effect of Localized Heating on Three-Dimensional Flat-Plate Oscillating Heat Pipe," *Advances in Mechanical Engineering*, vol. 2, p. 465153, Jan. 2010, doi: 10.1155/2010/465153.
 - [219] S. M. Thompson, P. Cheng, and H. B. Ma, "An experimental investigation of a three-dimensional flat-plate oscillating heat pipe with staggered microchannels," *International Journal of Heat and Mass Transfer*, vol. 54, no. 17, pp. 3951–3959, Aug. 2011, doi: 10.1016/j.ijheatmasstransfer.2011.04.030.
 - [220] Y. J. Youn and S. J. Kim, "Fabrication and evaluation of a silicon-based micro pulsating heat spreader," *Sensors and Actuators A: Physical*, vol. 174, pp. 189–197, Feb. 2012, doi: 10.1016/j.sna.2011.12.006.
 - [221] J. Qu, H.-Y. Wu, and Q. Wang, "Experimental Investigation of Silicon-Based Micro-Pulsating Heat Pipe for Cooling Electronics," *Nanoscale and Microscale Thermophysical Engineering - NANOSCALE MICROSCALE THERMO E*, vol. 16, pp. 37–49, Jan. 2012, doi: 10.1080/15567265.2011.645999.
 - [222] K.-H. Chien, Y.-T. Lin, Y.-R. Chen, K.-S. Yang, and C.-C. Wang, "A novel design of pulsating heat pipe with fewer turns applicable to all orientations," *International Journal of Heat and*

-
- Mass Transfer*, vol. 55, no. 21, pp. 5722–5728, Oct. 2012, doi: 10.1016/j.ijheatmasstransfer.2012.05.068.
- [223] K.-S. Yang, Y.-C. Cheng, M.-S. Jeng, K.-H. Chien, and J.-C. Shyu, “An Experimental Investigation of Micro Pulsating Heat Pipes,” *Micromachines*, vol. 5, no. 2, pp. 385–395, Jun. 2014, doi: 10.3390/mi5020385.
- [224] G. Spinato, “Thermo-Hydrodynamics in a Closed Loop Pulsating Heat Pipe,” Ecole Polytechnique Fédérale de Lausanne, 2014.
- [225] Miriam Manzoni, Mauro Mameli, C. de Falco, Lucio Araneo, Sauro Filippeschi, and Marco Marengo, “Toward A Design Of A Micro Pulsating Heat Pipe,” presented at the 4th European Conference on Microfluidics, Limerick, 2014.
- [226] G. H. Kwon and S. J. Kim, “Experimental investigation on the thermal performance of a micro pulsating heat pipe with a dual-diameter channel,” *International Journal of Heat and Mass Transfer*, vol. 89, no. Supplement C, pp. 817–828, Oct. 2015, doi: 10.1016/j.ijheatmasstransfer.2015.05.091.
- [227] K.-S. Yang, Y.-C. Cheng, M.-C. Liu, and J.-C. Shyu, “Micro pulsating heat pipes with alternate microchannel widths,” *Applied Thermal Engineering*, vol. 83, pp. 131–138, May 2015, doi: 10.1016/j.applthermaleng.2015.03.020.
- [228] S. Jun and S. J. Kim, “Comparison of the thermal performances and flow characteristics between closed-loop and closed-end micro pulsating heat pipes,” *International Journal of Heat and Mass Transfer*, vol. 95, pp. 890–901, Apr. 2016, doi: 10.1016/j.ijheatmasstransfer.2015.12.064.
- [229] Y. B. Kim, H. W. Song, and J. Sung, “Flow behavior of rapid thermal oscillation inside an asymmetric micro pulsating heat exchanger,” *International Journal of Heat and Mass Transfer*, vol. 120, pp. 923–929, May 2018, doi: 10.1016/j.ijheatmasstransfer.2017.12.101.
- [230] X. Liu, L. Xu, C. Wang, and X. Han, “Experimental study on thermo-hydrodynamic characteristics in a micro oscillating heat pipe,” *Experimental Thermal and Fluid Science*, vol. 109, p. 109871, Dec. 2019, doi: 10.1016/j.expthermflusci.2019.109871.
- [231] J. Lim and S. J. Kim, “Effect of a channel layout on the thermal performance of a flat plate micro pulsating heat pipe under the local heating condition,” *International Journal of Heat and Mass Transfer*, vol. 137, pp. 1232–1240, Jul. 2019, doi: 10.1016/j.ijheatmasstransfer.2019.03.121.
- [232] Q. Sun, J. Qu, J. Yuan, H. Wang, and S. M. Thompson, “Fluid Flow and Heat Transfer Characteristics of Micro Oscillating Heat Pipes With and Without Expanding Channels,” presented at the ASME 2019 6th International Conference on Micro/Nanoscale Heat and Mass Transfer, Dec. 2019, doi: 10.1115/MNHMT2019-3976.
- [233] V. Patel, N. Mehta, K. Mehta, A. Badgujar, S. Mehta, and N. Bora, “Experimental Investigation of Flat Plate Cryogenic Oscillating Heat Pipe,” *J Low Temp Phys*, vol. 198, no. 1, pp. 41–55, Jan. 2020, doi: 10.1007/s10909-019-02243-1.
- [234] C. Jung, J. Lim, and S. J. Kim, “Fabrication and evaluation of a high-performance flexible pulsating heat pipe hermetically sealed with metal,” *International Journal of Heat and Mass Transfer*, vol. 149, p. 119180, Mar. 2020, doi: 10.1016/j.ijheatmasstransfer.2019.119180.
- [235] D. S. Jang, D. Kim, S. H. Hong, and Y. Kim, “Comparative thermal performance evaluation between ultrathin flat plate pulsating heat pipe and graphite sheet for mobile electronic devices at various operating conditions,” *Applied Thermal Engineering*, vol. 149, pp. 1427–1434, Feb. 2019, doi: 10.1016/j.applthermaleng.2018.12.146.

-
- [236] G. P. Peterson, "Overview of Micro Heat Pipe Research and Development," *Appl. Mech. Rev.*, vol. 45, no. 5, pp. 175–189, May 1992, doi: 10.1115/1.3119755.
 - [237] J. A. Weibel and S. V. Garimella, "Chapter Four - Recent Advances in Vapor Chamber Transport Characterization for High-Heat-Flux Applications," in *Advances in Heat Transfer*, vol. 45, E. M. Sparrow, Y. I. Cho, J. P. Abraham, and J. M. Gorman, Eds. Elsevier, 2013, pp. 209–301.
 - [238] Q. Cai, B. Chen, and C. Tsai, "Design, development and tests of high-performance silicon vapor chamber," *J. Micromech. Microeng.*, vol. 22, no. 3, p. 035009, Feb. 2012, doi: 10.1088/0960-1317/22/3/035009.
 - [239] C. Ding, G. Soni, P. Bozorgi, B. D. Piorek, C. D. Meinhart, and N. C. MacDonald, "A Flat Heat Pipe Architecture Based on Nanostructured Titania," *Journal of Microelectromechanical Systems*, vol. 19, no. 4, pp. 878–884, Aug. 2010, doi: 10.1109/JMEMS.2010.2051019.
 - [240] M. Bulut, S. G. Kandlikar, and N. Sozbir, "A Review of Vapor Chambers," *Heat Transfer Engineering*, vol. 40, no. 19, pp. 1551–1573, Nov. 2019, doi: 10.1080/01457632.2018.1480868.
 - [241] N. Kumar *et al.*, "Design, fabrication, and performance evaluation of a novel orientation independent and wickless heat spreader," *International Journal of Heat and Mass Transfer*, vol. 153, p. 119572, Jun. 2020, doi: 10.1016/j.ijheatmasstransfer.2020.119572.
 - [242] G. S. Hwang, Y. Nam, E. Fleming, P. Dussinger, Y. S. Ju, and M. Kaviani, "Multi-artery heat pipe spreader: Experiment," *International Journal of Heat and Mass Transfer*, vol. 53, no. 13, pp. 2662–2669, Jun. 2010, doi: 10.1016/j.ijheatmasstransfer.2010.02.046.
 - [243] Q. Cai, B.-C. Chen, C. Tsai, and C. Chen, "Development of Scalable Silicon Heat Spreader for High Power Electronic Devices," *J. Thermal Sci. Eng. Appl.*, vol. 1, no. 4, pp. 041009–041009–7, Jun. 2010, doi: 10.1115/1.4001689.
 - [244] M. Ando *et al.*, "On-orbit demonstration of oscillating heat pipe with check valves for space application," *Applied Thermal Engineering*, vol. 130, pp. 552–560, Feb. 2018, doi: 10.1016/j.applthermaleng.2017.11.032.
 - [245] B. S. Taft and K. W. Irick, "ASETS-II OSCILLATING HEAT PIPE SPACE FLIGHT EXPERIMENT: THE FIRST SIX MONTHS ON ORBIT," *Frontiers in Heat and Mass Transfer*, vol. 12, May 2019, doi: 10.5098/hmt.12.24.
 - [246] S. Brungs *et al.*, "Facilities for Simulation of Microgravity in the ESA Ground-Based Facility Programme," *Microgravity Sci. Technol.*, vol. 28, no. 3, pp. 191–203, Jun. 2016, doi: 10.1007/s12217-015-9471-8.
 - [247] D. Mangini, M. Mameli, D. Fioriti, S. Filippeschi, L. Araneo, and M. Marengo, "Hybrid Pulsating Heat Pipe for space applications with non-uniform heating patterns: Ground and microgravity experiments," *Applied Thermal Engineering*, Jan. 2017, doi: 10.1016/j.applthermaleng.2017.01.035.
 - [248] R. Savino, Y. Abe, and R. Fortezza, "Comparative study of heat pipes with different working fluids under normal gravity and microgravity conditions," *Acta Astronautica*, vol. 63, no. 1–4, pp. 24–34, Jul. 2008, doi: 10.1016/j.actaastro.2007.12.037.
 - [249] M. Maeda, A. Okamoto, H. Kawasaki, and H. Sugita, "Development of Flat Plate Heat Pipe and the Project of On-orbit Experiment," doi: 10.2514/6.2011-5142.
 - [250] F. Creatini *et al.*, "Pulsating Heat pipe Only for Space (PHOS): results of the REXUS 18 sounding rocket campaign," *J. Phys.: Conf. Ser.*, vol. 655, no. 1, p. 012042, 2015, doi: 10.1088/1742-6596/655/1/012042.

-
- [251] B. S. Taft, F. F. Laun, S. M. Smith, and D. W. Hengeveld, "Microgravity Performance of a Structurally Embedded Oscillating Heat Pipe," *Journal of Thermophysics and Heat Transfer*, vol. 29, no. 2, pp. 329–337, 2015, doi: 10.2514/1.T4151.
- [252] M. Manzoni, M. Mameli, C. de Falco, L. Araneo, S. Filippeschi, and M. Marengo, "Non equilibrium lumped parameter model for Pulsating Heat Pipes: validation in normal and hypergravity conditions," *International Journal of Heat and Mass Transfer*, vol. 97, pp. 473–485, Jun. 2016, doi: 10.1016/j.ijheatmasstransfer.2016.02.026.
- [253] M. Mameli, L. Araneo, S. Filippeschi, L. Marelli, R. Testa, and M. Marengo, "Thermal response of a closed loop pulsating heat pipe under a varying gravity force," *International Journal of Thermal Sciences*, vol. 80, pp. 11–22, Jun. 2014, doi: 10.1016/j.ijthermalsci.2014.01.023.
- [254] M. Slobodeniuk, V. Ayel, R. Bertossi, C. Romestant, and Y. Bertin, "Infrared thermography of fluid flow in flat plate pulsating heat pipes tested under microgravity conditions," p. 9.
- [255] K. V. Paiva, M. B. H. Mantelli, and L. K. Slongo, "Experimental testing of mini heat pipes under microgravity conditions aboard a suborbital rocket," *Aerospace Science and Technology*, vol. 45, pp. 367–375, Sep. 2015, doi: 10.1016/j.ast.2015.06.004.
- [256] J. Gu, M. Kawaji, and R. Futamata, "Microgravity performance of micro pulsating heat pipes," *Microgravity sci. Technol.*, vol. 16, no. 1, pp. 181–185, Mar. 2005, doi: 10.1007/BF02945972.
- [257] J. Gu, M. Kawaji, and R. Futamata, "Effects of Gravity on the Performance of Pulsating Heat Pipes," *Journal of Thermophysics and Heat Transfer*, vol. 18, no. 3, pp. 370–378, Jul. 2004, doi: 10.2514/1.3067.
- [258] D. Mangini, M. Mameli, A. Georgoulas, L. Araneo, S. Filippeschi, and M. Marengo, "A pulsating heat pipe for space applications: Ground and microgravity experiments," *International Journal of Thermal Sciences*, vol. 95, pp. 53–63, Sep. 2015, doi: 10.1016/j.ijthermalsci.2015.04.001.
- [259] V. Ayel *et al.*, "Experimental study of a closed loop flat plate pulsating heat pipe under a varying gravity force," *International Journal of Thermal Sciences*, vol. 96, pp. 23–34, Oct. 2015, doi: 10.1016/j.ijthermalsci.2015.04.010.
- [260] V. Ayel, L. Araneo, P. Marzorati, C. Romestant, Y. Bertin, and M. Marengo, "Visualizations of the flow patterns in a closed loop flat plate PHP with channel diameter above the critical one and tested under microgravity," Jeju, Korea, p. 9.
- [261] V. Ayel, L. Araneo, P. Marzorati, C. Romestant, Y. Bertin, and M. Marengo, "Visualization of Flow Patterns in Closed Loop Flat Plate Pulsating Heat Pipe Acting as Hybrid Thermosyphons under Various Gravity Levels," *Heat Transfer Engineering*, vol. 40, no. 3–4, pp. 227–237, Feb. 2019, doi: 10.1080/01457632.2018.1426244.
- [262] M. Felt, M. Sinfield, B. Thompson, M. Munns, and K. Lloyd, "Thermal Conductance Measurement and Flexibility Enhancement of Flexible Thermal Links," p. 23, 2017.
- [263] M. J. Montesano, "Annealed Pyrolytic Graphite," *Advanced Materials & Processes*, vol. 164, no. 6, p. 44, Jun. 2006.
- [264] D. Hengeveld, M. Mathison, J. Braun, E. Groll, and A. Williams, "Review of Modern Spacecraft Thermal Control Technologies," *HVAC&R Research*, vol. 16, pp. 189–220, Mar. 2010, doi: 10.1080/10789669.2010.10390900.

-
- [265] H.-G. Moser, "SCT End-cap Module Components: Spines," SCT-IS-EN-0009, Jul. 2002. Accessed: Jun. 09, 2020. [Online]. Available: https://www.atlas.mpp.mpg.de/atlas_sct/spine_fdr.pdf.
 - [266] T. Guillemet, P.-M. Geffroy, J.-M. Heintz, N. Chandra, Y. Lu, and J.-F. Silvain, "An innovative process to fabricate copper/diamond composite films for thermal management applications," *Composites Part A: Applied Science and Manufacturing*, vol. 43, no. 10, pp. 1746–1753, Oct. 2012, doi: 10.1016/j.compositesa.2012.04.015.
 - [267] A. Balandin, "Thermal Properties of Graphene, Carbon Nanotubes and Nanostructured Carbon Materials," *Nature materials*, vol. 10, pp. 569–81, Jul. 2011, doi: 10.1038/nmat3064.
 - [268] C. Silvestri, "Carbon nanotube based solutions for on-chip thermal management," Delft University of Technology, 2017.
 - [269] F. S. Porter *et al.*, "The detector subsystem for the SXS instrument on the ASTRO-H Observatory," San Diego, California, USA, Jul. 2010, p. 77323J, doi: 10.1117/12.857888.
 - [270] S. J. Nieczkoski and E. A. Myers, "Highly-Conductive Graphite Thermal Straps Used in Conjunction with Vibration Isolation Mounts for Cryocoolers," in *Proceedings of the 18th International Cryocooler Conference*, Syracuse, New Yrk, Jun. 2014, p. 8.
 - [271] B. N. Tomboulia, "Lightweight, High-Temperature Radiator for In-Space Nuclear-Electric Power and Propulsion," University of Massachusetts Amherst, 2014.
 - [272] V. Perotto, M. Gottero, S. Mannu, R. Martino, and S. Tavera, "Design and Test of ExoMars Thermal Breadboard," presented at the 41st International Conference on Environmental Systems, Portland, Oregon, Jul. 2011, doi: 10.2514/6.2011-5118.
 - [273] I. M. McKinley, C. H. Smith, P. G. Ramsey, and J. I. Rodriguez, "Pyrolytic graphite film thermal straps: Characterization testing," *Cryogenics*, vol. 80, pp. 174–180, Dec. 2016, doi: 10.1016/j.cryogenics.2016.10.002.
 - [274] Y. Fu *et al.*, "Graphene related materials for thermal management," *2D Mater.*, vol. 7, no. 1, p. 012001, Oct. 2019, doi: 10.1088/2053-1583/ab48d9.
 - [275] X. Zhao *et al.*, "A review of studies using graphenes in energy conversion, energy storage and heat transfer development," *Energy Conversion and Management*, vol. 184, pp. 581–599, Mar. 2019, doi: 10.1016/j.enconman.2019.01.092.
 - [276] "Thermal LyNX graphene thermal straps have superior thermal efficiency and flexibility," *Thermal Space*. <https://thermal-space.com/thermal-lynx/> (accessed Jun. 09, 2020).
 - [277] J. B. Marcinichen, J. A. Olivier, V. de Oliveira, and J. R. Thome, "A review of on-chip micro-evaporation: Experimental evaluation of liquid pumping and vapor compression driven cooling systems and control," *Applied Energy*, vol. 92, pp. 147–161, Apr. 2012, doi: 10.1016/j.apenergy.2011.10.030.
 - [278] F. Tavakkoli, S. Ebrahimi, S. Wang, and K. Vafai, "Analysis of critical thermal issues in 3D integrated circuits," *International Journal of Heat and Mass Transfer*, vol. 97, pp. 337–352, Jun. 2016, doi: 10.1016/j.ijheatmasstransfer.2016.02.010.
 - [279] Jorgen Christiansen, "Serial powering presentation on issues and optimization," Oct. 29, 2019, Accessed: Apr. 01, 2021. [Online]. Available: https://indico.cern.ch/event/928451/attachments/2054533/3444680/serial_power_operation_optimization_v3.pdf.
 - [280] RD53 collaboration and Jorgen Christiansen, "RD53B Design Requirements," Technical Report CERN-RD53-PUB-19-001, Feb. 2019. Accessed: Apr. 01, 2021. [Online]. Available: https://cds.cern.ch/record/2663161/files/RD53B_Requirements_V3_1.pdf.

-
- [281] RD53 collaboration and Jorgen Christiansen, "RD53B users guide: Introduction to RD53B pixel chip architecture, features and recommendations for use in pixel detector systems," Nov. 2021. Accessed: Apr. 01, 2021. [Online]. Available: http://cds.cern.ch/record/2754251/files/users_guide_v10.pdf.
- [282] M. Garcia-Sciveres, "RD53 Status and Plans," presented at the 6th LHCC Report, Nov. 09, 2019, Accessed: Apr. 01, 2021. [Online]. Available: https://indico.cern.ch/event/835603/contributions/3502836/attachments/1905560/3147006/LHCC_status_report_2019_open-v3.pdf.
- [283] G. H. Kwon and S. J. Kim, "Operational characteristics of pulsating heat pipes with a dual-diameter tube," *International Journal of Heat and Mass Transfer*, vol. 75, pp. 184–195, Aug. 2014, doi: 10.1016/j.ijheatmasstransfer.2014.03.032.
- [284] T. Harirchian and S. V. Garimella, "A comprehensive flow regime map for microchannel flow boiling with quantitative transition criteria," *International Journal of Heat and Mass Transfer*, vol. 53, no. 13–14, pp. 2694–2702, Jun. 2010, doi: 10.1016/j.ijheatmasstransfer.2010.02.039.
- [285] C. Antoine, "Tensions des vapeurs; nouvelle relation entre les tensions et les températures," Académie de Sciences, Paris, 107, 1888. [Online]. Available: <http://visualiseur.bnf.fr/CadresFenetre?O=NUMM-3063&M=tdm>.
- [286] G. Spinato, N. Borhani, B. P. d'Entremont, and J. R. Thome, "Time-strip visualization and thermo-hydrodynamics in a Closed Loop Pulsating Heat Pipe," *Applied Thermal Engineering*, vol. 78, pp. 364–372, Mar. 2015, doi: 10.1016/j.applthermaleng.2014.12.045.
- [287] N. Borhani, B. Agostini, and J. R. Thome, "A novel time strip flow visualisation technique for investigation of intermittent dewetting and dryout in elongated bubble flow in a micro-channel evaporator," *International Journal of Heat and Mass Transfer*, vol. 53, no. 21, pp. 4809–4818, Oct. 2010, doi: 10.1016/j.ijheatmasstransfer.2010.06.011.
- [288] M. T. Blom *et al.*, "Failure mechanisms of pressurized microchannels: model and experiments," *Journal of Microelectromechanical Systems*, vol. 10, no. 1, pp. 158–164, Mar. 2001, doi: 10.1109/84.911105.
- [289] S. Woinowsky-Krieger and S. Timoshenko, *Theory of Plates and Shells*. McGRAWHILL-BOOKCOMPANY, 1959.
- [290] Ö. Vallin, K. Jonsson, and U. Lindberg, "Adhesion quantification methods for wafer bonding," *Materials Science and Engineering: R: Reports*, vol. 50, no. 4, pp. 109–165, Dec. 2005, doi: 10.1016/j.mser.2005.07.002.
- [291] Diego Álvarez, Jordan Degrange, Alessandro Mapelli, and Jérôme Noel, "Pressure resistance of silicon microchannels." CERN, Oct. 2017, Accessed: Apr. 08, 2021. [Online]. Available: <https://edms.cern.ch/ui/#!master/navigator/document?P:100177717:100676615:subDocs>.
- [292] P. Petagna, "Micro-channel cooling," presented at the EIC Tracking workshop, University of Virginia, Charlottesville, VA, Jul. 24, 2018, Accessed: Feb. 16, 2021. [Online]. Available: https://indico.cern.ch/event/722363/contributions/3031253/attachments/1691910/2722306/EIC-2018Jul24_Microchannel_2.pdf.
- [293] Christine H. Tsau, "Fabrication and Characterization of Wafer-level Gold Thermocompression Bonding," Massachusetts Institute of Technology, 2003.
- [294] M. M. V. Taklo, P. Storåas, K. Schjøberg-Henriksen, H. K. Hasting, and H. Jakobsen, "Strong, high-yield and low-temperature thermocompression silicon wafer-level bonding

- with gold,” *J. Micromech. Microeng.*, vol. 14, no. 7, pp. 884–890, May 2004, doi: 10.1088/0960-1317/14/7/007.
- [295] A. G. Evans and B. J. Dalgleish, “The fracture resistance of metal-ceramic interfaces,” *Acta Metallurgica et Materialia*, vol. 40, pp. S295–S306, Jan. 1992, doi: 10.1016/0956-7151(92)90289-Q.
- [296] S. Charlot, P. Pons, M. Dilhan, I. Vallet, and S. Brida, “Hermetic Cavities Using Gold Wafer Level Thermocompression Bonding,” *Proceedings*, vol. 1, no. 4, p. 607, Aug. 2017, doi: 10.3390/proceedings1040607.
- [297] S. M. Spearing, C. H. Tsau, and M. A. Schmidt, “Gold Thermocompression Wafer Bonding,” 2004. [Online]. Available: <http://hdl.handle.net/1721.1/3828>.
- [298] M. Yamamoto *et al.*, “Comparison of Argon and Oxygen Plasma Treatments for Ambient Room-Temperature Wafer-Scale Au–Au Bonding Using Ultrathin Au Films,” *Micromachines*, vol. 10, no. 2, p. 119, Feb. 2019, doi: 10.3390/mi10020119.
- [299] H. K. Sahoo, L. Ottaviano, Y. Zheng, K. Yvind, and O. Hansen, “Low temperature bonding of heterogeneous materials using Al₂O₃ as an intermediate layer,” in *Integrated Optics: Devices, Materials, and Technologies XXII*, San Francisco, United States, Feb. 2018, p. 28, doi: 10.1117/12.2289526.
- [300] H. Yang, S. Khandekar, and M. Groll, “Performance characteristics of pulsating heat pipes as integral thermal spreaders,” *International Journal of Thermal Sciences*, vol. 48, no. 4, pp. 815–824, Apr. 2009, doi: 10.1016/j.ijthermalsci.2008.05.017.
- [301] D. S. Jang, J. S. Lee, J. H. Ahn, D. Kim, and Y. Kim, “Flow patterns and heat transfer characteristics of flat plate pulsating heat pipes with various asymmetric and aspect ratios of the channels,” *Applied Thermal Engineering*, vol. 114, pp. 211–220, Mar. 2017, doi: 10.1016/j.applthermaleng.2016.11.189.
- [302] W. Qu and H. B. Ma, “Theoretical analysis of startup of a pulsating heat pipe,” *International Journal of Heat and Mass Transfer*, vol. 50, no. 11, pp. 2309–2316, Jun. 2007, doi: 10.1016/j.ijheatmasstransfer.2006.10.043.
- [303] Z. A. Syed Mohammed, M. A. S. Olimpo, D. P. Poenar, and S. Aditya, “Smoothing of scalloped DRIE trench walls,” *Materials Science in Semiconductor Processing*, vol. 63, pp. 83–89, Jun. 2017, doi: 10.1016/j.mssp.2017.02.006.
- [304] J. Lee and S. J. Kim, “Effect of channel geometry on the operating limit of micro pulsating heat pipes,” *International Journal of Heat and Mass Transfer*, vol. 107, no. Supplement C, pp. 204–212, Apr. 2017, doi: 10.1016/j.ijheatmasstransfer.2016.11.036.
- [305] G. Croce, P. D’agaro, and C. Nonino, “Three-dimensional roughness effect on microchannel heat transfer and pressure drop,” *International Journal of Heat and Mass Transfer*, vol. 50, no. 25, pp. 5249–5259, Dec. 2007, doi: 10.1016/j.ijheatmasstransfer.2007.06.021.
- [306] H. Y. Wu and P. Cheng, “An experimental study of convective heat transfer in silicon microchannels with different surface conditions,” *International Journal of Heat and Mass Transfer*, vol. 46, no. 14, pp. 2547–2556, Jul. 2003, doi: 10.1016/S0017-9310(03)00035-8.
- [307] J. Qu, A. Zuo, F. Liu, and Z. Rao, “Quantitative analysis of thermal performance and flow characteristics of oscillating heat pipes with different initial pressure,” *Applied Thermal Engineering*, vol. 181, p. 115962, Nov. 2020, doi: 10.1016/j.applthermaleng.2020.115962.
- [308] R. Senjaya and T. Inoue, “Effects of non-condensable gas on the performance of oscillating heat pipe, part II: Experimental study,” *Applied Thermal Engineering*, vol. 73, no. 1, pp. 1393–1400, Dec. 2014, doi: 10.1016/j.applthermaleng.2014.02.075.

-
- [309] B. S. Taft, "NON - CONDENSABLE GASES AND OSCILLATING HEAT PIPE OPERATION," *Frontiers in Heat Pipes*, vol. 4, no. 1, Aug. 2013, doi: 10.5098/fhp.v4.1.3003.
- [310] N. S. Dhillon, M. W. Chan, J. C. Cheng, and A. P. Pisano, "Non-invasive hermetic sealing of degassed liquid inside a microfluidic device based on induction heating," in *Proc. PowerMEMS 2011 Conference*, Seoul, South Korea, 2011, p. 4.
- [311] C. Li, X. Wang, C. Zhou, Y. Luo, Z. Li, and S. Li, "New encapsulation method using low-melting-point alloy for sealing micro heat pipes," *J Mech Sci Technol*, vol. 31, no. 6, pp. 2621–2626, Jun. 2017, doi: 10.1007/s12206-017-0504-7.
- [312] Y. LUO, C. JIA, C. LI, and X. WANG, "Packaging flat micro heat pipe using low melting point alloy," in *2018 19th International Conference on Electronic Packaging Technology (ICEPT)*, Aug. 2018, pp. 770–773, doi: 10.1109/ICEPT.2018.8480774.
- [313] P. Kittel, *Advances in Cryogenic Engineering: Parts A & B*. Springer Science & Business Media, 2012.
- [314] C. C. Lim, "Indium seals for low-temperature and moderate-pressure applications," *Review of Scientific Instruments*, vol. 57, no. 1, pp. 108–114, Jan. 1986, doi: 10.1063/1.1139130.
- [315] A. Singh, D. A. Horsley, M. B. Cohn, A. P. Pisano, and R. T. Howe, "Batch transfer of microstructures using flip-chip solder bonding," *Journal of Microelectromechanical Systems*, vol. 8, no. 1, pp. 27–33, Mar. 1999, doi: 10.1109/84.749399.
- [316] R. Straessle, Y. Pétremand, D. Briand, and N. F. de Rooij, "Evaluation of Thin Film Indium Bonding at Wafer Level," *Procedia Engineering*, vol. 25, pp. 1493–1496, 2011, doi: 10.1016/j.proeng.2011.12.369.
- [317] D. Lu and C. P. Wong, *Materials for Advanced Packaging*, 2nd Edition. Springer, 2016.
- [318] Javier Bilbao de Mendizabal, Didier Ferrere, François-Xavier Nuiry, and William Seez, "Irradiation of an IBL stave in a 10MeV beta beam," CERN, CERN, Technical Report ATL-INDET-PUB-2013-001, Jun. 2013. Accessed: Apr. 14, 2021. [Online]. Available: <https://cds.cern.ch/record/1557832/files/ATL-INDET-PUB-2013-001.pdf>.
- [319] N. S. Dhillon, J. C. Cheng, and A. P. Pisano, "Device Packaging Techniques for Implementing a Novel Thermal Flux Method for Fluid Degassing and Charging of a Planar Microscale Loop Heat Pipe," Aug. 2012, pp. 963–971, doi: 10.1115/IMECE2011-64944.
- [320] N. Singh Dhillon and A. P. Pisano, "Enabling two-phase microfluidic thermal transport systems using a novel thermal-flux degassing and fluid charging approach," *Journal of Micro-mechanics and Microengineering*, vol. 24, no. 3, p. 035021, Mar. 2014, doi: 10.1088/0960-1317/24/3/035021.
- [321] A.B. Duncan and G.P. Peterson, "Charge optimization for a triangular-shaped etched micro heat pipe | Journal of Thermophysics and Heat Transfer," *Journal of Thermophysics and Heat Transfer*, May 2012, doi: doi.org/10.2514/3.670.
- [322] O. S. Nadgauda, "Fabrication, Filling, Sealing and Testing of," MSc Thesis, Auburn University, Auburn, Alabama, 2006.
- [323] J. Lee, Y. Joo, and S. J. Kim, "Effects of the number of turns and the inclination angle on the operating limit of micro pulsating heat pipes," *International Journal of Heat and Mass Transfer*, vol. 124, pp. 1172–1180, Sep. 2018, doi: 10.1016/j.ijheatmasstransfer.2018.04.054.
- [324] S. Jun and S. J. Kim, "Experimental study on a criterion for normal operation of pulsating heat pipes in a horizontal orientation," *International Journal of Heat and Mass Transfer*, vol. 137, pp. 1064–1075, Jul. 2019, doi: 10.1016/j.ijheatmasstransfer.2019.03.163.

- [325] M. T. Kreutzer, F. Kapteijn, J. A. Moulijn, C. R. Kleijn, and J. J. Heiszwolf, "Inertial and interfacial effects on pressure drop of Taylor flow in capillaries," *AIChE Journal*, vol. 51, no. 9, pp. 2428–2440, 2005, doi: 10.1002/aic.10495.
- [326] B. S. Taft, A. D. Williams, and B. L. Drolen, "Review of Pulsating Heat Pipe Working Fluid Selection," *Journal of Thermophysics and Heat Transfer*, vol. 26, no. 4, pp. 651–656, Oct. 2012, doi: 10.2514/1.T3768.
- [327] J. Kim and S. J. Kim, "Experimental investigation on working fluid selection in a micro pulsating heat pipe," *Energy Conversion and Management*, vol. 205, p. 112462, Feb. 2020, doi: 10.1016/j.enconman.2019.112462.
- [328] M. B. Shafii, A. Faghri, and Y. Zhang, "Thermal Modeling of Unlooped and Looped Pulsating Heat Pipes," *J. Heat Transfer*, vol. 123, no. 6, pp. 1159–1172, Dec. 2001, doi: 10.1115/1.1409266.
- [329] P. Cheng and H. Ma, "A Mathematical Model of an Oscillating Heat Pipe," *Heat Transfer Engineering*, vol. 32, no. 11–12, pp. 1037–1046, Oct. 2011, doi: 10.1080/01457632.2011.556495.
- [330] R. Senjaya and T. Inoue, "Oscillating heat pipe simulation considering bubble generation Part I: Presentation of the model and effects of a bubble generation," *International Journal of Heat and Mass Transfer*, vol. 60, pp. 816–824, May 2013, doi: 10.1016/j.ijheatmasstransfer.2013.01.059.
- [331] S. Nishio, S. Nagata, S. Baba, and R. Shirakashi, "Thermal performance of SEMOS heat pipes," presented at the International Heat Transfer Conference 12, 2002, doi: 10.1615/IHTC12.2750.
- [332] V. S. Nikolayev, "A Dynamic Film Model of the Pulsating Heat Pipe," *Journal of Heat Transfer*, vol. 133, no. 081504, May 2011, doi: 10.1115/1.4003759.
- [333] Onishi H., Sawairi K., Y. Ito, and Tada Y., "Numerical study on heat transport characteristics in oscillating heat pipe under small temperature difference," presented at the First Pacific Rim Thermal Engineering Conference, Hawaii, USA, 2016.
- [334] Nagasaki T., Shimazaki T, Ito Y, and Hojo S, "Fundamental study on heat transport in pulsating heat pipe using a straight rectangular channel," presented at the 7th Thermal and Fluids Engineering Conference, 2008.
- [335] J. Jo, J. Kim, and S. J. Kim, "Experimental investigations of heat transfer mechanisms of a pulsating heat pipe," *Energy Conversion and Management*, vol. 181, pp. 331–341, Feb. 2019, doi: 10.1016/j.enconman.2018.12.027.
- [336] I. Chakraborty, W. C. Tang, D. P. Bame, and T. K. Tang, "MEMS micro-valve for space applications," *Sensors and Actuators A: Physical*, vol. 83, no. 1–3, pp. 188–193, May 2000, doi: 10.1016/S0924-4247(99)00382-9.
- [337] X. Yang, A. Holke, and M. Schmidt, "An Electrostatic, On/Off MEMS Valve for Gas Fuel Delivery of a Microengine," in *Solid-State Sensor, Actuator and Microsystems Workshop*, Hilton Head Island, SC, 2002, p. 4.
- [338] K. W. Oh and C. H. Ahn, "A review of microvalves," *Journal of Micromechanics and Microengineering*, vol. 16, no. 5, pp. R13–R39, May 2006, doi: 10.1088/0960-1317/16/5/R01.
- [339] C. Yang, X. Xie, S. Liu, and C. Livermore, "Resealable, ultra-low leak micro valve using liquid surface tension sealing for vacuum applications," Jun. 2017, pp. 2071–2074, doi: 10.1109/TRANSDUCERS.2017.7994481.

Appendix A. Uncertainty analysis

The estimations of the uncertainties of the experimental setup, and their propagation, was approached as n independent variables x_i affecting the quantity F , which can be expressed as

$$\delta F_{x_i} = \frac{\partial F}{\partial x_i} \delta x_i \quad (\text{A.1})$$

Assuming a Gaussian distribution of the uncertainties, the maximum uncertainty of F can be computed as a eucliden norm of the uncertainties:

$$\delta F_{x_i} = \left(\sum_{i=1}^n \left(\frac{\partial F}{\partial x_i} \delta x_i \right)^2 \right)^{\frac{1}{2}} \quad (\text{A.2})$$

Instruments errors, listed in Table A-1, were propagated in Table A-2 using the equation (A.2).

Table A-1. Error uncertainties of the instruments

Quantity	Error		Instrument
Test section temperature sensor	±0.3	°C	PT100
Input current	±0.30%	A	Tti PL330D
Input voltage	±0.10%	V	Tti PL330D
TEC current	0.50%	A	Tti 3518
TEC voltage	0.20%	V	Tti 3518
DAQ	±0.15	°C	Ni 9216
Charging ratio	± 5%		
Elements' positions	±0.30	mm	
Thickness	±20.00	um	
Width	±20.00	um	

Table A-2. Propagation of the uncertainties.

Quantity		Uncertainty
Input power	$\Delta P/P$	$\pm 0.316\%$
TEC power	$\Delta P/P$	$\pm 0.269\%$
Temperature	ΔT	± 0.33541
Maximum temperature error	$(\Delta T/T)_{max}$	$\pm 4.792\%$
Test section cross-section	$\Delta A/A$	$\pm 1.7807\%$
Test section length	$\Delta L/L$	$\pm 0.857\%$
Apparent thermal conductivity	$\Delta K/K$	$\pm 5.193\%$

Appendix B. Applications-based Trade-off

A trade-off was conducted, based on the proposed applications, to compare the self-actuated micro heat pipes, as well as thermal straps.

B.1 Criteria

Table B-1. Selection criteria definitions and weights for each scenarios.

Criteria	Abbr.	Scenarios' Weights		
		#1	#2	#3
Technology Readiness Level: Criterion for estimating technology maturity. The technology is evaluated from 1 (basic principles observed) to 9 (actual system proven in operational environment), based on ISO 16290	C1	5	4	4
Improvable from State-of-the-Art: Some solutions of heat transport can be improved at different level. This criterion is based on the current understanding of the phenomena, researched conducted and applications observed	C2	2	3	3
Heritage from macro-scale HP: Heritage from similar technology used at macro-scale	C3	1	1	1
Heritage from flown HP: Heritage from similar technology used in space mission	C4	2	1	1
Reliability: Heat transport solution have to transport heat between two locations over time without failure	C5	5	5	5
Low activation: This criterion considers the induced radioactivity of the material used to transport heat. The irradiation levels and decay rates of the activated materials are dependent upon the elements of the material. The goal is to reduce the waste foot print of the system used	C6	2	5	5
Radiation hardness: The device have to be resistant to damage or malfunctions caused by radiation.	C7	5	5	5
Radiation length: This characterize the transparency of the device to particles. It is the mean length to reduce the energy of an electron by 1/e, usually given in centimetre	C8	2	5	5
Electromagnetic interference / electromagnetic compatibility: It characterize the ability of operating in a shared environment while, at the same time, not affecting other equipment within the same environment.	C9	4	3	3
Equivalent thermal conductivity: property to conduct heat across a distance	C10	4	4	4
Cooling capacity: technology capacity to remove heat from an area	C11	4	4	4
Thermal Figure of Merit: It characterizes the performance of the device. In this case, the definition is the maximal temperature gradient in the cooling device divided by the heat flux. Note that others figures of merit exist.	C12	2	2	2
Performance affected by heat: Thermal performances of a device are affected by its heat	C13	3	3	3
Performances affected by orientation: Orientation relative to gravity affects the thermal performances	C14	5	5	4
Anisotropic heat conduction: Conduction of heat by the solutions are higher in one direction than in the others. Bulk material have also anisotropic heat conduction	C15	2	2	2
Non-magnetic: This property is important when the device is placed in	C16	3	5	5

Table B-1 (continued)

Criteria	Abbr.	Scenar- ios' Weights	Cri- te- ria	Abbr.
		#1		
Coefficient Thermal Expansion: capacity of CTE matching with silicon device's one	C17	3	4	4
Material compatibility: Compatibility of material for thermal solution with environment	C18	5	4	4
Pliability: It characterize the ability to be bent to interface locations that are not on the same level or orientation	C19	2	2	1
Modularity: The ability of the device to be separated and recombined	C23	3	5	4
Interfaceable: The ability of the solution to be interface to the cold and heat source, as well as the thermal quality of the interface	C24	3	4	3

B.2 Scenarios

Three possible application of how μ OHPs could be used in HEP experiments and space applications are shown in the following subsections.

Scenario 1

Several PCBs containing silicon components are placed onboard a satellite. For each PCB, the cooling of the silicon components is done using a SCL placed under the heating components of the PCB. A PCL runs between the SCLs present on the PCBs to evacuate the heat. Furthermore, feedthroughs and through-silicon vias could be integrated in the SCL to connect the silicon chips to the PCB through the SCL, as illustrated in Figure B.1.

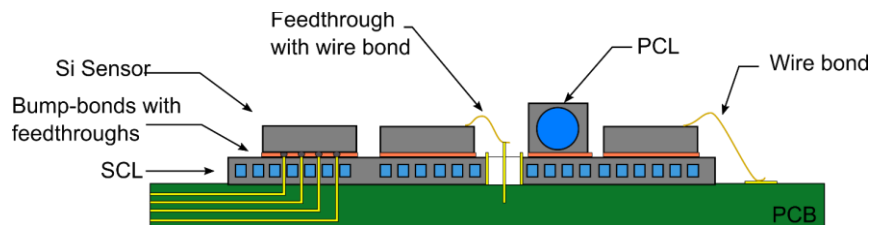


Figure B.1. Scheme of the possible integration with bump-bonded or wire-bonded components.

The small footprints of the components, approximatively 2mm^2 , coupled with power density ranging from hundreds of mW/cm^2 to $50\text{W}/\text{cm}^2$, leads to non-uniform heating of the substrate. The SCLs homogenize the temperature of the components, and a PCL links them to transfer the heat to radiators.

Scenario 2

Multiple silicon components, with a medium form factor of $20 \times 40\text{mm}^2$, are distributed on a single supporting structure. Chips provide low ($0.2\text{W}/\text{cm}^2$) to medium ($10\text{W}/\text{cm}^2$) heat fluxes and operate in radiation environments. They are placed at different orientations, relatively to gravity, as depicted in Figure B.2. They should be able to function in all orientations and high reliability,

provide a modular and easy interface with minimal weight. SCLs are interfaced to single PCL running along each structure. If the conditions allow to replace the PCL by a gas flow, the SCLs would function as heat spreaders.

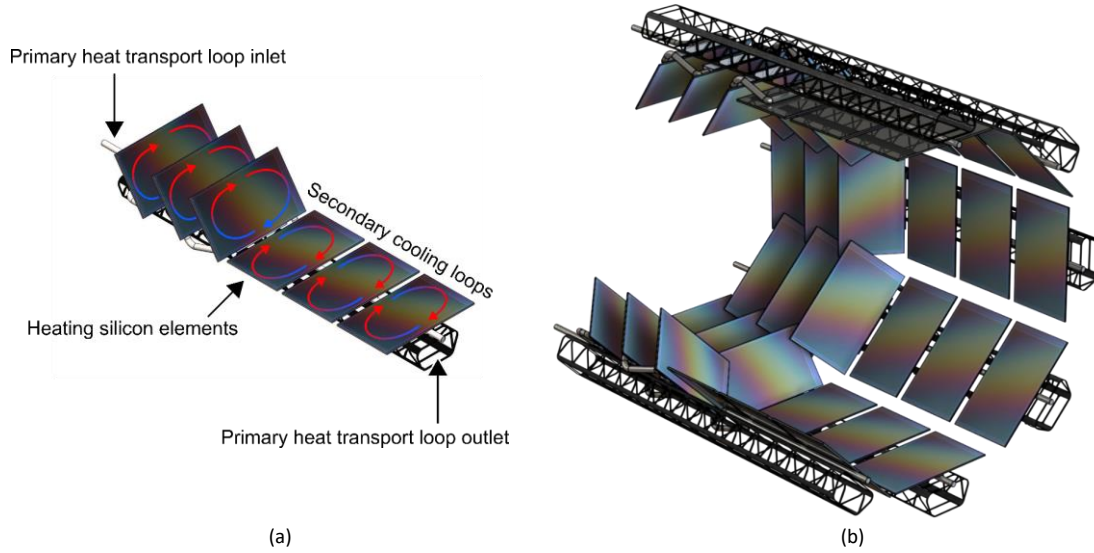


Figure B.2. Schematic of the silicon heating elements distributed on a stave with different orientations. (a) Isolated stave with elements' description. (b) Illustration of integration of staves in a cylindrical way.

Scenario 3

A single, large ($80 \times 60 \text{ mm}^2$) silicon device is considered as the target to cool, as illustrate by Figure B.3. The SCL is directly positioned on the backside of the silicon device and two pipes are attached to the SCL as PCL. The PCB serves as the mechanical support to the SCL and the silicon sensor.

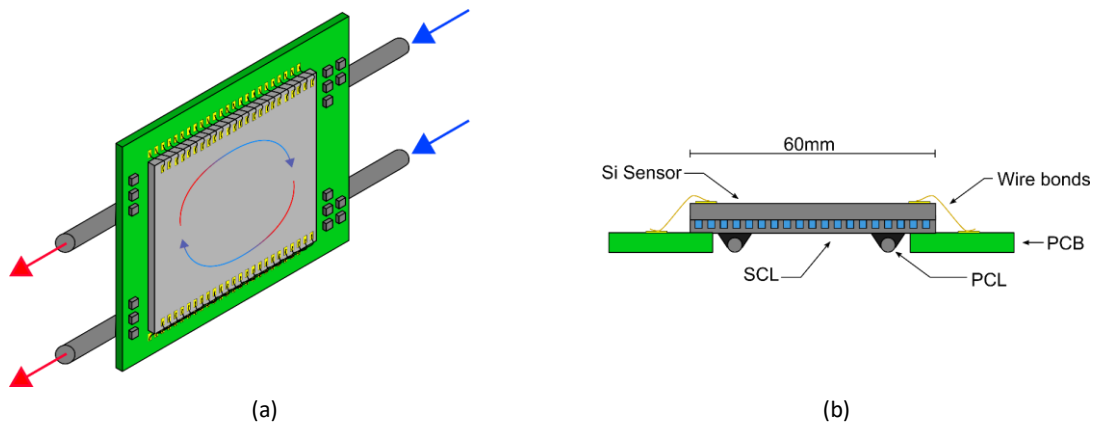


Figure B.3. (a) Schematic view of the apparatus considered for the third scenario. (b) Cross-section of the apparatus.

The sensor is exposed to a heat flux ranging from 2 W/cm^2 to 10 W/cm^2 , mainly distributed near the wire-bond pads, and high radiation doses. The silicon sensor operates in vacuum and requires a reliable cooling system that allows modularity, as well as radiation hardness. The compatibility of the SCL, and PCL, with vacuum is also required.

B.3 Evaluation

A score is attributed arbitrarily to each cooling solution for each criterion over the three scenarios. Table B-2, Table B-3 and Table B-4 summarize the scores and totals for scenario 1, 2 and 4, respectively.

Table B-2. Evaluation results of the passive heat transport devices according to the scenario 1.

		Cooling solutions						
		<i>Weight</i>	Micro-GHP	Micro-CPL	Micro-LHP	Micro-OHP	Micro-VC	Thermal Strap
Criteria	C1	5	9	9	9	6	9	9
	C2	2	5	4	4	8	4	1
	C3	1	5	5	5	5	5	1
	C4	2	8	9	9	7	9	9
	C5	5	9	9	9	9	9	9
	C6	2	9	9	9	9	9	9
	C7	5	9	9	9	9	9	9
	C8	2	6	6	6	6	6	6
	C9	4	5	5	5	5	5	5
	C10	4	6	5	5	8	6	9
	C11	4	4	7	8	7	6	9
	C12	2	5	6	5	5	5	5
	C13	3	2	2	2	2	2	2
	C14	5	3	3	3	7	3	9
	C15	2	9	9	9	9	9	9
	C16	3	9	9	9	9	9	9
	C17	3	8	8	8	8	8	8
	C18	5	5	5	5	5	5	5
	C19	2	2	2	2	2	2	7
	C20	3	3	3	3	3	3	3
	C21	4	5	5	5	5	5	6
	C22	5	7	7	7	7	7	8
	C23	3	6	6	6	6	6	5
	C24	3	7	7	7	7	7	2
	<i>Total</i>		488	498	500	517	496	541

Table B-3. Evaluation results of the passive heat transport devices according to the scenario 2.

		Cooling solutions						
		<i>Weight</i>	Micro-GHP	Micro-CPL	Micro-LHP	Micro-OHP	Micro-VC	Thermal Strap
Criteria	C1	4	9	9	9	6	9	9
	C2	3	5	3	3	8	5	1
	C3	1	5	5	5	5	5	1
	C4	1	8	9	9	7	9	9
	C5	5	8	8	8	8	8	9
	C6	5	9	9	9	9	9	9
	C7	5	8	8	8	8	8	8
	C8	5	6	6	6	6	6	6
	C9	4	5	5	5	5	5	5
	C10	4	6	5	5	8	7	9
	C11	4	4	7	8	7	6	9
	C12	2	5	6	5	5	5	4
	C13	3	2	2	2	2	2	2
	C14	5	4	4	4	7	4	9
	C15	2	9	9	9	9	9	9
	C16	5	9	9	9	9	9	9
	C17	4	8	8	8	8	8	8
	C18	4	5	5	5	5	5	5
	C19	2	2	2	2	2	2	7
	C20	3	3	3	3	3	3	3
	C21	4	5	5	5	5	5	6
	C22	5	7	7	7	7	7	8
	C23	5	6	6	6	6	6	5
	C24	4	7	7	7	7	7	4
	Total		551	556	558	582	564	598

Table B-4. Evaluation results of the passive heat transport devices according to the scenario 3.

		Cooling solutions						
		<i>Weight</i>	Micro-GHP	Micro-CPL	Micro-LHP	Micro-OHP	Micro-VC	Thermal Strap
Criteria	C1	4	9	9	9	6	9	9
	C2	3	5	3	3	8	5	1
	C3	1	5	5	5	5	5	1
	C4	1	8	9	9	7	9	9
	C5	5	8	8	8	8	8	9
	C6	5	9	9	9	9	9	9
	C7	5	8	8	8	8	8	8
	C8	5	7	7	7	7	7	7
	C9	3	5	5	5	5	5	5
	C10	4	6	5	5	8	7	9
	C11	4	4	7	8	7	6	9
	C12	2	5	6	5	5	5	4
	C13	3	2	2	2	2	2	2
	C14	4	3	3	3	7	3	9
	C15	2	9	9	9	9	9	9
	C16	5	9	9	9	9	9	9
	C17	4	8	8	8	8	8	8
	C18	4	5	5	5	5	5	5
	C19	1	2	2	2	2	2	6
	C20	2	3	3	3	3	3	4
	C21	3	5	5	5	5	5	5
	C22	5	7	7	7	7	7	8
	C23	4	6	6	6	6	6	5
	C24	3	7	7	7	7	7	6
	Total		525	530	532	557	538	573

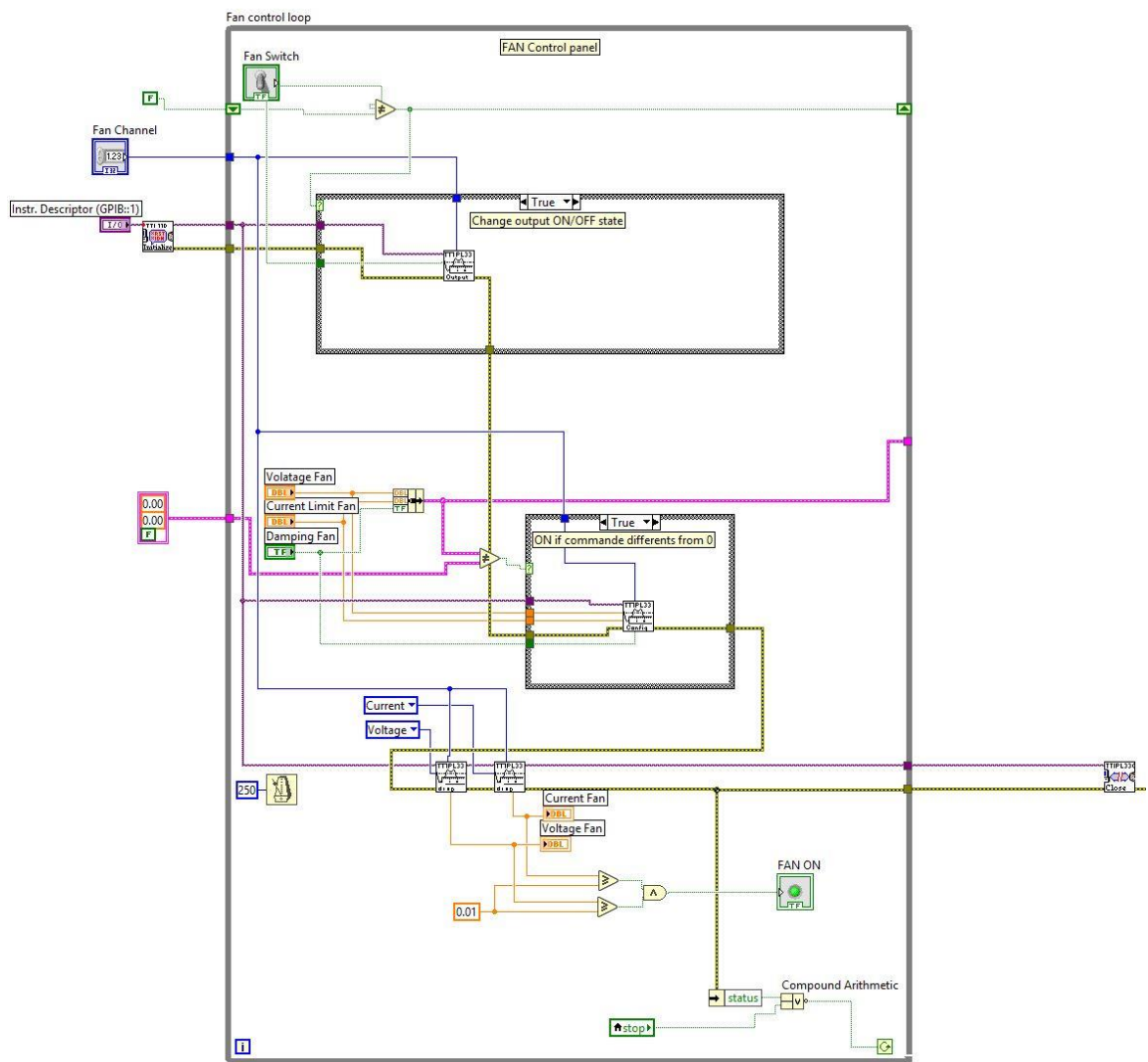


Figure C.4. Loop controlling the cooling fan of the heatsink.

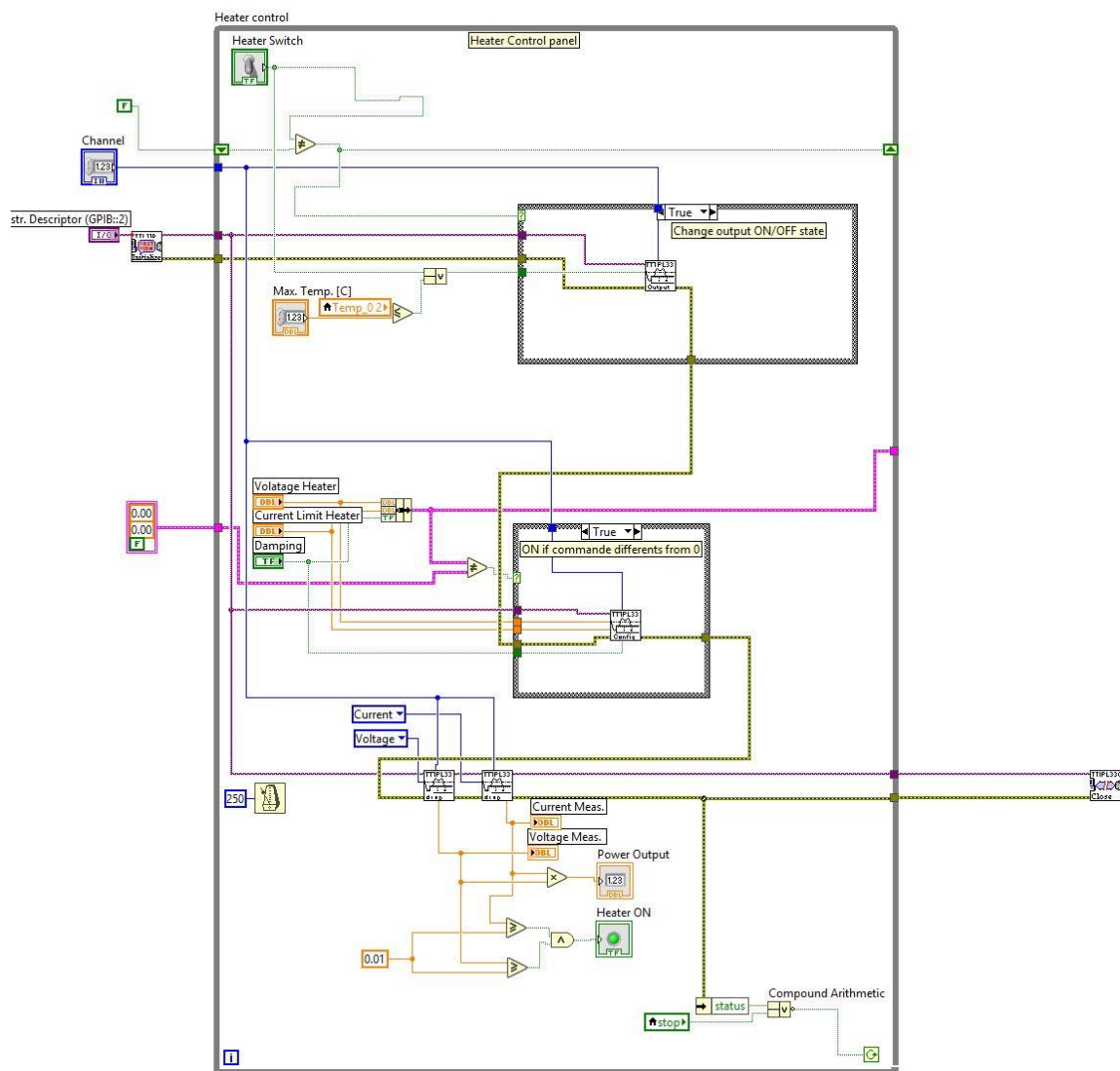


Figure C.5. Loop control of the heating element.

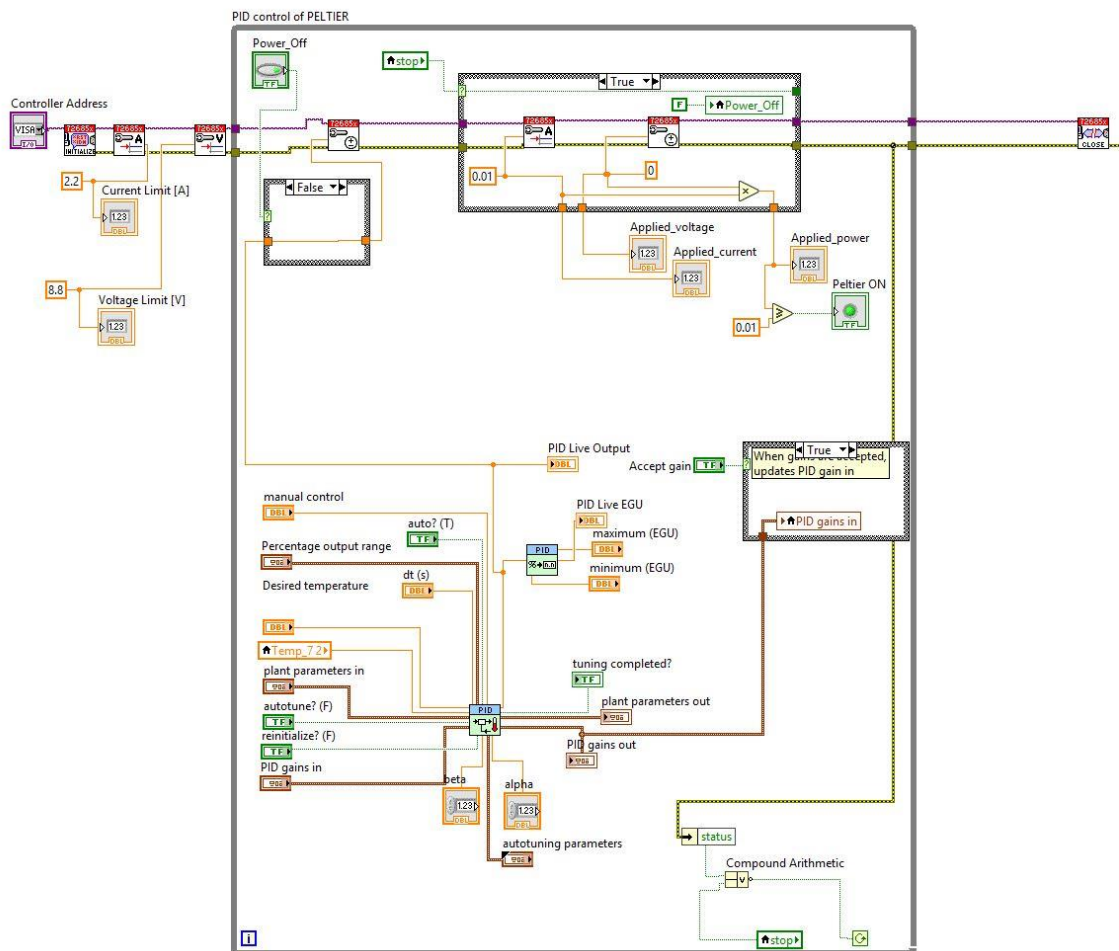
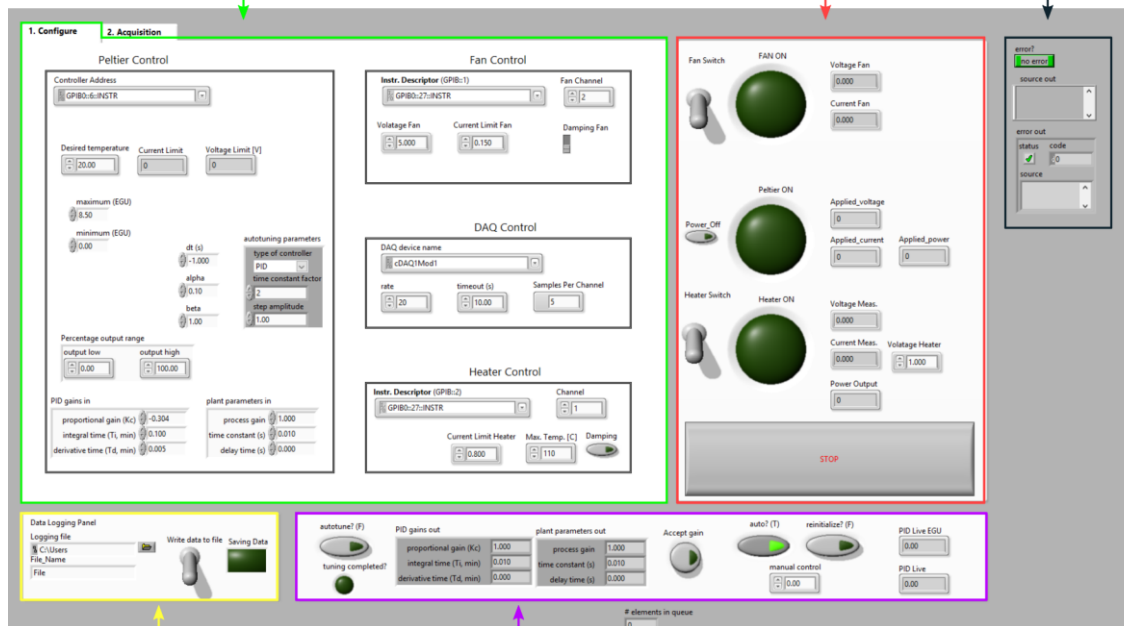


Figure C.6. PID loop controlling the TEC module.

Configuration and acquisition panel

Control panel

Error messenger



Data logging
configuration panel

Auto PID gains

Figure C.7. Overview of the user interface.

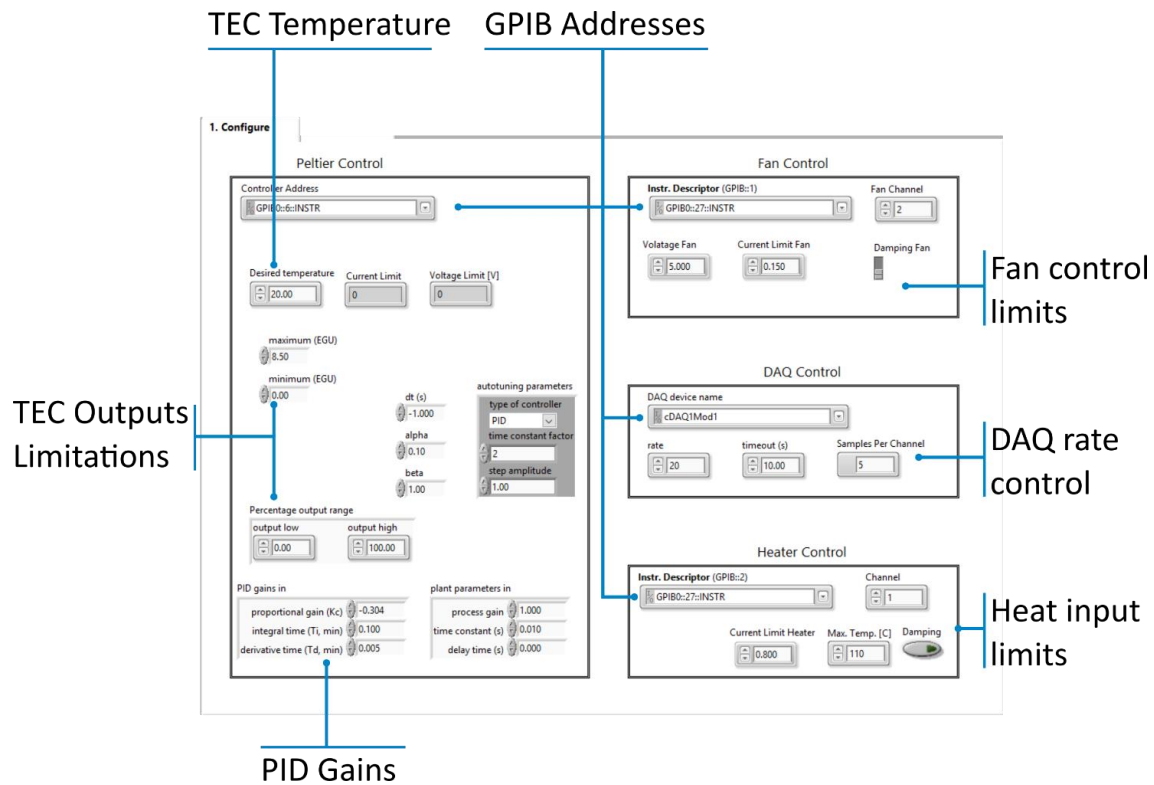


Figure C.8. Details of the configuration panel.

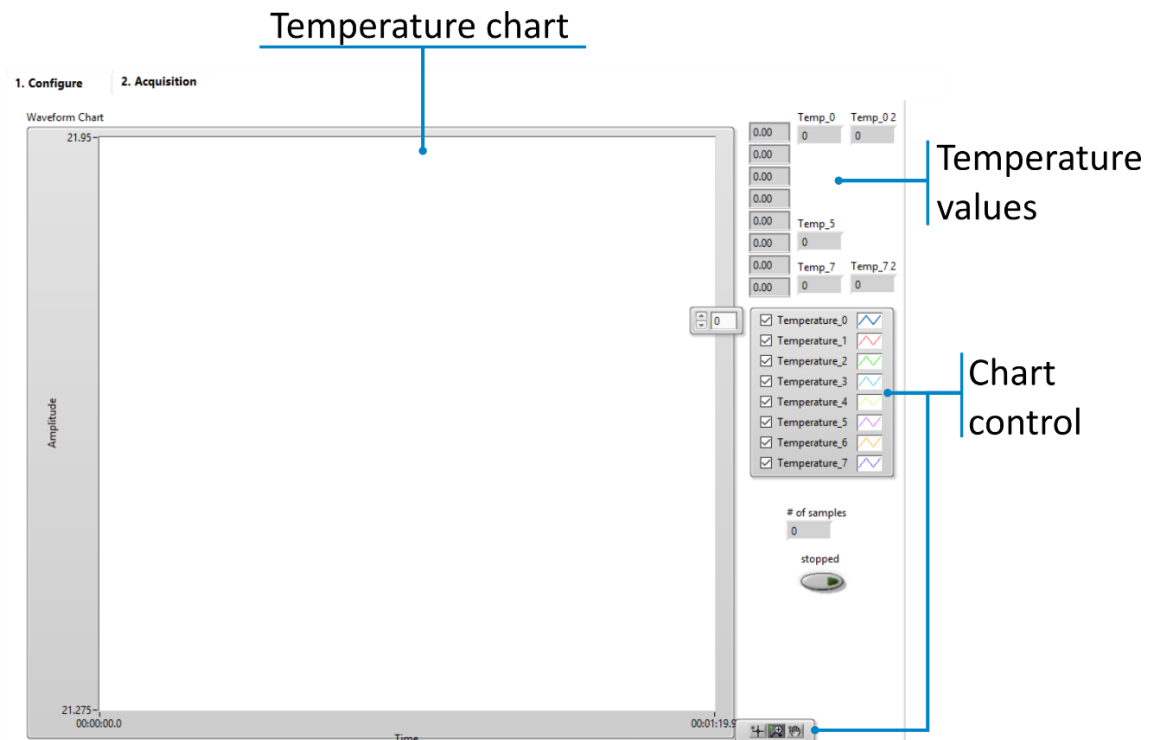


Figure C.9. Details of the Acquisition panel.

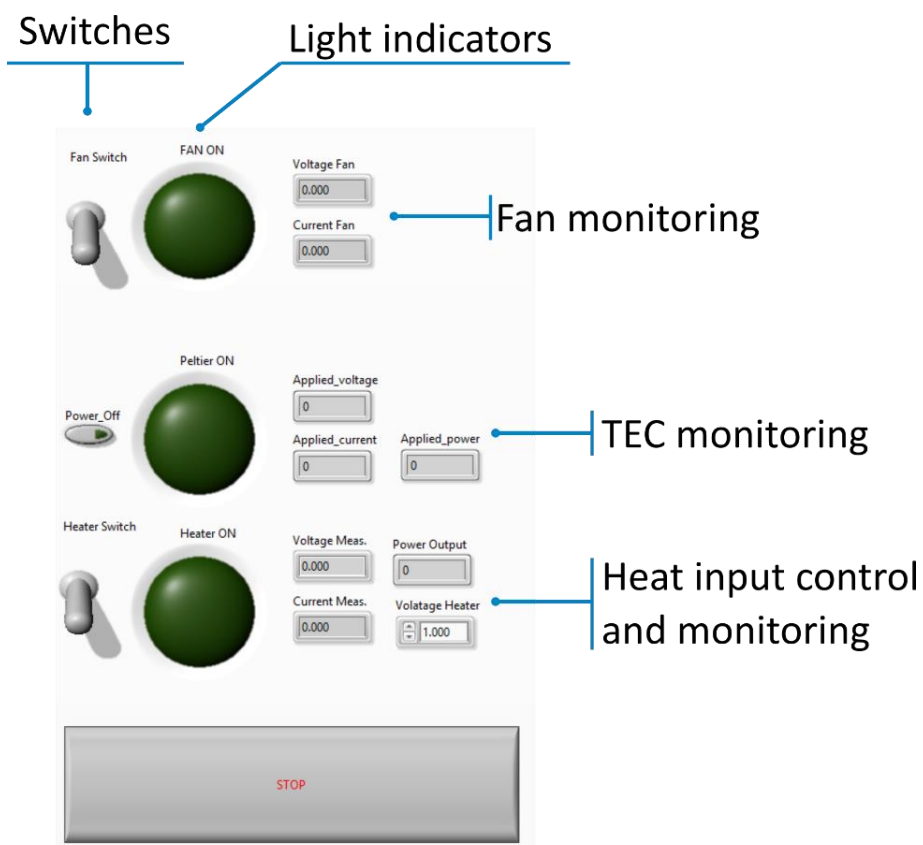


Figure C.10. Details of the control panel.


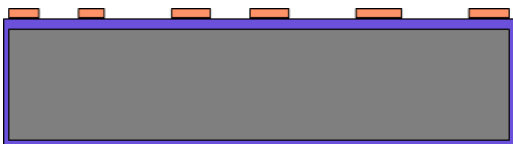
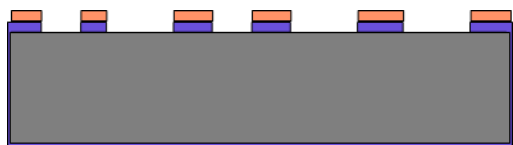
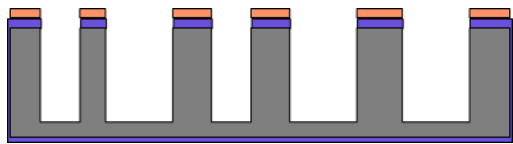
Appendix D. Microfabrication Process Flows

D.1 Silicon and Glass Prototypes

Table D-1. Masks and substrates for anodic bonding.

Photolith masks			
Mask #	Critical Dimension	Critical Alignment	Remarks
1	10um	First Mask	Dicing and alignment marks on the backside
Substrate Type			
1x Silicon <100>, Ø150mm, 625um thick, DSP, Prime, p type, 0.1-0.5 Ohm.cm 1x Borofloat Pyrex, >, Ø150mm, 500um thick			

Table D-2. Anodic bonding - Processing wafers A

Step	Process description	Cross-section after process
01	Substrate: Si test <i>Wet Oxidation</i> Machine: <i>Centrotherm</i> Thickness: 2um	
02	Photolithography #1 Machine: MLA150 + EVG150 PR : AZ9260 – 14um (HMDS) <i>Hard Contact</i> <i>Post bake (2h @85°C)</i> Mask : CD = 10um	
03	RIE SiO2 Machine: SPTS Wafer side: <i>frontside</i> Etch thickness: 2000nm Mask: PR Mask thickness: 14um Etch stop material: Si	
04/05	DRIE Si Machine: AMS (SOI_accurate, 40s) Wafer side: <i>backside</i> Etch thickness: 400um Mask: PR / SiO2 Mask thickness: 14/2um Etch stop material: <i>bulk</i> + Resin strip (plasma O2 + remover + plasma O2)	




Step	Process description	Cross-section after process
06	BHF 7:1 (<i>SiO₂ etch</i>) Machine: (Z14) Temperature: <i>RT</i> Thickness: <i>2000nm</i> Time: <i>30min</i> Spindrying: <i>Yes</i>	
07	Wet Oxidation Machine: <i>Centrotherm</i> Thickness: <i>1um</i>	
08	BHF 7:1 (<i>SiO₂ etch</i>) Machine: (Z14) Temperature: <i>RT</i> Thickness: <i>1um</i> Time: <i>15min</i> Spin-drying: <i>yes</i>	

Table D-3. Anodic bonding - Processing wafers B.



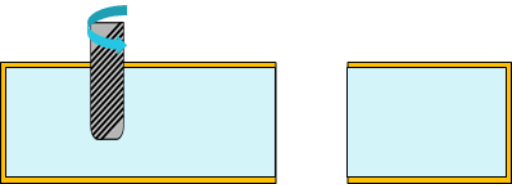
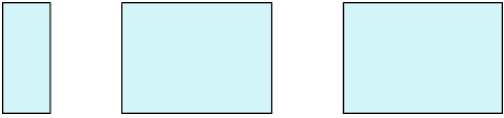
Step	Process description	Cross-section after process
09	Substrate: Borosilicate <i>Wet Oxidation</i> Machine: <i>Centrotherm</i> Thickness: <i>0.5um</i>	
10	Wax Deposition	
11	Micromachining	
12	Wax stripping and wafer cleaning	

Table D-4. Anodic bonding – Wafers A to wafers B

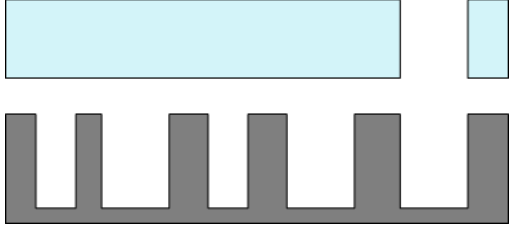
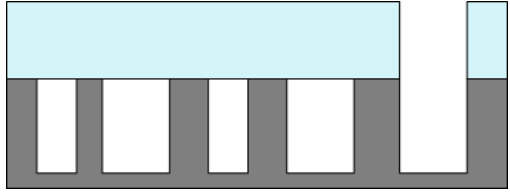
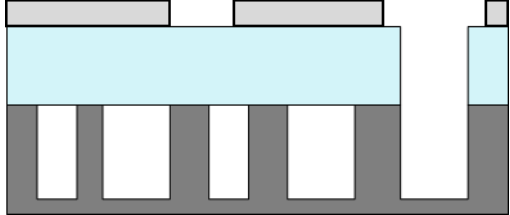
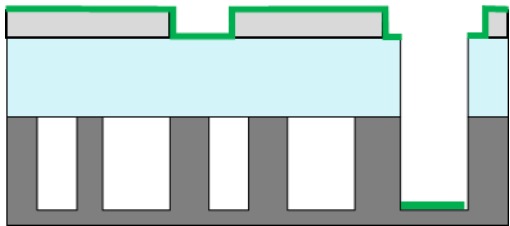
Step	Process description	Cross-section after process
13	Substrates preparation (Piranha bath)	
14	Anodic Bonding Machine: SB6 Temperature: 400°C Voltage 700 V Force: 1.1 kN	

Table D-5. Anodic bonding – Thin-films deposition at the inlets





Step	Process description	Cross-section after process
15	Stencil alignment (coarse alignment)	
16	Sputtering and evaporation Layer 1 – TiW – 300nm Layer 2 – Ti – 30nm Layer 3 – Au – 500nm	









D.2 Silicon Proof-of-Concept Demonstrators

Table D-6. Masks and substrates for thermocompression

Photolith masks			
Mask #	Critical Dimension	Critical Alignment	Remarks
1	10um	First Mask	Dicing and alignment marks on the backside
2	30um	15	Gold structuration
3	30um	15	Inlet partial etching
4	30um	15	Microchannels and inlet etching (and opening)
Substrate Type			
2x Silicon <100>, Ø150mm, 525um thick, DSP, Prime, p type, 0.1-0.5 Ohm.cm			

Table D-7. Gold thin-films wafer thermocompression - Processing wafers A

Step	Process description	Cross-section after process
01	Substrate: Si test <i>Wet Oxidation</i> Machine: Centrotherm Thickness: 0.5um	
02	Photolithography #1 <i>(BS alignm. and dicing marks)</i> Machine: MLA150 + EVG150 PR : AZ1512 – 1.5um (HMDS) Mask : CD = 5um	
03	RIE SiO2 Machine: SPTS Wafer side: backside Etch thickness: 500nm Mask: PR Mask thickness: 1.5um Etch stop material: Si	
04/05	RIE Si Machine: AMS (SOI_accurate, 40s) Wafer side: backside Etch thickness: 3um Mask: PR Mask thickness: 1.5um Etch stop material: bulk + Resin strip (plasma O2 + remover + plasma O2)	

Step	Process description	Cross-section after process
06	Wafer flip and inspection	
07	Gold deposition with adhesion layer (Ti/Au/Ti) Machine: EVA760 (DP650) Thick-ness: 30nm/500nm/30nm	
08	Photolithography #2 Machine: MLA150 + EVG150 PR : AZ1512 - 1.5μm (dehydration) Mask : CD = 30um + Tepla plasma O ₂ descum (10s)	
09	BHF 7:1 (Ti etch) Machine: (Z14) Temperature: RT Thickness: 30nm Time: 1min Spindrying: no	
10	Au wet etch Machine: Arias acid (Z14) Temperature: RT Thickness: 500nm Time: 3min Spindrying: manual	
11	BHF 7:1 (Ti etch) Machine: (Z14) Temperature: RT Thickness: 30nm Time: 1min Spindrying: no	
12	Resin strip (wet) Machine: Remover 1165 (Z2)	
13	SiO₂ deposition RF Sputtering Machine: Spider 600 (10min) Thickness: 600nm	

Step	Process description	Cross-section after process
14	Photolithography #3 Machine: MLA150 + EVG150 PR : AZ1512 – 1 μ m (HMDS) Mask : CD = 30 μ m	
15	RIE SiO2 Machine: SPTS (SiO2_PR_3:1) Wafer side: top Etch thickness: 1100nm Mask: PR Mask thickness: 1 μ m Etch stop material: Si + Resin strip	
16	Photolithography 4 Machine: ACS200 + EVG 150 PR : AZ10xt-60 – 10 μ m (15 μ m) Mask : CD = 30 μ m	
17	Wafer Flip	
18	Al deposition (backside) Material: Aluminium Thickness: 2 μ m Machine: DP650	
19	Wafer Flip + 5h-12h in oven @85°C (Heraus Z14)	
20	DRIE Si Machine: AMS Wafer side: top Etch thickness: 150 μ m Mask: PR Mask thickness: 10 μ m Mask2: SiO2 Mask thickness: 1.1 μ m Etch stop material: bulk	

Step	Process description	Cross-section after process
21	RIE SiO₂ Machine: SPTS (SiO ₂ _PR_1:1) Wafer side: top Etch thickness: 1100nm Mask: PR Mask thickness: 10um Etch stop material: Si	
22	DRIE Si Machine: AMS Wafer side: top Etch thickness: 400um Mask: PR Mask thickness: 10um Mask2: SiO ₂ Mask thickness: 0.6um Etch stop material: SiO ₂	
23	Resin strip Plasma O ₂ + Remover 1165 + Plasma O ₂	
24	Al etch (wet) Machine:	
25	BHF 7:1 (Ti + SiO₂) Machine: Z2 Temperature: RT Thickness: 500nm Time: 5min (Possibility to replace Ti by Cr to limit underetch)	

A

Table D-8. Gold thin-films wafer thermocompression - Processing wafers B

Step	Process description	Cross-section after process
26	Substrate: Si test Wet Oxidation Machine: Centrotherm Thickness: 0.5um	

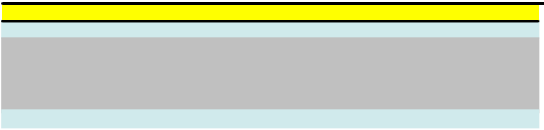
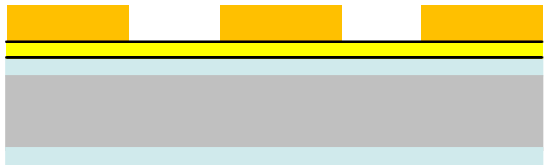






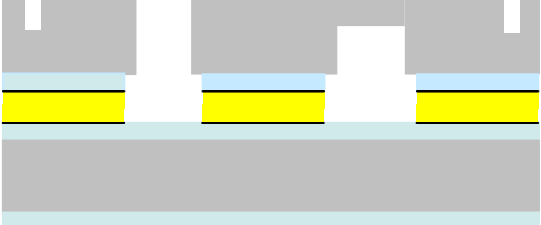

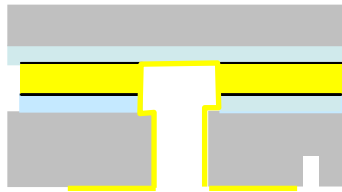
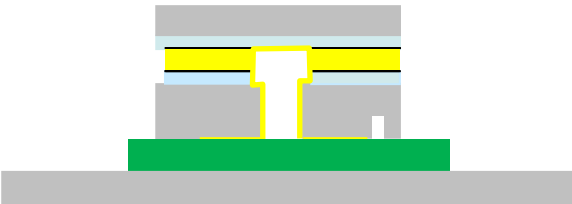
Step	Process description	Cross-section after process
27	Gold deposition with adhesion layer (Ti/Au/Ti) <i>DC Sputtering</i> Machine: BAS 450 Thickness: 30nm/500nm/30nm	
28	Photolithography #2 Machine: MLA150 + EVG150 PR : AZ1512 – 1.5μm (dehydration) Mask : CD = 30um	
29	BHF 7:1 (Ti etch) Machine: Temperature: RT Thickness: 30nm Time: 1min	
30	Au wet etch Machine: Arias Acid (Z14) Temperature: RT Thickness: 500nm Time: 3min Spindrying: manual	
31	BHF 7:1 (Ti etch) Machine: Temperature: RT Thickness: 30nm Time: 1min	
32	Resin strip (wet) Machine: Colliard wet bench	
33	BHF 7:1 (Ti etch) Machine: Temperature: RT Thickness: 30nm Time: 1min Spindrying: Yes	

Table D-9. Gold thin-films wafer thermocompression - Wafer Bonding (wafer A to wafer B)

Step	Process description	Cross-section after process
34	Substrates preparation (surfaces activation Pirhana)	
35	Bonding Machine: SB6 (EVG 520) Temperature: 300°C Time: 1h Force: 15 kN Alignement:	
36	Gold deposition with adhesion layer (Ti/Au) in the inlets Machine: DP650 Thickness: 30nm/500nm <i>With shadow mask, inspection of sidewall deposition !</i>	
37	Dicing	
38	Grinding Machine: DAG810 Face: Backside Thickness to remove: 100µm <i>Only selected chips (!SiO2!)</i>	
39	CMP (optional) Machine: Steag MECAPOL E460 Face: Backside Thickness to remove: polishing <i>Chips on carrier with wafergrip</i>	
40	Dicing	

Appendix E. Charging methods

A controlled fluid charging is a major challenge to obtain an operational micro heat pipe. The quantity of fluid presents in the channels accounts for a large contribution to the operations of the micro-devices. Furthermore, precisely measuring and controlling the small amount of working fluid is extremely difficult.

Several methods were used in the literature. Each one presents advantages and limitations that need to be taken in account. Some are more suited for large-scale production when others are reserved to laboratories environment.

E.1 Back-filing

Beyond few exceptions, the charging system includes a container with the working fluid, a mass balance, a vacuum pump and corresponding lines. The vacuum pump role is to remove all fluid from the interior of the heat pipe and the fluidic lines. The mass balance monitors the quantity of fluid injected. The charging line is typically located in the cold section of the device. After removing present fluids in the device by vacuum pumping, the working is pulled in its liquid phase by the vacuum into the device. Using two fluidic lines with specific roles eases the charging process compared to a unique fluidic line with both roles. The working fluid can be pulled more efficiently in the device with two lines, further reducing the NCGs.

E.2 Micro-syringe

Precision syringes with a low internal volume bellow one millilitre are used for liquid or gaseous sampling in chromatography analysers. Similar syringes are used to charge micro heat pipe whether it has one or two charging lines. At first, working fluid is charged in the syringe and locked in it by a valve. The syringe is connected to the evacuating and charging system with the liquid isolated from the micro heat pipe. Vacuum is pulled in the charging lines and the micro heat pipe until the desired pressure is reached. At this point, the vacuum line is closed and the liquid injected. Once the plunger of the syringe down to the dead point, the charging line is closed and the micro heat pipe can be disconnected.

E.3 Thermodynamic Equilibrium Method

Based on thermodynamic equilibrium, the technique relies on the condensation of the vapour phase of the heated working fluid. The working fluid is partially evaporated and condensate in the charging line. After the interior of the heat pipe is evacuated, the condensate is pushed in the device by the generated vapour and fill completely the volume of the microchannels. The pressure can be controlled by controlling the temperature of the evaporated working fluid. The working fluid charge is exposed to vacuum and partially flash. Consequently, the pressure of the vacuum chamber increases and a new thermodynamic equilibrium is achieved. The volume of

the vacuum chamber and the vacuum level determine the amount of liquid that flashes. Thus, the quantity of vapour in the micro heat pipe. This technique requires a careful calibration and reliable control of the temperature of along all the charging system due to the temperature drop generated by the flashing of the liquid in the micro-device. The higher limitation of these method rests in the higher deviation of the charged volume compared to the other methods proposed.

E.4 Capillary Tubing Methods

By using a similar setup and by replacing the vacuum chamber by a capillary tube, the control of the charging ratio could be refined. The liquid removal is implemented by pushing liquid into the tube until the desired quantity is present in the heat pipe. The quantity of removed liquid is proportional to the length and diameter. A large reservoir of working fluid is connected to one port of the micro heat pipe while the second port is open to the ambient, or better a recycling system. The fluid flows inside the device. Valves placed along the connected capillaries control the in-going and out-going flows.

E.5 Vapour Flushing and Condensation

This technique uses vapour phase to push unwanted gases out of the micro heat pipe and then, by condensation, fill the same heat pipe [193], [319], [320]. The Figure E.1 illustrates the charging process. At first, the liquid in the reservoir is boiled and generates high pressure in the reservoir. All unwanted gases exit the liquid and micro heat pipe, leaving only pure vapour and liquid from the working fluid. Secondly, the outlet port of the micro heat pipe is closed. The hot vapour flow stops. The vapour condensates thereby filling the micro heat pipe. As the required amount of liquid is present in the device, the inlet is closed.

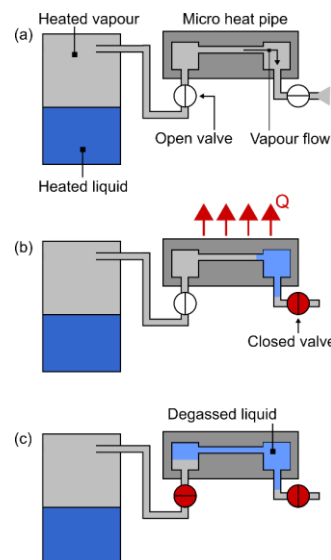


Figure E.1. A schematic of charging a micro heat pipe by vapour flushing and condensation (adapted from [320]). (a) Vapour fills the μ HP. (b) Vapour condensates when the μ HP is cooled and the outlet valve is closed. (c) Inlet valve is closed once the target quantity is reached.

E.6 Liquid Pumping

Alternatively, some experiments filled the micro heat pipe completely before gradually removing the fluid until the desired amount remained inside. Duncan and Peterson [321] charged their

silicon and glass micro heat pipe using a syringe after vacuum pumping the cavity. As the vapour became trapped in the evaporator section, heat was applied to it to remove the extra liquid by vapour expansion.

In a similar manner, the quantity of fluid in the device can be controlled by pumping the fully filled micro heat pipe through a series of valves and heated micro capillary tubing. The heat pipe array was immersed in temperature-controlled bath while the capillary tubing was heated and vapour flow through. The assumption made was that by monitoring the time the heat was applied and comparing it to the time required to fully empty the micro heat pipe from all the liquid, the quantity of liquid remaining inside could be determined.

E.7 Integration during the Fabrication

Nadgauda trapped the fluid inside the device during the fabrication [322]. The author used mercury and deionized water as working fluid. The substrate and lid were closed by Indium cold welding. The working fluids were deposited in the microchannels. A small gap between the lid and the substrate was created using a small blade, while a clamp kept the assembly together. The assembly was frozen by dipping it in liquid nitrogen. Once frozen, the blade was removed and the assembly was placed in a vacuum chamber. However, despite the force applied by the clamping mechanism, the Indium being frozen allows trapped air to be evacuated before any sealing occurs. When the temperature of the entire system increased, the sealing occurred before the fluids returned to its liquid state. An additional processing bake-out step is required to reinforce the bonding: the micro heat pipes are kept at 120°C for 20 minutes.

E.8 Discussion and Trade-off

The issues arising for the charging and degassing are postponed to a step after the microfabrication of the devices. Integrating both the charging and degassing of the working fluid during the fabrication would be feasible if expensive equipment modifications were done to inject a degassed fluid inside the channels during the bonding of the wafers. The alternatives rely on holes connected, or not, to a tube that allows vacuum pumping, degassing and charging. This requires tube-to-chip connections of good quality to ensure a functional micro-device.

Among the proposed solutions, the syringe-backed one offers an effective charging solution of an already degassed fluid. Furthermore, this solution allows working with only one inlet, on the contrary to some existing solutions. The repeatability and ease of use make it particularly suited for laboratory study. Therefore, the micro-syringe method was adopted as the charging system for the experiment.

Appendix F. Complementary Review for the Design of μ OHPs

The operating conditions and system boundaries directly influence the thermal behaviour of the μ OHP. Despite the many experimental and theoretical studies researched, the interaction of the different system parameters, shown in Figure F.1, remain unclear.

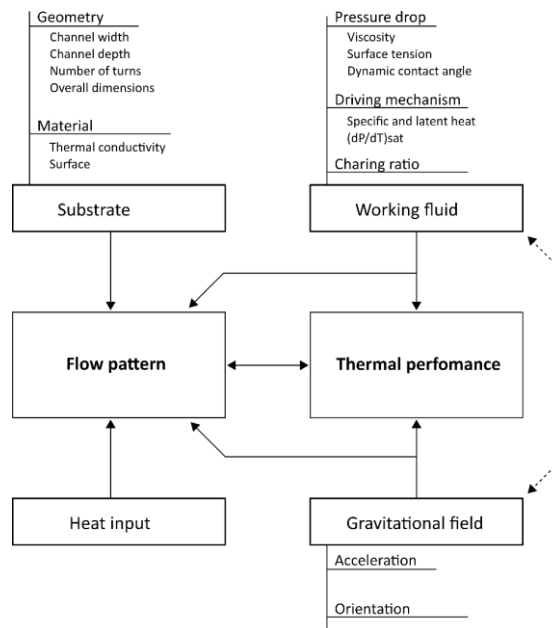


Figure F.1. Parameters affecting the flow pattern and thermal performance of the OHP and μ OHPs.

F.1 Geometry and Hydraulic Diameter

The cross-section of the microchannels (e.g. circular, trapezoidal, rectangular or square) influences the operating range of the micro oscillating heat pipe. The maximum allowed heat flux, as well as the start-up heat flux, are observed to increase with the hydraulic diameter [304]. In addition, A thinning of the liquid film results from the existing pressure gradient, which leads to an increase in the heat transfer capabilities and the operating range.

The maximal operational power input and orientation of a μ OHP are significantly affected by the number of turns. Lee et al. [323] observed that a greater number of turns results in a higher maximum allowed heat flux. Furthermore, they observed a dependency of the limiting inclination angle with the number of turns present in the μ OHP as they test μ OHPs with 5, 10, 15 and 20 turns. The μ OHPs with 20 turns featured similar maximum allowable heat flux and thermal resistance, whether in horizontal or vertical positions, with the evaporator at the bottom.

F.1.1 Criterion for Horizontal Operation

While a simple option to guarantee an operating device would be to design a μ OHP with a sufficiently high number of turns, this approach often clashes with the space constraints associated with the design of the thermal management device. Jun and Kim [324] developed a criterion that would guarantee a μ OHP to work in horizontal position. They assumed that the oscillating motion of the slug and plugs could be modelled as a mass-spring-damper system and that the damping coefficient affects the amplitude of the oscillations. Therefore, they postulated that a negative damping coefficient induced a large-amplitude oscillating motion of the fluid, which was experimentally verified. The vapour damping force acts as a driving force in the μ OHP, and therefore it needs to be appropriately larger than the frictional force to suppress the positive damping. Based on the Figure of Merit principle for conventional heat pipes, they defined a figure of merit for normal horizontal operations of oscillating heat pipe ($M_{PHP,HNOP}$) as:

$$M_{PHP,HNOP} \propto \frac{\text{Vapour damping force}}{\text{Frictional damping force}} \quad (\text{F.1})$$

They assumed that the length of the liquid slug between two vapour plugs was directly proportional to the charging ratio of the working fluid. Thus, the frictional damping (γ_f) coefficient was expressed as the product of the viscosity of the liquid phase (μ_l), the effective length (L_{eff}) and the charging ratio (ϕ):

$$\gamma_f = \mu_l L_{eff} \phi \quad (\text{F.2})$$

The damping coefficient of the two adjacent vapour plugs ($\gamma_{v,i}$ and $\gamma_{v,i+1}$) was expressed as:

$$-(\gamma_{v,i} + \gamma_{v,i+1}) \propto \frac{\kappa_v R_g \rho_v T_v D_h^2}{(1 - \phi) L_{eff}} \quad (\text{F.3})$$

Where κ_v is the thermal conductivity of the vapour phase and R_g is the gas constant.

By substituting the equations (F.2) and (F.3) in the equation (F.1) yields the Figure of Merit as:

$$M_{PHP,HNOP} \propto \frac{-(\gamma_{v,i} + \gamma_{v,i+1})}{\gamma_f} = \frac{\kappa_v R_g \rho_v T_v}{\mu_l \phi (1 - \phi)} \left(\frac{D_h}{L_{eff}} \right)^2 \quad (\text{F.4})$$

Based on their experimental results, coupled with the ones from Jun and Kim [228], and Charoensawan et al. [208], they proposed that the ratio D_h/L_{eff} had to be larger than 0.03 for the μ OHP to maintain similar heat transfer in bottom heating or horizontal configurations. However, they limited the research to μ OHPs operating with ethanol and used μ OHP with ten turns, which already influenced operations of an inclined μ OHP, as seen previously.

F.1.2 Dual-diameter for Horizontal Operations

On the other hand, Kwon and Kim [226], [283], based on Chien et al.'s work [222] developed a dual-diameter, or asymmetric, μ OHP that creates unbalanced capillary forces and vapour expansions favourable for the system's operations. They assumed a one-dimensional pressure gradient for slug-plug two-phase (dP_{tp}/dz) flow that is expressed as:

$$-\frac{dP_{tp}}{dz} = f \left(\frac{1}{2} \rho U^2 \right) \frac{4}{D_h} \quad (\text{F.5})$$

The friction factor (f) depends on the phase regimes. Kreutzer et al. [325] estimated the friction factors for the liquid and a vapour plug surrounded by liquid slugs, respectively, as:

$$f_l = \frac{16}{Re} \quad (\text{F.6})$$

$$f_{slug-plug} = \frac{16}{Re} \left[1 + \frac{7.16(3Ca)^{\frac{2}{3}}}{32L_{slug}^* Ca} \right] \quad (\text{F.7})$$

Where L_{slug}^* is the dimensionless slug length L_{slug}/D_h , Ca and Re are respectively the capillary and Reynolds numbers. Therefore, they expressed the total pressure drop (ΔP_f) as:

$$\Delta P_f = \left(\frac{8}{\pi} \left[1 + \frac{7.16(3Ca)^{\frac{2}{3}}}{32L_{slug}^*} \right] \frac{\mu_{TP}}{\rho_{TP}} \frac{1}{h^4} \left(1 + \frac{h}{w} \right)^4 \beta L + \frac{8\mu_l}{\pi\rho_l} \frac{1}{h^4} \left(1 + \frac{h}{w} \right)^4 (1 - \beta)L \right) \dot{m} \quad (\text{F.8})$$

Where β represents the fraction of the channel occupied by the liquid slug, h and w are the height and width of the microchannels, L is the length of channel and \dot{m} the mass flow rate.

They estimated the two-phase viscosity and density in function of the vapour quality (χ) and β as:

$$\mu_{TP} = \chi\mu_g + (1 - \chi)\mu_l \approx \mu_l \quad (\text{F.9})$$

$$\rho_{TP} = \beta\rho_g + (1 - \beta)\rho_l \approx (1 - \beta)\rho_l \quad (\text{F.10})$$

As viscosity and density of the liquid are higher than those of the vapour phase, total pressure drop can be rewritten as:

$$\Delta P_f = C_f \frac{\mu_l}{\rho_l} \frac{1}{h^4} \left(1 + \frac{h}{w} \right)^4 L \dot{m} \quad (\text{F.11})$$

Where C_f is the friction coefficient defined as a function of the channel length occupied by the liquid slug:

$$C_f = \frac{8}{\pi} \left(\frac{\beta}{1-\beta} \left[1 + \frac{7.16(3Ca)^{\frac{2}{3}}}{32L_{slug}^*} \right] + (1-\beta) \right) \quad (F.12)$$

In their specific case, they fixed the charging ratio of their experiments to 50%, or $\phi = 0.5$, and the coefficient to 4 as it was estimated to vary between 3.9 and 4.1 for the experimental conditions, albeit it depends also on the microchannel diameter and flow velocity. Since, they estimated the capillary pressure difference to be proportional to $\sigma(1/w_2 - 1/w_1)$ and the total frictional pressure drop to $C_f = \frac{\mu_l}{\rho_l} \left(1 + \frac{h}{w}\right)^4$, the figure of merit is expressed as the ratio of the maximum capillary driving pressure over the frictional pressure drop generated by the slugs and plugs:

$$M_{php} = \frac{N \rho_l \sigma \left(\frac{1}{w_2} - \frac{1}{w_1} \right)}{\mu_l C_f \left[N \left(\left(1 + \frac{h}{w_1}\right)^4 + \left(1 + \frac{h}{w_2}\right)^4 \right) + (N_t - N) \left(1 + \frac{h}{w}\right)^4 \right]} \quad (F.13)$$

With N and N_t the number of pair of dual-diameter microchannels and the total number of microchannels, respectively. M_{php} is directly influenced by the number of pairs of microchannels, as the authors highlighted. Kwon and Kim suggested that whenever the values of M_{php} are superior to $2 \cdot 10^5$ [kg/m^3s], μ OHPs would operate independently of the inclination angle.

Additionally, the diameter difference directly influences both the frictional pressure drop and the capillary pressure. Kwon and Kim defined a dimensionless hydraulic diameter difference as $\Delta D/D_{avg}$ and their experimental investigation concluded that an optimum dimensionless hydraulic diameter difference exists between 0.3 and 0.5 for channels' widths ranging from 200 μ m to 1800 μ m with ethanol and C_6F_{14} . Jang *et al.* [301] investigated the roles of the asymmetry and aspect ratios in dual-diameter channels with widths ranging from 800 μ m to 3.2mm. The optimums for both the asymmetry and the aspect ratio were found to be dependent on the power input and the associated flow pattern.

F.1.3 Microgravity and Hydraulic Diameter

The operations of OHP and μ OHP has been demonstrated to operate without or against the gravity field. Based on calculations, microgravity would lead to an unrealistically large diameter for OHP channels. Gu *et al.* [256] defined an upper limit for the hydraulic diameter in microgravity based on the surface energy and the kinetic energy. They assumed that the surface energy (E_s) has to be larger than the kinetic energy (E_k), per unit of volume, to maintain a stable slug-plug two-phase flow in circular ducts with a radius of curvature of the menisci equal to the duct's radius:

$$E_s \geq k E_k \quad (F.14)$$

With k , an empirical correction factor. This can also be expressed as,

$$\frac{\sigma}{r} \geq k \frac{1}{2} \rho_l U^2 \quad (\text{F.15})$$

Gu et al. used $k = 1$ in their model of transition from slug-plug to annular flow. The equation (F.15) can be rewritten as:

$$D_{max}^{og} \leq \frac{4\sigma}{\rho_l U^2} \quad (\text{F.16})$$

$$We \leq 4 \quad | \quad (\text{F.17})$$

In microgravity, the limit diameter reduces as the velocity increases. Harirchian and Garimella [284] included the inertial effects in their own definition of the threshold hydraulic diameter determining the transition from a slug-plug to an annular flow (confined and unconfined flow). They experimentally defined their convective confinement number and the transition limit as $Bo^{0.5} Re = 160$. Therefore, the maximal diameter based on this convective confinement number can be expressed as:

$$D_{max}^{Ga} \leq \sqrt{\frac{160\mu_l}{\rho_l U_l} \sqrt{\frac{\sigma}{g(\rho_l - \rho_v)}}} \quad (\text{F.18})$$

The critical diameter given by Harirchian and Garimella results in larger hydraulic diameters in microgravity than in ground operation. Therefore, testing a (μ) OHP based on this criterion applied to microgravity leads to stratified flow when on ground, typical from a loop thermosiphon. However, the same device operating in microgravity yields an oscillating slug-plug type flow [259].

F.1.4 Number of Turns

Increasing the number of turns reduces the influence of the orientation, as expressed in the equations (F.20), (F.21) and (F.22). It can be observed that in the horizontal position ($\alpha = 0^\circ$), only the maximal heat flux q''_{max} depends only on the film formation rate $q''_{max,form}$. The influence of the number of turns reaches a plateau value when the number of turns is high, as it is visible in Figure F.2. Therefore, a minimum of turn is mandatory to reduce the effect of the orientation of the operations of the μ OHP.

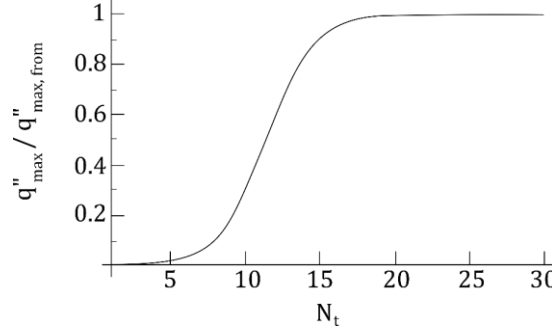


Figure F.2. Influence of the number of turn on the maximal heat flux in horizontal position accordingly to (F.20).

F.2 Heat Fluxes

As heat actuates the flow of the working fluid trapped in the micro-devices, the literature studied the operation range of various configurations of μ OHP. Lee and Kim [304] established a model of the thin film flow rate evaporation and the film flow rate in a single microchannel vertically oriented. They postulated that to remain within the operative range, the film flow rate had to be greater or equal to the evaporative rate, which is expressed as:

$$q''_{max} \approx C \frac{\rho_l^2 h_{lv} g D_h^3}{\mu_l L_e} \quad (F.19)$$

Where C is a constant based on experimental results with C_6F_{14} , ρ_l is the liquid density, h_{lv} the latent heat of vaporisation, g is the gravitational acceleration, D_h is the hydraulic diameter, μ_l the liquid's viscosity and L_e the evaporator's length.

They defined C for circular and square cross-sections as:

$$C = \begin{cases} 0.000226 & \text{for channel with circular cross-section} \\ 0.000388 & \text{for channel with square cross-section} \end{cases}$$

They extended the model to multi-turn and to horizontally operated μ OHP [323] and estimated the maximal heat fluxes (q''_{max}) as a function of the film-formation rate ($q''_{max,form}$), the falling-film rate ($q''_{max,fall}$), the inclination angle α and the number of turns n_t . This correlation is expressed as:

$$q''_{max} = \frac{q''_{max,fall} - q''_{max,form}}{1 + e^{\frac{n_t - (11.39 + 0.00132\alpha)}{1.61}}} + q''_{max,form} \quad (F.20)$$

With $q''_{max,fall}$ and $q''_{max,form}$ as:

$$q''_{max,fall} = \frac{\rho_l(\rho_l - \rho_v)h_{lv} g \sin(\alpha)}{3\mu_l A_e} \int_0^{2\pi} [\delta(\theta)]^3 r d\theta \quad (F.21)$$

$$q''_{max,form} = \frac{\rho_l h_{lv} L_e f}{A_e} \int_0^{2\pi} \delta(\theta) r d\theta \quad (F.22)$$

With f the frequency of liquid film formation, ρ_l and ρ_v the densities and A_e the evaporation area and δ the liquid film thickness. The liquid film thickness depends on the velocity of the liquid slug and vapour plugs and, thus, on the contact angle of the two phases and on the geometry of the microchannels.

The minimal heat flux (q_{min}) required to start the flow motion of the fluid is also a critical parameter in the operation of the μ OHPs. Two start-up phenomena have been identified by Sun et al. [206]: start-up with or without bubble nucleation. The first phenomenon was linked to the generation and expansion of bubbles in the liquid slugs. A minimum amount of energy had to be built up before oscillations could be triggered, as the working fluid absorbed the heat and increased the pressure. At a certain point, the heat started generating bubbles, which grew and activated the fluid loop. The second phenomenon was related to the strong liquid thin film evaporation, which generated the pressure gradient required. It resulted in vapour plugs emerging from the breakup of the liquids slug in the turns induced by the surface tension gradient. While both phenomena resulted in different temperature patterns, the initial two-phase distribution of the slugs and plugs along the microchannels significantly affected both occurrences.

Qu and Ma [302] suggested that the maximal heat transfer rate through the thin liquid film evaporation, just before the formation of bubbles on an active nucleation site, can be expressed as:

$$q_{min} = \frac{\lambda_l \Delta T}{r_{in} \ln \left[\frac{r_{in}}{r_{in} - \delta_l} \right]} \quad (F.23)$$

$$\Delta T = T_{sat} \left(\frac{1}{1 - \frac{R_g T_{sat}}{h_{lv}} \ln \left[1 + \frac{2\sigma}{P_{sat}} \left(\frac{1}{r_n} - \frac{1}{2(r_{in} - \delta_l)} \right) \right]} - 1 \right) \quad (F.24)$$

With ΔT the required wall superheat for bubble nucleation.

Qu and Hu [201] gave the following formulation for the superheat:

$$\Delta T = T_w - T_{sat} \geq \frac{2 \sigma T_{sat}}{8 h_{lv} \rho_v} \left(\frac{\rho_l}{\rho_l - \rho_v} \right) \quad (F.25)$$

Small hydraulic diameters lead to high-pressure drops and also tend to result in high superheat to start the μ OHP. Figure F.3 depicts the calculation of Taft et al. [326] for the minima heat flux for several working fluid as function of the fluid temperature, based on the equations (F.23) and (F.25).

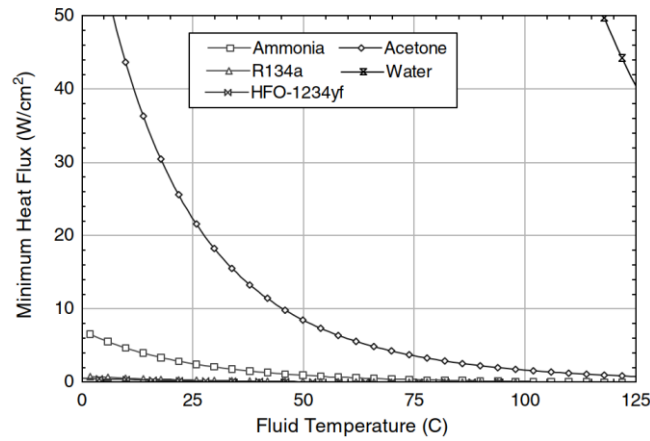


Figure F.3. Heat flu for PHP start-up as a function of bulk fluid temperature ($\epsilon = 2.5\mu\text{m}$, $r_{in} = 1\text{mm}$, $\delta_l = 10\mu\text{m}$) [326].

It is worth noting that combinations of different substrate materials and working fluids have not been directly studied. The contact angle varies for each combination, thus modifying the wetting of the inner surfaces of the microchannels and the evaporation rates of the fluids. Furthermore, the thermal conductivity (and diffusivity) is not taken in account. A highly thermally conductive material, despite allowing heat flow from the heated wall to the microchannels, is subject to transverse thermal conductivity, thus possibly requiring a larger heat flux to reach oscillations.

F.3 Working Fluids

The physical properties of the working fluids, such as surface tension, specific and latent heat, viscosity and contact angles, affects the pressure drops and the thermodynamics of the μOHPs .

An ideal working fluid would possess a large saturation pressure gradient, enhancing the driving pressure resulting from the evaporation [209] therefore, the potential driving pressure increases with the steepness of the gradient.

Additionally, the latent heat of vaporization determines bubble growth rate and shrinkage. Fluids with a low latent heat of vaporisation evaporate at lower power inputs than fluids with a high latent heat of vaporisation. Consequently, the pressure gradient is generated at lower heat loads for fluids possessing a low latent heat of vaporization, which translates into a start-up at lower power inputs. The specific heat of the fluids also influences the heat transfer capability of the device [215] and high values are favoured for high thermal performance.

The slug-plug flow depends on the contact angle hysteresis existing between the advancing and receding edges of the liquid slugs. This hysteresis creates a capillary resistance to the moving flow. Therefore, a fluid with a low contact angle hysteresis is preferable. However, the data available on the dynamic contact angle of liquid-substrate pairs is almost non-existent. The surface tension also influences the flows inside a μOHPs , as it influences the bubble nucleation and the contact angles. Also, as the surface tension change with the temperature, an additional capillary force is created. In general, low surface tension is preferable. The dynamic viscosity of the fluid

affects the start-up of the μ OHPs and their thermal performance as it directly influences the hydraulic resistance encountered in the microchannels by the mean of the shear force. Therefore low values of dynamic viscosity are preferred.

F.4 New Lower Hydraulic Diameter Limit

As introduced in section 2.3.4.3, the hydraulic diameter of microchannels plays an important role in the thermal performance self-sustained flows. Zhang and Faghri's upper limit [215] for the hydraulic diameter, as well as Dobson and Harms' lower limit [216], should guarantee an operating μ OHP. Qu et al. [217] introduced the operating characteristic of the μ OHP in their new definition of the lower limit of the inner diameter, resulting in reduced minimal hydraulic diameters compared to the proposition of Dobson and Harms. Their theoretical model was based on the pressure gradient from the evaporator and the condenser. Considering that the oscillations mainly occurs in the straight portions of the channels, gravitational are not taken into account because of high number of turns, and local pressure losses due to the bends can be neglected. The simplified equation can be written as [217]:

$$\frac{We\Theta}{EcJa^*} D^* \geq 32(1 - \phi)(2m + L^*)[Ca + 0.104(Ca - \phi)^{0.893} \phi^{0.05} Re^{0.405} Ca^{0.7387}] \quad (F.26)$$

Where ϕ , We , Θ , ϕ , Ec , Ja^* , D^* , m , L^* , Re and Ca are respectively, the charging ratio or the fraction of volume of the liquid phase, the Weber number, the dimensionless temperature, the Eckert number, the modified Jakob number, the ratio of inner diameter to the total length of the μ OHP, the number of U-turns, the ratio of the width to the length of the μ OHP, the Reynolds number and the Capillary number. They are defined as follow:

$$We = \frac{\rho_l U_{TP}^2 D}{\sigma} \quad (F.27)$$

$$\Theta = \frac{T_e - T_c}{T_e} \quad (F.28)$$

$$Ec = \frac{U_{TP}^2}{c_p(T_e - T_c)} \quad (F.29)$$

$$Ja^* = \frac{\rho_l \phi c_p (T_e - T_c)}{\rho_{v,c} (1 - \phi) h_{fg}} \quad (F.30)$$

$$D^* = \frac{D}{L_t} \quad (F.31)$$

$$L^* = \frac{L_w}{L_t} \quad (F.32)$$

$$Re = \frac{\rho U_{TP} D}{\mu} \quad (F.33)$$

$$Ca = \frac{\mu U_{TP}}{\sigma} \quad (F.34)$$

Where ρ is the density of the respective phases (l liquid, v vapour, v, c vapour at the condenser), U_{TP} the speed of the two-phase flow, D the hydraulic diameter, σ the surface tension, T_e and T_c

the temperature of the evaporator and condenser, c_p the specific heat capacity, h_{fg} the latent heat, μ the viscosity, L_t and L_w the overall length and width of channel constituting the heat pipe as shown in Figure F.4.

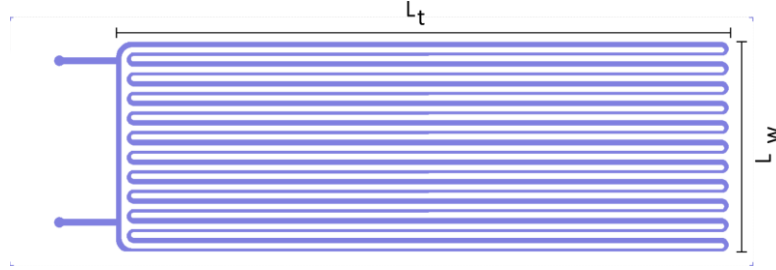


Figure F.4. Schematic representation of the values L_w and L_t used for the determination of the lower limit for hydraulic diameter of the microchannels.

The Weber number represents the entrainment limit in two-phase flow where the shear stress generated by the vapour phase on the liquid one entrains droplets in the vapour flow. It is expressed as the momentum of the vapour phase over the cohesion force restraining the liquid surface. The Eckert number Ec is used to characterize the heat transfer dissipation. It is expressed as the kinetic energy of the flow over the heat dissipation potential. The modified Jakob number Ja^* , characterises the ratio of sensible heat over latent heat absorbed during the phase change, for both evaporation and condensation. The Reynolds number Re is the ratio between the internal forces to viscous forces resulting from different fluid velocities. It helps to predict the different flow situation and the transitions between them. The ratio between the viscous forces and the surface tension acting on a liquid-gas interface defines the capillary number. The phenomena described by this dimensionless quantity governs the contact angle of a flowing droplet in a microchannel.

The proposed lower limit varies non-monotonically with the charging ratio. As the driving potential increases at the same time as the temperature gradient, the lower limit for hydraulic diameters decreases. This lower limit follows the same decreasing trend when the length and number of turns decrease. Gravity also plays a role; a smaller hydraulic diameter is required to operate in the vertical position with the evaporator at the bottom than at the horizontal position, which can be explained by the larger flow returning to the evaporator due to the gravity. The number of turns influences also the lower limit as the increasing number of turns increases the flow resistance. Thus, a greater number of turns leads to a larger hydraulic diameter.

F.5 Figure of Merit of the Working Fluid

Kim and Kim [327] proposed of Figure of Merit for the selection of the working fluid M_{PHP}^{WF} based on the ratio of the driving pressure over the frictional pressure drop of two adjacent vapour plugs. They expressed Figure of Merit M_{PHP}^{WF} as:

$$M_{PHP}^{WF} = \frac{\rho_l c_{p,l} \left(\frac{dP}{dT} \right)_{sat} Z R_g T_{sat}}{\mu_l h_{lv}} \quad (F.35)$$

Where T_{sat} is the saturation temperature, R_g is the gas constant, Z is the compressibility factor, $(dP/dT)_{sat}$ the pressure gradient in function of the temperature, h_{lv} , μ_l , ρ_l and $c_{p,l}$ are respectively the latent heat of vaporization, the liquid's viscosity, the liquid's density and the specific heat of the liquid phase. The saturation temperature T_{sat} was determined as the time-averaged value of the working fluid measured in the adiabatic section. The operating temperature and the working fluid allowed qualitative predictions of the thermal performance of the test μ OHPs with different working fluids. They tested one device half-charged with ethanol, C_6F_{14} , R134a, R245fa and HFE-7000. R134a yielded the highest value for M_{PHP}^{WF} in their study and performed the best.

In comparison, the Figure of Merit for conventional heat pipes $M_{CHP}^{WF} = \rho_l \sigma h_{lv} / \mu_l$ are not the same due to the underlying driving mechanism. Conventional heat pipes rely on capillary pumping from the wicking structures. Therefore, the changes in surface tension and liquid viscosity of the working fluid with respect to temperature is the dominating factor when operating conventional heat pipes. In contrast, the gradient of saturation pressure drives the fluid motion in an OHP.

F.6 Latent and Sensible Heat

The total heat transfer is a combination of phase change of the fluid, sensible heat and substrate thermal conduction. The sensible and latent heats cause a pressure difference that induces a thermally driven flow motion. Both sensible and latent heats are linked to the thermos-hydrodynamic behaviour of two-phase flows in μ OHPs. Thus, they partially govern their own thermal performance. Heat transfer mechanisms are not fully understood after decade long investigations.

Sahffi et al. [328] proposed a theoretical heat transfer model highlighting that sensible heat is the dominant heat transfer mechanism. Cheng and Ma [329] and Zhang et Faghri [172] developed mathematical models for oscillating two-phase flows, predicting that the dominant component was the sensible heat, contributing to more than 90% of the total. By accounting for bubble generation by nucleate boiling, Senjaya and Inoue [330] obtained a model describing a total of 74% of heat transferred as sensible heat. Additionally, optical measurements of the contraction-expansion rate of bubbles inside OHP, conducted by Nishio *et al.* [331], concluded that latent heat contributed for less than 15% of the total heat exchange.

However, several conflicting results regarding the contribution ratios of sensible and latent heat have been reported. Nikolayev [332] determined that the contribution of the latent reached 82% in the evaporator and 71% in the condenser with the help of a numerical model. In addition, Onishi et al. [333] concluded that the latent heat was responsible for 90% of the total heat transferred according to their model they developed of a single-turn OHP. Nagasaki et al. [334] studied, experimentally and numerically, a straight rectangular OHP and found that the latent and sensible heat's contributions were similar. Furthermore, Jo et al. [335] used infrared thermometry and high-speed flow visualisation measurements to determine that the latent heat transfer by phase change dominates the heat transfer with a contribution ranging from 66% to 74%. They concluded that the phase change heat transfer induced the oscillating motion by generating a pressure difference and significantly contributed to the total heat transfer, while the sensible heat transfer can be considered as a by-product of the two-phase flow.

Appendix G. High-speed Times Strips

Time-strip analyses were conducted on a multi-turn μ OHP. The times strips were realized, centred around the evaporator, in horizontal position. The identification of the channel pairs is done accordingly to Figure G.1

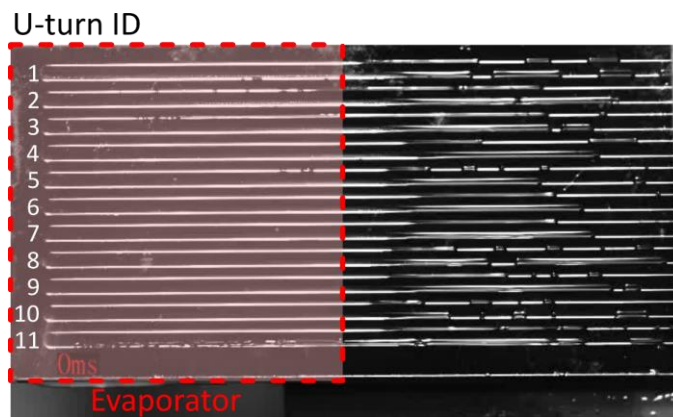
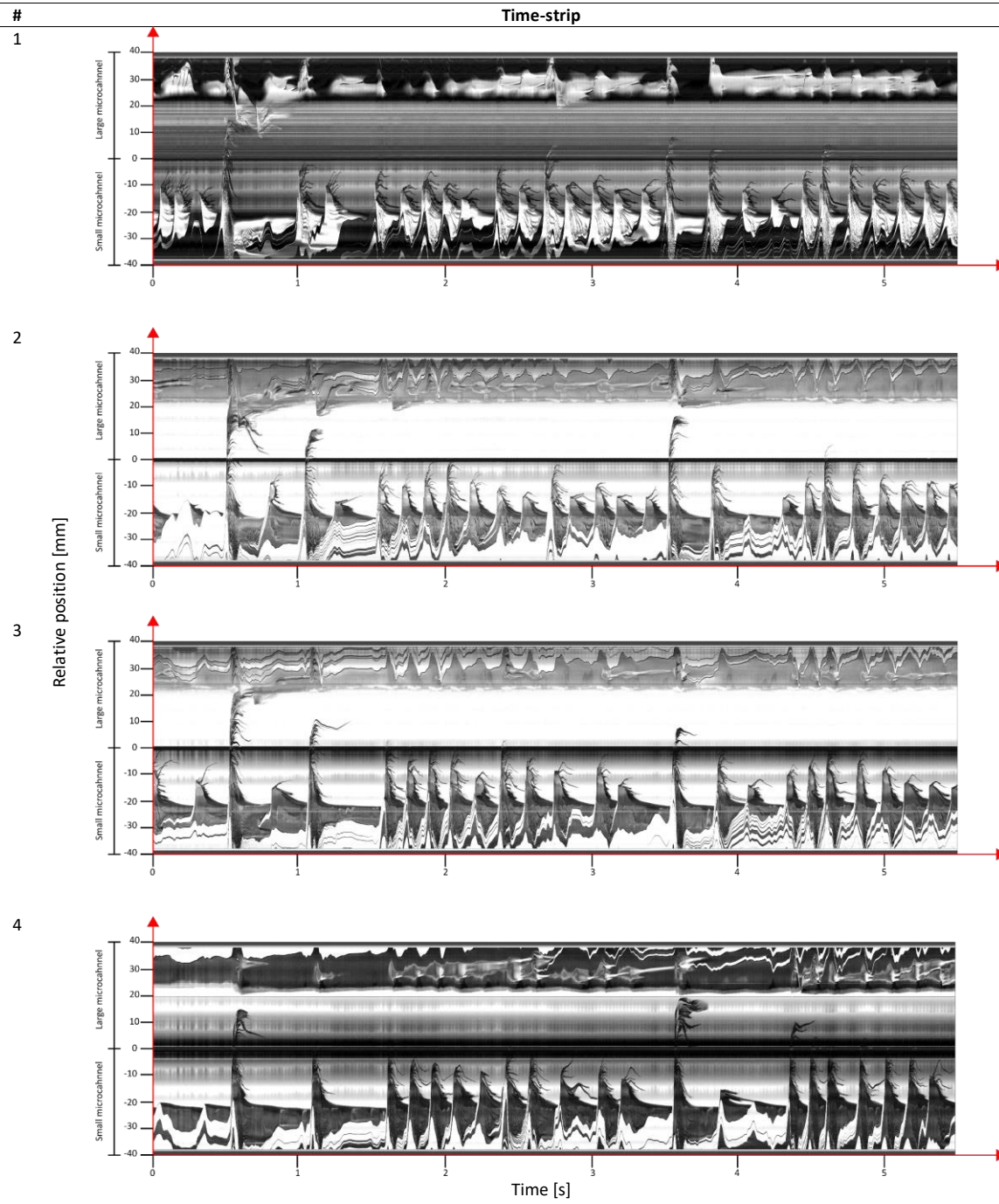
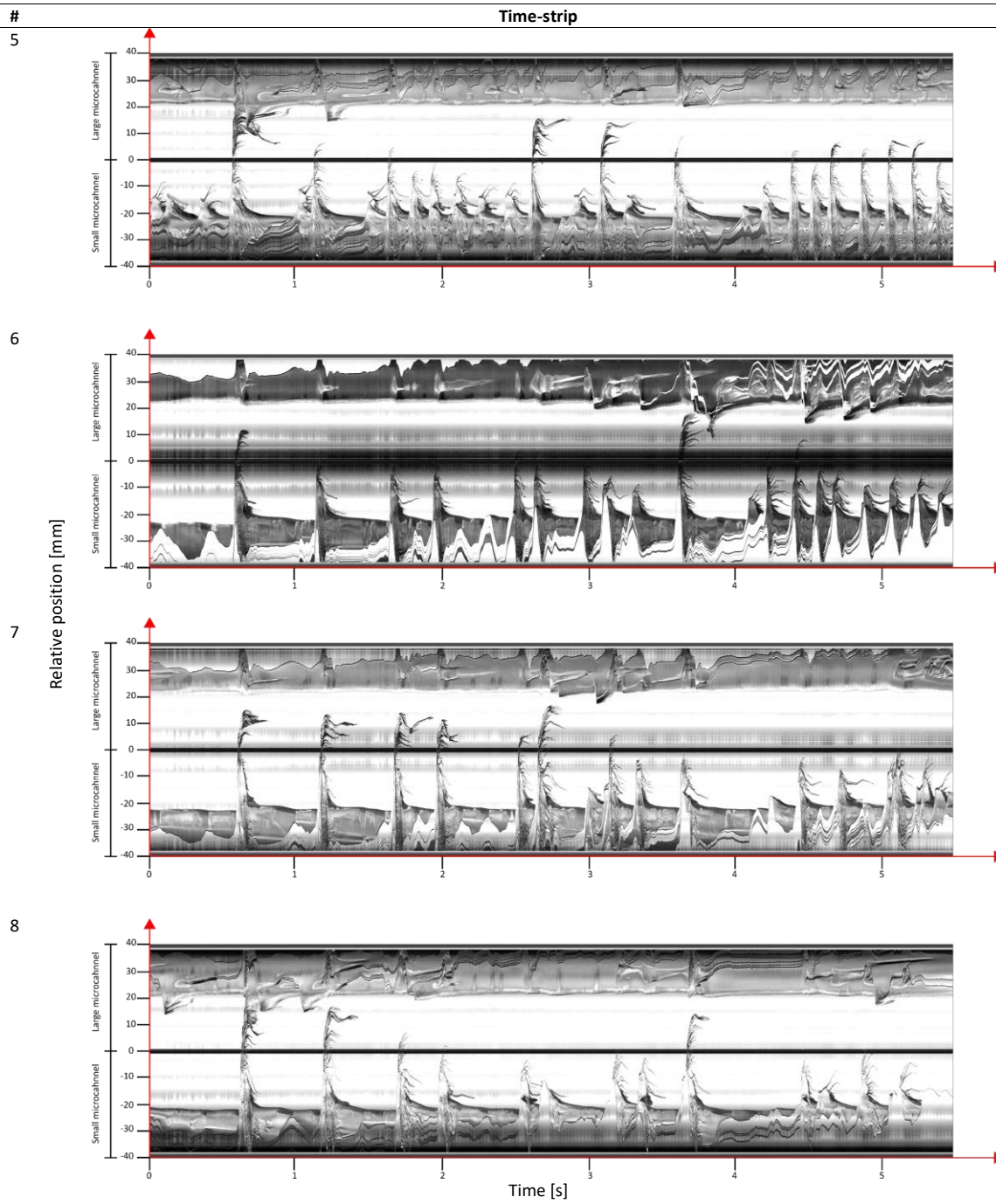


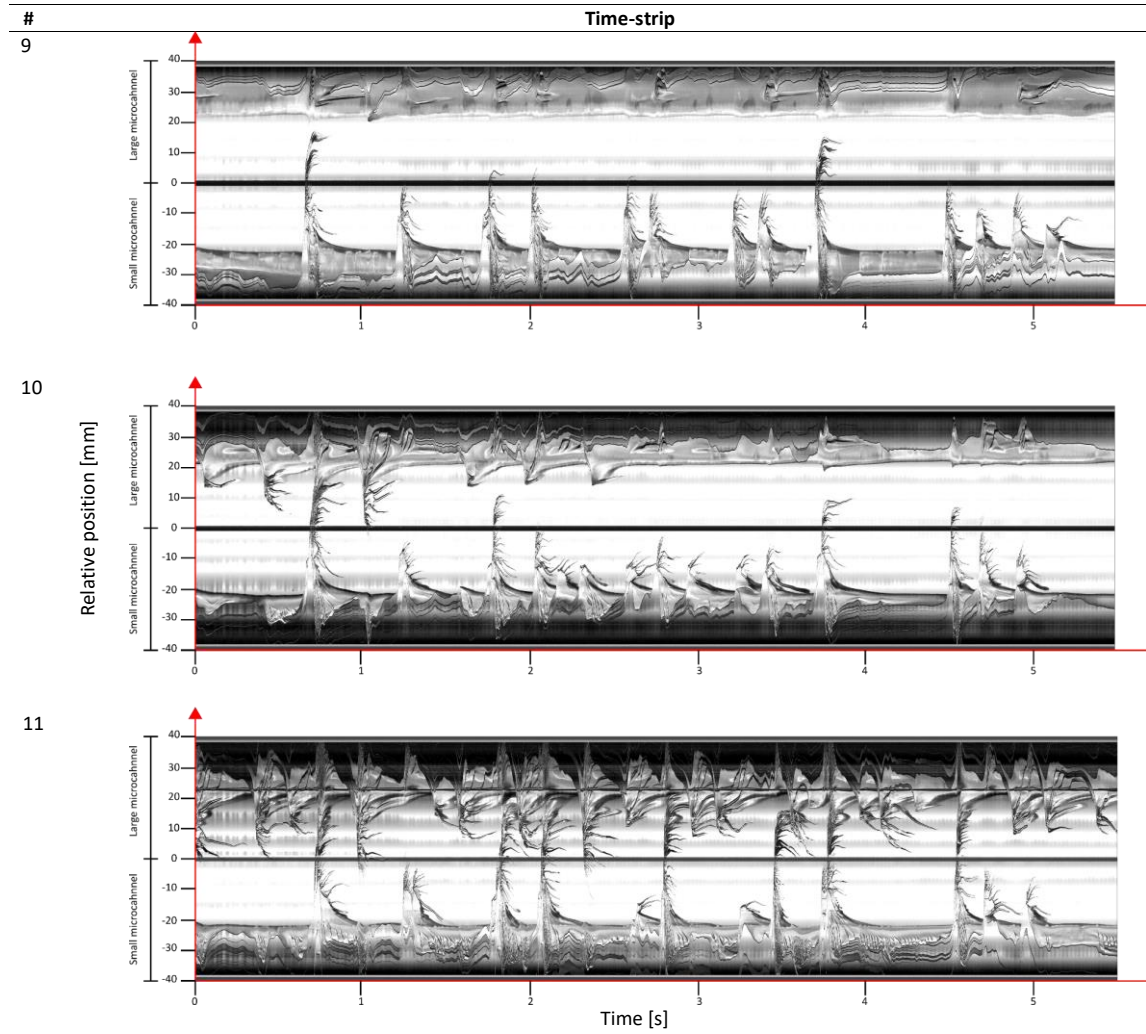
Figure G.1. Identification of the different U-turn in the evaporator for time-strips.

The image was realized either with a high-speed camera Photron FASTCAM Mini AX coupled to a Tokina Macro lens (100mm), or with a camera equipped with an EyeTrak 19MP high-speed sensor; and two lights.

a. Acetone at 11W ($\varphi = 50\%$, $\alpha = 0^\circ$)







Appendix H. Existing Packaging and Sealing Solutions

I.1 Valve Sealing

The most common sealing solution used in experimental research on micro heat pipe is a valve positioned on the charging line with a tube connected to the micro heat pipe. Although valves offer a solution easy to setup and allow changing the working fluid's inventory or the working fluid itself, the inerrant weight and volume occupied make them unsuitable in a real word application. It should be noted that no literature has revealed the use of MEMS micro-valves as sealing solution. These MEMS have been widely studied and continue to be developed for various applications, ranging from biological to space-related applications. These kinds of valves are usually actuated by piezoelectric, electrostatic or thermal means [336]–[339]. But an external actuation is also feasible.

I.2 Tube Crimping

This technic, inherited from metallic and larger heat pipe technology, is used for micro heat pipes. A tube is brazed or soldered at the outlet of the micro-device and connected the charging apparatus. After charging, the tube is crimped. It proved being reliable when correctly done, without adding mass excessively. Dedicated tools compressed the connected fill tube. In the case of plastic tubing, heat is applied simultaneously to seal the tube. In the case of metallic tubing, higher pressure is required to achieve an airtight seal by cold welding, or if heat is applied, brazing can be done.

H.3 Induction Hole Sealing

Dhillon and Pisano developed a non-invasive fill-hole sealing system based on induction heating and solder ($\text{Sn}_{96}\text{Ag}_4$) preforms [193], [310]. The system aimed to seal hermetically silicon and borofloat glass devices by melting a pre-form of solder material, as illustrated in Figure H.1(a). A time-varying magnetic field was applied, using an induction coil, to the thin-film (Ti, Ni and Au) patterned bond pad around the inlet. After injecting the working fluid into the device, the thin-film heated by induction melted the donut-shaped preform positioned over the inlet. The pre-form melted at 221°C and flowed over the inlet, sealing it after cooling down. One successful result test is shown in Figure H.1(b), (c) and (d). Despite the advancement of this solution, no further application has been found in the literature.

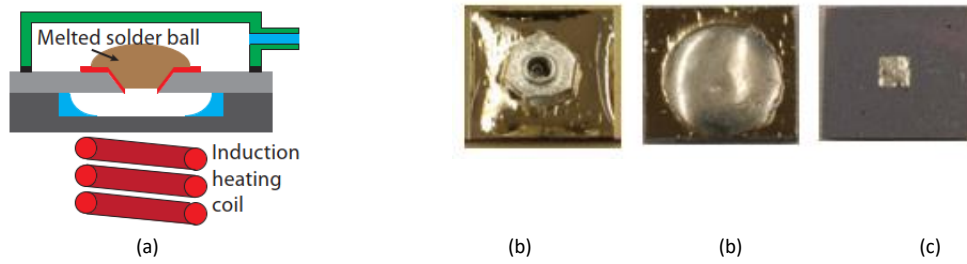


Figure H.1. Induction hole sealing [193]. (a) Schematic of the magnetic sealing system. Example of successful sealing of a sample immersed in water (0.17g, 8.4s, 400W): (b) initial pad, (c) front view after melting, (d) View from the back after melting.

However, the process attested to depend on the induction-time. The solder melted by absorbing the heat from the magnetic bond pad. With a short induction time, the energy was insufficient to melt the solder. If the induction time was prolonged further, the molten alloy would spread away from the inlet due to the hydrophilic behavior of the molten solder and the shape of the thin-film. Additionally, the used solder flux, even if soluble in the working fluid, might have generated unwanted NCGs.

H.4 Low Melting Point Alloy Pumping

Li et al. [311], [312] developed two sealing systems based on bismuth-lead low-melting-point alloys (LMPA) for silicon and borofloat glass micro heat pipes. Both developed systems relied on a zigzagging, or staggered, charging channel with two holes in the borofloat glass lid. The two holes had different diameters: a large one and a small one. The largest one was located the farthest from the micro heat pipe's microchannels, while the small one was located in-between. Li *et al.* placed the LMPA over the large hole and melted it so that it partially filled the charging microchannel. A polypropylene tube linked the smaller hole to the evacuating and filling system. After adding the required amount of working fluid in the microchannels, the LMPA was heated again until it melted. It advanced in the microchannel up to the entrance of the heat pipe's microchannels, as illustrated by Figure H.2(a) and (b). Figure H.2 (c) displays the setup used to flow the LMPA in the channel.

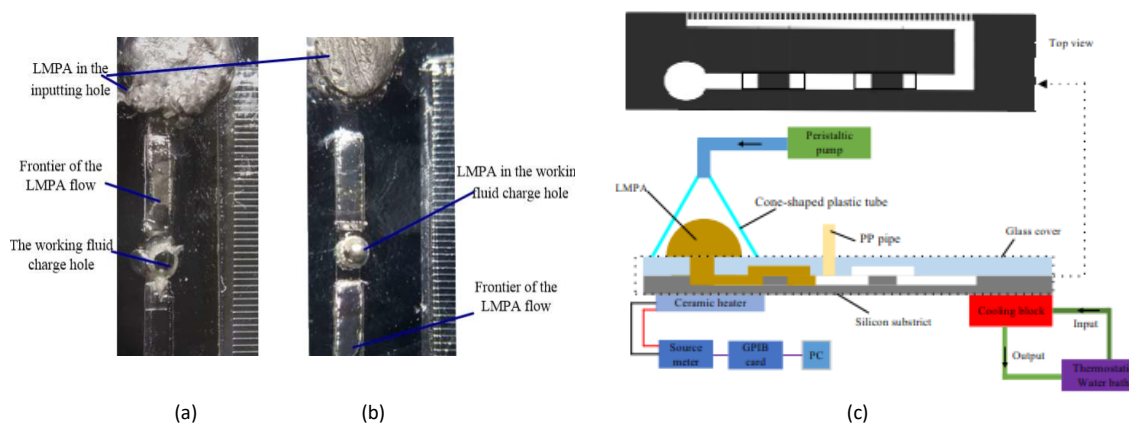


Figure H.2. Magnetic sealing technique. (a) Picture of the charging channel with the LMPA in place before sealing. (b) Picture of the charging channel after charging. The LMPA reached the charging hole and continued in the channel, sealing it. (c) Schematic of the LMPA charging method. [312].

The results showed good potential application to seal micro heat pipes with increased reliability and in a non-invasive way. However, Newton rings and gaps between the wall and the alloy appeared after cooling despite the ability of the alloy to expand over time after solidification.

H.5 Solutions Comparison

Sealing a μ HP with a valve remains the only solution to temporarily enclose liquid in the device. This solution happens to be advantageous if frequent charging or re-charging of the device is foreseen. MEMS-based ones could provide a hermetic and permeant sealing system, with the inconvenience of increasing production and design complexity. Tube crimping, induction sealing and LMPA pumping aim to seal the micro-engineered devices permanently. Among these three techniques, tube crimping presents the inconvenience to be based on an attached tube that protrudes from the device. After sealing, a small protrusion, the tube, remains attached to the silicon, whereas the other two solutions do not have a protrusion after sealing. Sealing by melting a solder preform is an efficient approach under the right parameters. Nevertheless, the nickel thin-film layer and the combination of the material properties of the Sn96Ag4 solder and its CTE might lead to mechanical stress and failure arising from the thermal cycles. The solution proposed by Li et al. [311], [312] used a complex structure in the silicon and glass with an expanding LMPA. Additionally, the two holes on the glass side turn out to be an additional complexity in the system as both have to be hermetically connected. At last, the total volume of LMPA presents a clear disadvantage in terms of occupied footprint in the layout.

In summary, the solutions reviewed do not provide a satisfactory, ready-to-use solution for the sealing of the μ OHPs within the applications' frame. New ways have to be investigated to obtain a hermetical sealing solution with a low footprint and high reliability.

Appendix I. Finite Elements Methods simulation

A transient 2-D CFD analysis using Volume of Fluid (Vof) method was conducted on a single-turn μ OHP using ANSYS Fluent 17.2.

I.1 Volume-of-Fluid method

VoF is an Eulerian numerical method used to model multiples fluids and their free surfaces. The method is based on a fraction function defining the volume fraction of each fluid present in each cell. When a cell is empty, the fraction equals zero; when it is full, the fraction equals one. The normal direction, \mathbf{n} in Figure I.1, of the interface is defined where the fraction's value changes more rapidly, leading to blurry free-surface separations.

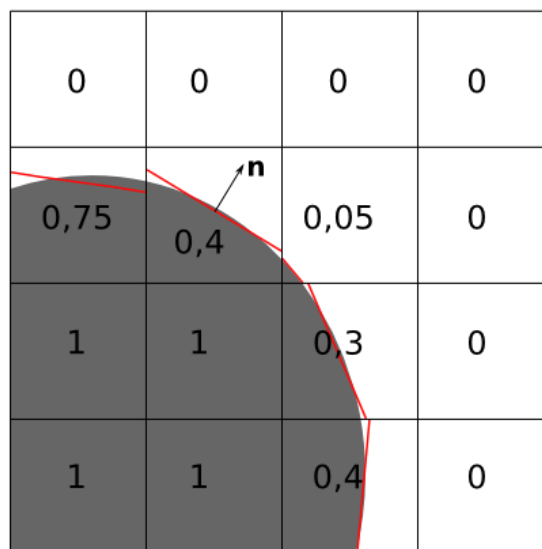


Figure I.1. Scheme of phase affectation in Cartesian grid using piecewise linear interface calculation. (Ikosaeder – 11 march 2014 – CC By-SA 3.0)

However, in cases where large velocity gradients between the phases occur, the accuracy of the velocities computed near the interface can be adversely affected.

I.2 Physical model and method

I.2.1 Physical model

The structure consists of two rectangular U-turns with symmetric microchannels that possessed a width of $350\mu\text{m}$ separated by a $300\mu\text{m}$ wall. Only the fluid of the μ OHP was considered in this analysis.

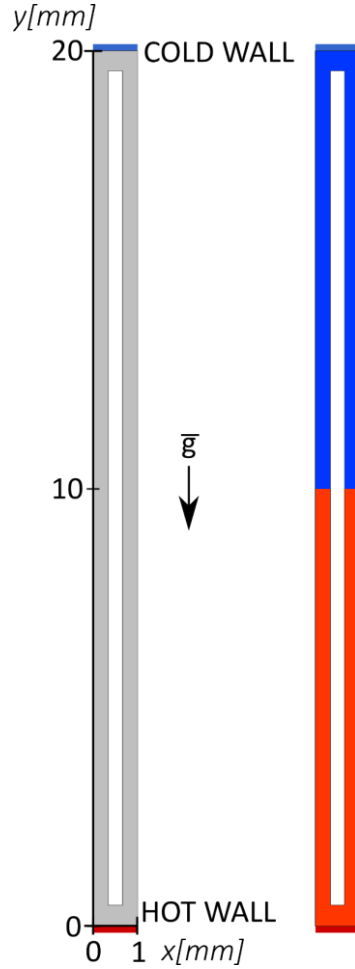


Figure I.2. Model representation (left) and the two different volumes patched (right).

The geometry was set with liquid water at the bottom and vacuum at the top, which are respectively in red and blue in Figure I.2 for a charging ratio of 50%. The model was used for two cases with (i) an imposed temperature gradient and (ii) a fixed cold temperature and an imposed power input. Both cases relied on a cold wall temperature of 293K. The first case imposed a temperature of 383K at the hot wall, and the second imposed a heat flux of $1\text{W}/\text{cm}^2$.

I.2.2 Method

The VoF method imposes to define the fluids present in the analysis. In this case, three were present: vacuum (air at very low pressure), liquid water and vapour water. Their respective physical properties were manually inserted. The roles of the walls were also determined to select which walls were heating, cooling and where the symmetry and adiabatic conditions have to be imposed.

As no inlet or outlet are present in the current model, the elements constituting the mesh were patched with vacuum in the upper part ($y > 10\text{mm}$) and liquid water in the bottom one ($y \leq 10\text{mm}$). This configuration imposed to run few steps, three in for both cases, without energy equations to simulate the liquid flashing. Energy equations were enabled for the rest of the simulations.

A pressure-based solver was used.

I.2.3 Mesh

A quadrilateral meshes uniformly populated the model, as visible in Figure I.3. The mesh remained stationary during the analysis.

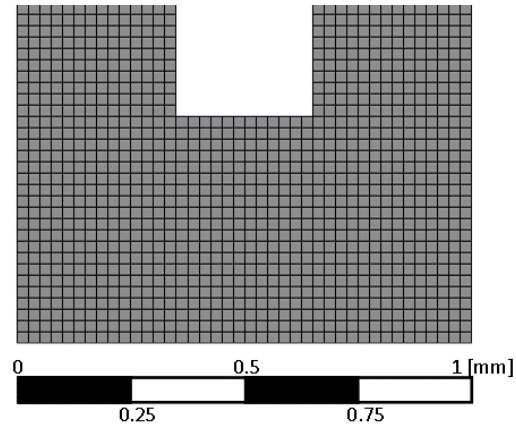


Figure I.3. Detail of the mesh at the U-turn.

I.2.4 Conditions

Transient simulations used a pressure-based solver for the simulations. Water was considered at saturation and the gravitational acceleration was fixed as 9.81m/s^2 . A small initial time step of 10^{-4}s was used but was reduced over the iterations in case of convergence issue, down to 10^{-5}s . Residuals for energy and velocity equations had to remain lower than 10^{-6} and 10^{-4} for the mass residuals.

I.3 Results

I.3.1 CASE I: Imposed temperature gradient

The results resulting from the imposed temperature gradient are presented from the step where energy equations were unable to the step initiating divergence. The temperature and volume fraction of liquid water are presented side-by-side.

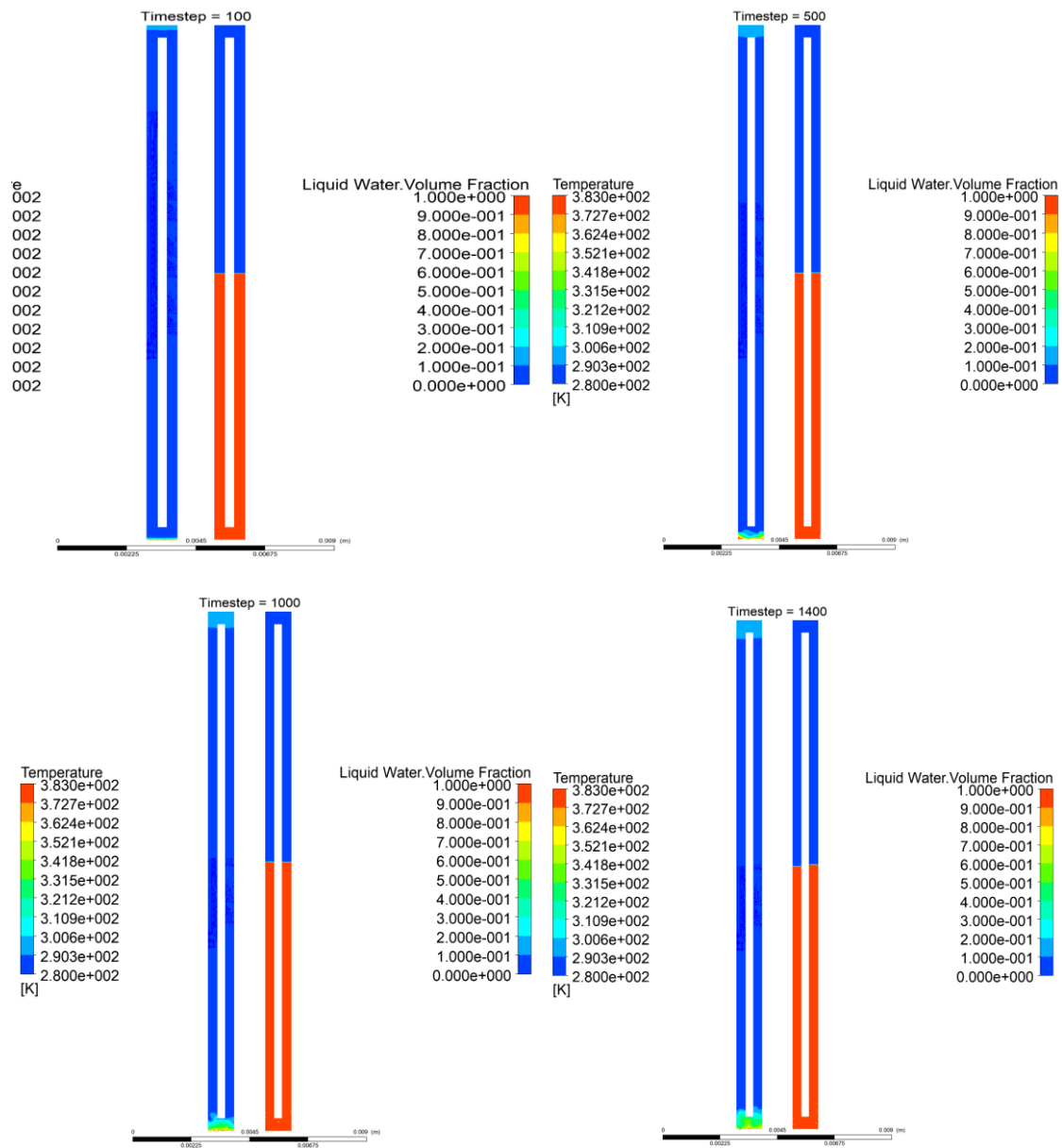


Figure I.4. Temperature and volume fraction of water at different time steps.

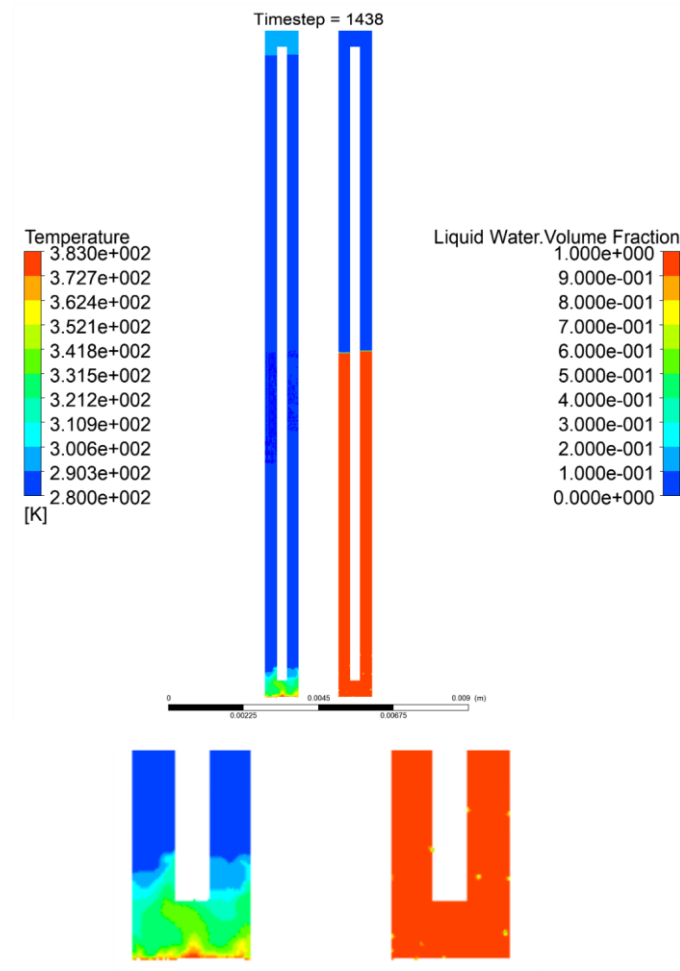


Figure I.5. Temperature and liquid water volume fraction at the last step with details of the evaporator. Small bubbles rises from the heated wall.

This case reached a divergent state after only 1438 steps. Nevertheless, bubble nucleation was observed at the evaporator, but not in sufficient quantity to trigger liquid displacement.

I.3.2 CASE II: Imposed heat flux

The temperature and volume fraction of liquid water are presented side-by-side.

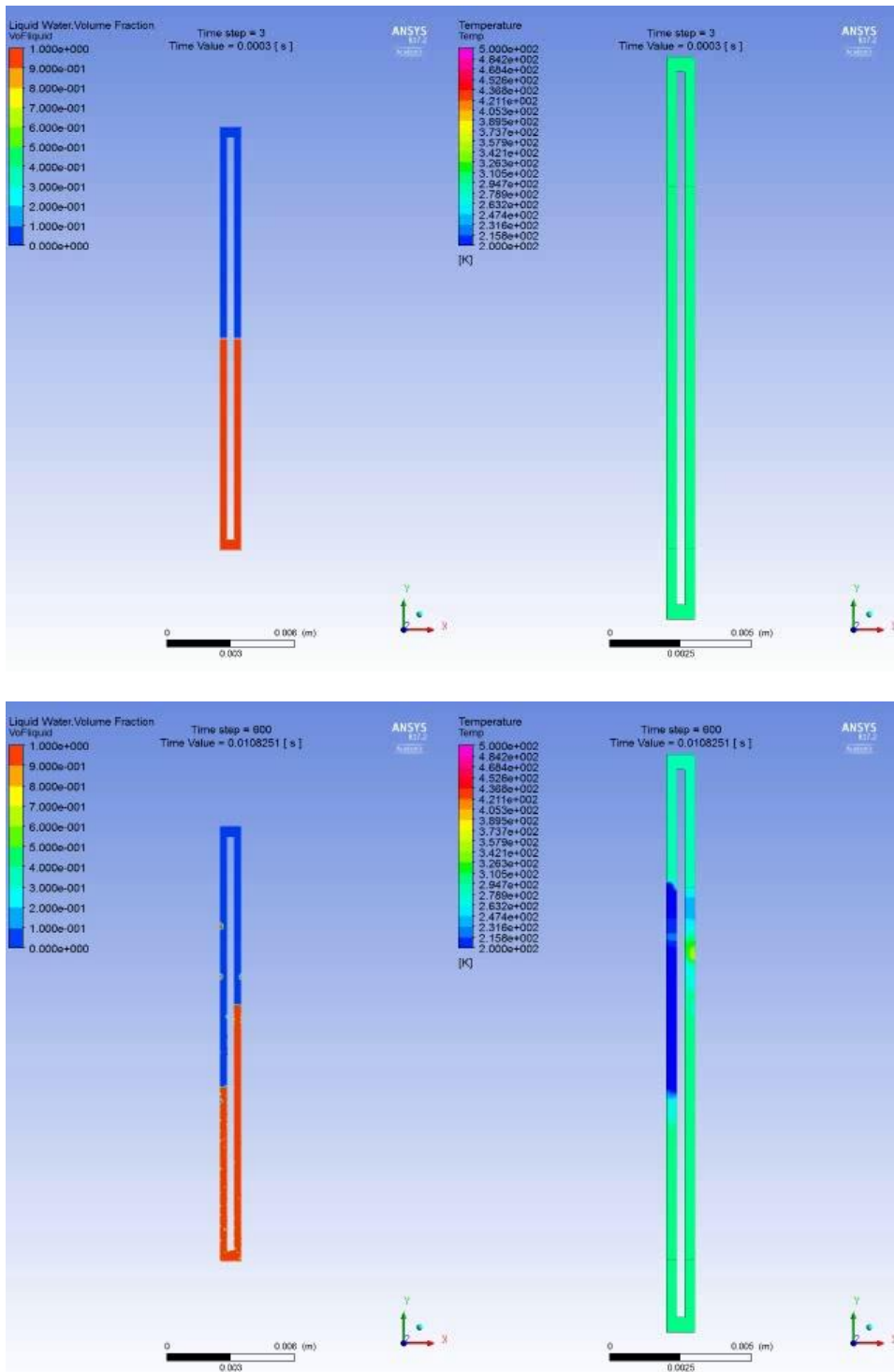


Figure I.6. Temperature and liquid water volume fraction side-by-side at different time steps of the second case.

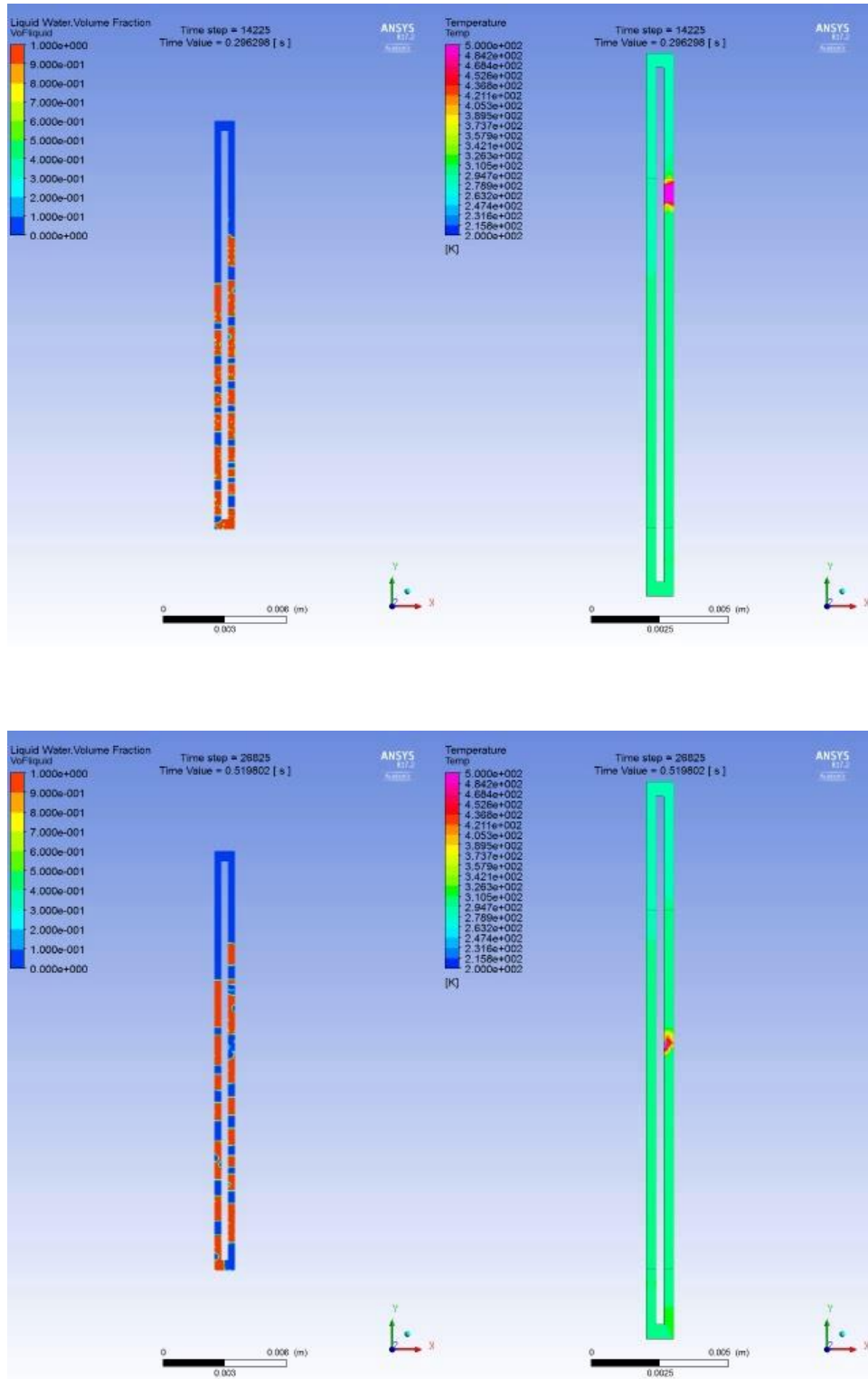


Figure I.7. Temperature and liquid water volume fraction side-by-side at different time steps of the second case.

28803 time steps were realized for this case before it diverged. The results showed formation of liquid slugs and vapour plugs. They oscillated without a preferential direction. On the other hand, temperature remained stable at the exceptions of the high variations visible. These variations probably resulted from numerical artefacts.

I.4 Conclusion

The present cases failed to represent actual working μ OHP. Furthermore, the model presented here only include the liquid of the μ OHP, not the substrate. This last might have an important role in the overall performance of the device. One solution would be to implement of Fluid-Solid Interaction using ANSYS' workbench. The model would include two sub-models, one for the transient heat conduction in the solid and one for the liquid, as presented here, which would be iteratively solved. Each model would then determine the conditions for the next step of the other sub-models.

Copyright Licenses

List of used figures with author's credits and permission identified at the time of publication. Those who recognize themselves in uncredited illustrations are invited to make it known. The author thanks all those who agreed to give their authorisation for reproduction and adaptation of their illustration in this work, and all others for their comprehension.

Figure 2.5(a)	© 1999-2021 CERN. (License: CC-BY-3.0)
Figure 2.5(b)	© IOP Publishing Ltd and Sissa Medialab srl. Reproduced by permission of IOP Publishing. All rights reserved. Reproduced with permissions of authors.
Figure 2.6(a)	© 2021 EP Department / CERN (https://copyright.web.cern.ch/)
Figure 2.6(b)	© 2013-2021 CERN (License: CC-BY-3.0)
Figure 2.8(a)	RightLink 5030170076834. Reprinted from A. Mapelli, "Microfabricated silicon substrates for pixel detectors assembly and thermal management a.k.a. Silicon Microchannel Cooling Plates", 2020, with the permission of Elsevier B.V.
Figure 2.8(b)	© 2019 CERN. (License : CC BY 3.0). Reprinted from G.A. Rinella et al., "The NA62 GigaTrack: a low mass high intensity beam 4D tracker with 65 ps time resolution on tracks", JINST, 2019. Published by IOP Publishing Ltd on behalf of Sissa Medialab.
Figure 2.9(a)	Reproduced with permissions of authors.
Figure 2.9(b)	RightLink 5030170076834. Reprinted from A. Mapelli, "Microfabricated silicon substrates for pixel detectors assembly and thermal management a.k.a. Silicon Microchannel Cooling Plates", IWASI, 2020, with the permission of Elsevier B.V.
Figure 2.10(a)	CC BY-NC-ND 4.0. Reprinted from O.A. De Aguiar Francisco et al. "Microchannel Cooling techniques at LHCb", PoS 26th International Workshop on Vertex Detectors (Vertex 2017), 2018.
Figure 2.10(b)	Reproduced with permissions of authors. Image courtesy of NIKHEF. Original content from O. A. De Aguiar Francisco, "Microchannel cooling techniques for the LHCb VELO Upgrade", 26th International Workshop on Vertex Detectors (Vertex 2017), 2017.
Figure 2.10(c)	Reproduced with permissions of authors.
Figure 2.11(a-b)	© 2013 IEEE. Reprinted, with permission, from G.Fiorenza et al. "An innovative polyimide microchannels cooling system for the pixel sensor of the upgraded ALICE inner tracker", 2013.
Figure 2.12	© 2013-2021 CERN (License: CC-BY-3.0)

Figure 2.13(a-h)	© IOP Publishing Ltd and Sissa Medialab srl. Reproduced with permission of IOP Publishing and authors. All rights reserved.
Figure 2.14(a-b)	RightLink 5030170076834. Reprinted from A. Mapelli, “Microfabricated silicon substrates for pixel detectors assembly and thermal management a.k.a. Silicon Microchannel Cooling Plates”, 2020, with the permission of Elsevier B.V.
Figure 2.21	© 2014 International Cryocooler Conference Inc., Boulder, Colorado. All rights reserved.
Figure F.3	CCC MarketPlace License ID 1112600-1. From S. Jun and S. J. Kim, “Experimental study on a criterion for normal operation of pulsating heat pipes in a horizontal orientation”, 2019; reprinted by permission of the American Institute of Aeronautics and Astronautics, Inc.
Figure H.1	Adapted, with the permission of the author, from N. S. Dhillon, “Micro-Columnated Loop Heat Pipe: The Future of Electronic Substrates,” PhD Thesis, 2012.
Figure H.2	© 2018 IEEE. Reprinted, with permission, from Y.Luo et al., “Packaging flat micro heat pipe using low melting point alloy”, in 19th ICEPT, 2018.
Figure I.2	Ikosaeder – 11 march 2014. (License: CC BY-SA 3.0)

Curriculum Vitae

Personal Information

Name	Timothée Frei
Nationality	Swiss

Education

2017 – 2021	PhD Student, Space Innovation, Swiss Federal Institute of Technology Lausanne (EPFL), Switzerland.
2017	Master of Science in Mechanical Engineering, Minor In Space Technologies, Swiss Federal Institute Of Technology Lausanne (EPFL), Switzerland.
2015	Bachelor of Science in Mechanical Engineering, Swiss Federal Institute of Technology Lausanne (EPFL), Switzerland.

Experience

2017 – 2021	European Organization for Nuclear Research (CERN), Experimental Physics Department (EP-DT-DD), Geneva, Switzerland – PhD Student, Part-time.
2017 – 2021	PhD Student, Swiss Centre for Electronics and Microtechnology (CSEM), Neuchâtel, Switzerland – PhD Student – Part-time.
2016 – 2019	ARES II experiment (ESA's REXUS/BEXUS Program), Microfluidic experiment aboard a sounding rocket – Payload Manager.
July – Sept. 2016	European Organization for Nuclear Research (CERN), Geneva – internship.